Stable Isotope Composition of Surface Vapour and Precipitation at the Southwest Coast of Norway

Yongbiao Weng

Thesis for the degree of Philosophiae Doctor (PhD)
University of Bergen, Norway
2021

UNIVERSITY OF BERGEN

Stable Isotope Composition of Surface Vapour and Precipitation at the Southwest Coast of Norway

Yongbiao Weng

Thesis for the degree of Philosophiae Doctor (PhD)
at the University of Bergen

Date of defense: 16.04.2021

Year: 2021

Title: Stable Isotope Composition of Surface Vapour and Precipitation at the Southwest Coast of Norway

Name: Yongbiao Weng

Print: Skipnes Kommunikasjon / University of Bergen

Scientific environment

This study has been carried out at the Geophysical Institute, University of Bergen and the Bjerknes Centre for Climate Research. The work has been supported by the Research Council of Norway through projects FARLAB (grant no. 245907) and SNOWPACE (grant no. 262710). I have been enrolled in the Research School on Changing Climates in the Coupled Earth System (CHESS).

FARLAB
Facility for advanced isotopic research and monitoring of weather, climate and biogeochemical cycling

Forskningsrådet

CHESS
Research school on changing climates in the coupled earth system

BJERKNES CENTRE
for Climate Research

UNIVERSITY OF BERGEN
Faculty of Mathematics and Natural Sciences

Acknowledgements

First and foremost, I want to express my sincere gratitude to *Harald Sodemann*, for being inspiring and encouraging, both as a scientist and a teacher. Thanks for being supportive at all times, including the extension period. Thanks also for including me in the fieldwork on two cruises.

I also want to thank *Idar Barstad*, for inspiring alternative thinking and providing good suggestions at the mid-stage of my PhD.

Many people have scientifically contributed to the completion of this work. I want to express my appreciations to *Pål Tore Mørkved* for the great support in the laboratory and joyful discussions, to *Astrid Fremme* and *Mika Lanzky* for the help on WaterSip tool, to *Hans-Christian Steen-Larsen* and *Anne-Katrine Faber* for helpful discussions.

I want to thank the colleagues at GFI in general for shaping a supportive and cheerful atmosphere, and for arranging regular and diverse social activities. In particular, I would like to thank my first and longest officemate *Astrid*, for both the laugh in the office and the fun events arranged outside the office. I also thank our continuously expanding "IsoMet" group for the happy times during the meetings and retreats. Thanks to *Omar Guernaoui* and *Peter Yu Feng Siew* for the happy accompanies during irregular working hours.

The PhD journey would not be so enjoyable without inspiring times outside the office. With this regard, I want to thank among others *Rebecca Gugerli*, *João Hackerott*, and *Lucas Höppler* for the happy exploration tours at the early stage of my PhD. Also, thank *Erica Madonna* and *Paul Hezel* for adding extra joys now and then.

I would like to thank *Harald*, *Paul*, *Alena Dekhtyareva*, *Alexandra Touzeau*, and *Maria Arvaniti*, for providing feedback on the thesis manuscript.

Special thanks to Prof. *Lide Tian*, my previous supervisor at the Chinese Academy of Science, for encouraging me to pursue the study abroad back to 2011.

Last but not least, I want to thank my parents for their incredible efforts to raise all their kids and to have firmly supported every one of us to receive an education even though they are barely able to read.

It has been a great experience to live in this lovely town surrounded by nature. I have enjoyed this journey very much and will treasure the memories of the sea, the mountains, and of course, most relevantly, the rain.

Yongbiao Weng
Bergen, 20 December 2020

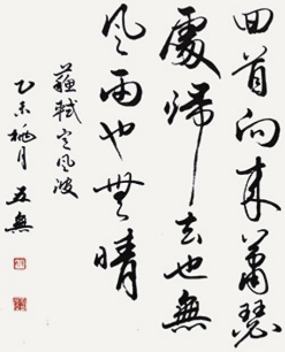

Looking back, I see the dreary beaten track,
I'll be gone,
So will the wind, the rain, and the shining sun.

Su Shi (1037-1101, Northern Song Dynasty)

Abstract

A better understanding of the water cycle has become even more crucial under the present condition of climate change. The stable isotopes of hydrogen and oxygen have been used for decades as powerful tracers to provide insights into the water cycle. While substantial understanding has been achieved, disputes remain on what processes set the observed isotope signal. Besides, albeit its great usefulness, no systematic isotope observations have existed in western Norway, which is a midlatitude location influenced by distinct weather systems (e.g. North Atlantic cyclones, cold air outbreaks) and swift precipitation formation.

In this thesis, I present a systematic isotope observation of surface vapour and precipitation at the southwest coast of Norway between December 2016 and November 2019. The observation consists of high-resolution samplings for targeted weather events and long term (quasi-daily) routine samplings. To facilitate these observations, a stable water isotope laboratory with 3 laser spectrometers has been established.

To ensure high-quality data acquisition, we thoroughly assess the instrument performance in many aspects. One important aspect is the correction of the *mixing ratio dependency*. In Paper I, we systematically investigate the mixing ratio dependency in a range from 500 to 23 000 ppmv. We find that the mixing ratio dependency systematically varies with the isotope composition of measured vapour. We refer this as *isotope composition-mixing ratio dependency* and have developed a scheme to correct for this dependency-introduced bias. Using in situ measurements from an aircraft measurement, we demonstrate the importance of the correction at low mixing ratios. Stability tests over up to 2 years indicate that the first-order dependency is a constant instrument characteristic that may be primarily related to spectroscopy.

In Paper II, we present a case study of a 24-h land-falling "atmospheric river" event on 07 December 2016, with high-resolution paired measurements of near-surface vapour and precipitation stable isotopes. We observe a stretched, "W"-shaped evolution of isotope signals. Combining surface meteorological observations, we identify the influences on the isotopic signals from below-cloud processes, weather system characteristics, transport history, and moisture source conditions. We thus revisit the interpretations of previous studies on such precipitation events and emphasise that cloud microphysics and below-cloud processes are important factors influencing surface precipitation isotope signals.

Paper III presents the 3-year paired observation of surface vapour and precipitation stable isotopes. The isotopic variation on different time scales is investigated. We observe a weak diurnal variation and a moderate seasonal variation. On the multi-day time scale, we observe a clear association between the isotope signals and the regional weather regimes. We also compare the *d*-excess observations with model predictions based on Lagrangian moisture source diagnostic and previously suggested d-RH$_{SST}$ relationships. We find that the models correctly reproduce the variation patterns, but with substantial offsets. While further investigations are required, our observations are of great importance for extending the sparse existing isotope observation network and enabling potential comparison with different models.

In a combination of the three papers above, this work makes an important contribution to the interpretation of near-surface stable isotope observations on a range of time scales, from sub-hourly to synoptic, to inter-annual. It highlights the value of stable isotope observations for advancing our knowledge of the atmospheric hydrological processes.

List of papers

This thesis consists of an introductory part and three scientific papers. Chapter 1 presents the motivation and objectives. Background of stable water isotopes is provided in Chapter 2, while the study region and the regional atmospheric circulations are described in Chapter 3. Chapter 4 presents instrumentation, data and methods, and Chapter 5 summarises the main results. Discussions and further remarks are given in Chapter 6. The papers included in this thesis (Chapter 7) are:

I. **Yongbiao Weng**, Alexandra Touzeau, and Harald Sodemann (2020), *Correcting the impact of the isotope composition on the mixing ratio dependency of water vapour isotope measurements with cavity ring-down spectrometers*, Atmospheric Measurement Techniques, 13 (6), 3167–3190, `https://doi.org/10.5194/amt-13-3167-2020`

II. **Yongbiao Weng**, Harald Sodemann, and Aina Johannessen (2020), *High-resolution stable isotope signature of a land-falling atmospheric river in southern Norway*, Weather and Climate Dynamics Discussions, `https://doi.org/10.5194/wcd-2020-58`

III. **Yongbiao Weng** and Harald Sodemann (in preparation), *Stable isotope composition of surface vapour and precipitation at the southwest coast of Norway*

Other relevant contributions

(A) Iris Thurnherr, Anna Kozachek, Pascal Graf, **Yongbiao Weng**, Dimitri Bolshiyanov, Sebastian Landwehr, Stephan Pfahl, Julia Schmale, Harald Sodemann, Hans Christian Steen-Larsen, Alessandro Toffoli, Heini Wernli, and Franziska Aemisegger (2020), *Meridional and vertical variations of the water vapour isotopic composition in the marine boundary layer over the Atlantic and Southern Ocean*, Atmospheric Chemistry And Physics, 20, 5811–5835, `https://doi.org/10.5194/acp-20-5811-2020`

(B) Renfrew, I. A., Pickart, R. S., Våge, K., and 63 others including **Weng, Y.** (2019), *The Iceland Greenland Seas Project*, Bulletin of the American Meteorological Society, 100 (9), 1795–1817, `https://doi.org/10.1175/BAMS-D-18-0217.1`

Contents

Chapter 1

Introduction

A better understanding of the weather and climate systems are always desired because of their great impacts on society. This has certainly become even more crucial under the present condition of climate change. Climate change, or global warming, is observed to be most substantial at high latitudes (*IPCC*, 2014). In a warming climate, a spin-up of the water cycle and thus a higher precipitation amount is expected in some regions. Globally speaking, the changes in the precipitation pattern will redistribute the water resources, leading to potential floods and droughts. Locally, an increasing trend in the precipitation amounts has been observed in most areas of Norway during the period 1895-2004 (*Hanssen-Bauer*, 2005). Along with the precipitation amount, extreme precipitation events have also become more frequent (*Alfnes and Førland*, 2006; *Groisman et al.*, 1999). Some precipitation extremes have caused severe infrastructure damage (e.g. *Steensen et al.*, 2011; *Stohl et al.*, 2008). To anticipate the changes in precipitation in a warming climate, it is important to solidify our understanding of the relevant physical mechanisms (e.g. moisture origin, moisture transport, and cloud microphysics) leading to precipitation.

The stable isotopes of hydrogen and oxygen have been used for decades as powerful tracers to improve our understanding of the water cycle (*Dansgaard*, 1964; *Gat*, 1996). Water molecules exist under various isotopic forms and the most abundant stable water isotopologues are $H_2^{16}O$, $H_2^{18}O$ and $HD^{16}O$. Owing to mass and symmetry differences, these water species have slightly different physical properties (i.e. saturation vapour pressure, molecular diffusivity) and are thus redistributed at each phase change. This redistribution is called *isotope fractionation* and it will cause an enrichment or depletion of heavy isotopes. For example, water vapour is relatively depleted in heavy isotopes comparing with the water from which it originates. The isotopic enrichment or depletion in various waters is normally quantified as the deviation from a reference water: $\delta = (R_{\text{sample}}/R_{\text{VSMOW}} - 1)1000‰$, where R (e.g. $^{18}R = [H_2^{18}O]/[H_2^{16}O]$) is the *isotope ratio*, and VSMOW is the international reference water (Vienna Standard Mean Ocean Water; *IAEA*, 2009). Since the isotope fractionation depends on the physical conditions (e.g. temperature, saturation status) in which it occurs, observations of stable water isotopes can provide information of the atmospheric hydrological processes.

A brief historical overview on stable water isotope studies

In the 1950s, systematic investigations emerged to study the stable isotope abundances in meteoric waters and their driving factors (*Dansgaard*, 1953, 1954; *Epstein*, 1956, 1953; *Gonfiantini and Picciotto*, 1959). On the basis of some 400 water samples collected globally from rivers, lakes, and precipitation, *Craig* (1961) noted that the relationship between δ^{18}O and δD in worldwide natural meteoric waters can be represented by $\delta D = 8\delta^{18}O + 10$, which is later referred to as the *Global Meteoric Water Line* (GMWL). The slope of the GMWL arises from equilibrium isotope fractionation, whereas the intercept reflects the deviation from equilibrium fractionation, or in other words, a result of non-equilibrium isotope fractionation. The intercept varies at different evaporation conditions. It is later defined by *Dansgaard* (1964) in a general manner as a secondary parameter, namely *deuterium excess* or *d-excess*.

To understand their temporal and spatial variations, the isotope compositions of precipitation have been monitored worldwide. The most influential effort of such kind is the *Global Network of Isotopes in Precipitation* (GNIP) organised by the International Atomic Energy Agency (IAEA) and the World Meteorological Organization (WMO) at a monthly scale since 1960. Through the global observations, several leading isotope effects have been identified (*Araguás-Araguás et al.*, 2000; *Dansgaard*, 1964; *Rozanski et al.*, 1993). The most fundamental isotope effect is the *temperature effect*, where the temperature difference influences the saturation status of air mass and thus drives the gradual rainout of heavy isotopes. The temperature effect manifests itself in the following descriptive forms: a latitude effect, a continental effect, an altitude effect, and a seasonal effect. The other isotope effect emerging in many tropical islands and monsoon climate regions is the so-called *amount effect*, which describes the negative correlation between the amount of precipitation at the surface and the heavy isotope content in precipitation (*Dansgaard*, 1964; *Lee and Fung*, 2008; *Rozanski et al.*, 1993). These established relationships between isotope variations in precipitation and changing climate conditions (in particular the temperature) have since been used as the basis for interpreting paleoclimate proxies such as ice cores (e.g. *Johnsen et al.*, 1989).

While it is important to understand the long-term isotopic variation and its implication for the past climate conditions, it is also highly relevant to study the short-term isotopic variation in order to understand present-day, short-lived weather systems.

On the synoptic time scale, studies reveal that the precipitation isotopes can depict strong variations among events (*Crawford et al.*, 2013; *Guan et al.*, 2013; *Risi et al.*, 2008) as well as within a single event (*Coplen et al.*, 2008, 2015; *Miyake et al.*, 1968). For example, analyses of single rainfall events have revealed variations in δD of 58 ‰ in California at sub-hourly time resolution (*Coplen et al.*, 2008). A higher-resolution study in Australia measured variations of up to 95 ‰ within a single 4-h period (*Munksgaard et al.*, 2012). Several typical intra-event trends, such as "L", "V", and "W" shapes, have been identified by *Muller et al.* (2015). By testing how well these substantial and fast isotopic variations are reproduced in the numerical weather simulations, it may be possible to constrain the model's parametrisations of sub-grid scale physics (*Bony et al.*, 2008; *Risi et al.*, 2008), which are hard to achieve using conventional meteorological observations such as temperature and humidity (*Field et al.*, 2014; *Yoshimura et al.*, 2014).

In the last decade, owing to the availability of new spectroscopic technologies (*Crosson*, 2008; *Kerstel*, 2004; *Kerstel and Gianfrani*, 2008), have the investigations of stable isotopes of water vapour dramatically increased (*Galewsky et al.*, 2016; *Steen-Larsen et al.*, 2015, 2014a). Comparing with the precipitation, the observation of water vapour isotopes yields several benefits. (1) While precipitation is an integrated product collected mainly on the ground, the water vapour is present throughout all stages of the water cycle. (2) The vapour observation can be conducted continuously and not restricted to precipitation periods. (3) The vapour measurements can be directly carried out in the field (e.g. on mobile platforms such as ship and aircraft), or even in a remote location under unmanned conditions. (4) The vapour measurement is in real-time and at a high time resolution (in the order of seconds). With all the above advantages, the observation of water vapour isotopes has been conducted at various locations of interest such as at ocean surface (e.g. *Benetti et al.*, 2017; *Bonne et al.*, 2019) and in the lower troposphere (e.g. *Sodemann et al.*, 2017), hence adding information on how water is evaporated, transported, mixed, and eventually condensed in clouds.

Research gaps

Although fundamental understanding has been achieved, disputes remain in the scientific community on what sets the isotope compositions. For example, *Coplen et al.* (2008) have sampled the precipitation during a land-falling "atmospheric river" event in southern California at a time resolution of 30 min. They interpreted the isotopic variation during the rainfall event in relation to cloud height, using a Rayleigh distillation model. Investigating the same event, with an isotope-enabled weather prediction model, *Yoshimura et al.* (2010) instead emphasised the roles of horizontal advection and post-condensation processes. This scientific controversy and other studies (e.g. *Pfahl et al.*, 2012) have also demonstrated the value of high temporal-resolution isotope observations for evaluating isotope-enabled circulation models. However, such dedicated isotope observations have been limited. We hereby present a simultaneous observation of surface vapour and precipitation isotopes obtained at a time resolution of 10∼30 min during an "atmospheric river" event in southern Norway, aiming to shed new light on the so-far unresolved controversy and at the same time to provide a valuable dataset for future model evaluation (Paper II).

In addition to understand the mechanisms within a specific precipitation event, it is also important to examine the local isotopic variability and to understand its driving forces in a long term. To this end, I present 3 years near-continuous measurements of the stable isotope composition of surface vapour and precipitation at our study site in Bergen and investigate the isotopic variability at different time scales (Paper III).

To facilitate the isotope observations, we have established a stable water isotope laboratory and deployed three laser spectrometers. To ensure data quality, we have thoroughly assessed the instrument performance and established high-quality laboratory routines. This is particularly important for in situ water vapour measurement at our study site, where the water mixing ratio varies from 1500 ppmv in cold and dry days to nearly 20 000 ppmv in warm and humid days. With this wide range, the isotope measurement suffers from a mixing-ratio-dependent deviation, which needs to be carefully characterised and corrected for (Paper I).

Being located in the midlatitude, our study site at Bergen is influenced by various weather systems, from the dominating North Atlantic cyclones to the marine cold air outbreaks from polar regions. A rather direct oceanic moisture origin and distinct circulation patterns make our site a natural laboratory to study the driving mechanisms of the isotopic variations. Also, Bergen is located in between several existing monitoring sites (i.e. Bermuda, south Greenland, Iceland, Svalbard, and Siberia) with long-term vapour isotope time series, enabling potential future comparison with different models.

Objectives and outline

The overall aim of the work is to gain insights into the atmospheric hydrological cycle through the stable isotope observations in surface vapour and precipitation. The general questions are: (i) What do we learn from paired measurements of surface vapour and precipitation? (ii) How does the vapour help to learn about what the precipitation means? (iii) Knowing that many factors have been involved between moisture source and the final precipitation collected on the ground, how can we interpret the measured isotope signal? With these questions in mind, I carried out this study, from characterising the instruments, establishing and maintaining the observation platform, to routine sampling and measuring, and finally analysing and interpreting the observations. Specifically, the following research questions have been addressed:

1. *How to do paired isotope measurements?*

   The laser spectrometers are systematically characterised before being deployed. One important aspect, the impact of the isotope composition on the mixing ratio dependency, is closely investigated and corrected for using a proposed scheme (Paper I). Using an established calibration routine, isotope compositions of in situ surface vapour are continuously monitored. On the same site, precipitation is collected at a high time resolution (10∼30 min; Paper II) for targeted events and on a quasi-daily basis in a long term (Paper III).

2. *What processes influence the paired isotope signals of a weather event?*

   This is mainly addressed with a detailed case study on a land-falling "atmospheric river" event (Paper II). Besides, several additional weather events have been observed and analysed (Appendix C; *Pellaud*, 2018).

3. *What is the long-term isotopic variability at the southwest coast of Norway?*

   A 3-year time series of isotope observation of surface vapour and precipitation is presented and its variability on different (diurnal/multi-day/seasonal) time scales is investigated (Paper III).

4. *What do we learn from the comparison between the observations and the models?*

   A zero-dimensional Rayleigh model and a one-dimensional below-cloud interaction model are used to interpret the isotopic evolution during a precipitation event (Paper II). The Craig–Gordon evaporation model with closure assumption and an empirical linear d-RH$_{SST}$ relationship are used to estimate d-excess at moisture sources (Paper III). The performances of these simple isotope models are discussed in comparison with the observations.

In the following chapter, the concepts of stable water isotopes are introduced and the isotope processes in the atmospheric water cycle are reviewed. Then, the study region and the regional atmospheric circulations are described (Chapter 3). In Chapter 4, the instrumentation for meteorological and isotopic observations is presented, along with a Lagrangian tool for moisture source diagnostic. The main results of this work are summarised in Chapter 5, followed by discussions and further remarks (Chapter 6). In the end, the three papers produced from this work are provided (Chapter 7).

Chapter 2

Stable water isotopes

This chapter briefly reviews the stable water isotopes. First, the basic concepts and notations are introduced (Sect. 2.1). Then, the principles of isotope fractionation are explained (Sect. 2.2). Next, the isotope processes occurring in the atmospheric water cycle are described (Sect. 2.3). Finally, an overview of simple isotope models is provided (Sect. 2.4).

2.1 Basic concepts

Isotopes are atoms whose nuclei contain the same number of protons but a different number of neutrons. Isotopes occupy the same position in the periodic table of the elements and can be simply denoted in the form of ^{m}E, where m denotes the mass number (sum of protons and neutrons). Naturally occurring oxygen has three stable isotopes: ^{16}O, ^{17}O, and ^{18}O. Naturally occurring hydrogen has also three isotopes: ^{1}H (abbreviated to H), ^{2}H (deuterium, abbreviated to D), and ^{3}H (tritium, abbreviated to T). The natural abundances of the isotopes in water are shown in Table 2.1.

Table 2.1: Natural abundances of the oxygen and hydrogen isotopes in water (Gat et al., 2001).

Oxygen isotope	Abundance [%]	Hydrogen isotope	Abundance [%]
^{16}O	99.759	^{1}H	99.985
^{17}O	0.037	^{2}H (D)	0.015
^{18}O	0.204	^{3}H (T)*	<10^{-15}

* Radioactive isotope (unstable).

Water is in fact a mixture of isotopically distinct molecular species, among them nine stable ones:

$$\begin{array}{lll} \mathbf{H_2^{16}O} & \mathbf{HD^{16}O} & D_2^{16}O \\ H_2^{17}O & HD^{17}O & D_2^{17}O \\ \mathbf{H_2^{18}O} & HD^{18}O & D_2^{18}O \end{array}$$

The vast majority of water molecules in nature is $H_2^{16}O$, followed by $H_2^{18}O$ and $HD^{16}O$. These three most common species are the focus of most studies on the hydrological cycle.

The isotope ratio (R)

Heavy isotopes (^{17}O, ^{18}O, D) have very small absolute abundances (Table 2.1) and are also called rare isotopes. Light isotopes (^{16}O, H) have dominating absolute abundances, and are also called abundant isotopes. To intuitively quantify the abundance of isotopes in a reservoir, it is favourable to introduce the isotope ratio R, which is defined as:

$$R = \frac{\text{abundance of rare isotope}}{\text{abundance of abundant isotope}}$$

To be more specific, there are two definitions of the isotope ratio. One is *molecular isotope ratio*, where the isotope ratio is determined using the abundances of the isotopic water molecules (i.e. [$H_2^{16}O$], [$H_2^{18}O$], [$HD^{16}O$]). The value of molecular isotope ratio refers, for instance, to the measurement of isotope ratios by recently developed laser spectrometry. The other definition is *atomic isotope ratio*, where the abundances of the isotopic atoms (i.e. [^{16}O], [^{18}O], [^{1}H], [^{2}H]) are used. The value of atomic isotope ratio refers to the conventional measurement involving mass spectrometry. Nonetheless, in all practical cases, the difference between the molecular isotope ratio and the atomic isotope ratio is much smaller than the measurement precision, principally owing to the very low abundances of the rare isotopes (*Kerstel*, 2004). It can be shown that the isotope ratios by the two definitions are equal to a first-order approximation, and the approximation is even better when using δ values (*Mook and De Vries*, 2001). Unless mentioned otherwise, the definition of molecular isotope ratio is used here as almost all of the measurements in this work are based on laser spectrometry.

The δ notation

The absolute value of R is very small due to the small abundance of rare isotopes. It is much easier to express the relative or absolute difference between two samples. Fortunately, the biggest interest is also given to the isotopic variations among different waters. Therefore, the isotopic enrichment or depletion in a water sample is often converted to its deviation from that of a common standard. The deviation is quantified in terms of the δ notation as:

$$\delta = \frac{R_{\text{sample}} - R_{\text{standard}}}{R_{\text{standard}}} \cdot 1000‰ = \left(\frac{R_{\text{sample}}}{R_{\text{standard}}} - 1 \right) \cdot 1000\ ‰, \tag{2.1}$$

where R_{sample} and R_{standard} refer to the isotope ratios of the sample and the standard, respectively.

The δ values are usually expressed in per mil (‰) to obtain convenient numerical values. For atmospheric waters, the internationally-accepted standard is the Vienna Standard Mean Ocean Water (VSMOW) defined and distributed regularly by the International Atomic Energy Agency (IAEA) in Vienna (*IAEA*, 2009). Typical δ values of water in the hydrological cycle are shown in Table 2.2.

2.2 Stable isotope fractionation

In this section, I provide a brief introduction to the principles of isotope fractionation. More comprehensive explanations can be found in e.g. *Mook and De Vries* (2001), *Gat et al.* (2001) and *White* (2015).

Table 2.2: Typical δ values of water in the hydrological cycle (Mook and De Vries, 2001).

	δ^{18}O [‰]	δD [‰]
VSMOW	0	0
Ocean water	-6 ∼ 3	-28 ∼ 10
Actic sea ice	-3 ∼ 3	0 ∼ 25
Marine moisture	-15 ∼ -11	-100 ∼ -75
Lake Chad	8 ∼ 16	15 ∼ 50
Alpine glaciers	-19 ∼ -3	-130 ∼ -90
Greenland	-39 ∼ -25	<-200 ∼ -150
Antarctica	-60 ∼ -25	<-200 ∼ -150
(Sub)Tropical precipitation	-8 ∼ -2	-50 ∼ -20
Mid-latitude rain*	-10 ∼ -3	-80 ∼ -20
Mid-latitude snow*	-20 ∼ -10	-160 ∼ -80

* Summer/winter precipitation at IAEA, Vienna.

2.2.1 Theoretical background

Different isotopic water molecules do not behave identically. According to the quantum theory, the mass of an atom affects its vibrational (as well as rotational and translational) motions therefore the strength of chemical bonds and the physiochemical properties (e.g. saturation vapour pressure) of the molecule (*Criss*, 1999). The molecule containing heavy isotopes has a lower vibrational frequency than the molecule containing light isotopes, and will thus have a lower zero-point energy (the energy of the molecule at absolute zero temperature in the ground state). This means that the bonds formed by the heavy isotopes are stronger than bonds involving light isotopes. Therefore, during a phase change or a chemical reaction, molecules bearing the heavy isotopes will, in general, react less readily than those bearing the light isotopes (*Hoefs*, 2004). This redistribution of isotopes between two substances or two phases of the same substance with different isotope ratios is called *isotope fractionation*.

The isotope fractionation factor (α, ε)

The fractionation effect can be quantified by the isotope fractionation factor α, which is defined as the ratio between the isotope ratio in the new compound/phase and that in the original compound/phase in a chemical reaction or a physical phase transition. For the study of atmospheric waters, α is considered for the phase changes between vapour (v), liquid (l), and solid water (s). For example, the isotope fractionation factor for an evaporation process is given as:

$$\alpha_{vl} = \frac{R_v}{R_l} = \frac{\delta_v + 1}{\delta_l + 1}. \tag{2.2}$$

The isotope fractionation effect is normally small, i.e. $\alpha \approx 1$. Thus the deviation of α from 1, ε, is also often used (similar to the δ value, ε is also expressed in [‰]):

$$\varepsilon = (\alpha - 1) \cdot 1000\ ‰, \tag{2.3}$$

where $\varepsilon > 0$ ($\alpha > 1$) indicates the enrichment and $\varepsilon < 0$ ($\alpha < 1$) the depletion of the rare isotopes in the new phase.

The actual value of the fractionation factor depends on the isotopic species, the temperature and the rate of reaction. (1) Due to the bigger mass difference, the fractionation factor (ε) is roughly 8 times stronger for D than for ^{18}O. (2) The value of fractionation factor decreases as the temperature increases (*Majoube*, 1971a; *Merlivat and Nief*, 1963). For instance, *Majoube* (1971a) determined an equilibrium fractionation factor $\alpha = 1.0117$ at 0 °C and $\alpha = 1.0098$ at 20 °C for the transition from liquid to vapour. This can be explained by the decreasing difference of the vibrational frequency between light and heavy isotopes due to the increasing vibration as temperature rises. At sufficiently high temperatures, isotope fractionation can disappear. (3) An extra fractionation effect can be introduced by the kinetic fractionation where the molecules containing light isotopes react faster.

2.2.2 Equilibrium fractionation

It is important to distinguish between two kinds of isotope fractionation: *equilibrium fractionation* and *kinetic fractionation*. Equilibrium (also called thermodynamic) fractionation, is the isotope redistribution involved in a thermodynamic equilibrium reaction. It is a fully reversible process and is temperature dependent. For the phase changes of water, given sufficient long reaction time, an isotopic equilibrium between the two phases will be reached. In nature, equilibrium fractionation is considered to occur during the evaporation or condensation under saturated conditions (e.g. during formation of liquid cloud). The equilibrium fractionation factor can be determined by laboratory experiments and reasonable agreement has been shown between experiment data and thermodynamic calculations (e.g. *Richet et al.*, 1977). The isotopic evolution during equilibrium fractionation process can be simulated with a classical Rayleigh distillation model (see Appendix B.1).

2.2.3 Kinetic or non-equilibrium fractionation

Kinetic fractionation are normally associated with fast, incomplete, or one-direction (i.e. irreversible) physical/chemical processes like pure evaporation, diffusion, dissociation reactions, and biologically mediated reactions (*White*, 2015). Normally, molecules containing light isotopes have lower dissociation energies and will react faster. The reaction rates (or diffusion velocities) of water molecules are: $D_{\mathrm{H_2^{16}O}} > D_{\mathrm{HD^{16}O}} > D_{\mathrm{H_2^{18}O}}$. Isotope fractionation process in nature, e.g. evaporation of ocean or other water bodies, is usually neither purely kinetic nor purely equilibrium; it is also referred to as *non-equilibrium fractionation*.

Non-equilibrium fractionation has important consequences for evaporation processes in nature. The extent of non-equilibrium fractionation depends mainly on the humidity gradient over the water surface and sea surface temperature (*Merlivat and Jouzel*, 1979; *Pfahl and Sodemann*, 2014). It induces a change in a second-order parameter, deuterium excess (the other analogous second-order parameter is ^{17}O-excess, which is briefly reviewed in Appendix A).

The deuterium excess (*d*-excess)

The deuterium excess is defined as the surplus of deuterium caused by the deviation from the equilibrium fractionation (*Dansgaard*, 1964):

$$d = \delta\mathrm{D} - 8\delta^{18}\mathrm{O}. \tag{2.4}$$

On a global scale, the ratio of the two equilibrium fractionation factors, $\varepsilon_D/\varepsilon_{^{18}O}$, is approximately 8 (*Craig*, 1961). The d-excess quantifies the deviation from the ratio expected during global equilibrium conditions.

Equilibrium fractionation is usually regarded to not change the d-excess. Strictly said, this is not correct. The ratio $\varepsilon_D/\varepsilon_{^{18}O}$ is temperature dependent and varies between 8.6 at 0 °C and 7.7 at 30 °C (*Majoube*, 1971a). Due to the definition of d-excess, this can cause slight change of d-excess even during equilibrium fractionation. This artefact can be eliminated by using an *adjusted d-excess* which is defined as (*Pfahl and Wernli*, 2008):

$$d_{\mathrm{adj}} = \delta \mathrm{D} - \frac{\delta \mathrm{D}_{\mathrm{eq}}(T)}{\delta^{18}\mathrm{O}_{\mathrm{eq}}(T)} \delta^{18}\mathrm{O}. \tag{2.5}$$

Nevertheless, assuming a steady source origin and insignificant variations of the water surface temperature, the artefact is insignificant and the values of d-excess are dominant by the non-equilibrium fractionation. Under this approximation and the consideration that equilibrium fractionation occurs during formation of liquid cloud, the initial d-excess signal reflecting the evaporation conditions at moisture origin should be preserved during atmospheric transport and rainout processes. Thereby, d-excess signal observed locally is often used as an indicator of the evaporation conditions at moisture origin.

The further interpretation of the d-excess signal has been controversial. The theoretical study by *Merlivat and Jouzel* (1979) demonstrates a dependence of d-excess in the evaporated vapour over the ocean surface on the relative humidity of the near-surface air with respect to the saturation vapour pressure at the ocean surface ($\mathrm{RH_{SST}}$), the sea surface temperature (SST), and surface wind speed. These theoretical considerations led to interpretations of variations of ice core d-excess as proxies of changes of the moisture source $\mathrm{RH_{SST}}$ (*Jouzel et al.*, 1982) or SST (*Johnsen et al.*, 1989; *Uemura et al.*, 2012). The latter interpretation has been challenged by *Pfahl and Sodemann* (2014) who argued that, at synoptic timescales (from hours to days), the observed d-excess in oceanic boundary layer water vapour shows primary and robust dependence on $\mathrm{RH_{SST}}$ (*Angert et al.*, 2008; *Gat et al.*, 2003; *Pfahl and Wernli*, 2008; *Uemura et al.*, 2008). This disputation draws attention to the impact of time scales when interpreting isotope signals. Besides, the importance of surface wind speed could not be validated so far in the existing observations (*Bonne et al.*, 2019; *Steen-Larsen et al.*, 2015, 2014a).

2.3 Stable isotope processes in atmospheric water cycle

Following the steps involved in moisture transport, the stable water isotope processes occurring in the atmospheric water cycle can be briefly described as (Fig. 2.1):

① Evaporation at sea surface. Combination of an equilibrium (air saturated) interface and a molecular diffusion layer above (where non-equilibrium fractionation takes place and diffusion speed depends on humidity gradient) (*Craig and Gordon*, 1965).

② Turbulent surface layer. No isotope fractionation.

③ Formation of cloud. Equilibrium process that can be described by Rayleigh distillation models (*Dansgaard*, 1964).

④ Cloud microphysics under warm conditions. Formation of liquid precipitation.

⑤ Precipitation. Preferable removal of heavy isotopes.

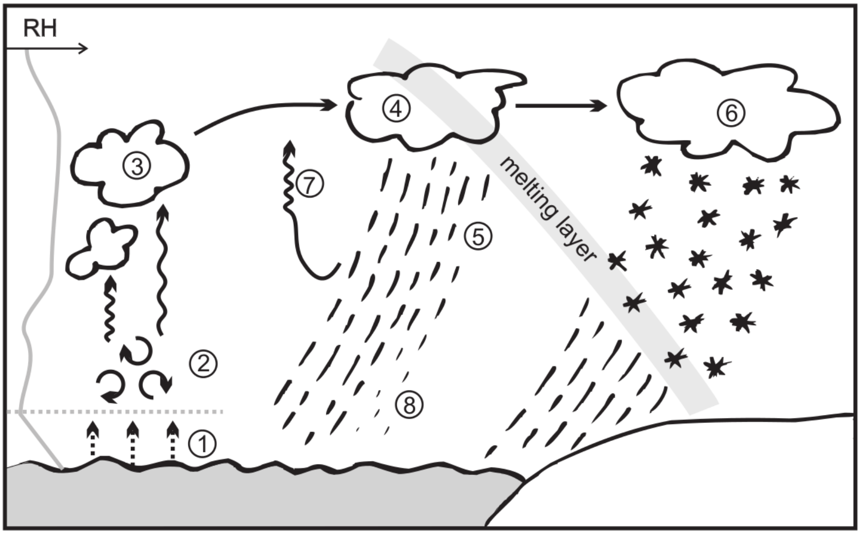

Figure 2.1: Schematic of isotope fractionation processes in the atmospheric hydrological cycle (from Sodemann, 2006). See text for details.

⑥ Cloud microphysics under cold conditions. Formation of solid (snow/graupel/hail) precipitation, involving kinetic fractionation in supersaturation conditions (*Jouzel and Merlivat*, 1984).

⑦ Water vapour recycling. Already depleted water vapour can be fed back to the condensation process.

⑧ Below-cloud processes. Evaporation of falling raindrops, and isotopic exchange between raindrops and ambient water vapour.

Each time when the phase change occurs, the environment conditions leave an imprint on the generated phase and the remaining phase. And it is clear that the vapour/precipitation isotopes collected on the observation site is an integrated signal resulting from source evaporation conditions, transport history, and other small scale processes.

(1) *Evaporation conditions at the moisture source*. As mentioned in the previous section, *d*-excess in local precipitation or vapour can be used as an indicator of the evaporation conditions in the source area. For example, high *d*-excess observed in Bergen can be associated with the so-called marine cold air outbreak events (*Aemisegger*, 2018; *Aemisegger and Sjolte*, 2018), where the cold dry air from polar land areas moves over the relatively warm ocean and triggers strong evaporation (see Sect. 3.2.2).

(2) *Depletion of heavy isotopes due to rainout process during transport*. When being transported to a colder environment, an air mass gradually cools down, reaches saturation, and progressively loses its water content. During the rainout, heavy isotopes preferably go to the condensation phase. This gradual rainout of heavy isotopes can be described by a Rayleigh distillation model (*Dansgaard*, 1964). The extent of rainout essentially depends on the temperature difference between the moisture source and the condensation height on the precipitation site. A larger temperature difference leads to a greater degree of rainout and thus a more depleted isotope composition in the arrival vapour/precipitation.

(3) In addition to the first-order processes described above, *small scale processes* such as cloud microphysics and evaporation/equilibration of falling precipitation, are complicating the interpretation of the isotope signals observed on the ground. For example, a kinetic effect exists at snow formation and the effect is sensitive to the supersaturation conditions with respect to ice (*Jouzel and Merlivat*, 1984). This makes it difficult to predict the isotope composition (especially *d*-excess) of the condensation products. For deep convective systems, factors such as condensate lifting, convective detrainment and unsaturated downdrafts can play critical roles in the control of the isotope composition of precipitation (*Bony et al.*, 2008). Below-cloud evaporation and equilibration are also observed to have modified the precipitation isotope signals in many precipitation events (e.g. *Barras and Simmonds*, 2009; *Miyake et al.*, 1968).

On climate time scales, the isotope compositions observed from global meteoric waters can be explained by the first-order factors such as the source conditions (e.g. $\mathrm{RH}_{\mathrm{SST}}$, SST) and the temperature difference between moisture source and measuring site (①→⑥; *Dansgaard* (1964)). On a shorter time scale, however, the isotope composition of water vapour and precipitation can be largely influenced by, for example, the below-cloud processes (⑦⑧; *Lawrence and Gedzelman* (1996); *Muller et al.* (2015)). How the different processes, from the below-cloud processes to moisture source conditions, contribute throughout a weather event, is investigated in a detailed case study in Paper II.

2.4 Simple isotope models

In this section, I briefly present the classical Rayleigh distillation model, the C–G evaporation model, and the model describing below-cloud evaporation and equilibration. All these models are referred to as *simple isotope models* and describe the isotope fractionation at each phase change within an isolated air mass or a simple box-budget system. Despite being simple, they have been remarkably successful in describing the primary stable isotope processes.

Phase change and Rayleigh distillation model

The Rayleigh distillation model describes the evolution of a multiple-phase system in which one phase is continuously removed to the other phase through fractional distillation. Despite its simplicity, it is a powerful framework to describe the isotopic enrichment or depletion as material moves between reservoirs in an equilibrium process. The Rayleigh equation can be applied to open and closed systems. In an open system, the formed material is immediately removed. In a closed system, the material removed from one reservoir accumulates in a second reservoir in such a manner that isotopic equilibrium is maintained between the two reservoirs (e.g. condensation of vapour to cloud droplets with no precipitation).

The isotopic enrichment or depletion by the Rayleigh process is formulated as:

$$R = R_0 f^{\alpha-1}, \tag{2.6}$$

where R_0 is the initial isotope ratio, f the fraction of the remaining material, and α the equilibrium fractionation factor. Similar formulas can be derived for cases including non-equilibrium processes (e.g. in supersaturated or undersaturated conditions). In these cases, an appropriate fractionation factor instead of the equilibrium fractionation factor needs to be introduced (e.g. *Jouzel and Merlivat*, 1984, see also Appendix B.1.2).

Evaporation in a fixed atmosphere and Craig–Gordon model

The classical Rayleigh model describes the evaporation process in an ideal situation with no interactions between the evaporating water and the ambient atmosphere. Such situations can occur in laboratories with carrier gases such as dry air or nitrogen. In nature, however, evaporation occurs in an ambient atmosphere of certain humidity and isotope composition. Thereby, the influence of the ambient atmosphere on the evaporating process must be considered.

Based on observations and experiments (*Craig et al.*, 1963), *Craig and Gordon* (1965) suggested a laminar layer model (henceforth the *C–G model*) as a frame to describe the isotope fractionation during evaporation of an isolated water body in an atmosphere of fixed humidity and isotope composition. According to the C–G model, the isotope ratio of the evaporation flux can be expressed as:

$$R_E = \frac{\alpha^* R_L - hR_A}{(1-h)\alpha_k}, \tag{2.7}$$

where $\alpha^* = R_V/R_L$ is the equilibrium fractionation factor relating the isotope ratio of the evaporating water (R_L) to the isotope ratio of the generated vapour (R_V), R_A the isotope ratio of the fixed atmosphere, h the relative humidity with respect to liquid surface temperature, and $\alpha_k = \rho'/\rho$ the non-equilibrium fractionation factor resulting from differences in the diffusivity of the isotopic water molecules (ρ') and the diffusivity of abundant water molecules (ρ; *Merlivat*, 1978).

The closure assumption

One tricky variable in Eq. (2.7) is the isotope ratio of the fixed atmosphere (R_A). Since the atmosphere is not independent in an ocean-atmosphere system, the information of R_A must be provided in detail. However, this is generally impractical due to inadequate observations on the ocean surface and the difficulty of separating the advective contribution from the evaporative contribution to R_A (*Jouzel and Koster*, 1996). To simplify the problem, *Merlivat and Jouzel* (1979) introduced the so-called *closure assumption* considering a steady-state global-scale hydrological cycle. In this case, the evaporation is balanced with precipitation and all the water in the atmosphere is in the end precipitated, therefore, $R_E = R_A = R_P$. In other words, evaporation is the only source of the moisture in the fixed atmosphere. Applying this closure assumption, Eq. (2.7) is simplified to the following formulation:

$$R_E^c = R_A^c = \frac{\alpha^* R_L}{h + (1-h)\alpha_k}. \tag{2.8}$$

Now R_E can be obtained from h, SST, and α_k, without including the feedback from R_A.

Although the closure assumption is initially formulated for the closed global-scale cycle, *Aemisegger and Sjolte* (2018) suggest that it can also be justified on a regional scale where the evaporation flux contributes substantially to the local humidity. Otherwise, despite its usefulness, the closure assumption is shown to be generally insufficient on the local scale, leading to a systematic bias in the modelled isotope compositions (*Jouzel and Koster*, 1996).

Below-cloud evaporation and equilibration

A raindrop falling below the cloud base undergoes evaporation (when the ambient air is undersaturated) and equilibration (when the ambient air is near to saturation) processes. The evaporation process of a single raindrop can be essentially described by the C–G model for an isolated water body (*Stewart*, 1975), since a raindrop can be considered simply as an isolated water body that has a spherical shape and moves in a fixed atmosphere. When falling in a (near-)saturated atmosphere, a single raindrop gradually attains isotopic equilibrium with the atmospheric vapour.

Setting water drops to suspend in vertical streams of N_2, Ar, or He gas with relative humidities of around 0, 50, and 100 %, *Stewart* (1975) performed experiments to determine the effects of evaporation and isotopic exchange of the drops. They found that the observed isotopic enrichments in a dry or unsaturated atmosphere agrees with the C–G model predictions and the equilibration in a saturated atmosphere can be reproduced with a relaxation model.

The $\Delta\delta\Delta d$-diagram

Graf et al. (2019) demonstrated a useful interpretative framework, the so-called $\Delta\delta\Delta d$-diagram, to quantify the below-cloud processes and their effects on the isotope composition of ambient vapour and rain.

The $\Delta\delta\Delta d$-diagram shows the difference between the isotope composition (δD and d-excess) of equilibrium vapour from precipitation samples (denoted as $\delta_{p,eq}$ and $d_{p,eq}$) and those of ambient vapour (δ_v and d_v):

$$\Delta\delta = \delta \mathrm{D}_{p,eq} - \delta \mathrm{D}_{\mathrm{v}}, \tag{2.9}$$

$$\Delta d = d_{p,eq} - d_v, \tag{2.10}$$

where the notation $\Delta\delta$ refers to $\Delta\delta D$ (a similar notation can be defined for $\Delta\delta^{18}$O, which produces a very similar $\Delta\delta\Delta d$-diagram as that for $\Delta\delta D$). The equilibrium vapour from precipitation is calculated as the isotope composition of vapour that is in equilibrium with rain at ambient air temperature (*Aemisegger et al.*, 2015; *Craig and Gordon*, 1965): $\frac{\delta_{p,eq}}{1000} + 1 = \alpha_{vl}\frac{\delta_p}{1000} + 1$, where α_{vl} is the fractionation factor during liquid to vapour phase transition following *Majoube* (1971a).

Essentially, the C–G model and the below-cloud evaporation model are also Rayleigh-type models, and can be formulated into Rayleigh-type forms (Table 2.3). Examples of modelled isotopic evolutions under different conditions are shown in Fig. 2.2. Detailed descriptions including mathematical derivations of the simple isotope models can be found in Appendix B.

Table 2.3: Rayleigh-type equations to describe the isotopic evolution of the remaining reservoir under different conditions. The transport resistance is here assumed to be purely due to diffusion (i.e. $\rho \propto D^{-1}$).

	Conditions	Equation (in R and δ notation)		Fractionation factor adapted
Evaporation	open system (saturated)	$R = R_0 f^{\alpha-1}$	$\delta = (1+\delta_0)f^{\alpha-1} - 1$	$\alpha = \alpha_{vl} < 1$
	open system (undersaturated)	$R = R_0 f^{\alpha-1}$	$\delta = (1+\delta_0)f^{\alpha-1} - 1$	$\alpha = \frac{1}{\alpha_k \alpha_{lv}}$, where $\alpha_{lv} > 1$, $\alpha_k = \frac{D}{D'}(1-h)+h > 1$, $h = \frac{e_v}{e_l}$
	closed system	$R = \frac{R_0}{f+\alpha(1-f)}$	$\delta = \frac{1+\delta_0}{f+\alpha(1-f)} - 1$	$\alpha = \alpha_{vl} < 1$
	C–G model	$R = R_0 f^{\alpha-1}$	$\delta = (1+\delta_0)f^{\alpha-1} - 1$	$\alpha = \frac{\alpha_{vl} - h\frac{R_a}{R_l}}{(1-h)\frac{D}{D'}}$, where $\alpha_{vl} < 1$
Condensation	saturation over ice	$R = R_0 f^{\alpha-1}$	$\delta = (1+\delta_0)f^{\alpha-1} - 1$	$\alpha = \alpha_{sv} > 1$
	supersaturation over ice	$R = R_0 f^{\alpha-1}$	$\delta = (1+\delta_0)f^{\alpha-1} - 1$	$\alpha = \alpha_k \alpha_{sv}$, where $\alpha_{sv} > 1$, $\alpha_k = \frac{S_i}{\alpha_{sv}\frac{D}{D'}(S_i-1)+1} < 1$, $S_i = \frac{e_v}{e_i}$

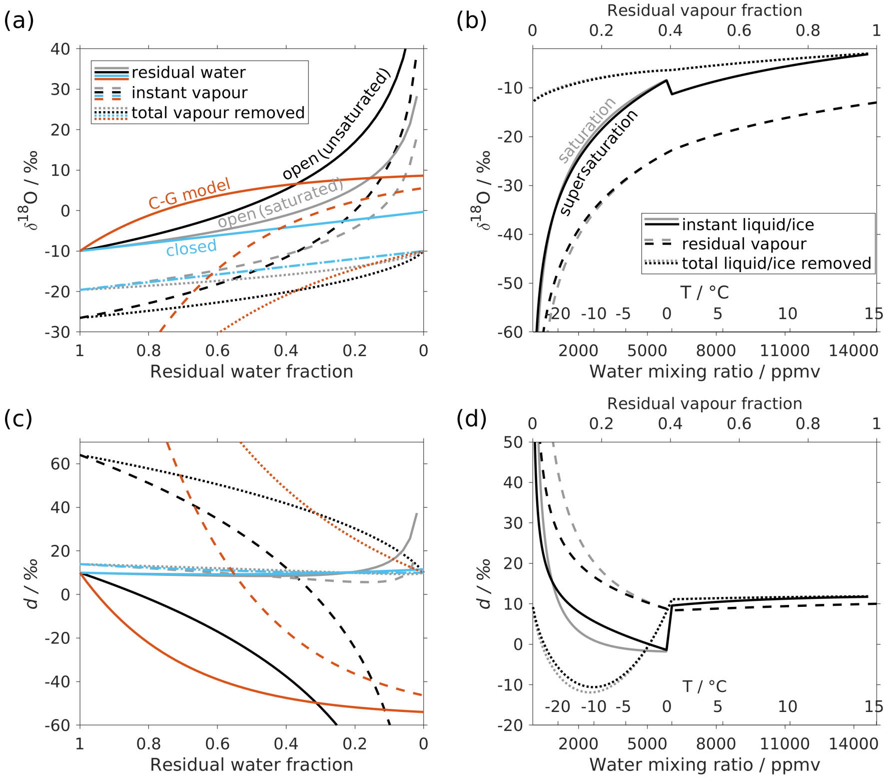

*Figure 2.2: Isotopic evolution during **(a), (c)** Rayleigh evaporation, and **(b), (d)** Rayleigh condensation. Rayleigh evaporation occurs at 20 °C (thus a constant fractionation factor) for initial liquid isotope compositions of $\delta^{18}O$ = -10 ‰ and δD = -70 ‰ (d = 10 ‰), in open system with unsaturated (RH = 75 %; black) or saturated (grey) environment, and in closed system (blue). In addition, the result of C–G evaporation model (i.e. open system including feedback from a "free atmosphere" which has fixed isotope compositions of $\delta^{18}O$ = -13 ‰ and δD = -94 ‰ (d = 10 ‰) and a fixed relative humidity (RH = 75 %)) is presented (red).*

Rayleigh condensation occurs under continuous cooling (thus the temperature-dependent fractionation factor is also continuously changing) starting from T = 20 °C and RH = 75 %. The initial vapour isotope compositions are $\delta^{18}O$ = -13 ‰ and δD = -94 ‰ (d = 10 ‰). For the deposition of ice below 0 °C, two cases are presented. The saturation case (grey) is a classical Rayleigh process where vapour forms ice crystals under equilibrium conditions, using the saturation pressure over ice (e_i). The supersaturation case (black) takes into account the supersaturation over ice where the ambient vapour pressure is $e_v = S_i e_i$. S_i is the defined saturation ratio, as e_v/e_i, and here takes the form $S_i = 1 - 0.004T$ after Risi et al. (2010). In this case, the fractionation factor combining equilibrium and kinetic effects given by Jouzel and Merlivat (1984) is used.

*The Rayleigh equations used in **(a-d)** can be found in Table 2.3.*

Chapter 3

Regional atmospheric circulation

This chapter presents the atmospheric circulation patterns that influence our study site. First, the study site and the local climatology is introduced (Sect. 3.1). Then, three specific weather systems (i.e. atmospheric river, cold air outbreak, and blocking) are presented (Sect. 3.2). Finally, the weather regimes classified by *Grams et al.* (2017) are introduced (Sect. 3.3).

3.1 Study site

Our study site is located in the city of Bergen (60.38 °N, 5.33 °E; Fig. 3.1, red cross) at the southwest coast of Norway. Due to the heat absorption in summer and release in winter by the ocean, the dominating westerly wind, and the Gulf Stream, the local climate is generally mild and temperate (*Seager*, 2006; *Seager et al.*, 2002). The average annual temperature of Bergen during 1961-1990 was 7.6 °C, with the highest and lowest monthly average being 14.3 °C in July and 1.3 °C in January, respectively (*http://sharki.oslo.dnmi.no*).

The other climate feature is the abundant and frequent precipitation throughout the year. The average annual precipitation in Bergen during 1961-1990 was 2250 mm, with the highest and lowest monthly average being 283 mm in September and 106 mm in May, respectively (*http://sharki.oslo.dnmi.no*). The large precipitation amount results from the fact that: (1) Bergen is located at the end of the climatological North Atlantic storm track (Fig. 3.1a; *Wernli and Schwierz*, 2006), and (2) the moisture flux confronts the Scandinavian Mountains and thus undergoes strong orographic lifting along the coast (Fig. 3.1b).

3.2 Specific weather system

3.2.1 Atmospheric river

Moisture transport to Bergen is often connected to elongated meridional structures of high integrated water vapour (IWV) flux known as atmospheric rivers (*Pasquier et al.*, 2019; *Ralph et al.*, 2004; *Zhu and Newell*, 1998). An impressive visual characteristic of the atmospheric rivers is that they can be identified as long, narrow bands of high IWV extending from the (sub)tropics to the midlatitudes on the passive microwave satellite imagery (Fig. 3.2). Quantitatively, an atmospheric river can be defined as a moisture plume whose IWV value exceeds 2 cm and persists for >2000 km in the along-plume direction and <1000 km in the cross-plume direction (*Ralph et al.*, 2004). While the IWV has commonly been used to define the atmospheric rivers, more relevant for the ensuing orographic precipitation is the associated water

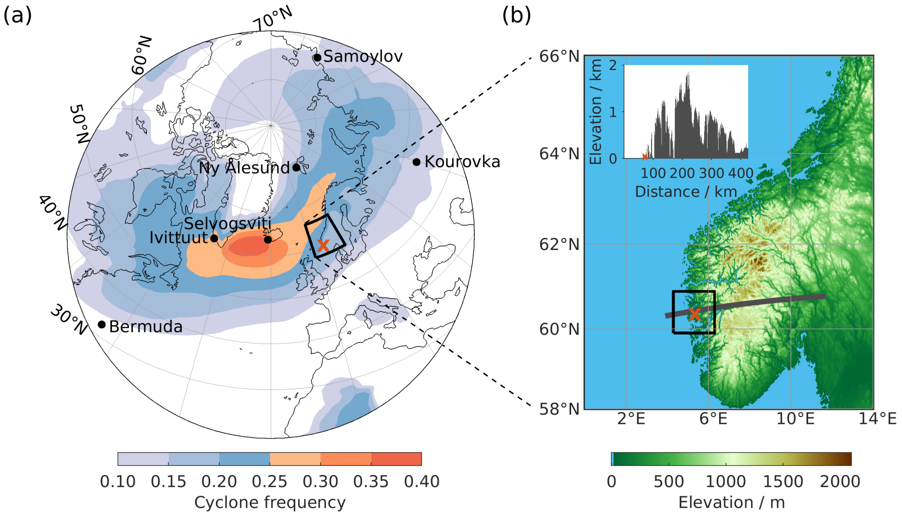

*Figure 3.1: **(a)** North Atlantic and Arctic region and the climatological cyclone frequency during 1979-2014 based on ERA-Interim reanalysis data. Black rectangle indicates approximately southern Norway. Black dots indicate isotope monitoring sites. **(b)** Topography of Southern Norway. Inset shows the cross section from west to east along the thick black line as an example of the orographic steepness (source: norgeskart.no). Black rectangle indicates the target region for the WaterSip moisture diagnostic tool. The location of Bergen is indicated with red crosses in **(a-b)**.*

vapour flux, also called integrated vapour transport (IVT; *Lavers et al.*, 2014, 2016). The IVT in a typical atmospheric river is about 1.6×10^8 kg s^{-1}, which is similar to the flux in the Amazon River (*Newell et al.*, 1992). *Zhu and Newell* (1998) showed that the atmospheric rivers may carry essentially the total meridional transport observed in the extratropical atmosphere although they occupy only about 10 % of the total area.

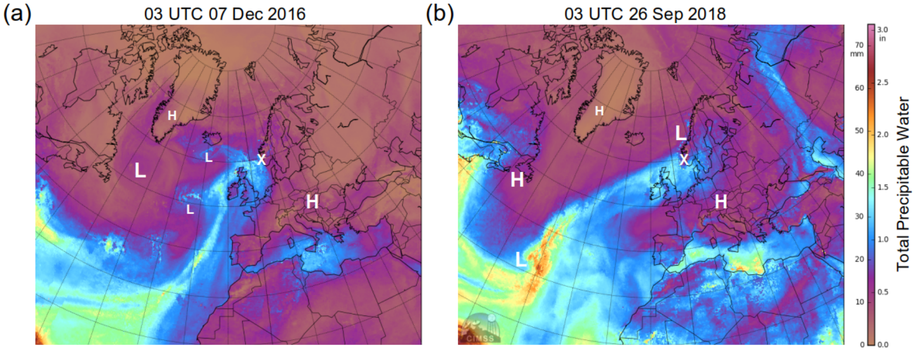

*Figure 3.2: Vertically integrated water vapour (or total precipitable water) of North Atlantic region for **(a)** 03 UTC 07 Dec 2016 and **(b)** 03 UTC 26 Sep 2018. Cross indicates the location of Bergen. L and H labels indicate centres of low-pressure and high-pressure systems, respectively. Imagery courtesy of Morphed Integrated Microwave Imagery at CIMSS (MIMIC-TPW) from the Cooperative Institute for Meteorological Satellite Studies (CIMSS) (http://tropic.ssec.wisc.edu/real-time/mtpw2).*

Atmospheric rivers are normally connected to extratropical cyclones (*Bao et al.*, 2006). The water vapour originates in the warm sector south of the cyclone centre, converges along the trailing cold front, and finally feeds the so-called warm conveyor belt (WCB) – a strongly ascending moist airstream that rises above the warm front (on the time scale of 2 days), and produces intense precipitation (*Eckhardt et al.*, 2004). Using a mesoscale model and water vapour tracer tagging method, *Sodemann and Stohl* (2013) found that cyclones were reinforcing the atmospheric rivers by advecting water vapour along the trailing cold fronts. At the same time, the WCB was feeding off the atmospheric rivers by large-scale ascent and precipitation. They also noted that pronounced atmospheric rivers could persist in the domain throughout more than one cyclone's life cycle.

Although tropical moisture appears to dominate at the early stage of atmospheric rivers, local moisture convergence in the extratropical cyclones plays an important or even dominating role for the subsequent maintenance of atmospheric rivers (*Bao et al.*, 2006). *Sodemann and Stohl* (2013) revealed that, in cyclone cores, fast turnover of water vapour by evaporation and condensation was leading to rapid assimilation of water from the underlying ocean surface. This indicates that the long-range atmospheric rivers are more likely associated with multiple cyclones rather than a direct advection of moist air from the tropics to midlatitudes.

The atmospheric rivers confronting orographic lifting can form heavy precipitation and potential floods. Examples of such situations can be found at the west coast of U.S. with the North Pacific storm track confronting the Rocky Mountains (*Ralph et al.*, 2004, 2006; *Zhu and Newell*, 1998), and, in this study, at the west coast of Norway with the North Atlantic storm track confronting the Scandinavian Mountains (*Azad and Sorteberg*, 2017; *Stohl et al.*, 2008).

3.2.2 Cold air outbreak

Located at 60 °N, our study site is also strongly influenced by polar air masses, especially in the winter season. One such example is the marine cold air outbreak (CAO), which is formed when cold and dry polar air masses flow equatorward from an ice shelf or across the sea ice boundary over the relatively warm open ocean. CAOs are characterised by a large air-sea temperature difference, thus strong heat and moisture fluxes from the ocean into the atmosphere and intense convective mixing (*Papritz and Sodemann*, 2018; *Papritz and Spengler*, 2017). On a satellite image, marine CAOs are recognisable with cloud streets that develop off the sea ice edge, as well as a transition toward cellular convection (Fig. 3.3).

From a weather system perspective, CAOs can in principle be induced by both anticyclones and cyclones. Using the terminology of weather regimes, *Papritz and Grams* (2018) found that the cyclonic regimes, the Greenland blocking regime and the Atlantic ridge regime would provide favourable conditions for CAO formation in the northeastern North Atlantic region (see Sect. 3.3).

CAOs provide a distinct mark in the generated atmospheric vapour with an intense-evaporation signal embedded in the water isotopes. To this end, the isotope measurements close to the source and at locations downstream can provide insight into the moisture origin.

3.2.3 Atmospheric blocking

The term *atmospheric blocking* refers to a class of weather systems in the middle to high latitudes. Common characteristics of blocks are persistence, quasi-stationarity and obstruction of the usual westerly flow and/or storm tracks. Blocks often (but not always) exhibit a large anticyclonic anomaly and reverse the zonal flow such that net easterly winds are seen in some

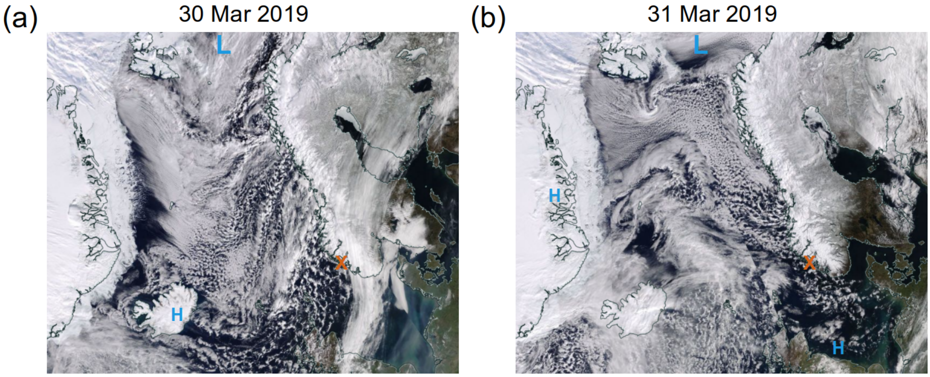

*Figure 3.3: Satellite imagery of North Atlantic region for **(a)** 30 March and **(b)** 31 March 2019. Red cross indicates the location of Bergen. L and H labels indicate the centres of low-pressure and high-pressure systems. Imagery courtesy of NASA Worldview application (https://worldview.earthdata.nasa.gov).*

part of the blocked region (*Woollings et al.*, 2018). In the anticyclonic regions of the blocks, cloud cover is largely reduced or eliminated due to the descending of dry air (Fig. 3.4).

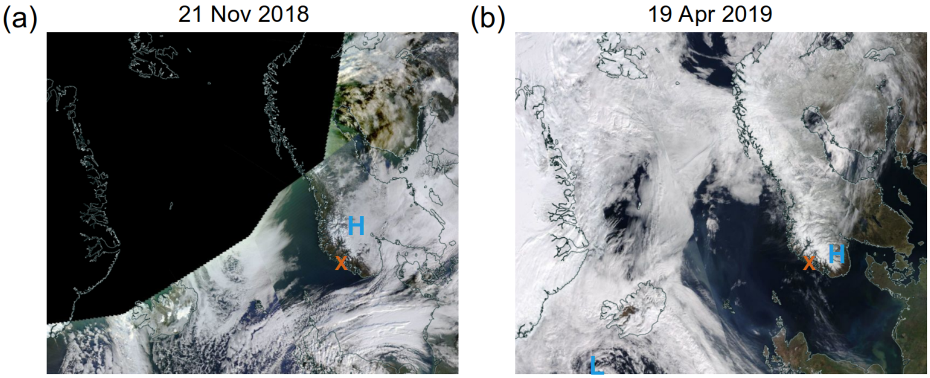

*Figure 3.4: As in Fig. 3.3, but for **(a)** 21 November 2018 and **(b)** 19 April 2019.*

By disrupting the usual westerly flow for an extended period such as a week or even longer, blocks are often associated with regional extreme weather, from heatwave in summer to severe cold in winter. In regions where blocking typically occurs, the prevailing oceanic westerly winds moderate the regional weather by providing warmth in winter and chill in summer. When these winds are obstructed during blocking, the result is, therefore, a seasonal extreme. The strongest impact of blocking comes from its persistence, which allows temperature and moisture anomalies to build up. Besides, the reduced cloud cover also amplifies the extremes with net surface warming in summer and cooling in winter.

Common blockings include European blocking, Scandinavian blocking and Greenland blocking in the North Atlantic region.

3.3 Weather regimes

In above I have presented three well-recognised weather systems that have pronounced impacts on our study region. In a general manner, the variability in weather on a spatial scale of about 1000 km and for periods of more than five days can be categorised in so-called *weather regimes* (WRs; *Cassou*, 2008; *Ferranti et al.*, 2015; *Vautard*, 1990). A year-round classification of seven WRs (Fig. 3.5) has been employed by *Grams et al.* (2017) to characterise the large-scale flow variability in the Atlantic-European region.

WRs are obtained using empirical orthogonal function (EOF) analysis and k-means clustering. EOF analysis is performed on the 10-day low-pass-filtered and normalised geopotential height anomaly at 500 hPa (Z500') in the Euro-Atlantic domain (80 °W – 40 °E, 30 °N – 90 °N). Geopotential height anomalies are defined with respect to the 90-day running mean of the climatology for the respective date. Global data from ERA-Interim (*Dee et al.*, 2011) at 1 ° horizontal resolution are used 6-hourly from 1 January 1979 to 31 December 2015. The leading seven EOFs (76.7 % of explained variance) are used for the k-means clustering. The optimal number of clusters is seven based on the criterion that the anomaly correlation coefficient between the clusters is below 0.4. The objective 6-hourly WR index I_{wr} is obtained by projecting each 6-hourly Z500' to the cluster mean. Six-hourly time steps of a target period are attributed to a WR life cycle if $I_{\mathrm{wr}} > \sigma(I_{\mathrm{wr}})$ (the standard deviation of I_{wr} from 1 January 1979 to 31 December 2015), the period of $I_{\mathrm{wr}} > \sigma(I_{\mathrm{wr}})$ lasts for at least five days, and it contains a local maximum with a monotonic increase/decrease of I_{wr} during the previous/following five days. More details on WR identification can be found in *Grams et al.* (2017).

These WRs exhibit clear differences in surface weather on multi-day timescales. Three of these regimes are dominated by negative 500 hPa geopotential height anomalies and are referred to as *cyclonic regimes* (Atlantic trough – AT, Zonal regime – ZO, and Scandinavian trough – ScTr; Fig. 3.5a-c). The other four regimes are dominated by positive anomalies and are referred to as *blocked regimes* (Atlantic ridge – AR, European blocking – EuBL, Scandinavian blocking – ScBL, and Greenland blocking – GL; Fig. 3.5d-g). In general, blocked regimes exhibit high surface pressure, strongly reduced winds, and often fog and cold conditions during winter. Cyclonic regimes are characterised by strong winds, extratropical cyclones, and mild conditions. The cyclonic regimes, as well as to a lesser extent the EuBL regime, project positively on the NAO, while GL regime projects negatively on the NAO. The remaining blocked regimes, in contrast, show no strong link to the NAO with only weakly negative values of the NAO index (cf. supplement Table S1 in *Grams et al.*, 2017).

There are several advantages of using this classification of seven WRs. (1) The seven WRs provide a more detailed description of the large-scale circulation over the North Atlantic European region than the four weather regimes commonly used in other studies (*Cassou*, 2008; *Michel and Rivière*, 2011; *Michelangeli et al.*, 1995). (2) The WRs are based on the seven leading EOFs explaining more than 75 % of the variance and thus cover almost the full range of large-scale flow variability. In contrast, the bimodal NAO or AO are typically derived from the first EOF explaining about 20-25 % of the variance (*Papritz and Grams*, 2018). (3) The seven WRs describe the major part of variability on sub-seasonal (10-60 days) time scales, in contrast to the NAO or AO, which describe the variability on seasonal and inter-annual time scales. (4) This approach allows identifying regimes year-round, i.e. each of the seven flow patterns can occur in all seasons, in contrast to the focus on one specific season in other studies (e.g. *Cassou*, 2008; *Ferranti et al.*, 2015).

The classification of seven WRs has already been adopted in studies of marine CAOs (*Papritz and Grams*, 2018) and atmospheric rivers (*Pasquier et al.*, 2019).

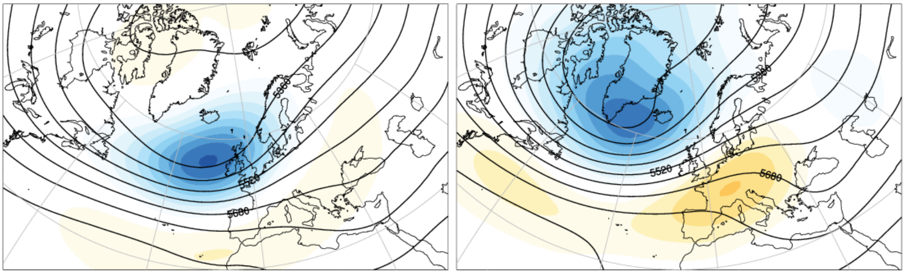
(a) Atlantic trough (AT, **9.0%**) **(b) Zonal regime** (ZO, **9.1%**)

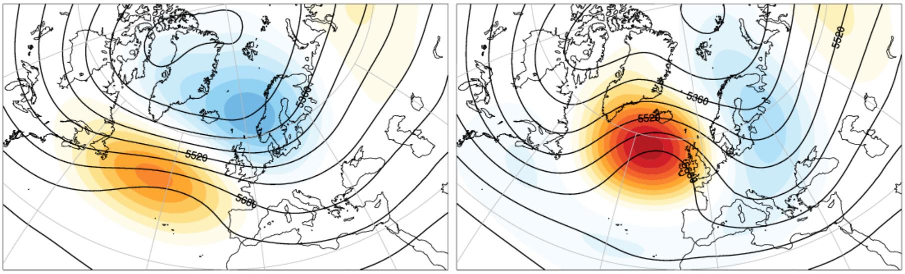
(c) Scandinavian trough (ScTr, **10.3%**) **(d) Atlantic ridge** (AR, **9.0%**)

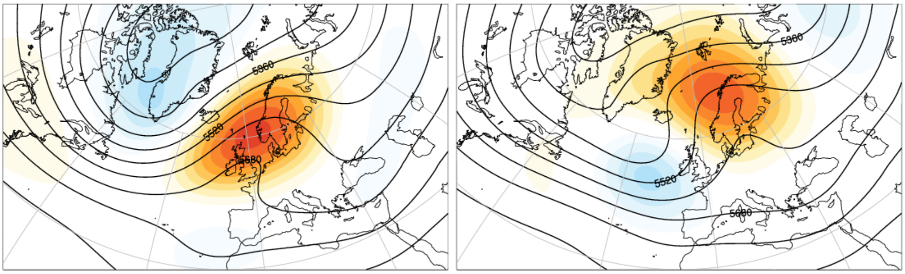
(e) European blocking (EuBL, **10.1%**) **(f) Scandinavian blocking** (ScBL, **10.9%**)

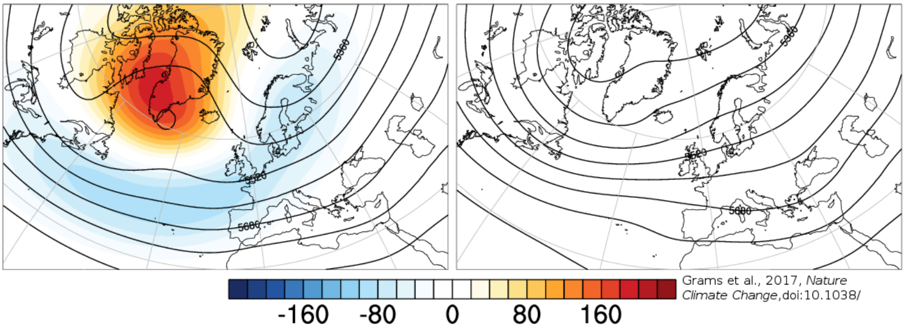
(g) Greenland blocking (GL, **10.1%**) **(h) no regime** (no, **31.5%**)

Grams et al., 2017, *Nature Climate Change*,doi:10.1038/

Figure 3.5: Atlantic-European weather regimes indicated with mean low-pass filtered (10 days) 500 hPa geopotential height anomalies (Z500', shading, every 20 geopotential meters). Mean absolute 500 hPa geopotential height (Z500, black contours, every 40 geopotential meters) for all days attributed to one of the seven weather regimes ***(a-g)*** *and to no regime* ***(h)****. The regime definition is based on normalised data for the entire year. Regime name, abbreviation, and annual frequency (in percent) indicated in the sub-figure caption. Figure after Grams et al. (2017) and can be found at* https://christiangrams.wordpress.com/balancing-europes-wind-power.

Chapter 4

Instrumentation, data and methods

This chapter presents the instrumentation, data and methods used in this study. First, meteorological instrumentation at the sampling site is presented (Sect. 4.1). Then, the isotope measuring procedure (including measuring techniques, calibration of work standards and instruments, correction of isotope composition–mixing ratio dependency, and minimisation of memory effect) are briefly explained (Sect. 4.2). Next, the isotope observations of surface vapour and precipitation are presented (Sect. 4.3). Finally, the Lagrangian moisture source diagnostic is introduced (Sect. 4.4).

4.1 Surface meteorological observations

Routine meteorological observations used in this work have been performed on the rooftop observatory (45 m a.s.l) of the Geophysical Institute (GFI), University of Bergen, and at one Norwegian met office station (WMO station Bergen-Florida, ID 50540) at ground level (12 m a.s.l.), located at a distance of 70 m from the rooftop station (Fig 4.1). The rooftop instrumentation consisted of a Micro Rain Radar (MRR-2, METEK GmbH, Elmshorn, Germany), a Total Precipitation Sensor (TPS-3100, Yankee Environmental Systems, Inc., USA), a Parsivel^2 disdrometer (OTT Hydromet GmbH, Kempten, Germany) and an automatic weather station (AWS-2700, Aanderaa Data Instruments AS, Bergen, Norway).

Total precipitation sensor (TPS-3100)

The TPS-3100 (Fig. 4.1a) is an automatic precipitation gauge. It provides 1-min real-time snow and liquid precipitation rates (*Yankee Environmental Systems, Inc.*, 2011). The sensor consists of two individually heated plates (5 inches in diameter) that are maintained at the same elevated temperature by precisely controlled electrical heaters. The top plate is exposed to precipitation; the lower plate, insulated from the upper plate, is shaded from precipitation. The power delivered to the lower plate is used to factor out wind cooling (which also yields a measurement of wind speed). After a correction for both ambient temperature and wind speed, the difference in the power required to evaporate rain or snow off the top plate yields the instantaneous precipitation rate. The sensor works reliably over a ±50 °C range.

Parsivel^2 disdrometer

The OTT Parsivel^2 (Fig. 4.1b) is a laser-based optical system. It provides 1-min comprehensive measurement of particle size and velocity for all types of precipitation (*OTT Hydromet GmbH*, 2015). According to the size and velocity, the Parsivel^2 classifies the particles into one of 32 sizes and 32 velocity classes, respectively. The size classes range from 0.2 to 5 mm;

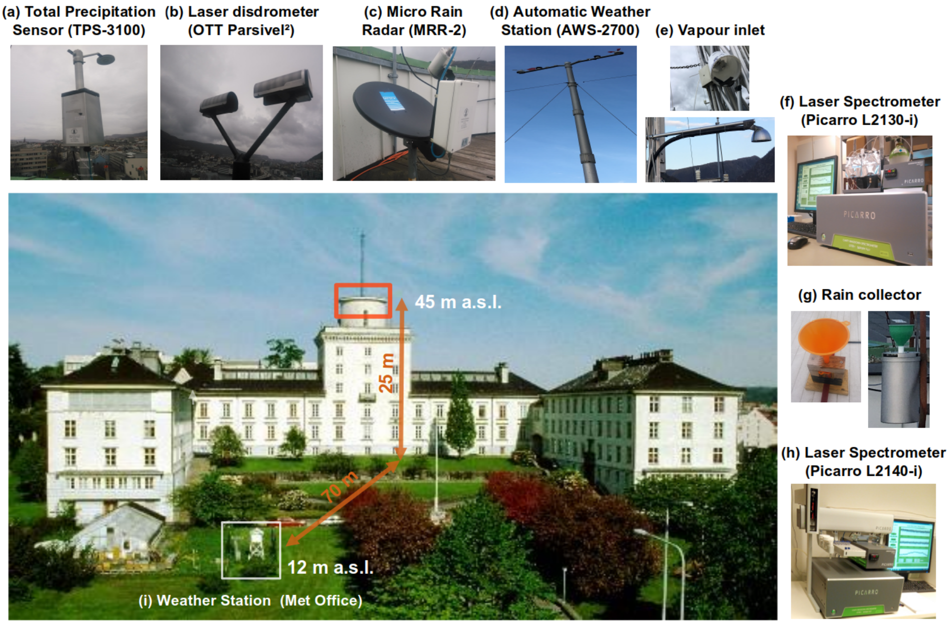

Figure 4.1: Instrumentation on the measuring site. Most instruments ***(a-g)*** *are set up on the rooftop of the tower (red rectangle). One total precipitation sensor* ***(a)****, one laser disdrometer* ***(b)*** *and one micro rain radar* ***(c)*** *provides high resolution precipitation characteristics such as rain rate, droplet size and fall velocity. One automatic weather station* ***(d)*** *provides standard meteorological parameters including temperature, humidity, wind speed and direction. The ambient vapour is sampled through an inlet (****(e)****; upper one used between 07 December 2016 and 01 June 2017, bottom one used afterwards) on the rooftop and measured continuously for the isotope composition through a laser spectrometer (Picarro L2130-i;* ***(f)****) sitting in the tower room. A rain sampler (****(g)****; left is a home-made rain collector used for high-resolution sampling within a targeted precipitation event, and right is a commercially-available rain sampler used for quasi-daily sampling) samples the precipitation which is later measured in the laboratory on the other laser spectrometer (Picarro L2140-i;* ***(h)****). A weather station from the Norwegian met office (WMO station Bergen-Florida, ID 50540;* ***(i)****) operates in a nearby location; it monitors the standard weather parameters at 2 m above surface. Photography of the building from https://www.uib.no/en/gfi/53059/about-gfi.*

the velocity classes range from 0.2 to 20 m s^{-1}. These raw data are generated for each measurement period (60 s here). They are then used to calculate the type, intensity and kinetic energy of the precipitation, the visibility in the precipitation, and the equivalent radar reflectivity. In addition, the raw number of particles are converted into a per-diameter-class volumetric drop concentration (Nd, unit [$mm^{-1}m^{-3}$]) following *Raupach and Berne* (2015). The mass-weighted mean diameter (Dm, unit [mm]) is also calculated. The drop size distribution is an important precipitation characteristic that can be used among others to evaluate the extent of below-cloud evaporation (e.g. *Graf et al.*, 2019).

Micro rain radar (MRR-2)

The MRR-2 (Fig. 4.1c) is a small vertical pointing Doppler radar profiler. The version used here operates at 24 GHz and resolves 32 range gates with a height resolution of 100 m (*METEK Meteorologische Messtechnik GmbH*, 2012). MRR-2 can be used to estimate the drop size distribution at different heights. This feature allows to investigate the formation of precipitation and to derive the precipitation rate. The other feature is that it can indicate the melting layer (also known as the bright band). The melting layer is an altitude interval where snow melts to form rain; it appears as a bright band in the observations of radar reflectivity (*Battan*, 1973; *White et al.*, 2002, 2003). The melting layer is a useful feature for characterising precipitation events (*Coplen et al.*, 2008, 2015; *Muller et al.*, 2015).

Automatic weather station (AWS-2700)

Measurements of standard meteorological parameters (air temperature, pressure, relative humidity, horizontal wind speed and direction) were provided by an Automatic Weather Station (Fig. 4.1d) on the rooftop at GFI. Besides, an official weather station from the Norwegian met office (WMO station Bergen-Florida, ID 50540) is located on the ground level about 70 m away (Fig. 4.1i). The WMO station is at 12 m a.s.l., which is about 33 m lower than the rooftop platform. Apart from the same variables as measured by AWS-2700 on the rooftop, it also provides the measurement of precipitation rate. A subset of standard meteorological parameters available from the TPS-3100 and the WMO station was consistent with the AWS-2700 data.

4.2 Stable water isotope measuring procedure

In this section, the principles behind the measuring techniques for stable water isotopes are briefly introduced (Sect. 4.2.1). Then, the calibration of work standards is presented (Sect. 4.2.2). Next, a calibration of the instruments for the measurement of ambient pressure and water mixing ratio is demonstrated (Sect. 4.2.3). Finally, two aspects, isotope composition–mixing ratio dependency (Sect. 4.2.4) and memory effect (Sect. 4.2.5), are addressed in order to optimise the instrument performance.

4.2.1 Measuring techniques

The water isotope ratios can be measured either by a mass spectrometer according to the atomic mass differences or by a laser spectrometer based on the spectral absorption properties of the isotopologues.

In principle, an Isotope Ratio Mass Spectrometer (IRMS) separates charged atoms or molecules based on their masses and their motions in electromagnetic fields (*De Groot*, 2004). The IRMS method provides measurements of high precision and accuracy. However, when using the IRMS method, water molecules need to be converted to a different gas before the measurement. For example, CO_2 equilibration method is used for δ^{18}O analysis (*Epstein*, 1953) and reduction of water to hydrogen gas is used for δD analysis (*Bigeleisen et al.*, 1952). As a result, δ^{18}O and δD are not simultaneously or directly analysed. Improvements have been made to pyrolyse the water molecules to CO and H_2 instead (*Begley and Scrimgeour*, 1997; *Gehre et al.*, 2004), but still in an indirect mode. Besides, the IRMS method consumes time. For instance, it requires several years to complete the measurement of a $2 \sim 3$ km long ice core (which yields tens of thousands of samples). In this study, we have used an IRMS only during the calibration of work standards and only for δ^{18}O.

In the last two decades, laser spectrometers, a new technique making use of photoabsorption by water molecules has been developed and succeeded in reaching the required precision level (*Brand et al.*, 2009; *Kerstel and Gianfrani*, 2008; *Kerstel et al.*, 1999). One commercially available type of laser spectrometer is the Cavity Ring-Down Spectrometer (CRDS) manufactured by Picarro Inc., USA.

The measurement principle of CRDS is based upon the absorption of a laser pulse at a wavelength specific to a given isotopologue (*Crosson*, 2008; *O'Keefe and Deacon*, 1988). When a measurement starts, the cavity quickly (in a few tens of microseconds) fills with laser light at one of the selected absorption wavelengths. After reaching a threshold level, the laser is abruptly switched off. At the same time, a photodetector measures the decay (ring down) of photons leaving the cavity through the semi-transparent mirrors (slightly less than 100 % reflectivity). The ring-down time is inversely related to the total optical loss in the cavity. For an "empty" cavity (when switching the light to wavelengths that are not absorbed by the target molecules), the ring-down time is solely determined by the reflectivity of the mirrors. For a cavity containing gas that absorbs light, the ring-down time will be shorter due to the additional absorption from the gas. The CRDS automatically and continuously compares these two types of ring-down times and uses those comparisons to calculate absorption intensities. The absorption intensities at all measured wavelengths generate an optical spectrum, which contains absorbance peaks that are unique to each molecule in the sample. The height or underlying area of each absorption peak is proportional to the concentration of the molecule that has generated the signal. The molecule concentrations are then used to calculate the (molecular) isotope ratios.

Comparing to IRMS, CRDS exhibits several advantages. (1) CRDS can directly and simultaneously measure both oxygen and hydrogen isotopes in one optical cavity. (2) Owing to its much-reduced weight and size, CRDS allows deployment on mobile platforms (e.g. aircraft and ship) to conduct in situ measurement. (3) CRDS can provide a measurement of high frequency (>1 Hz).

One challenge of the laser spectrometer, though, is that the measurements from laser spectrometers are often mixing-ratio dependent. Also, we have found that this mixing ratio dependency systematically depends on the isotope composition of measured water (Paper I). Consequently, a calibration of the measurements on different water mixing ratios and for different water standards is required for each specific instrument.

In this study, all the measurement of our isotope observations are carried out on two versions of Picarro analysers, namely L2130-*i* (serial number: HIDS2254; Fig. 4.1f) and L2140-*i* (serial number: HKDS2038 and HKDS2039; Fig. 4.1h).

4.2.2 Calibration of work standards

The reported isotope compositions (i.e. the δ values) slightly differ among the individual instruments. To obtain a reliable inter-comparison of the results measured in different laboratories, two water standards have been distributed worldwide by the International Atomic Energy Agency (IAEA) since 1968 (*Gonfiantini*, 1978). The two IAEA standards are known as VSMOW (Vienna Standard Mean Ocean Water) and SLAP (Standard Light Antarctic Precipitation).[1] Supplies of both VSMOW and SLAP were exhausted at the end of 2006 (*Lin et al.*, 2010). Meanwhile, VSMOW2 and SLAP2 (Table 4.1) had been produced by IAEA to replace VSMOW and SLAP, respectively. The isotope compositions of VSMOW2 and SLAP2 had been adjusted to be as close as possible to those of VSMOW and SLAP. They were found

---

[1] GISP (Greenland Ice Sheet Precipitation) is the third reference water with isotope composition approximately midway between VSMOW and SLAP and is used to verify the successful two-point calibration with VSMOW and SLAP (*IAEA*, 2009). GISP had been distributed by IAEA since 1977 (*Hut*, 1987) and has been exhausted in 2015.

by *Lin et al.* (2010) to be indistinguishable in their δ^{17}O and δ^{18}O values within measurement uncertainties. The measured δ values are then brought to the so-called VSMOW-SLAP scale via a two-point calibration using VSMOW2 and SLAP2 following the procedure described in *IAEA* (2009).

Table 4.1: The δ values of IAEA standards (IAEA, 2009) that are currently in use. The $\delta^{18}O$ and δD values of VSMOW are zero by consensus. The d-excess values are calculated with $d = \delta D - 8\delta^{18}O$ (Craig, 1961; Dansgaard, 1964).

	δ^{18}O [‰]	δD [‰]	*d*-excess [‰]
VSMOW2	0 ± 0.02^{a}	0 ± 0.3^{a}	0 ± 0.34
SLAP2	-55.5 ± 0.02^{b}	-427.5 ± 0.3^{b}	16.50 ± 0.34

[a] Standard uncertainty at 1 σ level calculated from results of calibrations performed at five laboratories.
[b] Same as above but at three laboratories.

The IAEA standards are often referred to as the primary standards. Due to the limit amount of the primary standards, laboratories are recommended to prepare their own work standards (also called internal or secondary standards) for daily use. The primary standards will be only used to calibrate the isotope compositions of the work standards.

The work standards in our laboratory were collected from different locations around Norway, from sea water and fresh water reservoir at west coast to snow on the inland mountains. All the standards have been filtered and then stored in inert foil gas sampling bag (Supel™ inert foil 1L SCV (Screw Cap Valve) gas sampling bag with Thermogreen® LB-2 (Low Bleed) septa), in a fridge at ~4 °C. The collapsible bag shrinks as standard is used, thus eliminating free air space and ensuring that an entire standard can be used without data degradation due to evaporation and re-condensation.

The calibration of work standards was carried out on a Picarro L2140-*i*. The ordered IAEA standards (20 mL each) were redistributed into 1.5 mL vials immediately upon opening. Each standard in the vials was injected 20 times. For comparison, δ^{18}O of work standards are also measured on IRMS. The reported δ^{18}O values from both Picarro and IRMS are in good agreement (Table 4.2). The majority of the isotope measurements in this study were calibrated using work standards GSM1 and DI.

4.2.3 Calibration of Cavity Ring-Down Spectrometers

A thorough assessment of the instrument performance is a prerequisite before deploying the instrument for reliable research. In this section, I present a calibration of the Picarro analysers used in this study.

Calibration of ambient pressure

The ambient pressure measured by Picarro L2130-*i* (HIDS2254) is calibrated against a vacuum gauge (APR250, Pfeiffer Vacuum GmbH, Germany) whose reading is monitored by a single-channel measurement and control unit (TPG261, SingleGauge™, Pfeiffer Vacuum GmbH, Germany). The Picarro appears to underestimate the ambient pressure (Fig. 4.2a). The offset can be corrected with a linear fit: $y = 0.9093x + 106.5$. The vacuum gauge is in turn calibrated against a digital barometer (PTB220TS, Vaisala Oyj, Finland). Results show that

Table 4.2: The δ values of work standards calibrated in May 2017 against IAEA standards on Picarro HKDS2038. Water mixing ratio is calibrated and isotopic dependency on the water mixing ratio is corrected. d-excess values are calculated with $d = \delta D - 8\delta^{18}O$. The error margin is calculated as standard deviation of the means. IRMS measurements were performed on Gasbench and Delta V+ (Thermo Fisher Scientific Inc., USA) in May 2016.

	Picarro L2140-*i*			IRMS
	δ^{18}O [‰]	δD [‰]	*d*-excess [‰]	δ^{18}O [‰]
GSM1	-33.07 ± 0.02	-262.95 ± 0.30	1.61 ± 0.34	-33.14 ± 0.04
VATS	-16.47 ± 0.02	-127.88 ± 0.30	3.88 ± 0.34	-16.47 ± 0.11
SVAL	-14.72 ± 0.02	-105.01 ± 0.30	12.75 ± 0.34	-14.71 ± 0.04
BRE	-12.68 ± 0.02	-91.01 ± 0.30	10.43 ± 0.34	-12.75 ± 0.07
DI	-7.78 ± 0.02	-50.38 ± 0.30	11.86 ± 0.34	-7.71 ± 0.15
SEA2	0.23 ± 0.03	1.26 ± 0.30	-0.58 ± 0.38	0.49 ± 0.10

the pressure measured by vacuum gauge is about 0.31 ± 0.08 hPa higher than that measured by the digital barometer. This offset is overall constant over the range of measured ambient pressure (from 999 to 1015 hPa during 6 days). The calibration function can be well represented with a simple linear fit: $y = x - 0.31$ (Fig. 4.2b).

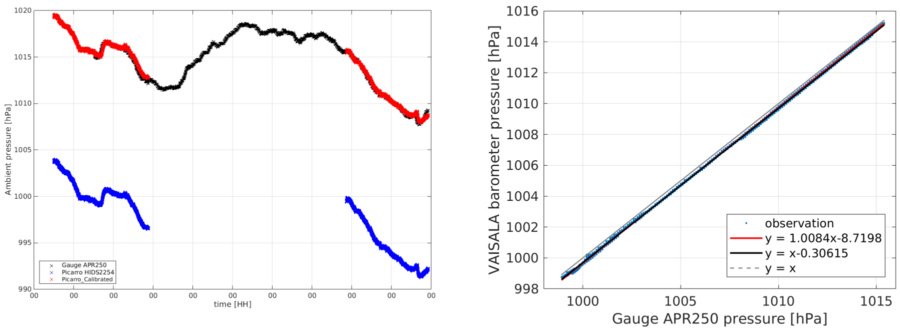

(a) Picarro L2130-i vs vacuum gauge.

(b) Vacuum gauge vs VAISALA barometer.

*Figure 4.2: **(a)** Ambient pressure measured by Picarro L2130-i (HIDS2254; blue) and vacuum gauge (APR250; black) between 12 UTC 01 June and 00 UTC 11 June 2016. Ambient pressure of Picarro L2130-i is calibrated (red) with a linear fit: $y = 0.9093x + 106.5$. Note that the measured pressure on Picarro (in unit of Torr) has been here converted to the unit of hPa (i.e. 1 Torr = $1/760 \times 1013.25$ hPa). **(b)** Ambient pressure measured by vacuum gauge (APR250) and VAISALA barometer (PTB220) between 13 UTC 14 June and 09 UTC 20 June 2016. The measurement by vacuum gauge is in turn calibrated to VAISALA barometer with: $y = x - 0.30615$.*

Calibration of (absolute) mixing ratio

Water mixing ratio measured by Picarro was calibrated with a dew point generator (LI-610, LI-COR Inc., USA). Picarro L2130-*i* was tested with two modes: *Flux Air* (~72 sccm) and *Air Low Flow* (~32 sccm). Ambient air was drawn through the dew point generator and reached saturation at the set temperature. The saturated air was guided to a cylinder for further mixing before entering the analyser of Picarro. To calculate the water mixing ratio (in [ppmv]) of saturated water vapour, both temperature and ambient pressure are needed. The temperature was the dew point of the generator, and the ambient pressure was measured with the vacuum gauge (APR250). The measurements appeared to not differ between the two Picarro modes and all fell very closely on a linear regression line (Fig. 4.3).

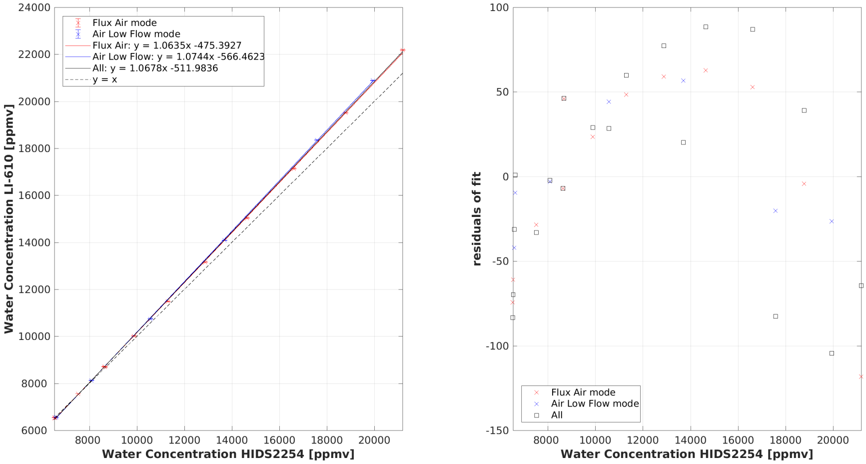

*Figure 4.3: **(left)** Water mixing ratios measured on Picarro L2130-i against the expected values from a dew point generator (LI-610). **(right)** Residuals of the corresponding linear fits. Dew points are in sequence set to 1, 3, 5, 7, 9, 11, 13, 15, 17, 19, 5, and 1 °C for Flux Air mode, and 1, 4, 8, 12, 16, 18, and 1 °C for Air Low Flow mode.*

One disadvantage of using the dew point generator is that saturation levels below the freezing point can not be generated. In the end, we could only obtain a calibration for the mixing ratio between 7000 and 21 000 ppmv. It is also worth to note that the intercept of the linear regression is not zero. This means that the linear relationship does not hold for very low mixing ratios.

4.2.4 Correcting mixing ratio dependency

In this section and the following section, I characterise two critical instrument behaviours and address the corresponding optimisations. It is worth to note that the calibrations are based on the specific instruments deployed in this work and are obtained in laboratory experiments. The characterised features may be subject to change either after a certain period or due to the relocation of the instrument (e.g. *Aemisegger et al.*, 2012), in which case, an independent instrument characterisation may be required.

The measurements of water isotopes via a laser spectrometer are affected by the water mixing ratio in two ways. (1) The precision of the measurement depends on the water mixing ratio. For the commercial laser spectrometer of Picarro, the best performance is obtained within an optimal water mixing ratio range of 19 000∼21 000 ppmv. As the water mixing ratio deviates from this range, especially towards the low levels, the measurement uncertainty grows quickly. (2) The isotopic value of the measurement is biased by water mixing ratio. This is often referred to as (water) *mixing ratio dependency* (e.g. *Aemisegger et al.*, 2012; *Bonne et al.*, 2014). The mixing ratio dependency is a prominent source of measurement bias outside the instrument's optimal performance range. This dependency should be characterised and corrected for.

The water mixing ratio dependency can be determined by measuring a stable vapour source of fixed isotope composition with changing water mixing ratios. There are typically three approaches to generate a stable vapour source: (1) using bubbling device such as a dew point generator; (2) continuously delivering liquid stream into a vaporiser via a device such as the Standard Delivery Module (SDM; Picarro Inc., USA); and (3) discretely injecting liquid samples into the vaporiser, manually or via a device such as an autosampler. Here we only present a calibration using discrete liquid injections of five water standards, for water mixing ratios between 15 000 and 24 000 ppmv.

Figure 4.4 shows the averaged per mil deviations ($\Delta\delta^{18}$O and $\Delta\delta$D) from the measured isotope values at 20 000 ppmv of the five water standards as a function of water mixing ratio. It appears that at the measured range of mixing ratios the choice of water standards has a minor impact on the dependency behaviour. Since the water mixing ratio is maintained most of the time within 19 000~21 000 ppmv (in very few occasions reaching 16 000 or 24 000 ppmv), the calibration can be carried out using one linear relationship determined from all the five water standards.

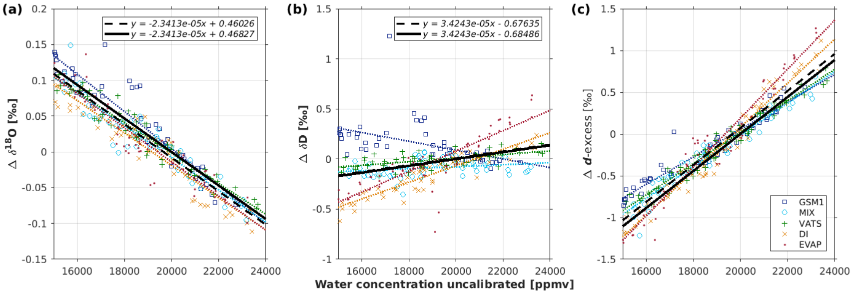

Figure 4.4: Isotopic dependency on water mixing ratio between 15 000 and 24 000 ppmv for ***(a)*** *δ^{18}O,* ***(b)*** *δD, and* ***(c)*** *d-excess. Five water standards of different isotope compositions (from depleted to enriched) are measured. The water mixing ratios presented here are not calibrated. Linear regression fits are presented for each water standard (dotted color lines), for all the five water standards (dashed black lines), and finally for all measurements and also constricting to cross the fixed point of [20000, 0] (solid black line). The corresponding fits for d-excess are calculated based on the fits for δ^{18}O and δD.*

In above, the correction of mixing ratio dependency for the measurements of liquid samples is presented. For direct in situ measurement of water vapour, mixing ratios can vary from below 500 ppmv in dry regions (e.g. polar regions or the middle and upper troposphere) to 30 000 ppmv or more in humid regions (e.g. the tropics). Also, at low mixing ratios, the mixing ratio dependency is found to be dependent on the isotope compositions. The details of a general calibration for a wide range of mixing ratios for vapour measurements are presented in Paper I.

4.2.5 Minimising memory effect

Memory is a challenge for liquid measurements. A memory effect is clearly visible during liquid injections when switching between vials, in particular when the isotope composition difference is large (*Penna et al.*, 2010, 2012; *van Geldern and Barth*, 2012). The memory effect in the current configuration extends over several injections. These injections have to be discarded, thus wasting analysis time and resources including dry gas, syringes, and septa. Removing as much as possible of this memory effect is thus highly desirable.

We have tested several measures that could potentially reduce the memory effect (Table 4.3). The tested measures focus on influences related to either the syringe (No. 1-5) or the water remaining in the measurement system (No. 6-19). One notable measure is the so-called "wet flushes". Wet flushes denote sample injections (into the vaporiser) that are processed as for sampling, but then discarded and evacuated to vacuum. This procedure primes the vaporiser in the same way as usual sampling would, but saves the time required for a complete sampling sequence. The wet flushes are by default deactivated in the Picarro vaporiser software. The isotope composition difference between the adjacent samples also plays a role in the amplitude of memory effect (*Penna et al.*, 2012). However, this aspect is not discussed in this context since we use the same two water standards (VATS and DI) throughout all the experiments.

Memory effect can be quantified directly in percentage (Fig. 4.5; *Gröning*, 2011). For each pair of adjacent vials, the isotopic difference (d) between the mean of the last 4 injections of each sample is considered as the "true" isotopic difference of these two samples ($d = true_1 - true_2$). The isotopic difference (e) between each previous injection and the "true" isotopic value of the second sample is calculated ($e = meas_2 - true_2$). The ratio $f = e/d * 100$ % is then regarded as the total memory contribution (in percentage) from the previous sample.

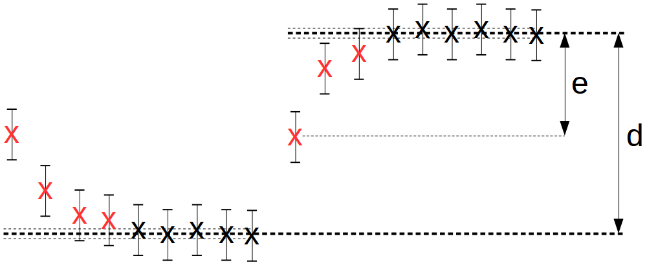

Figure 4.5: Schematic presentation of quantification of memory effect.

An injection is subject to memory effect when f exceeds a threshold. The thresholds defined here are 0.5, 1, and 5 % for δ^{18}O, δD, and d-excess, respectively (i.e. the δ value of this injection represents 99.5 %, 99 %, and 95 % of the target mean value). An improved measuring strategy would reduce the number of injections affected by the memory effect. Besides, being particularly sensitive, the f value of the first injection also provides a direct evaluation of different measures.

The number of memory-affected injections is plotted against the memory effect of the first injection in Fig. 4.6. Improved measuring strategies would shift the measures towards the lower-left corner of the evaluation graph. For all of δ^{18}O, δD and d-excess, the measures concerning syringe cleaning mainly stay in the middle and right side (black to bluish dots),

Table 4.3: Summary of the experiments for minimising memory effects. 12 injections have been performed for each vial of the listed experiments. Experiments 1-4 are regarding syringe cleaning aspect. They are not distinguishable to experiment 5, thus are not listed or discussed further here.

No.	Method	Time per vial	Other notes
Syringe (autosampler) aspect			
5	5 pre-rinse, 5 sample rinse	1.5 min	10 sec x10
Vaporiser aspect			
6	1 Wet flush between injections	24 min	2 min*inj
7	Open V1,V2 simultaneously	9 min	22 sec x2*inj
8	Open V1,V3 simultaneously	9 min	22 sec x2*inj
9	3 Wet flush between vials + V1,V2 + V1,V3	24 min	2 min x3 + 22 sec x2x2*inj
10	Additional dry flush + V1,V2 + V1,V3	37.5 min	1.5 min + (1.5 min + 22 sec x2x2)*inj
Vaporiser + Filter + Cavity			
11	1 Wet flush: 3 pulse	5 min	1 min + 4 min
12	2 Wet flush: 3 pulse (bad quality)	10 min	5 min x2
13	2 Wet flush: 3 pulse + LastClean (dry flush)	12 min	(5 min + 50 sec)x2
14	1 Wet flush: 3 pulse (x2 Conc.)	6 min	5 min + 50 sec + 10 sec
15	1 Wet flush: 1 pulse (x2 Conc.)	6 min	
16	2 Wet flush: 1 pulse (x2 Conc.)	12 min	6 min x2
17	2 Wet flush: 1 pulse (x2 Conc., x2 time)	17 min	(6+2.5 min) x2
18	3 Wet flush: 1 pulse (x2 Conc., x0.5 time)	15 min	(6-1 min) x3
19	3 Wet flush: 1 pulse (x2 Conc.)	18 min	6 min x3
^{17}O mode			
20	^{17}O mode high precision (default)	9 min	
21	^{17}O 2 Wet flush: 1 pulse (x2 Conc.)	12 min	6 min x2
22	^{17}O 1 Wet flush: 1 pulse (x2 Conc., x3 time)	10 min	6+4 min

while the measures with cleaning vaporiser and analyser are gathered on the left side (greenish to yellowish dots). This indicates that the main memory source stays in the section from the vaporiser to the analyser. Tests with ^{17}O mode (reddish dots) show the same tendency. It is worth to note that for *d*-excess, the memory effect is reduced from nearly 50 % to below 10 %. The substantial reduction is largely attributed to the adoption of wet flushes since the first injections occur after the abandoned wet flushes. A similar pattern is also clearly seen when comparing the memory effect for the first injections of the experiments (Fig. 4.7).

Based on our experiments, we conclude that: (1) Cleaning only syringe or vaporiser does not reduce the memory effect significantly; (2) Cleaning including the vaporiser, filter and cavity provides promising improvement; (3) The filter between vaporiser and cavity is possibly the main source for memory effect because of its large contact surface; (4) A wet flush (i.e. cleaning with the current water sample) is more efficient than a dry flush (cleaning with dry gas); (5) The impact of the wet flush is proportional to the time length of its implementation. A balance should be considered between reducing memory effect and saving time; (6) Water

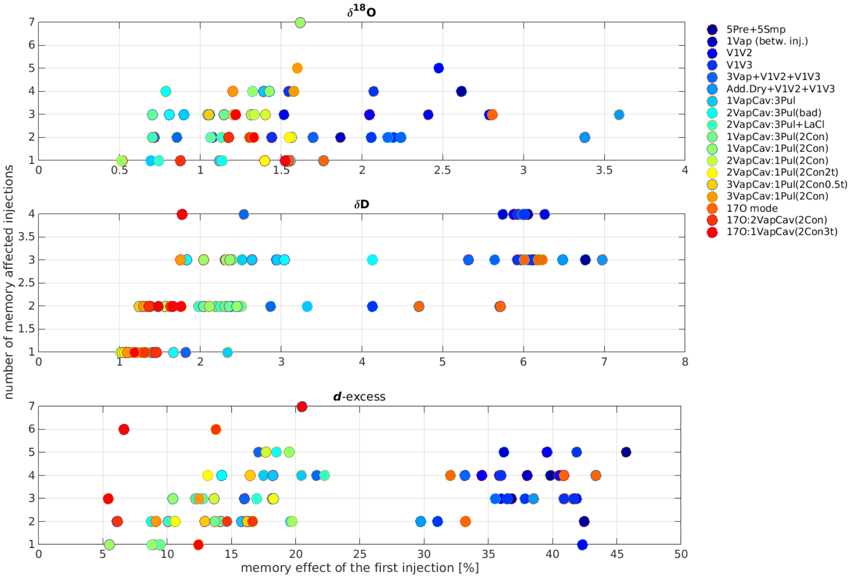

Figure 4.6: A 2D plot showing the evaluation of memory effect for the different tested measures. Different measures are indicated with colors: cleaning syringe (black; No. 5); cleaning the vaporiser (bluish; No. 6-10); cleaning vaporiser, filter, and cavity (greenish to yellowish; No. 11-19); and for tests on ^{17}O mode (reddish; No. 20-22). Experiment numbers and methods are described in Table. 4.3.

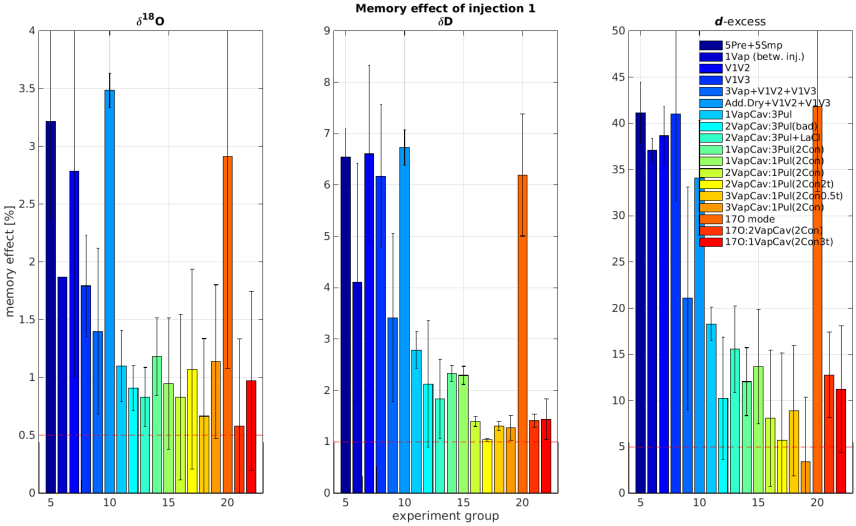

Figure 4.7: Averaged memory effect of the first injection for the tested measures. Each experiment is repeated 3 times. Red dashed lines indicate the thresholds for detecting memory affected injections.

is "sticky", and currently it is implausible to completely remove the memory effect.

The current measuring scheme

For the measurements in this work, we have adopted the measure with two wet flushes (each wet flush corresponds one pulse with doubled concentration; No. 16). With this measure, one injection in high-precision mode takes about 12 minutes. The memory effect of the first injection can be reduced to about 0.8 %, 1.4 %, and 8 % for δ^{18}O, δD, and d-excess, respectively. This is better than the third injection of the default method, which, after taking into account the previous two injections, consumes in total 18 minutes. As a result, it saves about one hour by measuring every 10 samples.

In our current measuring scheme, the standards are measured with 12 effective injections, with two preceding double-peak wet flushes, thus requiring a total of 16 injections. Samples are commonly run with 6 effective injections, thus a total of 10 injections including the two double-peak wet flushes. The isotope composition between the samples of one run typically varies less than the jump from the last standard and the first sample. Therefore, the first sample is duplicated in the run and then discarded in the analysis. A drift-standard is introduced after 10 samples in the run sequence and is measured as if it were a sample.

4.3 Stable water isotope sampling and analysis

Stable isotope observations in this work include the sampling and analysis of both surface vapour and precipitation.

4.3.1 Stable isotope composition of surface vapour

The isotope compositions of ambient water vapour have been continuously monitored with a CRDS (most time Picarro L2130-*i* and occasionally Picarro L2140-*i*; Fig. 4.1f) on the rooftop of GFI since 07 December 2016. The inlet is located about 1 or 2 m above the surface (about 25 m above the ground) and is shaded from precipitation with a downward-facing plastic cup (replaced with a stainless steel bowl after 12 December 2017; Fig. 4.1e). The ambient air was continuously pumped to the analyser, through a 4 m of 1/4 inch PFA tubing before 01 June 2017 and a 4 m of 1/4 inch stainless steel tubing afterwards. From 08 June 2017, the tubing was covered by a heating wire along with insulation (PE) foam and heated to about 50 °C. A manifold pump (N6022, KNF, Germany) was added after 22 November 2017 to increase the air flux to about 10 sccm. The needed air flux is then drawn from the inlet line to the Picarro analyser by another pump, protected from reverse flow through a check-valve.

The measurements were calibrated using a commercial calibration system (SDM A0101, Picarro Inc., USA) and a vaporiser (A0211, Picarro Inc., USA). During the calibration, the work standard was evaporated into dry air at 140 °C; the generated standard vapour was then measured for 20 min at a mixing ratio around $\sim$20 000 ppmv. Two work standards (GSM1 and DI) bracketing the typical isotope compositions of the local vapour were used. The dry air was supplied from a customer gas drying unit, i.e. a molecular sieve (MT-400-4, Agilent Inc., Santa Clara, USA) filled with Drierite desiccants, before 11 September 2017 and a synthetic air cylinder (synthetic air 5.5, purity 99.9995 %, Praxair Norge AS) afterwards. The calibration was carried out every 11 hours before 25 August 2017 and every 23 hours afterwards.

The vapour data were processed in the following steps. (1) The raw data were corrected for mixing ratio dependency using the correction function in Paper I. (2) The entire calibration period of each calendar month was processed. First, all the SDM calibration periods were identified. Then, for each identified calibration period, the median values of mixing ratio, δ^{18}O and δD were calculated. The measurements deviating from the median value by more than 0.5 ‰ in δ^{18}O or 4.0 ‰ in δD were discarded to remove variations generally caused by bursting bubbles or SDM deficiencies. Finally, the remaining data of each period were averaged and the standard deviation was calculated. (3) The vapour measurements were calibrated to SLAP-VSMOW scale using qualified calibrations in the above step. For each segment of vapour measurement, the data were calibrated using the two nearest (available) calibrations. (4) Finally, the calibrated vapour data were averaged over 1-min, 10-min, 1-hour, 6-hour, and 24-hour intervals using centre averaging.

4.3.2 Stable isotope composition of precipitation

At the same location, the precipitation was manually sampled. For high-resolution sampling within a particular precipitation event, we used a customer rain collector (Fig. 4.1g, left). The collector consisted of a PE funnel of 10 cm diameter, which directed the collected water into a 20 mL open-top glass bottle. The bottle and funnel were dried between each sample using a paper wipe. The sampling interval was adjusted according to the precipitation intensity and was normally between 10 and 30 min. To sample quasi-daily precipitation, we used a commercially available rain sampler (Palmex d.o.o., Zagreb, Croatia; Fig. 4.1g, right). The rain water was collected through a funnel and an intake tube before entering a 1 L plastic bottle. The bottle was manually replaced with a dry one every time before new sampling. The collected precipitation sample from either device was immediately transferred to a 1.5 mL glass vial (part no. 548-0907, VWR, USA) and closed with an open-top screw cap with PTFE/rubber septum (part no. 548-0907, VWR, USA) to prevent evaporation until sample analysis.

The samples were stored at 4 °C before being analysed for their isotope compositions in the laboratory. During the analysis, an autosampler (A0325, Picarro Inc., USA) transferred ca. 2 μL per injection into a high-precision vaporiser (A0211) heated to 110 °C. After blending with dry N_2 (Nitrogen 5.0, purity > 99.999 %, Praxair Norge AS), the gas mixture was directed into the measurement cavity of a CRDS (Picarro L2140-*i*; Fig. 4.1h) for about 7 min with a typical mixing ratio around 20 000 ppmv. To reduce memory effects between samples, two wet flushes consisting of 5 min of vapour mixture at 50 000 ppmv were applied to the analyser at the beginning of each new sample. Three standards (12 injections each, plus wet flushes) were measured at the beginning and end of each batch which was typically consisted of 20 samples (6 injections each, plus wet flushes). The averages of the last 4 injections were used for further processing.

The measurements were first corrected for mixing ratio dependency using one linear regression function for a mixing ratio range between 15 000 and 23 000 ppmv (Sect. 4.2.4). Then the data were calibrated to SLAP-VSMOW scale using the two measured work standards. The long term (one year) reproducibility of liquid sample analysis has been estimated to be 0.15 ‰ for δ^{18}O and 0.66 ‰ for δD, resulting in a measurement uncertainty of 1.05 ‰ for *d*-excess.

4.4 Lagrangian moisture source diagnostic

A Lagrangian method (*Sodemann et al.*, 2008a,b) is used to identify moisture sources of surface vapour and precipitation in the target region.

Firstly, the trajectories of the air parcels arriving in the target region are calculated. We have used the air parcel trajectory dataset from *Läderach and Sodemann* (2016), which has been extended to 15 UTC 30 August 2019 in this work. The dataset has been calculated using the Lagrangian particle dispersion model FLEXPART V8.2 (*Stohl et al.*, 2005), with wind and humidity fields from ERA-Interim reanalysis of the 6-hourly ECMWF data (*Dee et al.*, 2011). In the case of precipitation, the trajectories are extracted for all air parcels precipitating over the target region. For this study, the diagnostic was run with a target area of ca. 110×110 km centred over Bergen (59.9-60.9 °N and 4.3-6.3 °E), including both land and ocean area (Fig. 3.1b, black box).

Then, the *WaterSip* tool (*Fremme and Sodemann*, 2019; *Sodemann et al.*, 2008a) is used to identify the moisture uptake based on the calculated trajectories. WaterSip assumes that for each 6 h time step the change in specific humidity in the air parcels (Δq_c) exceeding a threshold value is due to either evapotranspiration or precipitation. The moisture accounting provides a fractional contribution of each evaporation event to the final vapour or precipitation in the target region. In this work, the thresholds are set to be 0.2 g kg^{-1} for Δq_c, 20 days for the backward trajectory length, and relative humidity >80 % for precipitation formation over the target region. These thresholds result in a source attribution for about 98 % of the estimated arrival vapour or precipitation in WaterSip. They also lead to reasonable precipitation estimates for the study region (Paper II and III). Note that here the moisture uptake identified both within and above the boundary layer is taken into account.

Chapter 5

Summary of scientific papers

Paper I: Correcting the impact of the isotope composition on the mixing ratio dependency of water vapour isotope measurements with cavity ring-down spectrometers

Yongbiao Weng, Alexandra Touzeau, and Harald Sodemann (2020), Atmospheric Measurement Techniques, 13 (6), 3167–3190, `https://doi.org/10.5194/amt-13-3167-2020`

Paper I systematically investigates how the mixing ratio dependency in a range from 500 to 23 000 ppmv of three commercial cavity ring-down spectrometers is affected by the isotope composition of water vapour. We find that the known mixing ratio dependence of laser spectrometers for water vapour isotope measurements varies with isotope composition (as an example, the characterisation results on Picarro L2130-i are shown in Fig. 5.1). We refer this as *isotope composition-mixing ratio dependency* and have developed a scheme to correct for this dependency-introduced bias. Using in situ measurements from an aircraft measurement, we demonstrate that the correction is most substantial at low mixing ratios. Stability tests over up to 2 years indicate that the first-order dependency is a constant instrument characteristic that may be primarily related to spectroscopy.

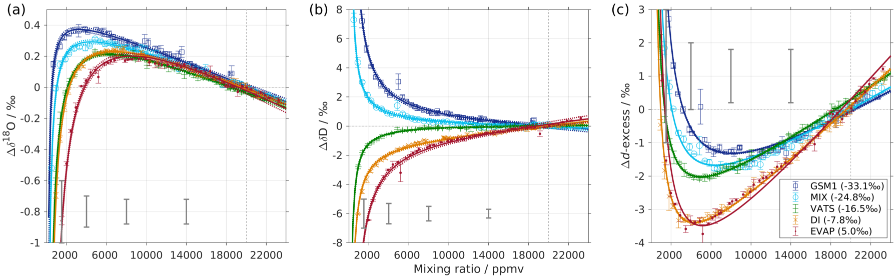

Figure 5.1: Mixing ratio dependency of uncalibrated measurements for **(a)** $\delta^{18}O$, **(b)** δD *and* **(c)** *d-excess for 5 standard waters (GSM1, MIX, VATS, DI and EVAP) on Picarro L2130-i. The calibration method is discrete liquid injection via an autosampler. Mixing ratio dependency is expressed as a deviation (Δ) of the measured isotope composition from that at 20 000 ppmv. Symbol and error bar represents the mean and the standard deviation, respectively. Solid lines are fits ($y = \frac{a}{x} + bx + c$) and dashed lines are the 95 % confidence interval. Measurements and fits for d-excess are calculated ($\Delta d = \Delta\delta D - 8 \cdot \Delta\delta^{18}O$). The typical standard deviations of a single injection at selected mixing ratios are indicated with grey error bars. (Fig. 1 of Paper I)*

Paper II: High-resolution stable isotope signature of a land-falling atmospheric river in southern Norway

Yongbiao Weng, Harald Sodemann, and Aina Johannessen (2020), Weather and Climate Dynamics Discussions, `https://doi.org/10.5194/wcd-2020-58`

Paper II presents high-resolution paired measurements of near-surface vapour and precipitation stable isotopes during a land-falling "atmospheric river" event at the southwest coast of Norway on 07 December 2016. We observe a stretched, "W"-shaped evolution of isotope signals (Fig. 5.2). Combining meteorological observations, we identify the influences on the isotope signals from below cloud processes, weather system characteristics, transport influence, and moisture source conditions. We thus revisit the interpretations given in previous studies on such precipitation events and emphasise that cloud microphysics and below-cloud processes are important factors influencing surface precipitation isotope signals.

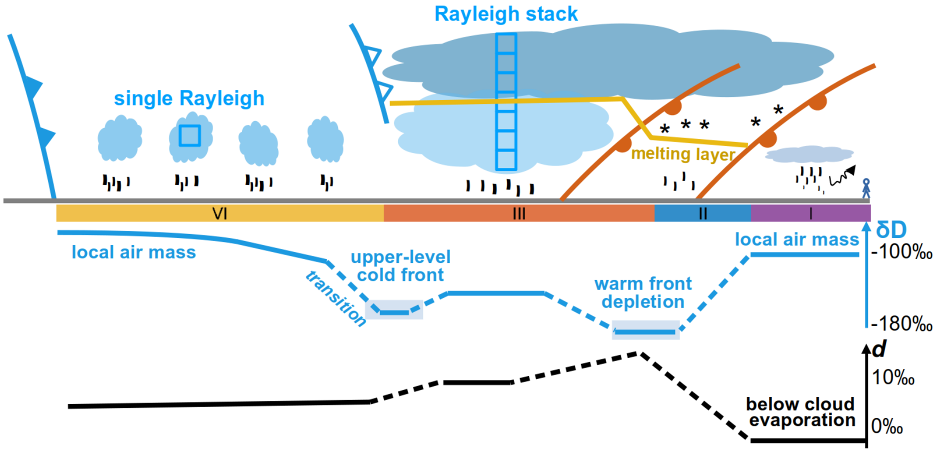

Figure 5.2: Schematic presentation of the land-falling atmospheric river event in Bergen on 07 December 2016. Identified precipitation stages are indicated with color bars. (Fig. 9 of Paper II)

Paper III: Stable isotope composition of surface vapour and precipitation at the southwest coast of Norway

Yongbiao Weng and Harald Sodemann (2020), to be submitted to Tellus

Paper III presents 3 years of paired surface vapour and precipitation stable isotope measurements at the southwest coast of Norway from December 2016 to November 2019 (Fig. 5.3). The isotopic variation on different time scales is investigated. We observe an overall weak diurnal variation and a moderate seasonal variation. On the multi-day time scale, we observe a clear association between the isotope signals and the regional weather regimes. The time series of d-excess is estimated based on the source conditions identified by a Lagrangian moisture source diagnostic tool, using both an empirical and a theoretically predicted d-RH_{SST} relationship. Comparing the model estimates with observations, we find that the models correctly reproduce the variation patterns, but with substantial offsets. While numerous research questions of interest require further investigations, our observations are of great importance for extending the sparse existing isotope observation network in the region of the North Atlantic storm track.

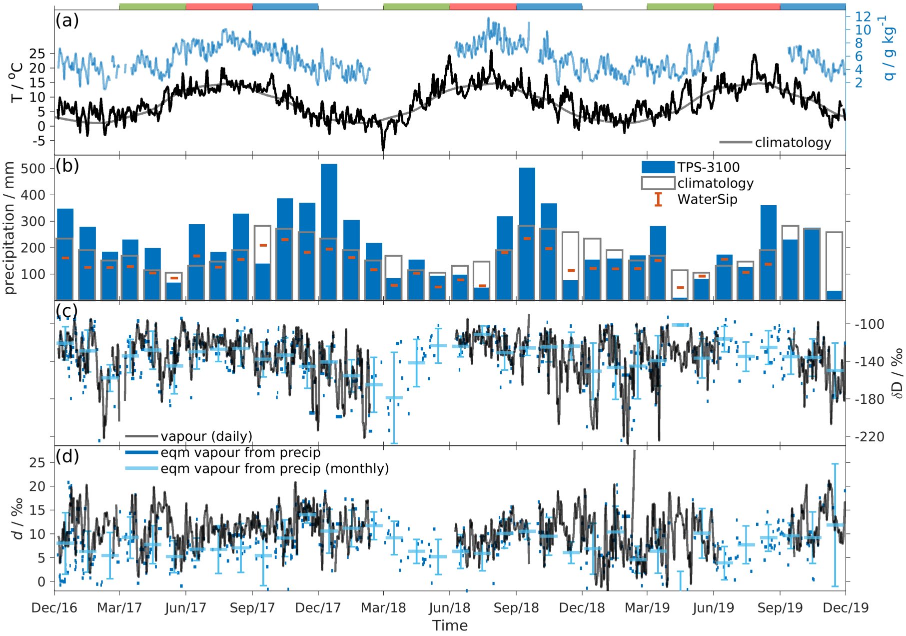

Figure 5.3: Time series of meteorological and isotopic observations in Bergen between 01 December 2016 and 30 November 2019. ***(a)*** *Daily air temperature observed (black line), climatology (grey line), and daily specific humidity observed (blue line).* ***(b)*** *Monthly precipitation rate observed (blue bar), climatology (open bar), and estimated from WaterSip (red errorbar).* ***(c)*** *Daily δD of surface vapour (black line), equilibrium vapour from event-based (quasi-daily) precipitation (dark blue segments) and its monthly average (light blue segments with error bar).* ***(d)*** *Same as* ***(c)*** *but for d-excess. Seasons are indicated with colour bars (green: MAM, red: JJA, blue: SON, and blank: DJF) at the top of the figure. (Fig. 2 of Paper III)*

Other relevant contributions

Paper (A): Meridional and vertical variations of the water vapour isotopic composition in the marine boundary layer over the Atlantic and Southern Ocean

Iris Thurnherr, Anna Kozachek, Pascal Graf, ***Yongbiao Weng****, Dimitri Bolshiyanov, Sebastian Landwehr, Stephan Pfahl, Julia Schmale, Harald Sodemann, Hans Christian Steen-Larsen, Alessandro Toffoli, Heini Wernli, and Franziska Aemisegger (2020), Atmospheric Chemistry And Physics, 20, 5811–5835,* `https://doi.org/10.5194/acp-20-5811-2020`

Paper A presents a 5-month continuous time series of ship-based measurements of water vapour isotopes in the Atlantic and the Southern Ocean from November 2016 to April 2017. The drivers of meridional isotopic variations in the marine boundary layer are analysed using Lagrangian moisture source diagnostics. Results show that the expected range of isotopic signals at a given latitude strongly depends on the large-scale circulation. Furthermore, the time series recorded at 8.0 and 13.5 m above the ocean surface provide estimates of vertical isotopic gradients in the lowermost marine boundary layer. The vertical isotopic gradients appear to be particularly large during high wind speed conditions with increased contribution of sea spray evaporation or low wind speed conditions due to weak vertical turbulent mixing. This demonstrates the potential of such measurements for estimating sea spray evaporation and turbulent moisture fluxes.

My contribution in this study is to have performed the isotope measurements between 22 March and 11 April 2017 (leg 4) and provided feedback on the manuscript.

Paper (B): The Iceland Greenland Seas Project

Renfrew, I. A., Pickart, R. S., Våge, K., and 63 others including ***Weng, Y.*** *(2019), Bulletin of the American Meteorological Society, 100 (9), 1795–1817,* `https://doi.org/10.1175/BAMS-D-18-0217.1`

Paper B presents an overview of the Iceland Greenland Seas Project (IGP). The field campaign was executed over Iceland and southern Greenland Seas during February and March 2018, with the deployment of a range of observing platforms, including a research vessel and an aircraft. One of the main scientific aims of the IGP is to characterise the atmospheric forcing and the ocean response of coupled processes. The campaign observed the life cycle of a long-lasting cold air outbreak over the Iceland Sea and the development of a cold air outbreak over the Greenland Sea. Repeated profiling revealed their immediate impact on the ocean, while a comprehensive hydrographic survey provided a rare picture of these subpolar seas in winter.

My contribution in this study is to have performed the vapour isotope measurement, collected precipitation and ocean surface water samples for water isotope analysis, and participated in the daily meteorological observations on the research vessel between 26 February and 22 March 2018 (leg 2).

Chapter 6

Discussion and further perspectives

What do we learn from paired isotope measurements of liquid precipitation and water vapour in the boundary layer?

Our studies (Paper II and III) as well as other studies (e.g. *Bonne et al.*, 2020; *Graf et al.*, 2019; *Leroy-Dos Santos et al.*, 2020) show that the precipitation collected on the ground is usually in equilibrium with surface vapour. The falling time of a raindrop (supposing the raindrop falling from 2 km above ground) can range from ∼230 (raindrop diameter of 4 mm) to ∼1200 s (raindrop diameter of 0.4 mm; *Rogers and Yau*, 1996), which is comparable or much longer than the experiment-based relaxation time of a water drop in a vertical stream of near-saturated ($RH = 99.5$ %) N_2 (∼148 s; *Stewart*, 1975). *Jouzel* (1986) also noted that the time taken for falling water drops to equilibrate with the environment is usually comparable and often shorter than the time required to fall. These pieces of evidence can explain why the isotope composition of liquid precipitation often closely resembles that of the boundary layer vapour.

In our atmospheric river case study in Paper II, we also notice that the isotope signal in the boundary layer vapour is reflecting and slightly lagging behind (with about a half-hour offset) the isotope signal in the liquid precipitation. Near the ground, the temperature keeps increasing (from 5 to 11 °C) throughout the event as the warm air advances. Considering the temperature evolution, the isotope composition of surface vapour is expected to get enriched monotonically in heavy isotopes. However, we observe substantial and swift responses in the surface vapour isotope following the precipitation evolution. This indicates that the persistent precipitation leaves an imprint on the ambient vapour. This also emphasises the importance of two-way processes in the interactions below the cloud layer.

Finally, using the paired measurements, we reveal the clear signal of below-cloud evaporation at the beginning of the precipitation event when the ambient air is relatively undersaturated (Paper II). The net mass transfer directed away from raindrops induces kinetic fractionation effect and causes characteristic deviations in the d-excess of surface precipitation. This evaporation effect would be particularly relevant for light and/or short-time rainfalls in an undersaturated environment (e.g. in arid/semi-arid regions) and would not be obvious from only measuring surface vapour or precipitation.

How does the vapour help to learn about what the precipitation means?

Surface vapour measurement can provide additional, important information. For example, as mentioned above, with only precipitation isotope measurements, one would not know to what extent the surface precipitation is reflecting the cloud signal or the below-cloud processes. One would also not know whether the precipitation is driving the surface vapour or vice visa.

In addition, vapour measurement is important for revealing processes at the interface of atmosphere and Earth surface. For example, through monitoring the isotope composition of near-surface water vapour, precipitation, and the surface (0.5 cm) snow on Greenland, *Steen-Larsen et al.* (2014b) suggest that, in between precipitation events, changes in the surface snow isotope composition are driven by the changes in near-surface vapour isotope composition. This finding challenges the classical ice core data interpretation where the ice core stable isotope records are interpreted as reflecting precipitation-weighted signals. As another example, using vapour d-excess measurements, *Aemisegger et al.* (2014) characterised the evaporation source of low-level continental water vapour in northeastern Switzerland.

Compared with the precipitation, the observation of water vapour isotopes yields several advantages. (1) While precipitation is often an integrated product collected on the ground, water vapour can be measured at different stages (from source evaporation to atmospheric transport) of the water cycle and then be used to study the relevant processes. (2) The observation of water vapour can be conducted continuously and is not necessarily restricted to the precipitating conditions. (3) Owing to the recent technological advances (*Crosson*, 2008; *Kerstel*, 2004; *Kerstel and Gianfrani*, 2008), water vapour measurements can be directly made in the field and carried out on mobile platforms (e.g. ship and aircraft), or in a remote location under unmanned conditions. Also, the vapour measurement is in real-time and at a high time resolution (in the order of seconds). With the above advantages, the observation of water vapour isotopes has been dramatically expanded in the last decade (*Galewsky et al.*, 2016), adding comprehensive information for understanding the atmospheric water cycle.

On what time resolution should we take precipitation isotope samples?

Despite the same underlying physics, different pictures can emerge on different temporal and spatial scales. This resembles the case for other variables, such as temperature. For example, a strong diurnal cycle of temperature would not be seen on a seasonal or inter-annual time scale, although the seasonal or inter-annual temperature is calculated based on the hourly or minutely observations. The same applies to the isotope observations.

As stated previously, on short time (e.g. daily, hourly, sub-hourly) scales, the influences from small scale processes (e.g. cloud microphysics, below-cloud processes) and the fast changes of air masses become important (Paper II). The fast and substantial changes will be overlooked with sampling on a low time resolution. Therefore, high time resolution (in the order of 10 minutes, e.g. 10~30 minutes) sampling would be beneficial if one wants to study, for example, cloud microphysics or the fast evolution of weather systems.

While higher time resolution allows one to understand faster processes, knowing how these faster processes vary may not influence the way to interpret longer-time scale observations. For example, despite the possibly strong influence of below-cloud evaporation on the precipitation isotope, the rainfall contribution during the evaporation-stage in the case studied in Paper II was too small (<10 %) to markedly influence the isotope composition of the total event rainfall. In other words, the evaporation signal can be too small to be detected with a long sampling period or due to the uncertainty of sampling and analysing.

On a multi-day scale, the isotope signals are more associated with the variety of large scale circulations (Paper III). And on climate (e.g. seasonal, inter-annual, millennial) scales, the isotope signals can be basically explained by first-order processes such as the temperature difference between the source and sink (e.g. *Dansgaard*, 1964), the changes of the moisture source $\mathrm{RH_{SST}}$ (*Jouzel et al.*, 1982) or SST (*Johnsen et al.*, 1989; *Uemura et al.*, 2012). From this perspective, daily or monthly sampling is sufficient if one's interest is to study the seasonal or inter-annual variability. For studies on longer climatic time scales, one would turn to the proxies dating back to thousands of years, where the resolution varies from seasons to several thousands of years (e.g. *Svensson et al.*, 2008; *Wang et al.*, 2001).

How can the isotope observation help to improve the precipitation representation in the circulation model?

Precipitation bias in numerical weather simulations is often associated with poor parametrisations of sub-grid scale physics (*Mauritsen et al.*, 2012). To evaluate or constrain a model's parametrisations, it is often beneficial to use more and varied observations. This is to reduce the chances for a numerical simulation to produce "correct" results for the wrong reasons because of compensating errors (*Galewsky et al.*, 2016). Stable water isotopes have a unique potential to serve as the needed constraints, as they provide insights of moisture origin and phase change history. For example, the d-excess of formed precipitation involving supersaturation conditions is highly sensitive to the parametrisation of cloud microphysics (*Ciais and Jouzel*, 1994; *Jouzel and Merlivat*, 1984; *Risi et al.*, 2010). Another example, the isotope observations can be used to investigate the moisture turnovers (pick-up and release) which can not be detected by the conventional humidity measurements; while the specific humidity may not change or only change slightly after mixing of different air masses, the final isotope composition can change substantially. Therefore, as a new and independent observation, stable water isotopes may provide unique values to detect shortcomings in the representation of precipitation processes in numerical models. To this end, this work improves the data quality of the observation by a careful correction of instruments and provides a valuable high-resolution observation of a precipitation event as well as a long-term time series that expands the regional isotope observation network. These high-quality datasets have the potential to be used to assess cloud models or regional circulation models (*Pfahl et al.*, 2012; *Yoshimura et al.*, 2008).

What can we learn from the comparison between observations and models?

The comparison between the observations and the Rayleigh model simulation of the atmospheric river case in Paper II shows that even though the classical Rayleigh model can be suitable to represent the isotope composition near cloud top and in some convective situations, it reaches conceptual limitations for explaining surface precipitation and precipitation from deep stratiform clouds in frontal systems such as atmospheric rivers. This is because, in nature, precipitation formed above enters into subsequent air parcels below. We have therefore in Paper II suggested to consider instead an entire stack of Rayleigh-model air parcels as a better representation of stratiform cloud processes. In this stack of Rayleigh models, each stack of air parcel contributes to the precipitation by condensation/deposition, rimming, scavenging, and partially equilibrating with the water vapour on passing through. Given such a vertically coupled perspective, the vapour from lower levels can contribute substantially to the surface precipitation. Therefore, compared with a single cloud top or condensation temperature from one Rayleigh process, a vapour-mass-weighted average condensation temperature from the vapour column can better reflect the influences on the fractionation process in the entire cloud. It thus appears necessary to invoke more complex numerical tools in the interpretation, such as isotope-enabled numerical weather prediction models or Rayleigh-type models adapted to stratiform clouds.

In Paper III, we have estimated d-excess time series using both an empirical (*Pfahl and Sodemann*, 2014) and a theoretically predicted (*Merlivat and Jouzel*, 1979) d-$\mathrm{RH}_{\mathrm{SST}}$ relationship, based on the source conditions identified by a Lagrangian moisture source diagnostic. We find that the models correctly reproduce the variation patterns, but with substantial offsets. The comparison is providing interesting clues on when the models work well or when they do not work well. Further investigations on the influencing factors (e.g. land evaporation) behind these agreements or disagreements could improve our knowledge on the driving mechanisms in the water cycle (e.g. *Aemisegger et al.*, 2014).

What is the existing isotope observation network in the North Atlantic region and what can we learn from it?

Within the last decade, several long-term vapour isotope time series have been obtained in the North Atlantic and Arctic regions (Fig. 3.1). We have now expanded the existing isotope network with our observation in Bergen, which is a midlatitude location influenced by distinct weather systems (e.g. North Atlantic cyclones, cold air outbreaks) and frequent and intense precipitation. Also, the location of Bergen is in between those existing measurement stations. The long-range and well-spaced coverage of these observations favours potential future comparison with the isotope-enabled circulation models.

hIn addition, the observation network provides opportunities to investigate the atmospheric water cycle between source and sink. For example, combining simultaneous water vapour isotope measurements from three measuring stations along an atmospheric river bringing moisture from subtropics to Greenland, *Bonne et al.* (2015) provide the first observed case where the d-excess is conserved during atmospheric transport. In our case of Bergen, the observations in Bermuda (*Steen-Larsen et al.*, 2014a) and at the south coast of Greenland (*Bonne et al.*, 2014) or Iceland (*Steen-Larsen et al.*, 2015) can potentially provide the isotopic information of the upstream moisture sources when the moisture comes from the southwest. Similarly, when the moisture comes from the north, the observations in Svalbard (*Leroy-Dos Santos et al.*, 2020) will be beneficial.

Some future perspectives

Our case study in Paper II provides a unique stable isotope dataset of surface vapour and precipitation of an atmospheric river event in southwestern Norway. The uniqueness embodies in the high-resolution sampling, combined water vapour and precipitation isotope observation, and the first reported case of the region. This one case study demonstrates the important value of paired isotope measurements for data-model comparison and thus for improving our understanding of the complex processes driving isotopic variability in the atmospheric moisture in regional isotope-enabled models (*Dütsch et al.*, 2016; *Pfahl et al.*, 2012; *Yoshimura et al.*, 2008). More cases can be performed in the future to test the more general validity of the results obtained in this case study (Appendix C).

It would also be of interest to conduct isotope-involved laboratory experiments to study cloud microphysics. For example, *Steen-Larsen et al.* (2014b) suggest that laboratory experiments such as injecting an isotopically-known vapour into a snow disk of known isotopic composition at different temperature gradients may help to quantify the isotopic exchange processes at the snow surface. Similar experiments could also be conducted to study the kinetic fractionation effect during snow formation at supersaturation conditions with respect to ice, as demonstrated already in a simple experiment by *Jouzel and Merlivat* (1984). Certainly, further investigations in this direction would be needed, among others, to allow for validating the implementation of stable water isotopes in numerical circulation models.

Chapter 7

Scientific papers

Paper I

Correcting the impact of the isotope composition on the mixing ratio dependency of water vapour isotope measurements with cavity ring-down spectrometers

Yongbiao Weng, Alexandra Touzeau, and Harald Sodemann
Atmospheric Measurement Techniques, **13/6** (2020)

Atmos. Meas. Tech., 13, 3167–3190, 2020
https://doi.org/10.5194/amt-13-3167-2020

Atmospheric Measurement Techniques
Open Access
EGU

Correcting the impact of the isotope composition on the mixing ratio dependency of water vapour isotope measurements with cavity ring-down spectrometers

Yongbiao Weng, Alexandra Touzeau, and Harald Sodemann

Geophysical Institute, University of Bergen, and Bjerknes Centre for Climate Research, Bergen, Norway

Correspondence: Yongbiao Weng (yongbiao.weng@uib.no)

Received: 15 August 2019 – Discussion started: 23 October 2019
Revised: 30 April 2020 – Accepted: 11 May 2020 – Published: 16 June 2020

Abstract. Recent advances in laser spectroscopy enable high-frequency in situ measurements of the isotope composition of water vapour. At low water vapour mixing ratios, however, the measured stable water isotope composition can be substantially affected by a measurement artefact known as the mixing ratio dependency, which is commonly considered independent of the isotope composition. Here we systematically investigate how the mixing ratio dependency, in a range from 500 to 23 000 ppmv of three commercial cavity ring-down spectrometers, is affected by the isotope composition of water vapour. We find that the isotope composition of water vapour has a substantial and systematic impact on the mixing ratio dependency for all three analysers, particularly at mixing ratios below 4000 ppmv. This isotope composition dependency can create a deviation of ± 0.5 ‰ and ± 6.0 ‰ for δ^{18}O and δD, respectively, at ~ 2000 ppmv, resulting in about 2 ‰–3 ‰ deviation for the *d*-excess. An assessment of the robustness of our findings shows that the overall behaviour is reproducible over up to 2 years for different dry gas supplies, while being independent of the method for generating the water vapour and being the first order of the evaluation sequence. We propose replacing the univariate mixing ratio dependency corrections with a new, combined isotope composition–mixing ratio dependency correction. Using aircraft- and ship-based measurements in an Arctic environment, we illustrate a relevant application of the correction. Based on our findings, we suggest that the dependency on the isotope composition may be primarily related to spectroscopy. Repeatedly characterising the combined isotope composition–mixing ratio dependency of laser spectrometers when performing water vapour measurements at high elevations, on aircraft, or in polar regions appears critical to enable reliable data interpretation in dry environments.

1 Introduction

Stable water isotopes (hydrogen and oxygen) are natural tracers in the atmosphere and hydrosphere and have long been used to improve our understanding of the hydrological cycle and climate processes (Dansgaard, 1953, 1954; Gat, 1996). Advances in laser spectroscopy now allow for high-frequency in situ measurements of the isotope composition of water vapour in the atmosphere (Kerstel, 2004; Kerstel and Gianfrani, 2008). One commercially available type of instrument is the cavity ring-down spectrometer (CRDS) manufactured by Picarro, Inc., USA. The measurement principle of CRDS is based upon the absorption of a laser pulse at a wavelength specific to a given isotopologue (O'Keefe and Deacon, 1988; Crosson, 2008). The Picarro L2130-i and L2140-i CRDS analysers have an optimal performance within a water vapour mixing ratio of 19 000–21 000 ppmv (parts per million by volume), where high signal-to-noise ratios enable precise measurements. This range is typically maintained during liquid sample analysis. In situ measurements of the atmospheric water vapour isotopes are not constrained to this optimal mixing ratio range (Gupta et al., 2009). At lower water vapour mixing ratios, the measurement uncertainty increases due to weaker absorption and, thus, lower signal-to-noise ratios. Additionally, outside of this range, the measurement suffers from a mixing-ratio-dependent deviation of the isotope composition. Since atmospheric mixing ratios can

Published by Copernicus Publications on behalf of the European Geosciences Union.

vary from below 500 ppmv in dry regions (e.g. polar regions or the middle and upper troposphere) to 30 000 ppmv or more in humid regions (e.g. the tropics), an appropriate correction for this *mixing ratio dependency* for high-quality in situ measurements of atmospheric water vapour is required (e.g. Aemisegger et al., 2012; Bonne et al., 2014).

The water vapour mixing ratio dependency (hereafter *mixing ratio dependency*), sometimes also named the humidity isotope response (Steen-Larsen et al., 2013, 2014) or concentration dependency (Wen et al., 2012; Bailey et al., 2015) of infrared laser spectrometers for water isotopes, has been described in numerous studies (e.g. Lis et al., 2008; Schmidt et al., 2010; Sturm and Knohl, 2010; Bastrikov et al., 2014; Sodemann et al., 2017). Many studies found the mixing ratio dependency to be non-linear and, to some extent, specific to both the instrument used and the isotope composition measured. For example, reviewing the then-available systems for vapour generation on Picarro L1115-i and L1102-i analysers, Wen et al. (2012) showed that the mixing ratio dependency could vary for each specific instrument. Aemisegger et al. (2012) demonstrated that the mixing ratio dependency varies for different instrument types and generations and is affected by the matrix gas used during calibration. However, these authors did not find a substantial dependency on the isotope composition when testing four different standards. Bonne et al. (2014) speculated that the different mixing ratio dependency functions at low mixing ratios (below 2000 ppmv) for their two working standards are likely an artefact of residual water vapour after using a molecular sieve. Bailey et al. (2015) found the mixing ratio dependency to be clearly different for three tested standard waters, while emphasising the uncertainties from statistical fitting in which the characterisation data are infrequent. Sodemann et al. (2017) found a substantial impact from a mixing ratio dependency correction when processing aircraft measurements of d-excess over the Mediterranean Sea but did not account for different isotopic standards in detail. Bonne et al. (2019) characterised the mixing ratio dependency of their ship-based water vapour isotope measurements using four water standards and noted a dependency of the mixing ratio dependency on the isotope standard. They did not observe a significant drift in the dependency for measurements separated by several months. Using the ambient air dried through an Indicating Drierite as a carrier gas, Thurnherr et al. (2020) characterised the mixing ratio dependency for their customised L2130-i analyser operating with two different cavity flow rates. They observed a moderate dependency on the isotope composition with a normal cavity flow rate ($\sim$ 50 sccm) but found a much weaker, or negligible, dependency on the isotope composition with a high cavity flow rate ($\sim$ 300 sccm).

To summarise, only some previous studies have recognised the impact of the isotope composition of measured standards on the mixing ratio dependency as a significant uncertainty source. More importantly, no systematic investigation of the influence of the isotope composition on the mixing ratio dependency has been conducted so far. Given the potentially large impact of such corrections at very low water vapour mixing ratios, this is an important piece of research required for enabling the reliable interpretation and comparison of measurements at dry conditions (such as in the high-elevation or polar regions or from research aircraft).

Here we present a systematic analysis of the impact of the isotope composition on the mixing ratio dependency for three commercial CRDS analysers, namely one Picarro L2130-i analyser and two Picarro L2140-i analysers, by using five standard waters with different isotope compositions. Methods and data are presented in Sect. 2. Using the measurements from one analyser, we demonstrate the characterisation of the isotope composition–mixing ratio dependency in Sect. 3. We then evaluate the robustness of the isotope composition–mixing ratio dependency across the three analysers by also considering the different vapour generators, matrix gas compositions, measuring sequences, and temporal stability (Sect. 4). A new correction scheme is proposed in Sect. 5. Using water vapour isotope measurements from aircraft and a ship acquired during the Iceland–Greenland Seas Project (IGP) measurement campaign in the Iceland–Greenland seas (Renfrew et al., 2019) as a test case, we investigate the potential impact of the isotope composition–mixing ratio dependency correction in Sect. 6. We then discuss the potential origin of the influence of isotope composition on the mixing ratio dependency (Sect. 7). Finally, we provide recommendations on how to apply the correction scheme to other analysers (Sect. 8).

2 Methods and data

This section introduces the terminology used throughout the paper, explains the measurement principle of the instruments used, and provides an overview of the total of 15 experiments (Table 1) that have been conducted to evaluate the potential influencing factors on the isotope composition–mixing ratio dependency both separately and repeatedly. These 15 experiments can be separated into five categories with respect to their aims (Table 3). With these five categories, we assess the following influencing factors: the dependence on the vapour-generating method, the dependence on the specific instrument, the long-term stability of the dependence behaviour, the influence from the dry gas matrix, and the influence of the measuring sequence. In the end, we introduce the in situ measurement data that are used to illustrate the impact of correction.

2.1 Terminology

The abundance of stable water isotopes in a reservoir is quantified as the concentration ratio of the rare ($HD^{16}O$ or $H_2^{18}O$) to the abundant ($H_2^{16}O$) isotopologue. Note that the definition here is referred to as the molecular isotope ratio, as mea-

Table 1. Overview of all 14 characterisation experiments regarding the instrument, the vapour-generation method, the type of dry gas supply, the measured standard waters, the mixing ratio steps, the mixing ratio span, and the experiment time. For characterisations with injections, four injections are typically carried out at each mixing ratio. For characterisations with continuous vapour streaming via a Standard Delivery Module (SDM), normally 20–40 min of measurements are carried out at each mixing ratio. The values of the water concentrations are the uncalibrated values measured on the corresponding analyser. Instrument HIDS2254 is model type L2130-i, while instruments HKDS2038 and HKDS2039 are of model type L2140-i.

No.	Instrument	Method	Dry gas	Standard water	Steps	Span (ppmv)	Time
1	HIDS2254	Autosampler	Synthetic air	GSM1, MIX, VATS, DI, EVAP	47–49	∼ 500–23 000	Feb 2017
2		Autosampler	Synthetic air	GSM1, VATS, DI, EVAP	27–30	∼ 1000–23 000	May 2018
3		Autosampler	N_2	GSM1, VATS, DI, EVAP	25–29	∼ 500–23 000	May 2018
4		SDM	Synthetic air	DI	24	∼ 700–23 000	Jul 2016
5		SDM	Synthetic air	DI	11	∼ 1300–20 000	Feb 2018
6		SDM	Synthetic air	GSM1, DI	23,27	∼ 700–23 000	Jun 2018
7		SDM	N_2	GSM1, DI	13,16	∼ 1200–23 000	Jun 2018
8		SDM	Air through Drierite	GSM1	27	∼ 700–23 000	Dec 2016
9	HKDS2038	Autosampler	N_2	GSM1, MIX, VATS, TAP, EVAP	42–44	∼ 800–27 000	Jan 2017
10		Autosampler	N_2	GSM1, VATS, DI	36,29,19	∼ 600–30 000	Feb 2018
11		Autosampler	N_2	MIX	19	∼ 300–23 000	Dec 2019
12		Manual injection	Synthetic air	NEEM, GV, BERM	8	∼ 2400–24 000	Feb 2018
13		Manual injection	Synthetic air	NEEM, GV, BERM	8	∼ 2600–22 000	Mar 2018
14	HKDS2039	Autosampler	N_2	GSM1, MIX, VATS, DI, EVAP	45–47	∼ 500–27 000	Jan 2017
15		Autosampler	N_2	GSM1	20	∼ 500–24 000	Jul 2019

sured by laser spectrometry. Apart from statistical factors, this definition can be shown to be equal, in the first order, to the atomic isotope ratio R determined by mass spectrometry (Mook et al., 2001). The (molecular) isotope ratio of hydrogen in a water reservoir, for example, is then as follows:

$$^{2}R = \frac{[\mathrm{HD^{16}O}]}{[\mathrm{H_2^{16}O}]}. \qquad (1)$$

Isotope abundance is generally reported as a deviation of the isotope ratio of a sample relative to that of a standard, known as δ value, and is commonly expressed in units of per mil (‰) deviation from the Vienna Standard Mean Ocean Water 2 (VSMOW2) by means of $^{2}R_{\mathrm{VSMOW2}} = (155.76 \pm 0.05) \times 10^{-6}$ (Hagemann et al., 1970) and $^{18}R_{\mathrm{VSMOW2}} = (2005.20 \pm 0.45) \times 10^{-6}$ (Baertschi, 1976). The VSMOW2 is distributed by the International Atomic Energy Agency (International Atomic Energy Agency, 2009) and δ is expressed as follows:

$$\delta = \frac{R_{\mathrm{sample}} - R_{\mathrm{VSMOW2}}}{R_{\mathrm{VSMOW2}}} \cdot 1000\,‰. \qquad (2)$$

The magnitude of the deviation introduced by the mixing ratio dependency is typically at least 1 order of magnitude less than the span of the isotope compositions of the measured standards. To focus on the deviation of the measured isotope compositions at various mixing ratios (δ_{meas}) from the isotope composition at a reference mixing ratio (δ_{cor}), we use the $\Delta\delta$ notation, which is defined as follows:

$$\Delta\delta = \delta_{\mathrm{meas}} - \delta_{\mathrm{cor}}. \qquad (3)$$

We choose 20 000 ppmv as a reference level within the nominal optimal performance range of the CRDS analyser. The isotope composition at the exact value of 20 000 ppmv is thus obtained from a linear interpolation between the closest measurements above and below 20 000 ppmv (mostly between 19 000 and 21 000 ppmv). Note that all mixing ratios reported in this study are direct (raw) measurements from the CRDS and that the isotope composition–mixing ratio dependency correction is applied to the raw data before calibration.

While $\Delta\delta^{18}$O and $\Delta\delta$D are given directly by the definition above, the deviation for the secondary parameter d-excess $= \delta\mathrm{D} - 8 \cdot \delta^{18}\mathrm{O}$ (Dansgaard, 1964) is obtained from the following calculation: $\Delta d\text{-excess} = \Delta\delta\mathrm{D} - 8 \cdot \Delta\delta^{18}\mathrm{O}$.

2.2 Instruments

The instruments investigated in this study include two Picarro L2140-i analysers (serial nos. HKDS2038 and HKDS2039) and one Picarro L2130-i analyser (serial no. HIDS2254; all from Picarro, Inc., USA). Hereafter, we refer to each instrument by their serial number. The instruments record at a data rate of ∼ 1.25 Hz and with an air flow of ∼ 35 sccm through the cavity. To minimise instrument drift and errors from the spectral fitting, these CRDS systems control the pressure and temperature of their cavities at (80 ± 0.02) °C and (50 ± 0.1) Torr ((66.66 ± 0.13) hPa) precisely.

For the spectral fitting, the instruments target three absorption lines of water vapour in the region of 7199–7200 $\mathrm{cm^{-1}}$ (Steig et al., 2014). In the CRDS, a laser saturates the measurement cavity at one of the selected absorption wavelengths. After switching the laser off, a photodetector measures the decay (ring down) of photons leaving the cavity through the semi-transparent mirrors (slightly less than

100 % reflectivity). The ring-down time is inversely related to the total optical loss in the cavity. For an empty cavity, the ring-down time is solely determined by the reflectivity of the mirrors. For a cavity containing gas that absorbs light, the ring-down time will be shorter due to the additional absorption from the gas. The absorption intensity at a particular wavelength can be determined by comparing the ring-down time of an empty cavity to the ring-down time of a cavity that contains gas. The absorption intensities at all measured wavelengths generate an optical spectrum in which the height or underlying area of each absorption peak is proportional to the concentration of the molecule that generated the signal. The height or underlying area of each absorption peak is calculated based on the proper fitting of the absorption baseline. At lower water vapour concentrations, the signal-to-noise ratio decreases and the fitting algorithms are affected by various error sources (see Sect. 7).

As a custom modification, the L2130-i (serial no. HIDS2254) operates with two additional lasers that allow for rapid switching between the three target wavelengths, which enables a higher (5 Hz) data acquisition rate and a larger cavity-flow rate than a regular L2130-i. In the present study, we used the flow rates and measurement frequencies as for regular L2130-i analysers. The L2130-i uses peak absorption for the spectral fitting, whereas the L2140-i uses an integrated absorption within the spectral features (Steig et al., 2014). The L2140-i is therefore substantially less sensitive to the pressure broadening and narrowing of the absorption lines due to changes in the matrix gas that can affect older generation analysers, such as the L2120-i (Johnson and Rella, 2017). Manufacturer specifications commonly state a measurement range for vapour from 1000 to 50 000 ppmv. As a custom modification, all instruments used here have been calibrated down to 200 ppmv with an unspecified procedure by the manufacturer.

Water vapour measurements with these instruments have a total error budget that involves the uncertainty from the calibration standards projecting onto the VSMOW2 and Standard Light Antarctic Precipitation 2 (SLAP2; collectively VSMOW2–SLAP2) scale and from the time-averaging method employed for the native time resolution data. The Allan deviation quantifies the precision – depending on the averaging time interval. Previous studies found typical Allan deviations of $< 0.1\,‰$ for δ^{18}O and $\sim 0.1\,‰$ for δD at 15 700 ppmv for averaging times of 1–2 min for the L2130-i (Aemisegger et al., 2012) and similar values for these averaging times for the L2140-i (Steig et al., 2014). Any corrections for the mixing ratio dependency are applied to the raw data at a native time resolution. The uncertainty of any correction is thereby given from a combination of the averaging time of the vapour measurements at a given mixing ratio and the uncertainty of the employed calibration standards.

2.3 Standard waters

To identify the influence of the isotope composition on the mixing ratio dependency, we have used multiple internal standard waters calibrated on the international VSMOW2–SLAP2 scale to characterise the mixing ratio dependency. The standard waters include four laboratory standards in use at the Facility for Advanced Isotopic Research and Monitoring of Weather, Climate and Biogeochemical Cycling (FARLAB) of the University of Bergen and three laboratory standards in use at the isotope laboratory of the University of Iceland (UI; Table 2). For the FARLAB standards, one is obtained from snow in Greenland (GSM1), one is mountain snow from Norway (VATS), one consists of deionised tap water at Bergen (DI), and one is evaporated DI water (EVAP). Besides the four laboratory standards, we have also used an even mixing between GSM1 and VATS (MIX) and the uncalibrated deionised tap water (TAP). For the UI standards, one is from snow at the North Greenland Eemian Ice Drilling (NEEM) site in Greenland, one consists of groundwater in Reykjavik (GV), and one is Milli-Q® purified water based on ocean water from Bermuda (BERM). The isotope compositions of all the waters used span from $-33.52\,‰$ to $5.03\,‰$ for δ^{18}O and from $-262.95\,‰$ to $6.26\,‰$ for δD (Table 2).

2.4 Vapour-generation methods

We use two methods to generate vapour for characterising the isotope composition–mixing ratio dependency of the three instruments, namely discrete liquid injections and continuous vapour streaming. These are essentially two ways of generating a vapour sample to be analysed by the infrared spectrometers. Both methods involve the injection of a liquid standard water into a heated evaporation chamber in which the injected water is completely evaporated and mixed with a dry matrix gas.

2.4.1 Dry gas supply

Previous studies of Picarro CRDS analysers preceding the L2140-i show that the matrix gas has an influence on the characterisation of the mixing ratio dependence in the CRDS isotope measurement of water vapour (Aemisegger et al., 2012; Johnson and Rella, 2017). It is therefore important to know the influence of the matrix gas on the isotope composition–mixing ratio dependency to determine, depending on the measurement situation, a preferred method for obtaining the final correction relationship. The manufacturer recommends a customer-supplied gas drying unit (e.g. Drierite desiccants) to supply dry gas for the Standard Delivery Module (SDM) unit. Here we either used a single drying unit with ambient air or dry gas cylinders that contain synthetic air (synthetic air 5.5, purity 99.9995 %; Praxair Norge AS) or N_2 (Nitrogen 5.0, purity $> 99.999\,\%$; Praxair Norge

Table 2. Isotope compositions of the standard waters used in this study. The values are reported on the VSMOW2–SLAP2 scale. *FARLAB standards* are the laboratory standards used at FARLAB, University of Bergen, and *UI standards* are the laboratory standards used at the isotope laboratory of the University of Iceland. All the waters are at laboratory working standards, except MIX and TAP. MIX is obtained from an even mixing of GSM1 and VATS. TAP is deionised tap water from Bergen, Norway. The isotope compositions of these two waters are calibrated in experiment 9 by using the measured working standards. The σ for *FARLAB standards* represents the standard deviation of the mean for the six liquid injections, while σ for *UI standards* is a long-term standard deviation.

	δ^{18}O (‰)	σ (‰)	δD (‰)	σ (‰)	*d*-excess (‰)	σ (‰)
FARLAB standards						
GSM1	−33.07	±0.02	−262.95	±0.04	1.63	±0.17
MIX	−24.78	±0.02	−193.90	±0.08	4.30	±0.20
VATS	−16.47	±0.02	−127.88	±0.09	3.89	±0.18
DI	−7.78	±0.01	−50.38	±0.02	11.83	±0.10
TAP	−7.98	±0.01	−52.89	±0.05	10.97	±0.13
EVAP	5.03	±0.02	4.75	±0.11	−35.47	±0.16
UI standards						
NEEM	−33.52	±0.05	−257.1	±0.6	11.05	±0.72
GV	−8.54	±0.05	−57.7	±0.6	10.60	±0.72
BERM	0.52	±0.05	6.3	±0.6	2.10	±0.72

Table 3. Summary of the experiment design ordered by the aims and including the dependency on the vapour-generating method, the dependency on the tested instrument, the long-term stability of the dependency behaviour, the influence from the dry gas supply, and the influence of the measuring sequence.

Experiments	Factor	Instrument	Parameters	Figure
2, 6	Vapour generation	HIDS2254	Synthetic air	A1 (a–c)
3, 7	Vapour generation	HIDS2254	N_2	Not shown
6, 7, 8	Dry gas supply	HIDS2254	Synth. air, N_2, Drierite, SDM	A1 (d–f)
2, 3	Dry gas supply	HIDS2254	Synth. air, N_2, autosampler	Not shown
9, 11, 15	Measuring sequence	HKDS2038, HKDS2039	Autosampler, N_2	A1 (g–i)
3, 9, 14	Instrument type	HIDS2254, HKDS2038, HKDS2039	Autosampler, N_2	A2
1, 2	Long-term stability (15 months)	HIDS2254	Autosampler, synthetic air	A3
4, 5, 6	Long-term stability (20–25 months)	HIDS2254	SDM, Synthetic air	Not shown
9, 10	Long-term stability (11 months)	HKDS2038	Autosampler, N_2	Not shown
12, 13	Long-term stability (1 month)	HKDS2038	Manual inj., Synthetic air	Not shown

AS). We have tested the three types of dry gas supply, with the characterisation on instrument HIDS2254, for continuous vapour streaming, and we have characterised the three analysers using synthetic air and/or N_2 for discrete liquid injections. Ambient air dried through Drierite can still contain some moisture (typically about 200 ppmv when the ambient water vapour is around 10 000 ppmv), which can contribute a non-negligible fraction to the measured isotope composition at low mixing ratios (e.g. 10 % below 2000 ppmv). The use of several drying units in a row, which includes the vertical arrangement of drying units to prevent preferential gas flow, and careful handling of tubing tightness may provide the same background mixing ratio as with a gas cylinder (Kurita et al., 2012), but that has not been tested here.

2.4.2 Discrete liquid injections

The discrete liquid injections repeatedly generate vapour pulses by injecting between 0 and 2 µL of standard water from 1.5 mL PTFE/rubber-septum sealed vials with a 10 µL syringe (VWR, part no. 002977). Injections are operated by an autosampler (A0325; Picarro, Inc., USA) or by manual injection. Vaporisation of liquid water is achieved in a Picarro vaporiser (A0211; Picarro, Inc., USA) set to 110 °C. The vaporiser mixes the water vapour with synthetic air or N_2 from a gas cylinder at a pressure set to ∼ 170 hPa. The vaporiser chamber seals off for a few seconds to allow for sufficient mixing between the vapour and the matrix gas before delivering the mixture to the analyser at a highly stable mixing ratio.

Before switching to a new standard water, 8–12 injections of the new standard water at a mixing ratio of ∼

20 000 ppmv were applied each time to account for the memory effects from the previous injections. Then the sequence begins at the lowest (∼ 500 ppmv) and ends at the highest (∼ 23 000 ppmv) mixing ratio. Various mixing ratios are obtained by adjusting the injection volume in the 10 µL syringe. The injection volume was modified to be between 0.05 and 2.5 µL with a step of 0.05 µL, resulting in mixing ratios between approximately 500 and 23 000 ppmv with a step of ∼ 450 ppmv. Four injections in the high-precision mode (longer measurement period with approximately 10 min per injection) were applied to each mixing ratio, and the last three injections were then averaged for further analysis. Injections with an injection volume of 2 µL (∼ 19 000 ppmv) were carried out at the beginning and end of a sequence to account for potential instrument drift. A sequence for one standard water lasts approximately 35 h. The instrument drift within a sequence typically has a magnitude of (0.05 ± 0.02) ‰, (0.7 ± 0.1) ‰, and (0.4 ± 0.1) ‰ for δ^{18}O, δD, and d-excess respectively. The drift is 4–7 times larger than the uncertainty associated with the estimated drift but 1 order smaller than the deviation introduced by the mixing ratio dependency; it is corrected by assuming a temporal linearity during the sequence period.

Manual liquid injections were carried out during a field deployment where no autosampler was available. During manual injections, it is challenging to maintain a constant injection volume, and it is thus difficult to achieve a precise control of the water vapour mixing ratios. In this case, only injection volumes between 0.2 and 1.6 µL with a step of ∼ 0.2 µL are employed, which roughly corresponds to mixing ratios between 2400 and 24 000 ppmv with a step of ∼ 3000 ppmv. Despite the shorter measurement period (about 6 h), the instrument drift within a sequence increased by a factor of 2–3 for δ^{18}O ((0.16 ± 0.03) ‰) and δD ((1.65 ± 0.18) ‰), resulting in a drift of (0.37 ± 0.22) ‰ for d-excess. The relatively high instrument drift, when compared to the autosampler injections in the laboratory, is most likely due to the uncertainty introduced by the variable injection volume and the operation on a container on the deck of a research vessel (Renfrew et al., 2019). Instrument drift is corrected by assuming linear drift during each characterisation experiment. In all characterisation experiments, we applied three to five FARLAB standard waters when using an autosampler or three UI standard waters in the case of manual injections.

2.4.3 Continuous vapour streaming

To test the influence of the vapour-generation method, we used the continuous water vapour streaming of two laboratory standard waters (DI and GSM1). A continuous vapour stream is generated via a so-called Standard Delivery Module (SDM, A0101; Picarro, Inc., USA). The SDM is a device with two syringe pumps that provides automated delivery of two standard waters at up to three water concentrations per standard. The standard water is delivered to the Picarro vaporiser where it is instantly vaporised at 140 °C and simultaneously mixed with a dry matrix gas. The routines for vapour streaming at the different mixing ratios applied here follow recommendations by the manufacturer to characterise each instrument's mixing ratio dependency (SDM user manual; Picarro, Inc.). Mixing ratios between 600 and 24 000 ppmv were obtained by adjusting the liquid water injection speed of the syringe pumps from 0.002 to 0.8 μL s^{-1}. The generated standard vapour is continuously delivered to and measured by the spectrometer. During the characterisation, we measured about 25 mixing ratios at a step of ∼ 1000 ppmv (0.003 μL s^{-1}) for each standard water. Each mixing ratio is measured for 20–40 min, and the averaged value of a 5 min period close to the end of the measurement is used in the analysis. Due to unstable calibration performance, only sections of 1–2 min were used for the characterisations done in July 2016 and February 2018 for the laboratory standard DI on instrument HIDS2254.

A measurement sequence of standard GSM1 with ambient air dried through Drierite shows that the magnitude of the instrument drift during a 22 h measurement with the SDM is similar to that of the liquid injection with an autosampler. However, due to the lower precision of the SDM measurement, the instrument drift is comparable to – (0.10 ± 0.09) ‰ and (0.96 ± 0.36) ‰ for δ^{18}O and δD respectively – or smaller for the uncertainty associated with the estimated drift, i.e. (0.24 ± 0.78) ‰ for d-excess. Therefore, except for the measurement with standard GSM1 mentioned previously, the measurements with the SDM are not corrected for instrument drift.

2.5 In situ measurement data for studying the impact of the isotope composition–mixing ratio dependency correction

In order to test the impact of the isotope composition–mixing ratio dependency correction on actual measurements, we applied the proposed correction scheme to two data sets obtained from in situ vapour measurements during the Iceland–Greenland Seas Project (Renfrew et al., 2019) on board a research aircraft (analyser HIDS2254) and a research vessel (analyser HKDS2038) in March 2018 on the Iceland–Greenland seas (∼ 68° N, 12° W).

The HIDS2254 analyser was installed on board a Twin Otter research aircraft. The instrument was fixed on a rack on the right side of the non-pressurised cabin. A 3.5 m stainless-steel tube with 3/8 in. diameter, insulated and heated to 50 °C, was led from a backward-facing inlet located behind the right cockpit door to the analyser. A backward-facing inlet was selected to ensure that only vapour (and not particles or droplets) would be sampled. A manifold pump was used to draw the vapour through the inlet at a flow rate of about 8 slpm. The HIDS2254 took a sub-sample through a 0.2 m stainless-steel tubing in low-flow mode at a flow rate of ∼ 35 sccm. The selected vapour measurements from the aircraft were taken in the lower troposphere above the Iceland Sea during a cold air outbreak (CAO) on 4 March 2018. The particular water vapour measurement segment utilised here was taken during a 9 min long descent of the aircraft from 2900 to 180 m a.s.l. A Greenland blocking associated with northerlies in the Iceland–Greenland seas caused cold atmospheric temperatures, with an average of −12 °C at altitudes below 200 m. Accordingly, mixing ratios at low levels ranged from 2000 to 2700 ppmv. At higher levels, mixing ratios were as low as about 900 ppmv. After applying any correction schemes (see below), the water vapour isotope data from the aircraft are calibrated to the VSMOW2–SLAP2 scale using the long-term average of calibrations, with internal FARLAB laboratory standards on GSM1 and DI, by using the SDM from before and after the flight survey (details described in a forthcoming publication).

For the vapour measurements on board the research vessel (R/V *Alliance*), the HKDS2038 analyser was installed inside a heated measurement container that was placed on the crew deck at about 6 m above the water's surface. The ambient air was drawn into the container with a flow rate of around 8 slpm by a manifold pump through a 5 m long 1/4 in. stainless-steel tube and was heated to about 50 °C with self-regulating heating tape. The tube inlet was mounted 4 m above the deck and was protected from precipitation with a downward-facing tin can. The selected time period from the research vessel was acquired during a CAO event between 14 and 16 March 2018. At the beginning of the event, the mixing ratio dropped from 6000 to below 3000 ppmv within 2 h and then stayed at around 3000 ppmv for about 24 h before it increased to 8000 ppmv again.

3 Isotope composition–mixing ratio dependency

In this section we present the isotope composition–mixing ratio dependency from the characterisation result for the HIDS2254 instrument (Fig. 1). The characterisation is carried out using the method of discrete liquid injections (experiment 1). At each mixing ratio, a total of four injections are carried out in high-precision mode, and the last three injections are averaged for further analysis. The uncertainty at each mixing ratio is calculated as the standard deviation of the three injections taken; this standard deviation (colour error bars in Fig. 1) is substantially smaller than the standard deviation of one single injection (indicated by thick grey error bars in Fig. 1).

The mixing ratio dependency for δ^{18}O, displayed as the deviation $\Delta\delta^{18}$O, exhibits a skewed, inverse-U shape (Fig. 1a) for all of the water standards. As an example, standard GSM1 (dark blue symbols) starts with a deviation of −0.1 ‰ for a high mixing ratio of 23 000 ppmv, becomes positive after passing 20 000 ppmv, and continues increasing until reaching a maximum of around 3000 ppmv. Then $\Delta\delta^{18}$O quickly drops at lower mixing ratios and becomes negative again at around 500 ppmv. As the mixing ratio decreases further, the magnitude of the deviation increases substantially. Notably, the mixing ratio dependencies of the other four standard waters (light blue, green, orange, and red symbols for MIX, VATS, DI, and EVAP respectively) also depict an inverse-U shape. However, the maxima become smaller and shift towards higher mixing ratios (bottom right in Fig. 1a) with a more enriched isotope composition. This isotope-composition-related shift leads to an enlarged difference of $\Delta\delta^{18}$O between any of the standard waters. For example, $\Delta\delta^{18}$O for GSM1 (dark blue symbols) and EVAP (red symbols) differ by ∼ 0.9 ‰ at 2000 ppmv and by 2.0 ‰ at 1000 ppmv.

The isotope-composition-related shift is even more pronounced for $\Delta\delta$D (Fig. 1b). For the standard waters with relatively depleted isotope compositions (GSM1 – dark blue; and MIX – light blue), $\Delta\delta$D is positive and becomes larger as the mixing ratios decrease. For the standard waters with relatively enriched isotope compositions (VATS – green; DI – orange; and EVAP – dark red), $\Delta\delta$D becomes more negative with decreasing mixing ratios. This leads to an increasing divergence of the mixing ratio dependency at ∼ 15 000 ppmv and below. For example, $\Delta\delta$D for GSM1 (dark blue) and EVAP (red) differ by ∼ 11 ‰ at 2000 ppmv and by ∼ 21 ‰ at 1000 ppmv.

The isotope composition dependency of $\Delta\delta^{18}$O and $\Delta\delta$D has a substantial impact on the mixing ratio dependency of Δd-excess for different water standards. The mixing ratio dependency of Δd-excess below ∼ 15 000 ppmv now exhibits a U-shape, with the minimum located between 4000 (DI – orange) and 7000 ppmv (GSM1 – dark blue). The deviation for GSM1 (dark blue) and EVAP (red) differs by ∼ 3.8 ‰ at 2000 ppmv and by ∼ 5.3 ‰ at 1000 ppmv.

In summary, this characterisation shows that the mixing ratio dependency varies systematically according to the isotope composition of the measured standard water. It is most pronounced at low mixing ratios (below 10 000 ppmv) and also increases at lower mixing ratios. The substantial deviations are clearly important for in situ water vapour measurements in dry environments, particularly when the water vapour has large variations in the isotope composition. As demonstrated in Sect. 4, we find that this systematic isotope composition–mixing ratio dependency occurs irrespective of the vapour-generation method and dry gas supply and exists in a similar form in all three of the CRDS spectrometers characterised here.

The mixing ratio dependency of HIDS2254 seems to vary systematically with the isotope composition of the water standards, suggesting a potential spectroscopic origin (Sect. 7). This isotope composition–mixing ratio dependency will not be sufficiently removed by a uniform correction based on a single water standard. However, the dependency can be corrected if we can establish a correction function that takes both the mixing ratio and the isotope composition into account. First we investigate how robust and stable the de-

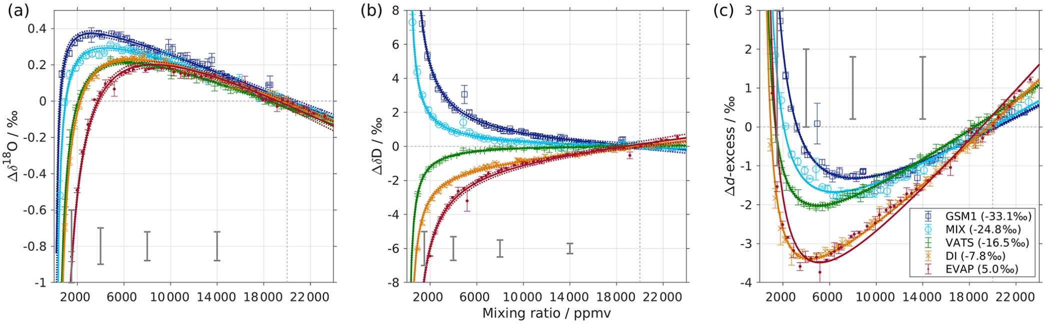

Figure 1. Mixing ratio dependency of uncalibrated measurements for **(a)** δ^{18}O, **(b)** δD, and **(c)** *d*-excess for five standard waters (GSM1, MIX, VATS, DI, and EVAP) on instrument HIDS2254 (Picarro L2130-i) with discrete liquid injections via an autosampler (experiment 1). Mixing ratio dependency is expressed as the deviation Δ of the measured isotope composition at each mixing ratio with respect to the reference mixing ratio of 20 000 ppmv. The symbol and error bar represents the mean and the standard deviation of the mean for the last three of a total of four injections at each mixing ratio. Solid lines are fits with the function $f(x) = \frac{a}{x} + bx + c$. Dashed lines are the 95 % confidence interval for the corresponding fit. Measurements and fits for *d*-excess are calculated with $\Delta d\text{-excess} = \Delta\delta\mathrm{D} - 8 \cdot \Delta\delta^{18}\mathrm{O}$. The typical 1 standard deviation of a single injection at the corresponding mixing ratio is indicated with grey error bars. Two outliers (at about 4300 and 8900 ppmv) are removed from the GSM1 measurements, and one outlier (at about 9000 ppmv) is removed from the VATS measurements.

scribed isotope dependency is over time before proposing a correction framework based on our characterisation results.

4 Robustness and temporal stability of the isotope composition–mixing ratio dependency

We carefully analysed the robustness of the isotope composition–mixing ratio dependency with respect to the choice of the method for vapour generation, the dry gas supply, the measuring sequence, individual instruments and instrument type, and its stability over time using 15 experiments in total (Table 1). Here we provide a summary of the results from these different experiments, with the detailed results given in Appendix A.

The robustness test indicates that the isotope composition–mixing ratio dependency is consistent across the two tested vapour-generation methods, i.e. discrete liquid injections and continuous vapour streaming (Appendix A1; Fig. A1a–c). Characterisations with synthetic air and N_2 are in agreement for δD but deviate for δ^{18}O (Appendix A2; Fig. A1d–f). A particularly substantial disagreement is found for the experiment using Drierite. This is likely caused by the contribution from water vapour remaining in the matrix air after the drying unit. The measuring sequence from high to low mixing ratios, or the reverse, shows a great similarity in the results, indicating that the potential hysteresis effects are not substantial (Appendix A3; Fig. A1g–i). However, we do note a different result for δ^{18}O at the lowest mixing ratio during one of the repeated experiments with MIX water (not shown). We suspect that the high sensitivity of the isotope composition–mixing ratio dependency at this range of δ^{18}O values could lead to pronounced deviations. While this aspect deserves further attention, we consider it as being second order with regards to the existence and cause of an isotope composition–mixing ratio dependency in the investigated CRDS instruments. Tests of all three analysers with discrete autosampler injections and N_2 as the matrix gas show a similar isotope composition–mixing ratio dependency in all three analysers investigated (Appendix A4; Fig. A2). The repeated characterisation of analysers HIDS2254 and HKDS2038 during a time period of up to 2 years shows that the isotope composition–mixing ratio dependency is an instrument characteristic that is, at the first order, constant over time (Appendix A5, Fig. A3).

In summary, the isotope composition–mixing ratio dependency is, at the first order, robust across a range of key parameters and stable over time. However, it is also apparent that individual instruments have a different strength, and it is the shape of the instrument characteristic that requires individual correction. In the next sections, we apply and evaluate a new scheme to correct for the isotope composition–mixing ratio dependency.

5 Correction framework

We now use the characterisation result previously obtained from instrument HIDS2254 as an example of how to derive a correction procedure for the isotope composition–mixing ratio dependency by following six sequential steps. Due to the systematic behaviour observed in Fig. 1, we chose a simple, traceable fitting procedure to obtain the two-dimensional correction function that can potentially be related to a physical cause. For the sake of simplicity, the equations in the following paragraphs are formulated to be valid for both δ^{18}O and δD.

5.1 General formulation

1. We obtain the mixing ratio dependency for each water standard as raw (uncorrected, uncalibrated) measurements of the isotope compositions. The water standards thereby cover a wide range of isotope compositions and different mixing ratios, particularly also at low mixing ratios.

2. We express the mixing ratio dependency for each water standard as the deviation of the raw measurements to the reference value at 20 000 ppmv (Eq. 3). The reference value is obtained from a linear interpolation between the closest measurements above and below 20 000 ppmv. These deviations are denoted as $\Delta\delta^{18}$O, $\Delta\delta$D, and Δd-excess as described in Sect. 2.1.

3. A suitable fitting function is fitted to the mixing ratio dependency of each standard water. Here we used fitting functions with the following form:

$$f_\delta(x) = \frac{a_\delta}{x} + b_\delta x + c_\delta, \tag{4}$$

   where x is the mixing ratio, δ indicates the isotope composition of the standard waters, and a_δ, b_δ, and c_δ are fitting coefficients for each water standard and isotope species.

4. We express the obtained fitting coefficients as a function of the isotope composition as $a(\delta)$, $b(\delta)$, and $c(\delta)$ for all the standard waters (Fig. 2, symbols). This reveals a dependency of the fitting coefficients on the isotope composition of the water standard. We now fit a suitable function to this dependency by using the following quadratic polynomial:

$$\begin{cases} a(\delta) = m_a(\delta - n_a)^2 + k_a, \\ b(\delta) = m_b(\delta - n_b)^2 + k_b, \\ c(\delta) = m_c(\delta - n_c)^2 + k_c, \end{cases} \tag{5}$$

   where δ is the isotope composition and m, n, and k are the respective fitting coefficients of the quadratic polynomials.

5. By replacing the parameters a_δ, b_δ, and c_δ in Eq. (4) with their parametric expressions in Eq. (5), we obtain the generalised fitting for the mixing ratio dependency, which is a function of both the mixing ratio x and the isotope composition of the measured water δ as follows:

$$f(x,\delta) = \frac{a(\delta)}{x} + b(\delta)x + c(\delta). \tag{6}$$

6. Using Eq. (6), we can now correct the measured isotope compositions to a reference mixing ratio at 20 000 ppmv when given any measured raw mixing ratio and isotope composition within the range investigated here. Thus, the isotope composition at 20 000 ppmv (δ_{cor}) is the unknown; its analytical solution is found by solving the following equation:

$$\delta_{\mathrm{meas}} - \delta_{\mathrm{cor}} = \frac{a(\delta_{\mathrm{cor}})}{h} + b(\delta_{\mathrm{cor}}) \cdot h + c(\delta_{\mathrm{cor}}), \tag{7}$$

   where h is the measured raw mixing ratio and δ_{meas} is the measured isotope composition at that mixing ratio. The right-hand side of the equation is the isotopic deviation determined from Eq. (6). The coefficients $a(\delta_{\mathrm{cor}})$, $b(\delta_{\mathrm{cor}})$, and $c(\delta_{\mathrm{cor}})$ are determined from Eq. (5). Equation (7) is a quadratic function; the procedure to obtain its analytical solution is given in Appendix C.

5.2 Correction function for analyser HIDS2254

We now exemplify the general steps given previously for the HIDS2254 analyser. The results from step 1 and 2 for HIDS2254 are presented in Sect. 3. Here we use a range from −33.07 ‰ to 5.03 ‰ for δ^{18}O and from −262.95 ‰ to 4.75 ‰ for δD, with mixing ratios between 500 and 25 000 ppmv (experiment 1 in Table 1).

The coefficients a_δ, b_δ, and c_δ obtained in step 3 from Eq. (4) for the five standard waters measured on instrument HIDS2254 are given in Table 4. While the magnitude differs between the coefficients, scaling analysis shows that each of the terms ($\frac{a}{x}$, bx, and c) on the right-hand side of Eq. (4) contributes similarly to the isotope composition–mixing ratio dependency (not shown). The fitting results from step 4 are shown in Fig. 1 (solid colour line). The choice of this type of function captures the behaviour of the isotope composition–mixing ratio dependency for both $\Delta\delta^{18}$O and $\Delta\delta$D of each standard water. Thus, the fit for Δd-excess is calculated from the fit of $\Delta\delta$ by $\Delta d\text{-excess}_{\mathrm{fit}} = \Delta\delta\mathrm{D} - 8 \cdot \Delta\delta^{18}\mathrm{O}$.

The coefficients m, n, and k obtained in step 4 in Eq. (5) are given in Table 5. The fitting results (solid line) with the fitting uncertainty (95 % confidence interval; black dotted line) are shown in Fig. 2. Since we only fit 5 data points, the fitting uncertainty is large, which results in a relatively large standard deviation for the isotope composition deviations $\Delta\delta$. This large standard deviation for $\Delta\delta$ can be reduced by using a bootstrapping approach (Efron, 1979) to estimate the fitting uncertainty in Eq. (5; Appendix B).

Following step 5, this results in a two-dimensional correction surface for each isotopologue as shown in Fig. 3 (black contours). For illustration purposes, some contours below 4000 ppmv are omitted for both δ^{18}O and δD. The isotope composition–mixing ratio dependency for both δ^{18}O and δD increases substantially at low mixing ratios. For δ^{18}O, the deviation changes from positive to negative as the mixing ratio decreases below ∼ 4000 ppmv. For δD, the deviation increases below 10 000 ppmv and splits into both positive and

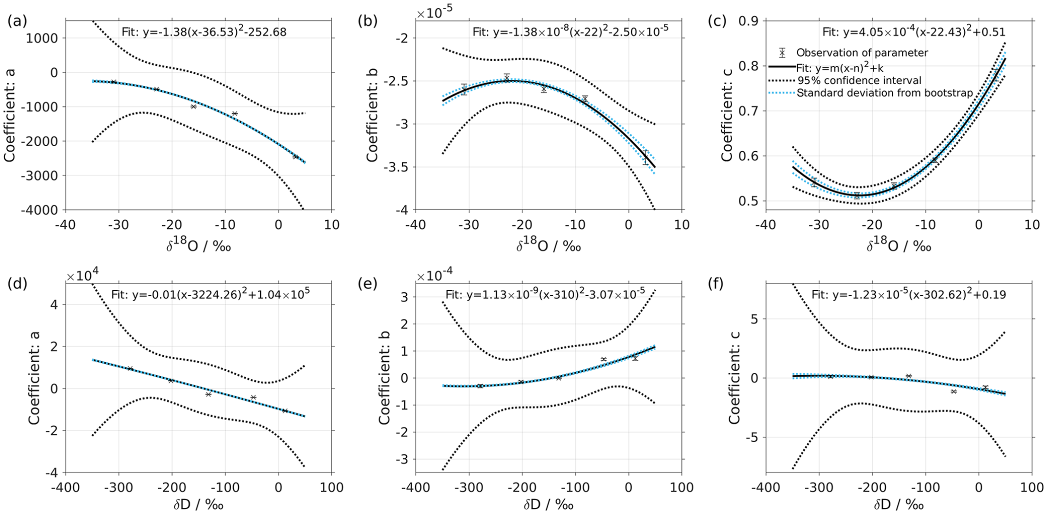

Figure 2. Dependency of fitting coefficients a, b, and c on δ^{18}O **(a–c)** and on δD **(d–f)**. The coefficients a, b, and c are from the fits for the five standard waters in Fig. 1. The solid line is the quadratic fit, with $f_j(y) = m_j(y - n_j)^2 + k_j$. The black dotted line shows the 95 % confidence interval. The blue dotted line shows the standard deviation estimated from a bootstrapping method.

Table 4. Fitting coefficients for the mixing ratio dependency behaviour of the five standard waters measured with HIDS2254. Coefficients a, b, and c are calculated with respect to the fitting function $f_\delta(x) = \frac{a_\delta}{x} + b_\delta \cdot x + c_\delta$. The reported uncertainty is 1 standard deviation. The fitting lines are shown in Fig. 1.

	Standard	a	b	c
δ^{18}O	GSM1	-275 ± 17	$-2.60 \times 10^{-5} \pm 7 \times 10^{-7}$	0.54 ± 0.01
	MIX	-489 ± 10	$-2.47 \times 10^{-5} \pm 5 \times 10^{-7}$	0.51 ± 0.01
	VATS	-996 ± 15	$-2.59 \times 10^{-5} \pm 5 \times 10^{-7}$	0.53 ± 0.01
	DI	-1200 ± 7	$-2.71 \times 10^{-5} \pm 4 \times 10^{-7}$	0.59 ± 0.01
	EVAP	-2470 ± 20	$-3.39 \times 10^{-5} \pm 8 \times 10^{-7}$	0.78 ± 0.01
δD	GSM1	9510 ± 170	$-2.96 \times 10^{-5} \pm 6.2 \times 10^{-6}$	0.12 ± 0.10
	MIX	3660 ± 90	$-1.47 \times 10^{-5} \pm 4.4 \times 10^{-6}$	0.07 ± 0.07
	VATS	-2780 ± 70	$-6.70 \times 10^{-7} \pm 1.88 \times 10^{-6}$	0.17 ± 0.03
	DI	-4220 ± 80	$6.93 \times 10^{-5} \pm 3.7 \times 10^{-6}$	-1.15 ± 0.06
	EVAP	$-10\,600 \pm 200$	$7.23 \times 10^{-5} \pm 6.6 \times 10^{-6}$	-0.79 ± 0.11

negative contributions – depending on the isotope composition. The uncertainty (1 standard deviation) for the deviation $\Delta\delta$ is typically 1 order of magnitude smaller than the $\Delta\delta$ values at the corresponding position.

The surface function exhibits the same features as those determined by the experimental results, underlining that the fitting procedure reflects the main characteristics of the isotope composition–mixing ratio dependency from the experimental data. At 20 000 ppmv, the correction function is not exactly 0, as the fit that is based on all the measurements is not constrained to the point [20 000, 0] ppmv. This deficiency could be addressed by a modified fitting procedure. Below 500 ppmv, the correction function has larger uncertainties due to the lack of measurements at this mixing ratio range. Note that the fitting functions used in Eqs. (4) and (5) are purely phenomenological and do not result from a particular physical model. Still, we recommend the proposed parameterisation to characterise individual instruments.

6 Impact of the isotope composition–mixing ratio dependency correction

We now investigate the impact of the isotope composition–mixing ratio dependency correction in situ measurements of

Table 5. Fitting coefficients for the isotope composition dependency of the mixing ratio dependency coefficients a, b, and c in Table 4. Coefficients m, n, and k are with respect to the fitting function $f_j(\delta) = m_j(\delta - n_j)^2 + k_j$. The reported uncertainty is 1 standard deviation. The fitting lines are shown in Fig. 2.

	Coefficient	m	n	k
$\delta^{18}O$	a	-1.38 ± 1.26	-36.5 ± 21.5	-253 ± 583
	b	$-1.38 \times 10^{-8} \pm 4.4 \times 10^{-9}$	-22 ± 4	$-2.50 \times 10^{-5} \pm 8 \times 10^{-7}$
	c	$4.05 \times 10^{-4} \pm 3.2 \times 10^{-5}$	-22.4 ± 0.8	0.51 ± 0.01
δD	a	-0.01 ± 0.25	$-3220 \pm 69\,300$	$1.04 \times 10^5 \pm 2.35 \times 10^6$
	b	$1.13 \times 10^{-9} \pm 2.12 \times 10^{-9}$	-310 ± 342	$-3.07 \times 10^{-5} \pm 5.73 \times 10^{-5}$
	c	$-1.23 \times 10^{-5} \pm 5.33 \times 10^{-5}$	-303 ± 759	0.19 ± 1.32

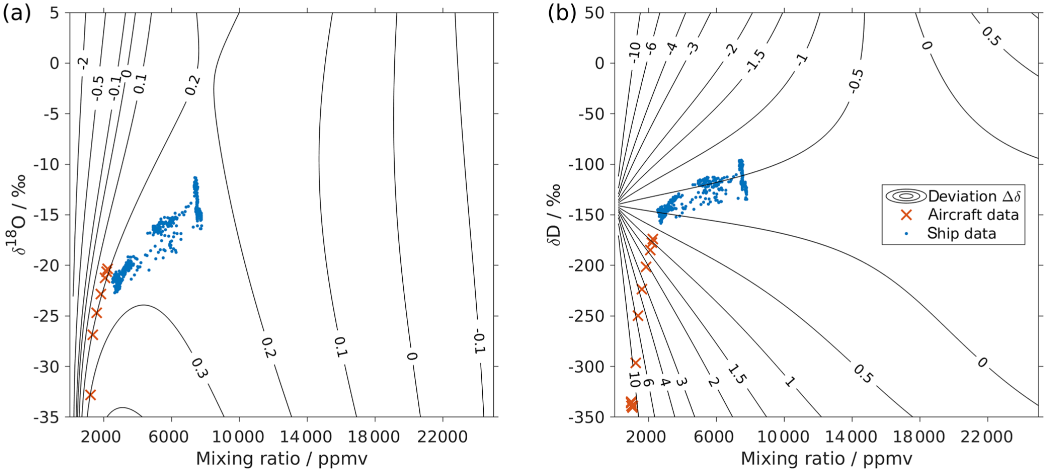

Figure 3. Surface function of the isotopic deviations for **(a)** δ^{18}O and **(b)** δD based on the isotope composition–mixing ratio dependency of instrument HIDS2254 (Picarro L2130-i). The x axis is the raw mixing ratio, and the y axis shows the raw isotope composition at 20 000 ppmv. Contours with numbers indicate the isotopic deviation of Δδ. Symbols show the isotope measurements over the Iceland Sea: measurements averaged to 1 min from an aircraft in the lower troposphere (red crosses) and measurements at a 10 min resolution from a research vessel (blue dots). The measurements from the aircraft were done with instrument HIDS2254 (Picarro L2130-i), and measurements on the research vessel were done with instrument HKDS2038 (Picarro L2140-i).

the isotope composition of water vapour with two CRDS analysers installed on board a research aircraft (HIDS2254) and a research vessel (HKDS2038; see Sect. 2.5).

6.1 Impact on the aircraft measurements

Low water vapour mixing ratios and a relatively wide range of (depleted) isotope compositions make water vapour isotope measurements from a research aircraft particularly suitable for demonstrating the impact of the new isotope composition–mixing ratio dependency correction. Figure 4 shows a vertical profile of 1 min averaged water vapour isotope measurements above the Iceland Sea (Sect. 2.5). During the descent of the aircraft from 2900 m a.s.l. to the minimum safe altitude, the water vapour mixing ratio gradually increases from about 800 ppmv at the top to 2300 ppmv near the surface (Fig. 4d). The stable isotope profiles (Fig. 4a–c) show three main characteristics. Above about 2000 m a.s.l., δ^{18}O and δD are depleted (∼ −42 ‰ and −320 ‰) with d-excess between 10 ‰ and 20 ‰. Between 2000 and 1400 m a.s.l., there is a transition where δ^{18}O and δD increase to around −30 ‰ and −240 ‰, respectively, and d-excess decreases to ∼ −5 ‰. Below 1400 m a.s.l., δ^{18}O, δD, and d-excess gradually increase until reaching about −22 ‰, −170 ‰, and 8 ‰, respectively, near the surface. The uncertainty (1 standard deviation) of the profile is obtained using the uncertainty propagation law, including the uncertainty (1 standard deviation) of the 1 min averaged data set (here the dominating source of uncertainty) and the uncertainty of the correction scheme.

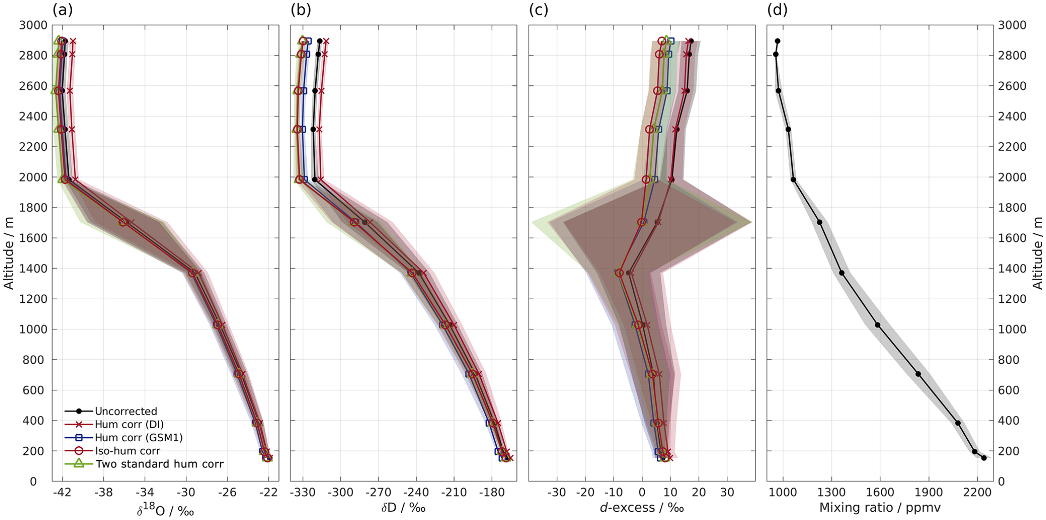

Figure 4. Vertical profiles of **(a)** δ^{18}O, **(b)** δD, **(c)** *d*-excess, and **(d)** mixing ratio measured by instrument HIDS2254 on an aircraft above the Iceland Sea on 4 March 2018. Shown are 1 min averaged profiles of the uncorrected data set (black line with dot) and four data sets using different isotope composition–mixing ratio dependency correction schemes as follows: the mixing ratio dependency of standard DI (orange curve with cross); standard GSM1 (blue curve with square); the isotope composition–mixing ratio dependency surface function (red curve with circle); and two mixing-ratio-dependency-corrected standards (green curve with triangle). All of the data sets are calibrated according to the VSMOW2–SLAP2 scale. Shading shows the total uncertainty (1 standard deviation) for the corresponding profiles. Note that the profile of δD has been adjusted 30 s forward to account for the longer response time of molecular HD^{16}O. The large uncertainty between 1400 and 2000 m for *d*-excess is partly due to the rapid evolution of the δ^{18}O and δD profiles, and it is partly due to the dephasing between the δ^{18}O and δD profiles caused by different response times.

First we investigate the impact of the new correction scheme introduced here. This correction, abbreviated as *iso-hum-corr*, modifies the uncorrected data set in the region above 2000 m a.s.l. by about −0.4 ‰ and −13.3 ‰ for δ^{18}O and δD, respectively, resulting in a change of about −10.4 ‰ for *d*-excess (Fig. 4; red circles vs. black dots). The impact of applying the new correction scheme to the aircraft measurements can be understood by examining where the data sets align in the correction surface function (Fig. 3; red crosses). For both δ^{18}O and δD, the aircraft data set is characterised by a low mixing ratio and depleted isotope compositions, and it is clustered in the bottom-left corner of the surface function. This is the most sensitive area of the correction, thus causing the largest deviations in the surface function.

To assess the benefit of the new isotope composition–mixing ratio dependency correction, we take this new correction scheme as the reference scheme and compare its impact to three other correction schemes. The first scheme only corrects for the mixing ratio dependency based on standard DI (*hum-corr-DI*, Fig. 4; orange crosses). The second correction follows the same procedure but is based on standard GSM1 (*hum-corr-GSM1*, Fig. 4; blue squares), and the third correction follows an approach proposed by Bonne et al. (2014) for in situ vapour measurements in southern Greenland. Instead of correcting the mixing ratio dependency for the vapour measurements, the Bonne et al. (2014) approach corrects the mixing ratio dependency for the calibration standards. Thus, by assuming that the mixing ratio dependencies of the two employed standards remain stable during the measurement period, the measured isotope compositions of these two standards are corrected by using the mixing ratio dependency function to the ambient air mixing ratio of each single vapour measurement. Then, the linear regression computed from these two corrected standard measurements against their certified values is applied to calibrate the vapour measurement to the VSMOW2–SLAP2 scale. This scheme is hereafter referred to as *2-std-hum-corr* (Fig. 4; green triangles).

The different correction schemes modify the uncorrected data set differently. The δ^{18}O profile is only marginally affected by the correction below 1400 m a.s.l. (Fig. 4a). For the measurements above 1400 m a.s.l., differences become more pronounced but are masked by the large uncertainty as the aircraft was descending through a strong mixing-ratio gradient. All corrections show clear deviations at elevations above 2000 m a.s.l., and we focus our comparison on this region.

The *hum-corr-DI* stands out, with a positive correction of about 0.8 ‰, while the other three schemes induce a negative correction of between −0.3 ‰ and −0.7 ‰. The δD profile exhibits a similar pattern but with more apparent differences between the correction schemes (Fig. 4b). This results in an even more pronounced correction in the *d*-excess profile (Fig. 4c).

The impact of applying the correction scheme using single standard water (thus accounting for only mixing ratio dependency) relies on the choice of the used standard water. Using the *hum-corr-DI* correction introduces the largest deviation (1.1 ‰, 18.3 ‰, and 9.5 ‰ for δ^{18}O, δD, and *d*-excess respectively), while using the *hum-corr-GSM1* correction produces results much closer to that of the reference scheme (with an offset of 0.1 ‰ and 4.2 ‰ for δ^{18}O and δD, respectively, and 3.4 ‰ for *d*-excess). For this specific aircraft measurement (where the surface condition is already quite dry during the cold air outbreak event) the isotope composition of standard GSM1 happens to closely resemble the average isotope composition of the measurement. However, in the case of a previously unknown range of isotope compositions or strongly varying conditions, a comprehensive characterisation of mixing ratio dependency with multiple standard waters can provide advantages and should be preferred. Unknown ranges are particularly likely for atmospheric measurements of vertical profiles in humid regions (e.g. the tropics and subtropics) or over a wide area from moving platforms.

Finally, applying the alternative calibration approach (*2-std-hum-corr*) used in Bonne et al. (2014) results in only slightly more depleted isotope values than the reference, with an offset of about −0.3 ‰ and −0.5 ‰ for δ^{18}O and δD, respectively, resulting in a change of 1.7 ‰ for *d*-excess. The small discrepancy between the *2-std-hum-corr* and *iso-hum-corr* is mainly due to three factors. First, depending on the number of the used standard waters, the interpolation scheme for the isotopic deviations in between those of the used standard waters can be different. The *2-std-hum-corr* makes use of the mixing ratio dependency functions of only two standard waters. In this way, the deviations can only be linearly interpolated between the two standard waters. In contrast, the reference scheme is able to account for non-linearities during interpolation by measuring five standard waters. Second, *2-std-hum-corr* corrects the two standard waters to the mixing ratio of the measurement while the reference scheme corrects the measurement to the mixing ratio of the two standard waters (i.e. the reference mixing ratio). Based on the mixing ratio dependency feature of the two standard waters, the choice of correcting the two standard waters will result in a higher slope for the VSMOW2–SLAP2 calibration line. Consequently, the measurements after calibration are stretched to two ends, i.e. the measurements with the isotope composition close to that of standard DI become more enriched and those close to that of standard GSM1 become more depleted. Finally, the mixing ratio dependency functions for GSM1 and DI in *2-std-hum-corr* (using the individual fit for GSM1 or DI respectively) are not exactly identical to those used in the reference scheme (from the surface function determined by the measurements of five standard waters). Despite the small discrepancy, the consistent results of *2-std-hum-corr* with that of the reference scheme indicate that a correction scheme using the mixing ratio dependency functions of only two standard waters covering the measured isotope composition range can work sufficiently well in certain situations.

6.2 Impact on the ship-based measurements

Applying the four different correction schemes to the ship-based measurement data has a much weaker impact on the corrected series of vapour measurements (not shown). After applying our isotope composition–mixing ratio dependency correction scheme, the uncorrected data set changes to the order of 0.06 ‰ and 0.15 ‰ for δ^{18}O and δD, respectively, leading to a change to the order of −0.5 ‰ for *d*-excess. This is mainly because these ship measurements were carried out at the ocean surface, with relatively high mixing ratios (from 2500 to 8000 ppmv) and less-depleted isotope compositions (−23 ‰ to −12 ‰ for δ^{18}O and −160 ‰ to −100 ‰ for δD) compared to the aircraft measurements. As shown in Fig. 3, the ship data (blue dots) are coincidentally located in an area with low sensitivity at the correction surface. A linear interpolation between two standards may not capture such a saddle point correctly. This indicates that measurements are not sensitive to the correction of the isotope composition–mixing ratio dependency under all conditions. Ultimately, however, the certainty about a reliable correction will only be achieved with a complete characterisation of the isotope composition and mixing ratios covered by the measurements.

7 Discussion

Our careful characterisation experiments show that the isotope composition–mixing ratio dependency affects measurements at low mixing ratios for all three investigated stable water isotope CRDS analysers. Here we discuss possible causes of the isotope composition–mixing ratio dependency. In particular, we explore to what extent this dependency is an artefact from mixing with water remaining within the analyser or whether it is an instrument behaviour resulting from spectroscopic effects.

7.1 Artefact from mixing

If we assume the dependency is as a result of mixing with remnant water, then there would mainly be two candidates for the background moisture source: (1) the remaining water vapour in the dry gas supply and (2) the remaining water vapour from previous measurements in the analyser. By changing the dry gas supply from the ambient air dried through Drierite to synthetic air or N_2 from cylinder, which typically provides a dry gas with a mixing ratio below 10 ppmv, we can exclude the possible influence of the background moisture in the dry gas supply. In order to quantify the amount and the isotope compositions of the remaining water vapour from previous measurements, we have applied several successive, so-called *empty injections* via the autosampler. Thus, no liquid is injected and only dry gas is flushed into the vaporiser. Results from these empty injections show that the remaining water vapour in the system typically has a mixing ratio of about 60–80 ppmv, with its isotope composition closely following those of the previous injections. If the mixing ratio dependency was a result of the mixing between the injected water and the remaining water vapour from previous measurement, then we would expect a mixing of two water vapour masses of the same isotope compositions at different mixing ratios when injecting the same standard water during a characterisation run. As a consequence, we would expect the mixed vapour to have the same isotope composition, which is not the case. Finally, the shape of the isotope composition–mixing ratio dependency with a maximum between 2000 and 6000 ppmv (Fig. 1a) is not consistent with the expectation of a memory effect that would monotonously increase with the decreasing mixing ratio. The slight hysteresis observed during the upward/downward calibration runs indicates that there may be contributions from remnant water on walls or filter surfaces in the analyser, for example, that only exchange once a sufficiently humid air mass is introduced into the analyser. Such contributions do, however, appear to be of second order when compared to the substantial changes of the mixing ratio dependency with the isotope composition.

7.2 Spectroscopic effect

Now we explore the second hypothesis, namely that the isotope composition–mixing ratio dependency is an instrument behaviour resulting from spectroscopic effects. The manufacturer recommends a procedure for water vapour dependency calibration using their SDM, or similar, device (Picarro Inc., 2017), which is similar to what we have employed. While the first-order effect can be removed from a linear fit, there are second-order, non-linear components that become more apparent the more the water concentration changes from the recommended range of operation (5000–25 000 ppmv). In the following paragraphs, we discuss the potential reasons for the origin of the water vapour and isotope dependency from a spectroscopic standpoint that is based on the published literature (Steig et al., 2014; Rella et al., 2015; Johnson and Rella, 2017).

The two modules of the CRDS analyser used in our experiments (i.e. Picarro L2140-i and L2140-i) target three absorption lines of water vapour in the region 7199–7200 cm^{-1}, namely near 7199.960, 7200.135, and 7200.305 cm^{-1} for $H_2^{18}O$, $H_2^{16}O$, and $HD^{16}O$ respectively (Fig. 5). These absorption lines broaden or narrow, depending on the partial pressure of the gas mixture in the cavity, and can be affected by changes in their baseline due to other strong absorption lines nearby. A fitting algorithm then fits the measured absorption spectrum to an expected model spectrum and adjusts the model parameters in order to minimise the residual error. Broadening/narrowing of lines due to changing gas mixture and baseline shifts are particular challenges to the fitting algorithm (Johnson and Rella, 2017) because this causes residuals that induce instrument error during the fitting procedure.

The L2130-i and earlier spectrometers use the absorption peak as a free parameter in the fitting algorithm. The peak shape and, thus, the peak amplitude can suffer from the above-mentioned broadening/narrowing effect, which introduces potential error under conditions of varying concentration or matrix gases. The fitting algorithms of the L2140-i spectrometers, in contrast, have a higher number of ring downs due to a different strategy for obtaining laser resonance and use a different laser stabilisation scheme. This allows us to fit the integrated absorption, rather than the peak amplitude, of each absorption line. Since the integrated absorption is a constant independent of pressure, the fitting is expected to be more accurate, with a low sensitivity to broadening/narrowing effects arising from changes of water concentrations and background gas compositions (Steig et al., 2014). One part of the retrieval algorithm is the removal of the baseline from the $H_2^{16}O$ spectrum. To this end, changes in the baseline from nearby strong absorption lines as a result of concentration changes or cross-interference from other gas species is a possible source of error for either fitting algorithm. Other possible sources of error can be absorption loss non-linearities due to small imperfections in the instrument, such as the non-zero shut-off time of the laser and the response time of the ring-down detector (Rella et al., 2015). Unless fitting algorithms take the actual line shapes into consideration directly, some residual effects are likely to persist.

The retrieval of H_2O concentration and the stable isotope compositions of $\delta H_2^{18}O$ and $\delta HD^{16}O$ (identical to $\delta^{18}O$ and δD) are implemented in a manner that is similar to the procedure described for CH_4 and $\delta^{13}CH_4$ (Rella et al., 2015). Considering a linear dependency of absorption to concentration (which is not always true), where the mole fraction of $H_2^{18}O$ (c_{18}) is related to the absorption peak height α_{18} with a proportionality constant k_{18} and an error offset ϵ_{18}, we have the following equation:

$$c_{18} = k_{18}\alpha_{18} + \epsilon_{18}. \tag{8}$$

Note that the expressions above should apply to both the L2130-i and L2140-i spectrometers, with the only difference being that the absorption peak height is replaced by the integrated absorption (Steig et al., 2014).

Based on the molecular definition of a δ value with respect to the VSMOW2, an isotope ratio of the sample $^{18}R = \frac{[H_2^{18}O]}{[H_2^{16}O]}$, and of VSMOW2 $^{18}R_{\mathrm{VSMOW2}} = (2005.20 \pm 0.45) \times$

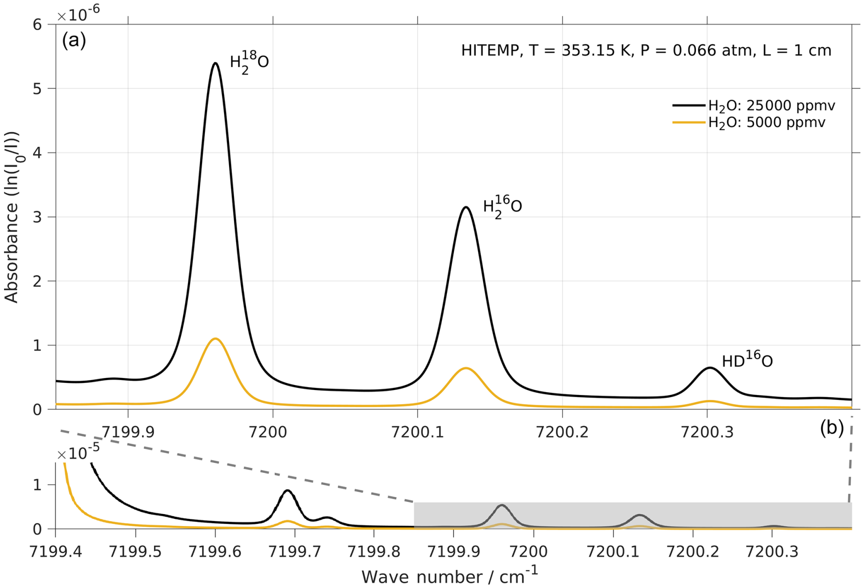

Figure 5. Absorption spectrum of $H_2^{18}O$, $H_2^{16}O$, and $HD^{16}O$ in the frequency range targeted by the laser of Picarro models L2130-i and L2140-i. Simulations with two water concentrations, i.e. 25 000 (black line) and 5000 ppmv (orange line), were performed by using http://spectraplot.com (last access: 19 February 2020) with the HITRAN–HITEMP database (Goldenstein et al., 2017). Simulation parameters are set according to the cavity conditions of the Picarro analyser as follows: $T = 80\,°C$, $P = 50\,$Torr, and $L = 1\,$cm. Panel **(a)** is an enlarged version of the shaded area in panel **(b)**.

10^{-6} (Baertschi, 1976), we have the following equation:

$$\delta H_2^{18}O \text{ [in ‰]} = 1000\left(\frac{{}^{18}R_{\text{sample}}}{{}^{18}R_{\text{VSMOW2}}} - 1\right). \tag{9}$$

The retrieval can then be formulated as follows:

$$\delta H_2^{18}O = 1000\left(\frac{k_{18}\alpha_{18} + \epsilon_{18}}{(k_{16}\alpha_{16} + \epsilon_{16})R_{\text{VSMOW2}}} - 1\right). \tag{10}$$

For an ideal spectrometer, the calibration coefficients are constants (i.e. $k_{18} = \kappa_{18}$ and $k_{16} = \kappa_{16}$), and the calibration offsets are 0 (i.e. $\epsilon_{18} = \epsilon_{16} = 0$). These assumptions lead to the expected retrieval for a spectrometer as follows:

$$\delta H_2^{18}O = \frac{1000}{R_{\text{VSMOW2}}}\frac{\kappa_{18}\alpha_{18}}{\kappa_{16}\alpha_{16}} - 1000. \tag{11}$$

The actual spectrometer is not ideal, but in most situations it has a highly linear and stable performance (Rella et al., 2015). Nevertheless, it can be calibrated based on the linear dependency of $\delta H_2^{18}O$ to $\frac{\alpha_{18}}{\alpha_{16}}$ by using a linear expression with the following form:

$$\delta H_2^{18}O = A\frac{\alpha_{18}}{\alpha_{16}} + B, \tag{12}$$

where the calibration constants A and B can be determined based on the measurable quantities $\delta H_2^{18}O$ and the $\frac{\alpha_{18}}{\alpha_{16}}$ from a reference instrument in the factory. These determined calibration constants deviate slightly from the expected values in Eq. (11). They are then transferred from the reference instrument to each new instrument of the same type (Rella et al., 2015).

If Eq. (12) is used for calibration of the water analysers (not reported in the published literature), then there are two potential sources of error. First, the dependencies on the isotope ratio may not be entirely linear (even when assuming a linear relationship the coefficient is not necessarily a constant and the offset is not necessarily 0) and remain as residuals. Second, the change of this relationship with the differing mixing ratio may remain unexplored. Furthermore, manufacturing tolerances will induce deviations from the reference instrument on which such an initial calibration has been carried out, and instruments therefore have to be calibrated individually to obtain suitable post-processing methods. The initial instrument calibration procedure may therefore be one potential origin for the isotope composition–mixing ratio dependency identified here.

Deviations from an ideal spectrometer stem from the potential spectrometer errors due to small imperfections of the instrument. One possible error is the absorption-loss offset that could occur when the baseline loss is not reproduced well by the fitting algorithm. This absorption offset then leads to a mole-fraction offset, namely ϵ_{18} in Eq. (8). The measured $\delta \mathrm{H}_2^{18}\mathrm{O}$, including the effect of absorption offset, can be formulated explicitly by following Rella et al. (2015) – and their Appendix S1.1 – as follows:

$$\delta \mathrm{H}_2^{18}\mathrm{O} = \frac{1000}{R_{\mathrm{VSMOW2}}}\left(\frac{k_{18}\alpha_{18}}{k_{16}\alpha_{16}} + \frac{\alpha_0}{\alpha_{16}}\right) - 1000, \tag{13}$$

where α_0 is the net absorption loss parameter that should, to the first order, be independent of water concentration and isotope ratio. Comparing this to Eq. (11) for an ideal spectrometer, the additional term of $\frac{\alpha_0}{\alpha_{16}}$ in Eq. (13) creates an inverse relationship with the water concentration and should be responsible for deviations from the ideal spectrometer that are mostly evident at low mixing ratios.

Another possible spectrometer error is the so-called absorption loss non-linearity, which describes effects due to a shorter or longer ring-down time than expected in the optimal range of operations. These effects can be included as additional terms, again by following Rella et al. (2015) – and their Appendix S1.2 – with a non-linear dependency of α_{18} on α_{16} (i.e. $\alpha_{18} \Rightarrow \alpha_{18} + \beta\alpha_{16} + \gamma\alpha_{16}^2$) as follows:

$$\begin{aligned}\delta \mathrm{H}_2^{18}\mathrm{O} = {} & \frac{1000}{R_{\mathrm{VSMOW2}}}\left(\frac{k_{18}\alpha_{18}}{k_{16}\alpha_{16}} + \gamma\frac{k_{18}\alpha_{16}}{k_{16}} + \frac{\alpha_0}{\alpha_{16}}\right) \\ & + \left(\frac{1000}{R_{\mathrm{VSMOW2}}}\frac{k_{18}}{k_{16}}\beta - 1000\right).\end{aligned} \tag{14}$$

The calibration coefficients are thus assumed constant. The non-linearities from spectral crosstalk between $\mathrm{H}_2^{16}\mathrm{O}$ and $\mathrm{H}_2^{18}\mathrm{O}$ or imperfections in the baseline removal of the $\mathrm{H}_2^{16}\mathrm{O}$ absorption spectrum are present in several terms; such effects require the calibration of each individual instrument to be accounted for. When written in this explicit form, it appears consistent with expectations that a systematic isotope composition–mixing ratio dependency may be detected from careful analyser characterisation. The equation can be further simplified as follows:

$$\delta \mathrm{H}_2^{18}\mathrm{O} = A\frac{\alpha_{18}}{\alpha_{16}} + \Gamma c_{16} + \frac{c_0}{c_{16}} + B'. \tag{15}$$

The difference between Eq. (15) and Eq. (12) represents the deviation from an ideal spectrometer due to non-linearities from imperfections in the baseline removal and spectral crosstalk between $\mathrm{H}_2^{18}\mathrm{O}$ and $\mathrm{H}_2^{16}\mathrm{O}$ and can be denoted as follows:

$$\Delta\delta \mathrm{H}_2^{18}\mathrm{O} = \Gamma c_{16} + \frac{c_0}{c_{16}} + \mathrm{Const.} \tag{16}$$

The dependency on water concentration (c_{16}) in Eq. (16) appears consistent with the mixing ratio dependency function (Eq. 7) identified in our systematic investigation of three analysers, supporting the hypothesis of a spectrometric origin for the isotope composition–mixing ratio dependency.

A similar form of mixing ratio correction is applied to the ^{17}O measurements using the L2140-i analyser in the study of Steig et al. (2014), and their Eq. 22, in which the integrated absorption area, instead of the peak amplitude, is used to calculate the absorption loss, and the crosstalk between $\mathrm{H}_2^{18}\mathrm{O}$ and $\mathrm{H}_2^{16}\mathrm{O}$ is modelled with a bilinear relationship. Steig et al. (2014) note that the introduction of an integrated absorption detection leads to a substantially improved behaviour for the mixing ratio dependency over the peak amplitude detection for δ^{18}O but not for δD, with the reason remaining unclear. It is also worth noting that their instrument has not been evaluated for the low mixing ratio range, which is the focus of this paper. It may be possible that part of the identified isotope composition dependency of the mixing ratio dependency stems from the, thus far, lacking systematic analysis of the low mixing ratio range of the analyser for this effect.

One aspect that is not addressed here, but may be valuable for further consideration in the future, is the availability of analysers with higher flow rates of above 300 sccm, for example, for use in research aircraft (Sodemann et al., 2017). Given recent indications that the flow rate affects the isotope composition–mixing ratio dependency (Thurnherr et al., 2020), forthcoming studies should explore the flow rate as an additional parameter. This requires the availability of suitable methods to generate standard vapour at these higher flow rates.

8 Final remarks and recommendations

We have systematically investigated the mixing ratio dependency of water vapour isotope measurements for three commercially available, infrared cavity ring-down spectrometers. We found that the mixing ratio dependency varies with the isotope composition of the measured vapour. We define this behaviour as the isotope composition–mixing ratio dependency. The dependency is robustly identified across three similar analysers, regarding several first-order parameters, and is found to be stable over time. Using the characterisation results of five standard waters from a Picarro L2130-i analyser as an example, we propose a correction scheme for this isotope composition–mixing ratio dependency. Using such a correction scheme, we can correct the isotopic measurements for any measured mixing ratio and isotope composition within the range investigated here.

To demonstrate the impact of the mixing ratio dependency correction, we have compared the proposed correction scheme with other published correction schemes, using in situ measurements from dry environments. The impact on the measurements is found to be most substantial at the low mixing ratios. Applying a correction scheme only accounting for the mixing ratio dependency relies on the choice of the standard water used. For an aircraft data set, using the mixing ratio dependency function based on the standard DI produces a large deviation from our proposed scheme; using the mixing ratio dependency based on standard GSM1 produces results similar to our proposed scheme, since it is closer to the average isotope composition of the aircraft data set. Finally, we have investigated the impact of applying a correction scheme used by Bonne et al. (2014). This approach produces results in good agreement with that of our approach. The small discrepancy is due to the interpolation scheme (linear or nonlinear) of the isotopic deviation, the choice of correcting mixing ratio dependency of the standards or that of the vapour measurement, and the small discrepancy in the mixing ratio dependency functions of the two standards. The consistent results indicate that a correction scheme using the mixing ratio dependency functions of only two standards covering the isotope composition could be sufficient if the correction surface can be sufficiently approximated by linear interpolation. Using ship measurements made at higher mixing ratio conditions, we find a weaker impact from the different correction schemes.

Given the non-monotonous characteristics of the isotope composition–mixing ratio dependency, we consider memory effects (i.e. mixing with water vapour from previous injections in the analyser) unlikely to be the dominating factor. This renders a spectroscopic origin as the most likely cause, possibly resulting from the imperfections of the fitting algorithm at low water concentrations or non-linearities in the fitting procedures (Rella et al., 2015).

The correction for the isotope composition–mixing ratio dependency is most relevant for in situ vapour isotope measurements where the ambient mixing ratio is low (below 4000 ppmv) and the isotope composition of the measured vapour spans a large range. At higher mixing ratios, the investigated CRDS analysers show a negligible dependency on either the mixing ratio or the isotope composition. If the isotope composition of ambient vapour varies in a small range during the sampling period, a simpler correction scheme could be employed by using the mixing ratio dependency of two, or even one, suitable standard water with a similar isotope composition to that of ambient vapour.

Based on our previous conclusions, we recommend identifying the isotope composition–mixing ratio dependency for all Picarro CRDS analysers used for in situ water vapour isotope measurements, particularly when low mixing ratio conditions are encountered.

If the measurements of multiple standard waters are not available, the approach used in Bonne et al. (2014) could be applied as an alternative correction approach. Their approach can produce similar results to that of the approach proposed here but requires the characterisation of the mixing ratio dependency of two carefully selected calibration standards in a linear range of the correction surface. If the isotope composition of the ambient vapour only varies within a small range during the sampling period, such as during measurements close to the ocean surface, it may be sufficient to correct for the mixing ratio dependency by using one standard water that has a similar isotope composition to that of the ambient vapour.

Our study is presently limited by the range of the standard waters used here (about $-33\,‰$-$5\,‰$ and $-263\,‰$-$5\,‰$ for δ^{18}O and δD respectively). Depending on the measurement environment, more depleted or enriched standards would be needed to derive a correction function over the entire measurement range of samples potentially encountered during atmospheric measurements. With all standards being close to the global meteoric water line (GMWL), one aspect that will likely be missed here is the potential cross-interference between δ^{18}O and δD (Chris Rella, personal communication, 2020). Identifying such cross-interference can be relevant for applications where vapour samples deviate substantially from the GMWL, such as from geothermal vapour sources. One potential approach for identifying such cross-interferences could be to repeat the present analysis with spiked water standards that deviate substantially from the GMWL.

Another limitation of the characterisations performed here is the substantial time demand. The characterisation method with liquid injections provides relatively high-precision performance but requires an autosampler and takes about 1–2 weeks for four standard waters. The characterisation method with the SDM can be automated more easily but requires manual intervention to apply more than two standards. A device that could provide any desired isotope composition and a given mixing ratio would be needed to fully automate the isotope composition–mixing ratio dependency of the instruments tested here.

A reproducible and accepted characterisation method is of utmost importance for comparing measurements across disparate locations and in bottom-up networks, particularly in the polar regions, and appears as a prerequisite for detecting representative signals in the stable isotope record on a regional scale. In particular, studies employing the d-excess as an indicator of moisture origin or other tracer applications are therefore likely to profit from a detailed characterisation of their analysers according to our characterisation procedure either before, during, or after field deployments.

Appendix A: Robustness and temporal stability

Here we detail the experiments conducted to assess the robustness of the isotope composition–mixing ratio dependency with regards to the vapour-generation method, the dry gas supply, the measurement sequence, the individual analyser and analyser type, and the temporal stability.

A1 Vapour-generation method

To investigate whether the isotope composition–mixing ratio dependency is influenced by the choice of vapour-generation method, we compare the characterisation result from discrete liquid injections and the SDM for instrument HIDS2254 (experiments 2 and 6; Fig. A1a–c). The same standard waters (GSM1 and DI) and dry gas supply (synthetic air) are used in the two experiments. The measurement, using the SDM, usually has a higher uncertainty since the continuous vapour streaming does not provide entirely constant mixing conditions, and the vapour stream can become unstable due to clogging and bubbles in the capillary. Overall, the results from the two vapour-generation methods exhibit consistent dependency behaviours. However, the discrepancy exists. For $\Delta\delta^{18}$O, there is an offset of 0.2 ‰-0.5 ‰ for DI between 1000 and 6000 ppmv. Inconsistency appears in GSM1 measurements below 2000 ppmv (Fig. A1a). For $\Delta\delta$D, the mixing ratio dependencies determined by the SDM method exhibit a slightly weaker dependency for both standard waters (Fig. A1b).

It is interesting to note that the result of the discrete liquid injections in February 2017 (experiment 1; Fig. 1) depicts a better agreement with that of the SDM in experiment 6 (comparison figure not shown). This indicates that the discrepancy in the results of the two vapour-generation methods could be due to the small instrument drift and the high measurement uncertainty at lower mixing ratios.

The experiments using N_2 as dry gas supply (experiments 3 and 8) also give a similar isotope composition–mixing ratio dependency between the two vapour-generation methods (not shown), confirming that the isotope composition–mixing ratio dependency does not depend substantially on either of the two tested methods.

A2 Influence of dry gas supply

Next, we investigate whether the type of dry gas supply has an influence on the characterisation results. To this end, we test the characterisation method via the SDM on instrument HIDS2254 with a supply of synthetic air, a supply of N_2, and a supply of dried ambient air through Drierite (experiments 6–8). The synthetic air and N_2 are tested with two standard waters (GSM1 and DI), and the Drierite is tested with one standard water (GSM1).

For the mixing ratio dependency on δ^{18}O, the measurement with Drierite disagrees strongly with those of synthetic air and N_2 (Fig. A1e). As the mixing ratio decreases below about 7000 ppmv, the measured GSM1 with Drierite exhibits a fast-increasing positive deviation while that of synthetic air or N_2 exhibits a rather flat dependency. The measurements with synthetic air and N_2 largely show a similar shape. A small discrepancy exists below 15 000 ppmv, where the two standard waters measured with N_2 exhibit a small negative offset (~ 0.5 ‰). The mixing ratio dependencies on δD from all three types of the dry gas supply are in good agreement, despite a small (< 1.5 ‰) offset between the measurement with synthetic air and that of N_2 (Fig. A1e). The calculated *d*-excess follows the shape of δ^{18}O, with different behaviours between the measurements with Drierite and those with synthetic air and N_2 below about 7000 ppmv (Fig. A1f). The *d*-excess of the experiment with N_2 exhibits a small positive offset (~ 0.5 ‰) compared to the measurement with synthetic air. Overall, characterisation results with synthetic air and N_2 exhibit a mixing ratio dependency in good agreement with the two investigated standard waters (GSM1 and DI). However, the characterisation result (for GSM1) with the Drierite differs significantly in δ^{18}O and, thus, *d*-excess.

The characterisation method of liquid injections via an autosampler is also tested with synthetic air and N_2. Again, the results exhibit a similar isotope composition–mixing ratio dependency from the two types of dry gas supply despite a small discrepancy for δ^{18}O of GSM1 below 2000 ppmv and a relatively larger offset (0.5 ‰–1.3 ‰) for δ^{18}O of DI below 10 000 ppmv (not shown). A test of synthetic air from a gas cylinder and dried ambient air from Drierite in the study of Aemisegger et al. (2012) also shows that the mixing ratio dependency is different for δ^{18}O while being more similar for δD. The observed discrepancy in the δ^{18}O deviation is possibly due to changes in the baseline of the spectrum around the ${}^1H_2^{18}O$ and ${}^1H_2^{16}O$ absorption peak, which is caused by slight differences in trace gas composition (Aemisegger et al., 2012; Rella et al., 2015).

A3 Influence from the measuring sequence

Finally, we investigate whether a measuring sequence with ascending or descending mixing ratio sequences influence the mixing ratio dependency characterisation. The mixing ratio dependencies of GSM1, MIX, and DI tap water that are characterised by ascending and descending mixing ratio sequences are shown in Fig. A1g–i. For both $\Delta\delta^{18}$O and $\Delta\delta$D (Fig. A1g and h), the results from the two measuring sequences are in good agreement for all three waters, indicating that the influence of the measuring sequence is minor. However, there is a slightly detectable weaker mixing ratio dependency for the descending mixing ratio sequence (e.g. $\Delta\delta$D for GSM1 and DI). One possible explanation for the slightly weaker dependency in the descending sequence is the memory effect from previous injections, e.g. some remaining water molecules would stick to the inner wall of the system (even after flushing the system with 12 injections at

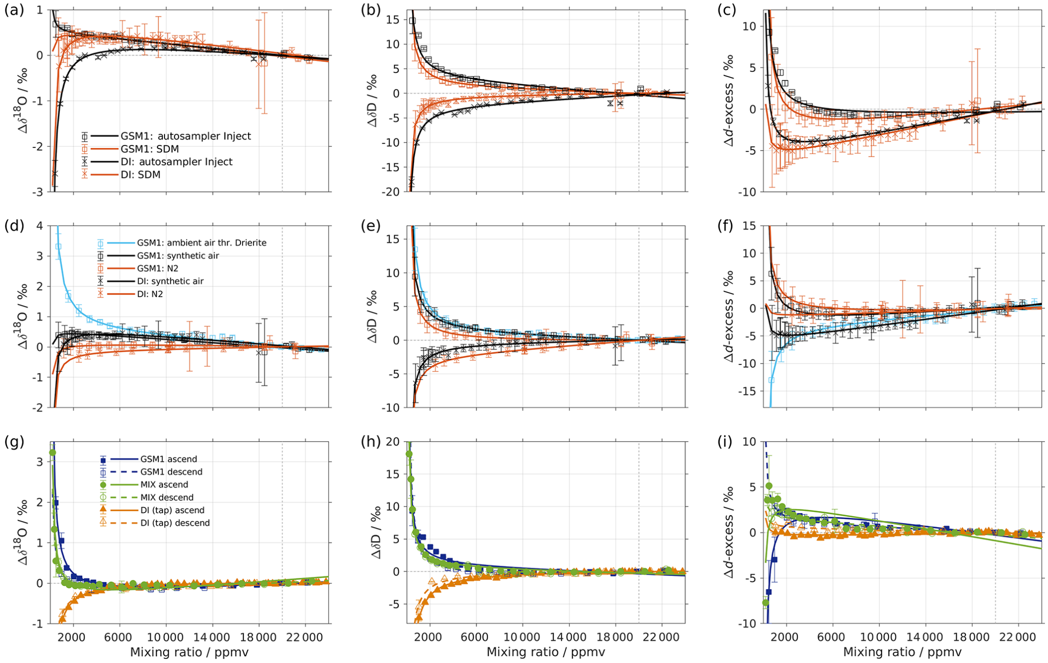

Figure A1. **(a–c)** Comparison of the isotope composition–mixing ratio dependency of uncalibrated measurements with two different characterisation methods for **(a)** $\delta^{18}O$, **(b)** δD, and **(c)** *d*-excess. The measurements are carried out on instrument HIDS2254 (Picarro L2130-i), either with discrete injections using an autosampler (black symbols; experiment 2) or with continuous vapour streaming by using the SDM (red symbols; experiment 6) and using synthetic air as the carrier gas for both. The symbol and error bar represents the mean and standard deviation of the mean for the last three of a total of four injections for the measurement via the autosampler, and the mean and standard deviation of the last 2–5 min of a 20–30 min long sequence for the measurement via SDM. The solid line represents the fit using the same function as in Fig. 1. Panels **(d–f)** are the same as **(a–c)** but compare different carrier gases. The measurements are carried out on instrument HIDS2254 (Picarro L2130-i), with continuous vapour streaming via SDM (experiments 6–8). Two standard waters (GSM1 and DI) are tested with synthetic air (black symbol) and N_2 (orange symbol). The standard water GSM1 is also tested with ambient air that is dried through Drierite (blue symbol). Panels **(g–i)** display the mixing ratio dependency of GSM1 (dark blue symbol), MIX (green symbol), and TAP water (orange symbol) with ascending (closed symbol) and descending (open symbol) mixing ratio sequences. Solid curves represent the fits for ascending mixing ratio sequences, and dashed curves represent the fits for descending mixing ratio sequences. All the measurements are uncalibrated and carried out with discrete injections using an autosampler with N_2 as the carrier gas. The measurements for TAP and MIX are carried out on instrument HKDS2038 (Picarro L2140-i; experiments 9 and 11). The measurements for GSM1 are carried out on instrument HKDS2039 (Picarro L2140-i), and one outlier at around 500 ppmv has been excluded (experiment 15).

20 000 ppmv) and still play a role during the characterisation measurements. If this is the case, the measurements from the descending mixing ratio sequence (starting with injections of higher mixing ratios at the beginning) would help to replace the remaining molecules through a molecular exchange and are therefore more likely to represent the true dependency behaviour. Nonetheless, the good agreement between the two measuring sequences indicates that the potential hysteresis effects, if any, are not substantial. The resulting mixing ratio dependencies for Δd-excess (Fig. A1i) exhibit an increasing positive deviation towards the low mixing ratios overall, except for one mixing ratio step of MIX and two mixing ratio steps of GSM1. This underlines the high sensitivity of *d*-excess measurements due to the increasing uncertainty of $\delta^{18}O$ and δD values at very low mixing ratios.

It is worth noting that we have repeated three experiments for MIX (only results from one of the experiments are shown here). For one of the three experiments (not shown), the measurements for MIX below 2000 ppmv exhibit an interesting contrast in $\Delta\delta^{18}O$. The measurement at the lowest mixing ratio (around 500 ppmv) has constrained the mixing ratio dependency into slightly opposite directions. The contrast is not well understood. It is possible that this contrast stems from the fitting uncertainties due to the constraining points lacking

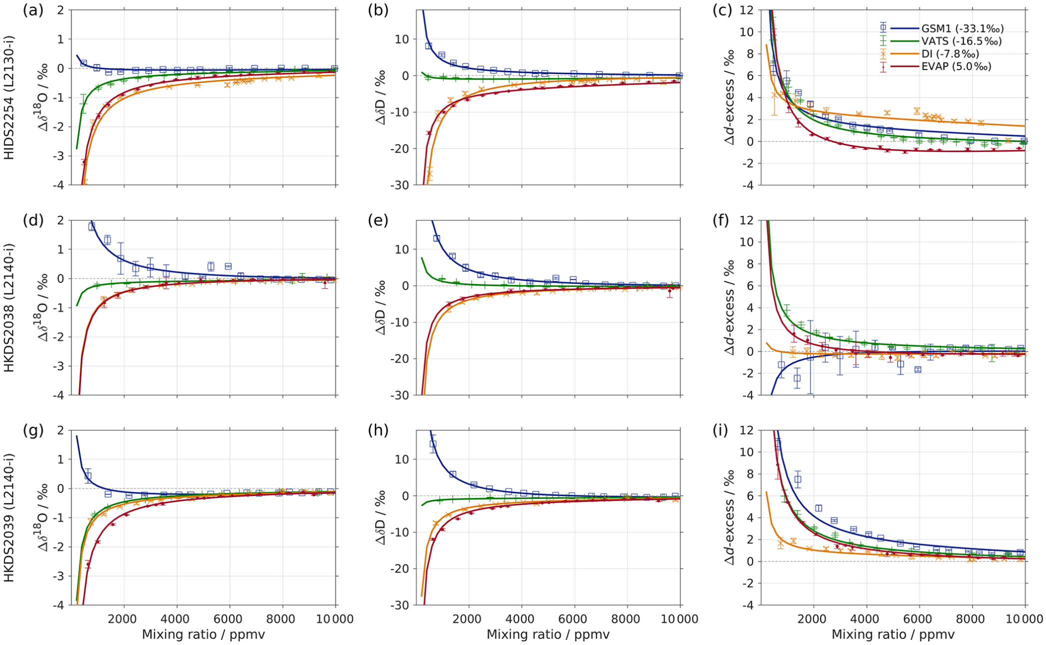

Figure A2. Mixing ratio dependency of uncalibrated measurements for instruments **(a–c)** HIDS2254, **(d–f)** HKDS2038, and **(g–i)** HKDS2039. The measurements are carried out with discrete injections by using an autosampler with N_2 as the carrier gas (experiments 3, 9, and 14). Only the data below 10 000 ppmv are shown. Symbols and solid lines indicate measurements and fits, respectively, as in Fig. 1.

at the low end of mixing ratios. The contrast is not observed for the repeated experiment with added mixing ratio steps (Fig. A1g; green). It is also possible that, for a standard in which the isotopic composition is close to a turning point in the correction surface (Sect. 5), hysteresis effects with opposing signs may become visible within the range of uncertainty. This can be also found, for example, in the small shift of the dependency shape in δD for VATS among the three analysers (Fig. A2b, e, and h; green curve). Further tests with more in-between standards, or a vapour-generation approach that does not suffer from memory, are needed to address this uncertainty in the dependency shape.

A4 Variations among CRDS analysers

To investigate the variations of the mixing ratio dependency between the individual instruments, we have repeated the same characterisation on three analysers (experiments 3, 9, and 14). The characterisation is carried out with four standard waters (GSM1, VATS, DI, and EVAP) by using liquid injections via an autosampler with N_2 as the mixing dry gas.

The characterisation results for the three analysers are shown in Fig. A2. For $\Delta\delta^{18}O$, the positive deviation for GSM1 below 4000 ppmv on instrument HKDS2038 is about 0.2 ‰–1.8 ‰ stronger than that of the other two analysers (Fig. A2a, d, and g; blue). The mixing ratio dependency of VATS below 4000 ppmv is nearly flat on instrument HKDS2038 while exhibiting a substantial negative deviation for the other two analysers. The mixing ratio dependencies for the other two standard waters (DI and EVAP) are in good agreement among the three analysers. For $\Delta\delta D$, the mixing ratio dependency of VATS below 2000 ppmv is slightly positive on instrument HKDS2038 while being nearly flat on the other two analysers (Fig. A2b, e, and h; green). The mixing ratio dependency for the other three standard waters (GSM1, DI, and EVAP) agree well among the three analysers. The calculated *d*-excess (Fig. A2c, f, and i) shows an increasing positive deviation towards the low end of the mixing ratio for almost all the standard waters measured on the three analysers except for DI and GSM1, which were measured on instrument HKDS2038 as their mixing ratio dependencies appear to be rather flat or even slightly negative.

Despite the minor difference in the magnitude of the deviations, it is clear that the isotope composition–mixing ratio dependency exists in all three analysers investigated here. The behaviour of the dependency is, to the first order, in good agreement across the analysers. For the standard waters with relatively depleted isotope compositions, the measurements of all three analysers exhibit a mixing ratio depen-

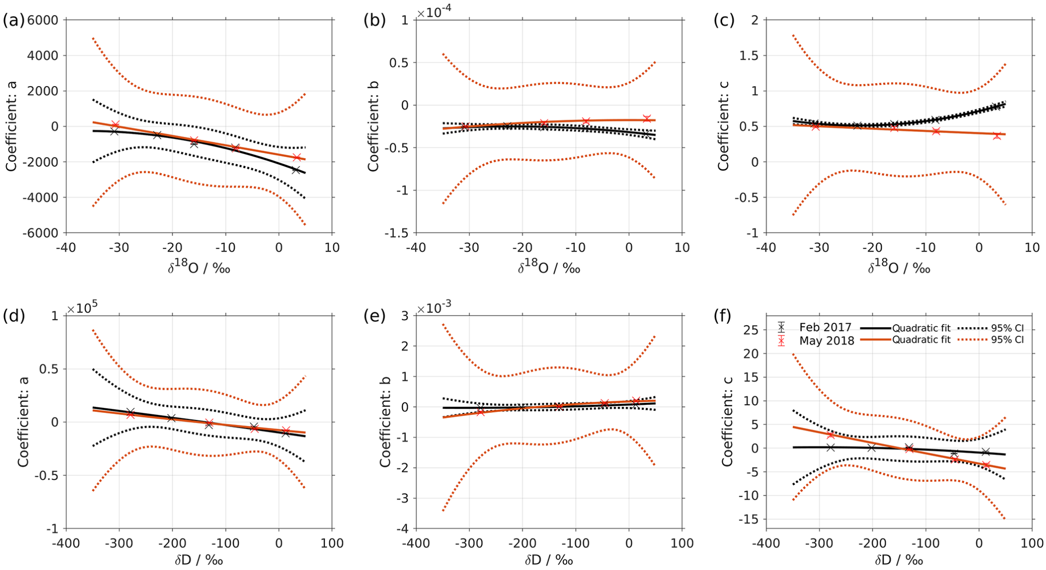

Figure A3. Same as Fig. 2 but a comparison between results in February 2017 (black symbols; experiment 1) and May 2018 (red symbols; experiment 2). A larger, 95 % confidence interval for the fit of May 2018 (red dotted line) is due to the fewer data points available (only four standards measured).

dency, where the isotopic value increases as the mixing ratio decreases. For the standard waters with relatively enriched isotope compositions, the measurements exhibit a reversed mixing ratio dependency.

A5 Long-term stability

To quantify the long-term stability of the isotope composition–mixing ratio dependency, we examine the temporal change of the fitting coefficients (a_δ, b_δ, and c_δ) in Eq. (4). Figure A3 shows the fitting coefficients for the mixing ratio dependency characterised by liquid injections on instrument HIDS2254 in February 2017 (experiment 1; black line) and in May 2018 (experiment 2; red line). For the characterisation in May 2018, only four standard waters are measured; this results in a fit with a relatively large, 95 % confidence interval. In this context the change over time is considered insignificant if the coefficients (and their fitted curve) from the characterisation in May 2018 are within the 95 % confidence bounds for the fitted curve from the characterisation in February 2017.

For the mixing ratio dependency on δ^{18}O, the change of coefficient a is insignificant. However, it is worth noting that the fitting coefficient a, with respect to standard GSM1 (Fig. A3a; the first data point), changes slightly from negative to positive. This small change results in an opposite mixing ratio dependency shape at a low mixing ratio. The change of the mixing ratio dependency for GSM1 partly reflects on the sensitivity of the instrument to a certain range of isotope compositions and partly on the uncertainty arising from both low instrument precision and a lack of measurements at low mixing ratios. The changes of coefficients b and c are substantial for the standard waters of relatively high δ^{18}O (Fig. A3b, c). A less negative b and a less positive c reflects a weaker mixing ratio dependency in May 2018. For the mixing ratio dependency on δD, a reasonable agreement is exhibited for all three fitting coefficients (Fig. A3d, e, and f); this points to the same basic shape of the mixing ratio dependency on δD after a 15-month period.

A repeated characterisation determined via the SDM with standard water DI in July 2016, February 2018, and June 2018 (experiments 4, 5, and 6) indicates that the mixing ratio dependency for standard water DI is still consistent after nearly 2 years (not shown). The mixing ratio dependencies of the three standard waters (GSM1, VATS, and DI) determined by liquid injections via an autosampler (experiments 9 and 10) and the other three standard waters (NEEM, GV, and BERM) via manual injections in instrument HKDS2038 (experiments 12 and 13) indicate a consistent isotope composition–mixing ratio dependency after a running of 1 year and 1 month respectively (not shown). Overall, the stability tests indicate that the isotope composition–mixing ratio dependency of each analyser is, to the first order, stable on a long-term basis (1–2 years).

Appendix B: Fitting uncertainty estimated using a bootstrapping approach

Since we only have 5 available data points to fit in Eq. (5), the resultant 95 % confidence interval of the fit is relatively broad (black dotted line; Fig. 2). This broad confidence interval results in a relatively large standard deviation for the isotopic deviation ($\Delta\delta$). For example, the resultant standard deviation for $\Delta\delta$ at 2000 ppmv is about 0.20 ‰, 2.69 ‰, and 3.13 ‰ for δ^{18}O, δD, and *d*-excess respectively. To reduce this large standard deviation for $\Delta\delta$, we use a bootstrapping approach (Efron, 1979) to estimate the fitting uncertainty in Eq. (5).

The bootstrapping approach can be explained by considering, for example, the coefficient a. For each individual observation of a, we generate 1000 random values under a normal distribution, with the mean and standard deviation being those of each available observation. We now obtain five sets of 1000 random values since we have 5 a from five standard waters. Then, we sample 1 value from each set of the 1000 random values and fit those 5 sampled values using Eq. (5). Finally, we repeat this process 1000 times, thus obtaining 1000 fits. The standard deviation of the 1000 fits is the standard deviation that is adopted here (blue dotted line; Fig. 2).

In this way, the standard deviations estimated for the coefficients a, b, and c are lowered to about 15, 0.4×10^{-6}, and 8×10^{-3} for δ^{18}O and 100, 3×10^{-6}, and 0.1 for δD respectively. This, in turn, substantially reduces the resultant standard deviation for $\Delta\delta$. For example, the standard deviation for $\Delta\delta$ at 2000 ppmv is reduced by a factor of 20, which is about 0.01 ‰, 0.11 ‰, and 0.14 ‰ for δ^{18}O, δD, and *d*-excess respectively.

Appendix C: Analytical solution for δ_{cor}

In the following, we derive the analytical solution for δ_{cor} in Eq. (7) at the reference mixing ratio (i.e. 20 000 ppmv). The derivation applies to both δ^{18}O and δD.

The coefficients $a(\delta_{\text{cor}})$, $b(\delta_{\text{cor}})$, and $c(\delta_{\text{cor}})$ are given according to Eq. (5) as follows:

$$\begin{cases} a(\delta_{\text{cor}}) = m_a(\delta_{\text{cor}} - n_a)^2 + k_a, \\ b(\delta_{\text{cor}}) = m_b(\delta_{\text{cor}} - n_b)^2 + k_b, \\ c(\delta_{\text{cor}}) = m_c(\delta_{\text{cor}} - n_c)^2 + k_c. \end{cases} \tag{C1}$$

By substituting Eq. (C1) into Eq. (7) and rearranging the terms, we calculate the following:

$$A\delta_{\text{cor}}^2 + B\delta_{\text{cor}} + C = 0,$$
$$\text{where} \begin{cases} A &= \frac{m_a}{h} + m_b h + m_c, \\ B &= 1 - \frac{2m_a n_a}{h} - 2m_b n_b h - 2m_c n_c, \\ C &= \frac{m_a n_a^2}{h} + m_b n_b^2 h + m_c n_c^2 + \frac{k_a}{h} \\ & \quad + k_b h + k_c - \delta_{\text{meas}}. \end{cases} \tag{C2}$$

Equation (C2) is a quadratic equation with its only physical solution being the following:

$$\delta_{\text{cor}} = \frac{-B + \sqrt{B^2 - 4AC}}{2A}. \tag{C3}$$

The coefficients m, n, and k are already obtained from the fits in Eq. (5). When given a measured mixing ratio, h, and the corresponding isotope composition, δ_{meas}, we can obtain the isotope composition at 20 000 ppmv, which is δ_{cor} according to the solution Eq. (C3).

Data availability. Data used in the generation of the figures are attached as a Supplement to this article.

Supplement. The supplement related to this article is available online at: https://doi.org/10.5194/amt-13-3167-2020-supplement.

Author contributions. YW and HS designed the study jointly. Experiments and data analysis was led by YW with contributions from AT. All authors contributed to the writing of the paper.

Competing interests. The authors declare that they have no conflict of interest.

Acknowledgements. The authors wish to thank Iris Thurnherr, Franziska Aemisegger, and Pascal Graf from the Institute for Atmospheric and Climate Sciences, ETH Zurich; Hans Christian Steen-Larsen and Sonja Wahl from the Geophysical Institute, University of Bergen; and Jean-Lionel Lacour and Tomas Foldes for the valuable discussions. We are grateful to Arny Erla Sveinbjornsdottir from the isotope laboratory of the University of Iceland for providing the UI standard waters. Jarle Berntsen from the Department of Mathematics at the University of Bergen is acknowledged for helping to identify a suitable fitting function. We are grateful to the scientists and other personnel who made the measurements during the Iceland–Greenland Seas Project campaign of 2018 possible. We thank Chris Rella for providing valuable comments on our paper. We would also like to express our gratitude to the editor and the three anonymous reviewers whose valuable comments have significantly helped to improve the clarity of this paper.

Financial support. This research has been supported by the Research Council of Norway (SNOWPACE (grant no. 262710) and FARLAB (grant no. 245907)).

Review statement. This paper was edited by Christof Janssen and reviewed by three anonymous referees.

References

Aemisegger, F., Sturm, P., Graf, P., Sodemann, H., Pfahl, S., Knohl, A., and Wernli, H.: Measuring variations of δ^{18}O and δ^{2}H in atmospheric water vapour using two commercial laser-based spectrometers: an instrument characterisation study, Atmos. Meas. Tech., 5, 1491–1511, https://doi.org/10.5194/amt-5-1491-2012, 2012.

Baertschi, P.: Absolute ^{18}O content of standard mean ocean water, Earth Planet. Sc. Lett., 31, 341–344, 1976.

Bailey, A., Noone, D., Berkelhammer, M., Steen-Larsen, H. C., and Sato, P.: The stability and calibration of water vapor isotope ratio measurements during long-term deployments, Atmos. Meas. Tech., 8, 4521–4538, https://doi.org/10.5194/amt-8-4521-2015, 2015.

Bastrikov, V., Steen-Larsen, H. C., Masson-Delmotte, V., Gribanov, K., Cattani, O., Jouzel, J., and Zakharov, V.: Continuous measurements of atmospheric water vapour isotopes in western Siberia (Kourovka), Atmos. Meas. Tech., 7, 1763–1776, https://doi.org/10.5194/amt-7-1763-2014, 2014.

Bonne, J.-L., Masson-Delmotte, V., Cattani, O., Delmotte, M., Risi, C., Sodemann, H., and Steen-Larsen, H. C.: The isotopic composition of water vapour and precipitation in Ivittuut, southern Greenland, Atmos. Chem. Phys., 14, 4419–4439, https://doi.org/10.5194/acp-14-4419-2014, 2014.

Bonne, J.-L., Behrens, M., Meyer, H., Kipfstuhl, S., Rabe, B., Schönicke, L., Steen-Larsen, H. C., and Werner, M.: Resolving the controls of water vapour isotopes in the Atlantic sector, Nat. Commun., 10, 1–10, 2019.

Crosson, E. R.: A cavity ring-down analyzer for measuring atmospheric levels of methane, carbon dioxide, and water vapor, Appl. Phys. B, 92, 403–408, 2008.

Dansgaard, W.: The abundance of O18 in atmospheric water and water vapour, Tellus, 5, 461–469, 1953.

Dansgaard, W.: The O18-abundance in fresh water, Geochim. Cosmochim. Ac., 6, 241–260, 1954.

Dansgaard, W.: Stable isotopes in precipitation, Tellus, 16, 436–468, 1964.

Efron, B.: Bootstrap Methods: Another Look at the Jackknife, Annals of Statistics, 7, 1–26, 1979.

Gat, J. R.: Oxygen and hydrogen isotopes in the hydrologic cycle, Annu. Rev. Earth Planet. Sci., 24, 225–262, 1996.

Goldenstein, C. S., Miller, V. A., Spearrin, R. M., and Strand, C. L.: SpectraPlot.com: Integrated spectroscopic modeling of atomic and molecular gases, J. Quant. Spectrosc. Ra., 200, 249–257, https://doi.org/10.1016/j.jqsrt.2017.06.007, 2017.

Gupta, P., Noone, D., Galewsky, J., Sweeney, C., and Vaughn, B. H.: Demonstration of high-precision continuous measurements of water vapor isotopologues in laboratory and remote field deployments using wavelength-scanned cavity ring-down spectroscopy (WS-CRDS) technology, Rapid Comm. Mass Spectr., 23, 2534–2542, 2009.

Hagemann, R., Nief, G., and Roth, E.: Absolute isotopic scale for deuterium analysis of natural waters. Absolute D/H ratio for SMOW 1, Tellus, 22, 712–715, 1970.

International Atomic Energy Agency: Reference Sheet for VSMOW2 and SLAP2 International Measurement Standards, IAEA, Vienna, 8 pp. (Rev 1 dated 11 July 2017), 2009.

Johnson, J. E. and Rella, C. W.: Effects of variation in background mixing ratios of N_2, O_2, and Ar on the measurement of δ^{18}O–H_2O and δ^{2}H–H_2O values by cavity ring-down spectroscopy, Atmos. Meas. Tech., 10, 3073–3091, https://doi.org/10.5194/amt-10-3073-2017, 2017.

Kerstel, E.: Isotope ratio infrared spectrometry, in: Handbook of stable isotope analytical techniques, chapter 34, edited by: de Groot, P. A., pp. 759–787, ISBN 978-0-444-51114-0, Elsevier, Amsterdam, 2004.

Kerstel, E. and Gianfrani, L.: Advances in laser-based isotope ratio measurements: selected applications, Appl. Phys. B, 92, 439–449, 2008.

Kurita, N., Newman, B. D., Araguas-Araguas, L. J., and Aggarwal, P.: Evaluation of continuous water vapor δD and δ^{18}O measurements by off-axis integrated cavity output spectroscopy, Atmos. Meas. Tech., 5, 2069–2080, https://doi.org/10.5194/amt-5-2069-2012, 2012.

Lis, G., Wassenaar, L., and Hendry, M.: High-precision laser spectroscopy D/H and $^{18}O/^{16}O$ measurements of microliter natural water samples, Anal. Chem., 80, 287–293, 2008.

Mook, W. G. and De Vries, J. J.: Environmental isotopes in the hydrological cycle: principles and applications, in: Environmental Isotopes in the Hydrological Cycle – Principles and Applications, International Hydrological Programme (IHP-V), Technical Documents in Hydrology, IAEA/UNESCO, 1, 30–31, 2001.

O'Keefe, A. and Deacon, D. A.: Cavity ring-down optical spectrometer for absorption measurements using pulsed laser sources, Rev. Sci. Instr., 59, 2544–2551, 1988.

Picarro Inc.: Calibration guide for Picarro analyzers, Rev 1., 18 pp., 2017.

Rella, C. W., Hoffnagle, J., He, Y., and Tajima, S.: Local- and regional-scale measurements of CH_4, $\delta^{13}CH_4$, and C_2H_6 in the Uintah Basin using a mobile stable isotope analyzer, Atmos. Meas. Tech., 8, 4539–4559, https://doi.org/10.5194/amt-8-4539-2015, 2015.

Renfrew, I. A., Pickart, R. S., Våge, K., Moore, G. W. K., Bracegirdle, T. J., Elvidge, A. D., Jeansson, E., Lachlan-Cope, T., McRaven, L. T., Papritz, L., Reuder, J., Sodemann, H., Terpstra, A., Waterman, S., Valdimarsson, H., Weiss, A., Almansi, M., Bahr, F., Brakstad, A., Barrell, C., Brooke, J. K., Brooks, B. J., Brooks, I. M., Brooks, M. E., Bruvik, E. M., Duscha, C., Fer, I., Golid, H. M., Hallerstig, M., Hessevik, I., Huang, J., Houghton, L., Jónsson, S., Jonassen, M., Jackson, K., Kvalsund, K., Kolstad, E. W., Konstali, K., Kristiansen, J., Ladkin, R., Lin, P., Macrander, A., Mitchell, A., Olafsson, H., Pacini, A., Payne, C., Palmason, B., Pérez-Hernández, M. D., Peterson, A. K., Petersen, G. N., Pisareva, M. N., Pope, J. O., Seidl, A., Semper, S., Sergeev, D., Skjelsvik, S., Søiland, H., Smith, D., Spall, M. A., Spengler, T., Touzeau, A., Tupper, G., Weng, Y., Williams, K. D., Yang, X., and Zhou, S.: The Iceland Greenland Seas Project, B. Am. Meteorol. Soc., 100, 1795–1817, https://doi.org/10.1175/BAMS-D-18-0217.1, 2019.

Schmidt, M., Maseyk, K., Lett, C., Biron, P., Richard, P., Bariac, T., and Seibt, U.: Concentration effects on laser-based $\delta^{18}O$ and δ^2H measurements and implications for the calibration of vapour measurements with liquid standards, Rapid Commun. Mass Spectr., 24, 3553–3561, 2010.

Sodemann, H., Aemisegger, F., Pfahl, S., Bitter, M., Corsmeier, U., Feuerle, T., Graf, P., Hankers, R., Hsiao, G., Schulz, H., Wieser, A., and Wernli, H.: The stable isotopic composition of water vapour above Corsica during the HyMeX SOP1 campaign: insight into vertical mixing processes from lower-tropospheric survey flights, Atmos. Chem. Phys., 17, 6125–6151, https://doi.org/10.5194/acp-17-6125-2017, 2017.

Steen-Larsen, H. C., Johnsen, S. J., Masson-Delmotte, V., Stenni, B., Risi, C., Sodemann, H., Balslev-Clausen, D., Blunier, T., Dahl-Jensen, D., Ellehøj, M. D., Falourd, S., Grindsted, A., Gkinis, V., Jouzel, J., Popp, T., Sheldon, S., Simonsen, S. B., Sjolte, J., Steffensen, J. P., Sperlich, P., Sveinbjörnsdóttir, A. E., Vinther, B. M., and White, J. W. C.: Continuous monitoring of summer surface water vapor isotopic composition above the Greenland Ice Sheet, Atmos. Chem. Phys., 13, 4815–4828, https://doi.org/10.5194/acp-13-4815-2013, 2013.

Steen-Larsen, H. C., Sveinbjörnsdottir, A. E., Peters, A. J., Masson-Delmotte, V., Guishard, M. P., Hsiao, G., Jouzel, J., Noone, D., Warren, J. K., and White, J. W. C.: Climatic controls on water vapor deuterium excess in the marine boundary layer of the North Atlantic based on 500 days of in situ, continuous measurements, Atmos. Chem. Phys., 14, 7741–7756, https://doi.org/10.5194/acp-14-7741-2014, 2014.

Steig, E. J., Gkinis, V., Schauer, A. J., Schoenemann, S. W., Samek, K., Hoffnagle, J., Dennis, K. J., and Tan, S. M.: Calibrated high-precision ^{17}O-excess measurements using cavity ring-down spectroscopy with laser-current-tuned cavity resonance, Atmos. Meas. Tech., 7, 2421–2435, https://doi.org/10.5194/amt-7-2421-2014, 2014.

Sturm, P. and Knohl, A.: Water vapor δ^2H and $\delta^{18}O$ measurements using off-axis integrated cavity output spectroscopy, Atmos. Meas. Tech., 3, 67–77, https://doi.org/10.5194/amt-3-67-2010, 2010.

Thurnherr, I., Kozachek, A., Graf, P., Weng, Y., Bolshiyanov, D., Landwehr, S., Pfahl, S., Schmale, J., Sodemann, H., Steen-Larsen, H. C., Toffoli, A., Wernli, H., and Aemisegger, F.: Meridional and vertical variations of the water vapour isotopic composition in the marine boundary layer over the Atlantic and Southern Ocean, Atmos. Chem. Phys., 20, 5811–5835, https://doi.org/10.5194/acp-20-5811-2020, 2020.

Wen, X. F., Lee, X., Sun, X. M., Wang, J. L., Tang, Y. K., Li, S. G., and Yu, G. R.: Intercomparison of four commercial analyzers for water vapor isotope measurement, J. Atmos. Ocean. Technol., 29, 235–247, https://doi.org/10.1175/JTECH-D-10-05037.1, 2012.

Paper II

High-resolution stable isotope signature of a land-falling atmospheric river in southern Norway

Yongbiao Weng, Harald Sodemann, and Aina Johannessen
Weather and Climate Dynamics (in open discussion)

https://doi.org/10.5194/wcd-2020-58
Preprint. Discussion started: 9 December 2020

Weather and Climate Dynamics Discussions
Open Access

High-resolution stable isotope signature of a land-falling Atmospheric River in southern Norway

Yongbiao Weng, Harald Sodemann, and Aina Johannessen
Geophysical Institute, University of Bergen, and Bjerknes Centre for Climate Research, Bergen, Norway
Correspondence: Yongbiao Weng (yongbiao.weng@uib.no) and Harald Sodemann (harald.sodemann@uib.no)

Abstract. Heavy precipitation at the west coast of Norway is often connected to elongated meridional structures of high integrated water vapour transport known as Atmospheric Rivers (AR). Here we present high-resolution measurements of stable isotopes in near-surface water vapour and precipitation during a land-falling AR event in southwestern Norway on 07 December 2016. In our analysis, we aim to identify the influences of moisture source conditions, weather system characteristics, and post-condensation processes on the isotopic signal in near-surface water vapour and precipitation.

A total of 71 precipitation samples were collected during the 24-h sampling period, mostly taken at sampling intervals of 10–20 min. The isotope composition of near-surface vapour was continuously monitored in-situ with a cavity ring-down spectrometer. Local meteorological conditions were in addition observed from a vertical pointing rain radar, a laser disdrometer, and automatic weather stations.

We observe a stretched, "W"-shaped evolution of isotope composition during the event. Combining isotopic and meteorological observations, we define four different stages of the event. The two most depletion periods in the isotope δ values are associated with frontal transitions, namely a combination of two warm fronts that follow each other within a few hours, and an upper-level cold front. The *d*-excess shows a single maximum, and a step-wise decline in precipitation and a gradual decrease in near-surface vapour. Thereby, isotopic evolution of the near-surface vapour closely follows the precipitation with a time delay of about 30 min, except for the first stage of the event. Analysis using an isotopic below-cloud exchange framework shows that the initial period of low and even negative *d*-excess in precipitation was caused by evaporation below cloud base. At the ground, a near-constant signal representative of the airmass above is only reached after transition periods of several hours. Moisture source diagnostics for the event show that the moisture source conditions for these steady periods are partly reflected in the surface precipitation at these times.

Based on our observations, we revisit the interpretation of precipitation isotope measurements during AR events in previous studies. Given that the isotopic signal in surface precipitation reflects a combination of atmospheric dynamics through moisture sources and atmospheric distillation, as well as cloud microphysics and below-cloud processes, we recommend caution regarding how Rayleigh distillation models are used during data interpretation. While the isotope compositions during convective precipitation events may be more adequately represented by idealized Rayleigh models, additional factors should be taken into account when interpreting a surface precipitation isotope signal from stratiform clouds.

1 Introduction

Precipitation can be considered as the end product of the atmospheric hydrological cycle. Weather systems lead to sequences of ocean evaporation, horizontal and vertical transport and mixing of atmospheric water vapour, microphysical processes within clouds on characteristic time scales (Läderach and Sodemann, 2016). The stable isotope composition of precipitation is, therefore, an integrated result of the isotopic fractionation, that occurs during phase changes in the atmosphere (Gat, 1996). In addition, post-condensation processes can influence the isotope composition below cloud base (Graf et al., 2019). Therefore, observations of stable water isotopes in precipitation hold the promise of allowing to extract information about moisture transport and moisture sources for individual weather events. Besides, detailed measurements of water isotopes provide the potential to constrain parameterisations in atmospheric models and thereby to improve weather prediction and climate models (Bony et al., 2008; Pfahl et al., 2012; Yoshimura et al., 2014).

Being located at the end of the North Atlantic storm track, precipitation on the west coast of Scandinavia is commonly related to the landfall of frontal weather systems. Extreme precipitation has been connected to so-called Atmospheric Rivers (ARs, Zhu and Newell, 1998; Ralph et al., 2004), that transport warm and moist air from more southerly latitudes poleward within their frontal structures. As such airmasses encounter the steep orographic rise along the Norwegian coast, they can yield abundant precipitation (Stohl et al., 2008; Azad and Sorteberg, 2017). Past studies have emphasized the long-range transport characteristics, and their connection to the large-scale atmospheric flow configuration during such AR events. From a model study using artificial water tracers, Sodemann and Stohl (2013) estimated that 30-50 % of the precipitation from AR events could be from latitudes S of 40 °N. However, an observational confirmation of such model-derived estimates currently remains elusive.

The use of precipitation isotopes to gain information at the time scale of weather-systems dates back to the pioneering study of Dansgaard (1953), which suggested that the ^{18}O-abundance in warm-frontal precipitation could be explained by a distinct fractionation process and below cloud evaporation. Since then, numerous studies have investigated the variation in precipitation isotopes between weather events and at different locations. Studies reveal that the isotope composition can vary substantially over short time scales. For example, analyses of single rainfall events have revealed variations in δD of between 7 ‰ for the case of southeast Australia (Barras and Simmonds, 2009) and 58 ‰ in California at sub-hourly time resolution (Coplen et al., 2008). A higher-resolution study in Cairns, Australia measured variations of up to 95 ‰ within a single 4-h period (Munksgaard et al., 2012). Several typical intra-event trends, such as "L", "V", and "W" shapes, have been identified by Muller et al. (2015). Despite numerous observations of the evolution of the isotope composition in rainfall over time and corresponding interpretation, it remains unclear how to separate the highly convoluted signal into the contribution from weather system characteristics, moisture sources, and below-cloud effects.

The complexity of the isotopic information contained in rainfall at the event time scale has lead to a scientific controversy regarding the interpretation of the isotope signal during AR events. Coplen et al. (2008) (henceforth C08) sampled the precipitation during a land-falling AR at the coast of southern California at a time resolution of 30 min. C08 interpreted the isotope variation in rainfall during the event in relation to cloud height, using a Rayleigh distillation model. Coplen et al.

(2015) expanded the dataset and interpretation to numerous additional events. Investigating the same event as C08 with an isotope-enabled weather prediction model, Yoshimura et al. (2010) (henceforth Y10) instead emphasized the roles of horizontal advection and post-condensational processes for the temporal evolution of the precipitation isotope signal. Using the simultaneous water vapour and precipitation isotope measurements in this study, we attempt to shed new light on this so-far unresolved controversy.

Here we present the analysis of highly resolved measurements of the stable isotope composition in precipitation and water vapour collected during a land-falling AR event in southwestern Norway during winter 2016. Thereby, we utilize a combination of observational and numerical methods, aiming to separate the moisture source information from effects related to moisture transport and precipitation processes.

In order to disentangle different factors that contribute to the isotope signal in precipitation, we adopt here a perspective where three sets of factors pertaining to the atmospheric water cycle can potentially have an influence. We hereby use the common δ notation as $\delta = \frac{R_{\text{sample}} - R_{\text{VSMOW}}}{R_{\text{VSMOW}}} \cdot 1000\ ‰$, where R (e.g. $^{2}R = \frac{[\text{HD}^{16}\text{O}]}{[\text{H}_2^{16}\text{O}]}$) is the isotope ratio, to quantify enrichment or depletion with respect to the Vienna Standard Mean Ocean Water standard (VSMOW) (Mook and De Vries, 2001; IAEA, 2009).

(1) Depletion of heavy isotopes due to an atmospheric distillation or rain out process. The rainout history during the transport is essentially depending on the temperature difference between the moisture source and the condensation height above the precipitation site. This has been historically known as the rainout effect and can be described with a Rayleigh distillation model (Dansgaard, 1964). A larger temperature difference leads to a greater rain out process and thus a more depleted isotope profile in the condensate, that ultimately translates to the precipitation. For example, Dansgaard (1953) explained the gradual enrichment of ^{18}O-abundance in the precipitation from a warm front with decreasing of the condensation temperature as the front passes the observation site.

(2) Ocean-atmosphere conditions at the moisture source affect the isotope composition of generated water vapour (Gat, 1996). The deviation from equilibrium fractionation during evaporation at the source can be quantified by the d-excess parameter, calculated as $d\text{-excess} = \delta\text{D} - 8 \cdot \delta^{18}\text{O}$ (Dansgaard, 1964). Specifically, theoretical studies and observations have shown that d-excess in the generated vapour over ocean surface is dependent on relative humidity (RH) with respect to sea surface temperature (SST), and to second-order to the SST itself in the source area (Merlivat and Jouzel, 1979; Uemura et al., 2008; Pfahl and Sodemann, 2014). As an example, high d-excess anomalies are usually observed in water vapour formed during so-called marine cold air outbreaks (Aemisegger and Sjolte, 2018; Aemisegger, 2018), where cold dry air moves over relative warm ocean waters and triggers strong evaporation (Papritz and Spengler, 2017; Papritz and Sodemann, 2018). In contrast, land regions and more calm ocean evaporation are associated with lower d-excess (Aemisegger et al., 2014; Thurnherr et al., 2020). The d-excess is often assumed to be conserved during transport. However, microphysical processes within and below clouds can influence the d-excess in local precipitation, and thus obscure information on the evaporation conditions in the source area (Jouzel and Merlivat, 1984; Graf et al., 2019).

(3) Microphysical processes within clouds and post-condensational exchange processes of falling precipitation can alter the isotope composition. While isotopic equilibrium can be assumed for rain formation in warm clouds, kinetic effect exists

https://doi.org/10.5194/wcd-2020-58
Preprint. Discussion started: 9 December 2020

at snow formation. Vapour deposition in a supersaturated environment with respect to ice, therefore, increases *d*-excess in precipitation (Jouzel and Merlivat, 1984). Liotta et al. (2006) proposed that higher *d*-excess also exists in orographic clouds since kinetic effects should be expected in the first step of droplet formation, while in-cloud droplets are short-lived, and thus can not reach equilibrium with the surrounding vapour. For deep convective systems, factors such as condensate lifting, convective detrainment and evaporation in unsaturated downdrafts can play a critical role in the control of the isotope of precipitation (Bony et al., 2008). Below cloud processes have been noted in many precipitation events from previous studies (Dansgaard, 1953; Ehhalt et al., 1963; Miyake et al., 1968; Barras and Simmonds, 2009; Guan et al., 2013; Wang et al., 2016). Below-cloud evaporation usually dominates at the beginning of a precipitation event, when the atmosphere below cloud base is still unsaturated. As the atmosphere gradually gets saturated, the isotopic exchange between raindrops and surrounding vapour intensifies (Graf et al., 2019). Depending on the intensity of below-cloud exchange processes, isotopes in precipitation can deviate more or less strongly from Rayleigh model expectations.

In the following, we present the unique dataset acquired during a land-falling frontal system, associated with an atmospheric river, at the end of the North Atlantic storm track. Using a combination of remote-sensing and in situ instrumentation (Section 2), we provide a detailed observation of meteorological parameters (Section 3) and the isotope composition in near-surface water vapour and precipitation (Section 4) during a substantial precipitation event on 07 Dec 2016 at Bergen, southwestern Norway. We first quantify below-cloud exchange processes by means of the interpretative $\Delta\delta\Delta$D framework proposed recently by Graf et al. (2019) (Section 5.1). Then, we relate the observed evolution of the isotope signal to weather system characteristics (Section 5.2). We hypothesise that the remaining signal then reveals the source conditions in the d-excess parameter. We therefore compare our observational results with moisture source conditions and d-excess predictions obtained from a Lagrangian moisture source diagnostic (Sodemann et al., 2008) and interpret the results in terms of assumptions and model deficiencies (Section 5.3). In a brief discussion, we attempt to contribute constructively to the dispute of C08 and Y10 (Section 6). Finally, conclusions are drawn in Section 7.

2 Data and methods

This section describes the measurement site, the installation and procedures used for acquisition of meteorological and isotopic information, weather prediction model data, and of the method for diagnosing moisture sources.

2.1 Measurement site

Bergen is located at the coast of southwestern Norway (60.3837 °N, 5.3320 °E), with an annual mean temperature of 7.6 °C during 1961-1990 (*sharki.oslo.dnmi.no*). Being located at the end of the climatological North Atlantic storm track (Wernli and Schwierz, 2006; Aemisegger and Papritz, 2018), extratropical cyclones frequently bring moist airmasses to the Norwegian coast. At the steep orographic rise from sea level to above 600 m in a distance of 2 km, the airmasses frequently produce intense precipitation. The average annual precipitation during 1961–1990 was 2250 mm, with the highest monthly average being 283 mm in September and lowest being 106 mm in May (Meteorologisk Institutt, *sharki.oslo.dnmi.no*).

Meteorological observations are performed operationally at the WMO station Bergen-Florida (ID 50540) at 12 m a.s.l. Additional measurements were acquired on the rooftop observatory (45 m a.s.l) of the Geophysical Institute (GFI), University of Bergen, located at a distance of 70 m from the WMO station. This additional instrumentation consisted of a Micro Rain Radar (MRR2, METEK GmbH, Elmshorn, Germany), a Total Precipitation Sensor (TPS-3100, Yankee Environmental Systems, Inc., USA), a Parsivel^2 disdrometer (OTT Hydromet GmbH, Kempten, Germany) and an automatic weather station (AWS-2700, Aanderaa Data Instruments AS, Bergen, Norway). A subset of these parameters (air temperature, pressure, RH, wind speed) from the AWS-2700 were consistent with the TPS-3100 and the WMO station measurements.

Precipitation rate was measured by 3 instruments. The TPS-3100 Total Precipitation Sensor is an automatic precipitation gauge that provides real-time solid and liquid precipitation rate at a 60 s time interval (Yankee Environmental Systems, Inc., 2011). The laser-based optical distrometer Parsivel^2 provides the precipitation intensity at a 60 s time resolution, using measurements of particle size and particle fall speed (OTT Hydromet GmbH, 2015). Comparison of these high-resolution precipitation measurements located at the rooftop with the rain gauge measurement from the WMO station Bergen-Florida at ground level indicates that the TPS-3100 overestimates precipitation slightly (up to 10 %), while the Parsivel^2 clearly underestimates the precipitation intensity (up to 40 %; see Appendix A). Hereafter, we utilize the precipitation rates from the TPS-3100 for further analysis.

In addition to precipitation rate, the Parsivel^2 distrometer provides drop size and velocity spectra by separating the precipitation into 32 size classes from 0.2 to 5 mm and 32 velocity classes from 0.2 to 20 $\mathrm{m\,s^{-1}}$. The instrument has been configured to record raw spectra at a 60 s time interval. The raw number of particles are converted into a per-diameter-class volumetric drop concentration ($\mathrm{mm^{-1}\,m^{-3}}$), including corrections following Raupach and Berne (2015). The drop size distributions are then characterized by the mass-weighted mean diameter D_m (mm). The drop size distribution is an important precipitation characteristic, among others to evaluate the extent of below-cloud evaporation (Graf et al., 2019).

Continuous vertical profiling of the hydrometeors during the event was conducted using the vertical-pointing doppler radar MRR2. Previous studies have demonstrated the value of these observations for stable isotope analysis in precipitation (C08; Muller et al., 2015). Operating at 24 GHz, the radar measures the height-resolved fall velocity of the hydrometeors and other derived parameters, such as height-resolved size distribution and liquid water content (METEK Meteorologische Messtechnik GmbH, 2012). Here, the MRR2 was set up with a vertical resolution of 100 m for its 32 range gates, resulting in a measurement range from 100 m to 3200 m. The high resolution in time and height enables monitoring of the phase and evolution of hydrometeors, and thus the evolution of melting layers (Battan, 1973; White et al., 2002, 2003).

2.2 Water vapour isotope measurements

The stable isotope composition of ambient water vapour was continuously measured with a cavity ring-down spectrometer (L2130-i, Picarro Inc., USA) from an inlet installed on the GFI rooftop observatory. Ambient air was continuously drawn through the 4 m long 1/4 inch unheated PTFE tubing with a flow rate of about 35 sccm. The inlet was shielded from precipitation with a downward-facing plastic cup.

The analyser was calibrated every 12 hours using a Standard Delivery Module (A0101, Picarro Inc., USA; hereafter SDM) and a high-precision vaporizer (A0211, Picarro Inc., USA). During the calibration, two laboratory standards bracketing the isotope composition of typical ambient vapour (GSM1: δ^{18}O = -33.07 ± 0.02 ‰, δD = -262.95 ± 0.30 ‰; DI: δ^{18}O = -7.78 ± 0.02 ‰, δD = -50.38 ± 0.30 ‰) were blended respectively with dry air supplied from a molecular sieve (MT-400-4, Agilent Inc., Santa Clara, USA). The generated standard vapour was then measured for 20 min each at a humidity level of ~20 000 ppmv.

The vapour data are post-processed and calibrated according to the following steps. (1) The raw data are corrected for isotope ratio–mixing ratio dependency using the correction function in Weng et al. (2020), which was determined for the same analyser used here. (2) For each calendar month, SDM calibration periods are identified. Then, the median value of mixing ratio, δ^{18}O and δD are obtained for each calibration period. The values that deviate from the median value by more than 0.5 ‰ in δ^{18}O or 4.0 ‰ in δD are discarded to remove variations due to bursting bubbles and other instabilities. The remaining data for each period are then averaged and the standard deviation calculated. Calibrations were retained if at least 60 % of the calibration period were kept after quality control. (3) The vapour measurements were calibrated to SLAP2-VSMOW2 scale following IAEA recommendations (IAEA, 2009). To this end, the two nearest bounding calibrations of sufficient quality were identified for each calendar day and each standard. Finally, the calibrated vapour data are averaged at a 10-minute interval using centred averaging.

2.3 Precipitation isotope sampling and analysis

Liquid precipitation was sampled at the GFI rooftop observatory at high temporal resolution with a manual rainfall collector, similar to the setup used in Graf et al. (2019). The collector consists of a PE funnel of 10 cm diameter, which directs the collected water into a 20 mL open-top glass bottle. A total of 71 precipitation samples were collected during the 24-h sampling period between 00:00 UTC 07 December and 00:00 UTC 08 December 2016. The sampling interval was adjusted according to the precipitation intensity. Two samples were collected over a 105 min interval, 8 samples with 20–40 min intervals, and 61 samples with 10–20 min intervals (ref. supplementary material). The bottle and funnel were dried between each sample using a paper wipe. The sample was immediately transferred from the bottle to a 1.5 mL glass vial (part no. 548-0907, VWR, USA) and closed with an open-top screw cap with PTFE/rubber septum (part no. 548-0907, VWR, USA) to prevent evaporation until sample analysis.

The samples were stored at 4 °C before being analysed for their isotope composition at FARLAB, University of Bergen, Norway. During the analysis, an autosampler (A0325, Picarro Inc.) transferred ca. 2 µL per injection into a high-precision vaporizer (A0211, Picarro Inc., USA) heated to 110 °C. After blending with N_2 (Nitrogen 5.0, purity >99.999 %, Praxair Norge AS), the gas mixture was directed into the measurement cavity of a cavity ring-down spectrometer (L2140-i, Picarro Inc., USA) for about 7 min with a typical mixing ratio of 20 000 ppmv. To reduce memory effects between sample, two so-called wet flushes consisting of 5 min of vapour mixture at 50 000 ppmv were applied to the analyzer at the beginning of each new sample vial. Three standards (12 injections each, plus wet flush) were measured at the beginning and end of each batch, consisting typically of 20 samples (6 injections each, plus wet flush). The averages of the last 4 injections were used for

https://doi.org/10.5194/wcd-2020-58
Preprint. Discussion started: 9 December 2020

further processing. The measurement data were first corrected for isotope–humidity dependency using a linear correction for the analyzer obtained over a humidity range of 15 000–23 000 ppmv. Then, data were calibrated to the SLAP2-VSMOW2 scale following IAEA recommendations (IAEA, 2009) using two secondary laboratory standards (VATS: δ^{18}O = -16.47 ± 0.02 ‰, δD = -127.88 ± 0.30 ‰; DI: δ^{18}O = -7.78 ± 0.02 ‰, δD = -50.38 ± 0.30 ‰). The long term reproducibility of liquid sample analysis at FARLAB has been estimated to 0.15 ‰ for δ^{18}O and 0.66 ‰ for δD, resulting in a measurement uncertainty of 1.05 ‰ for *d*-excess.

2.4 The concept of equilibrium vapour

Due to equilibrium and kinetic isotopic fractionation during phase transitions, the isotope ratios in water vapour and precipitation can not be directly compared to one another. Instead, we use the concept of *equilibrium vapour* to compare the state of both phases (e.g. Aemisegger et al., 2015). The equilibrium vapour from precipitation is the isotope composition of vapour that is in equilibrium with precipitation at ambient air temperature T_a. We calculate the equilibrium vapour of precipitation as

$$\frac{\delta_{\mathrm{p,eq}}}{1000}+1=\alpha_{\mathrm{l}\rightarrow\mathrm{v}}(T_a)\frac{\delta_{\mathrm{p}}}{1000}+1, \tag{1}$$

where $\alpha_{\mathrm{l}\rightarrow\mathrm{v}}(T_a)$ is the temperature-dependent fractionation factor of the liquid to vapour phase transition following Majoube (1971). We quantify the difference between equilibrium vapour from precipitation samples and ambient vapour then as

$$\Delta\delta \;=\; \delta\mathrm{D}_{\mathrm{p,eq}}-\delta\mathrm{D}_{\mathrm{v}}, \tag{2}$$

$$\Delta d \;=\; d_{\mathrm{p,eq}}-d_{\mathrm{v}}. \tag{3}$$

While a similar notation can be defined for $\Delta\delta^{18}$O, we use the notation $\Delta\delta$ to refer to $\Delta\delta$D only. Using the above deviations from isotopic equilibrium, Graf et al. (2019) introduced a useful interpretative framework to quantify the effect of below-cloud processes on the isotope composition of ambient vapour and precipitation. This so-called $\Delta\delta\Delta d$-diagram quantifies the deviation of δD and *d*-excess in the liquid from the vapour phase at ambient temperatures from isotopic equilibrium as indicators of evaporation and equilibration below cloud-base. We make use of this interpretative framework to quantify the below-cloud processes during the AR event studied here. In addition, we utilize a set of sensitivity studies with the Below-Cloud Interaction Model (BCIM, Graf et al., 2019) to identify the main influences during the case studied here in the $\Delta\delta\Delta d$-diagram. The sensitivity experiments are described in more detail in Appendix B.

2.5 Reanalysis and weather forecast data

The large-scale meteorological situation is depicted using the global ERA-Interim reanalysis data from the European Centre for Medium-Range Weather Forecast (ECMWF) re-gridded to a 0.75×0.75° regular grid. Moisture transport is quantified by the integrated water vapour transport (IVT; e.g. Nayak et al., 2014; Lavers et al., 2014, 2016), whereas mean sea level pressure (SLP) is used to depicts the location of weather systems.

In addition, air temperature, solid and liquid precipitation, cloud water and cloud ice were extracted as profiles across all model levels from ERA5 reanalysis data (Hersbach et al., 2020) with a 1-h time resolution. Lastly, air temperature, horizontal

https://doi.org/10.5194/wcd-2020-58
Preprint. Discussion started: 9 December 2020

wind speed and relative humidity at different pressure levels, as well as surface precipitation were retrieved from the archive of operational Harmonie-Arome forecasts in the MetCoop domain (Bengtsson et al., 2017). Operational forecasts initialized during the period 06 to 07 Dec 2016 were retrieved from the publicly accessible archive (http://thredds.met.no).

Furthermore, Morphed Integrated Microwave Imagery for total precipitable water (MIMIC-TPW) available from the Co-operative Institute for Meteorological Satellite Studies (CIMSS) are used to depict total column water at a given time instant. Satellite Meteosat Second Generation (MSG) imagery composited as Airmass RGB is used to link the actual airmass type and clouds to the modelled Meteorological situation. The colouring scheme for airmass interpretation was adapted from Zavodsky et al. (2013).

2.6 Lagrangian moisture source diagnostic

Moisture sources are a potential factor influencing the isotope composition in precipitation. Here we apply a quantitative Lagrangian moisture source diagnostic WaterSip (Sodemann et al., 2008) to diagnose the moisture sources for evaporation contributing to the AR event on 07 Dec 2016. The WaterSip method identifies moisture source regions and transport conditions from a sequentially weighted specific humidity budget along backward trajectories of air parcels that arrive over the target area.

More specifically, the method assumes that the change in specific humidity in an air parcel during each 6 h time step exceeding a threshold value is due to either evapotranspiration or precipitation. A sequential moisture accounting then provides the fractional contribution of each evaporation event to the specific humidity at an air parcel location, and by taking into account the sequence of moisture uptakes and losses, the final precipitation in the target area. For the AR event in this study, the thresholds are set to be 0.2 $\mathrm{g\ kg^{-1}}$ for Δq_c, with a 20-day backward trajectory length, and relative humidity >80 % to identify precipitation over the target region. These thresholds result in source attribution for over 98 %. Here, the moisture uptakes from both within and above the boundary layer (BL) have been taken into account (Sodemann et al., 2008; Winschall et al., 2014).

The basis of the WaterSip diagnostic applied here is the dataset of Läderach and Sodemann (2016), which we have extended over the entire ERA-Interim period. In that dataset, the global atmosphere is represented by 5 million air parcels of equal mass calculated using the Lagrangian particle dispersion model FLEXPART V8.2 (Stohl et al., 2005), with wind and humidity and other meteorological variables from the ERA-Interim reanalysis. For this study, the diagnostic was run with a target area of ca. 110×110 km centred over Bergen (59.9–60.9 °N and 4.3–6.3 °E), including both land and ocean regions. The precipitation event studied here was represented by in total 1100 trajectories arriving in the target area.

As with other methods to identify moisture source regions, the WaterSip diagnostic is associated with uncertainty due to threshold values, interpolation errors, and conceptual limitations (Sodemann et al., 2008; Sodemann, 2020). To enable a comparison with stable isotope observations, the WaterSip method predicts the d-excess from the evaporation conditions at the moisture sources using the empirical relation of Pfahl and Sodemann (2014). More specifically, the SST over ocean regions and the surface specific humidity from ERA-Interim are used to calculate RH with respect to SST, and then to calculate d-excess from the empirical relation $d = 48.2\ ‰ - 0.54\ ‰/\% \cdot \mathrm{RH}_{SST}$, using a weighted average of all contributing moisture sources.

https://doi.org/10.5194/wcd-2020-58
Preprint. Discussion started: 9 December 2020

3 Meteorological situation

On 7 of December 2016 a substantial amount of precipitation accumulated over southwestern Norway. The precipitation was related to the influx of moist air from an AR, whose structure appears as a band of high vertically integrated water vapour (IWV) in passive microwave satellite imagery (Fig. 1a). The AR reaches as a narrow band from the central North Atlantic to the study region, impacting the entire west coast of southern Norway. At 12 UTC on 07 Dec 2016, the head of the AR has spread out broadly over the North Sea and the UK. The ERA-Interim reanalysis reproduces the observed structure of IWV faithfully, albeit with an apparent tendency to higher maximum values (Fig. 1b). While the IWV has commonly been used to define ARs, more relevant for the ensuing orographic precipitation is the associated water vapour flux, expressed as IVT (Lavers et al., 2014, 2016).

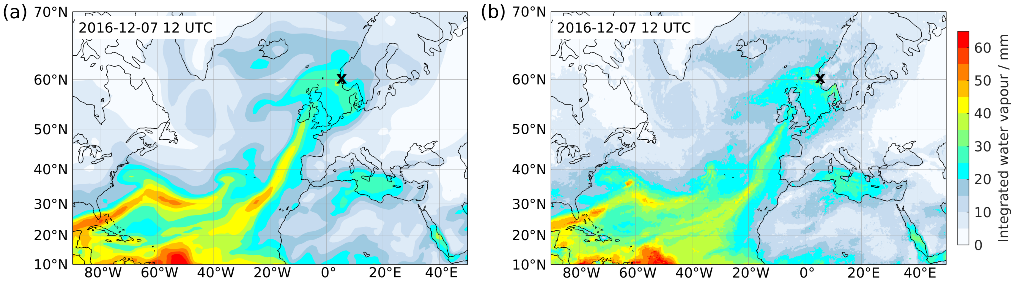

Figure 1. Vertically integrated water vapour (IWV) for the atmospheric river event occurring at 12 UTC 07 Dec 2016 in **(a)** Morphed Integrated Microwave Imagery at CIMSS (MIMIC-TPW) from the Cooperative Institute for Meteorological Satellite Studies (CIMSS) and **(b)** ERA-Interim analysis. The measurement site at Bergen is indicated by black cross.

The onshore flow of the large amounts of water vapour resulted in a prolonged precipitation event in Bergen, lasting from 00 UTC 07 Dec 2016 to 00 UTC 08 Dec 2016. Weather maps from the UK MetOffice show a sequence of surface warm fronts impinging upon southwestern Norway at 06 UTC on 07 Dec 2016 (Fig. 2a). This set of fronts is attached to a cyclone south of Iceland with core pressure of 985 hPa. The fronts are embedded in a pronounced westerly flow, bounded by a broad anticyclone with a centre over southeastern Europe and a core pressure of 1039 hPa. The individual warm fronts have approached one another over several days (not shown). We note that in the present case, the onshore water vapour flux is enhanced by the pressure gradient between the Icelandic low and the high-pressure over Europe. Similar configurations have been observed earlier to be associated with AR events in coastal western Norway (Azad and Sorteberg, 2017).

At 06 UTC on 07 Dec 2016, the first front has passed over land, as seen by the 850 hPa temperature north of Ålesund (Fig. 2c) and the widespread precipitation above $2\,\mathrm{mm\,h^{-1}}$ (Fig. 2d) obtained from the control forecast of the AROME MEPS regional forecasting system. The trailing warm front is still at a distance from the coastline, but already causes intense precipitation near

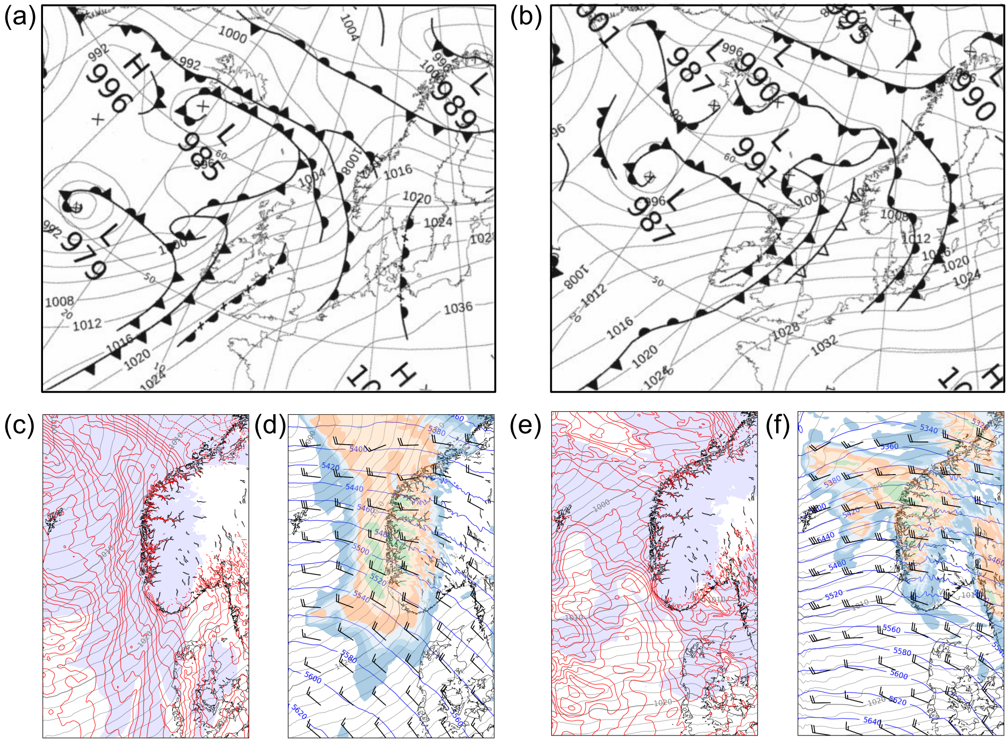

Figure 2. Overview of frontal structures during the precipitation event on 07 Dec 2016. Sea level pressure and surface fronts identified by the UK Met Office at **(a)** 06 UTC and **(b)** 18 UTC. **(c)** Sea level pressure (hPa, grey lines), air temperature (K, red lines), and relative humidity above 80 % (shaded) at 850 hPa at 06 UTC. **(d)** Sea level pressure (hPa, grey), 500 hPa geopotential height (g.p.m, blue), wind barbs at 500 hPa, and 1 h accumulated precipitation (mm, shaded) at 06 UTC. **(e)** As panel (c), but at 18 UTC. **(f)** As panel (d) but at 18 UTC. Panels (c) and (d) are from the 12 h MEPS forecast initialized at 18 UTC on 06 Dec 2016. Panels (e) and (f) are from the 06 h MEPS forecast initialized at 12 UTC on 07 Dec 2016.

https://doi.org/10.5194/wcd-2020-58
Preprint. Discussion started: 9 December 2020

the coast (Fig. 2d, green shading). At 18 UTC on 07 Dec 2016, the Icelandic cyclone has started to fill in, with the warm frontal system dissolving over southern Scandinavia. An upper-level cold front, trailed by a surface warm front approach the coast of southwestern Norway at this time (Fig. 2b). The temperature at 850 hPa shows the transition to a more cloud-free area with variable gradients as the upper-level cold air arrives over the North Sea (Fig. 2e). While there is still widespread precipitation over southern Norway, a more scattered precipitation regime sets in at this time (Fig. 2f).

3.1 Meteorological surface observations

Meteorological surface observations from the tower observatory are displayed for the AR event, lasting from 00:00 UTC on 07 Dec to 00:00 UTC on 08 Dec 2016 (Fig. 3). The local pressure at the height of the observatory gradually dropped from 1015 hPa at the start of the event to 997 hPa at 00 UTC on 08 Dec (Fig. 3a, blue line). As the warm airmass approached, the air temperature at the tower station gradually increased from 5.0 $^{\circ}\mathrm{C}$ at 05:00 UTC on 07 Dec 2016 to 11.0 $^{\circ}\mathrm{C}$ at 00:00 UTC 08 Dec 2016 (Fig. 3a, black line).

Precipitation already started forming before the increase of temperature, with precipitation rate from TPS-3100 (Fig. 3b, black line) below $1\ \mathrm{mm\,h^{-1}}$ between 00:00 and 03:30 UTC. Precipitation then steadily increased to 5.5 $\mathrm{mm\,h^{-1}}$ at 07:00 UTC, and varied thereafter on a generally high level throughout the rest of the day, with a brief intermission at 12:00 UTC, and ending on 23:30 UTC. Rainfall became in particular more variable after 14:30 UTC, reaching brief maxima above 7.0 $\mathrm{mm\,h^{-1}}$. The total precipitation amount during this 24-h event was 55.3 mm. Other instruments for precipitation measurements provide a similar time series of precipitation intensity, and comparable precipitation totals (Appendix A).

Relative humidity changed markedly during the event. Before 04:30 UTC, RH varied between 77 and 80 $\%$. As precipitation intensified, and before the temperature started to increase at 05:00 UTC, RH gradually increased to 92 $\%$ at 09:00 UTC, and remained between 92 and 95 $\%$ thereafter (Fig. 3b, blue line).

According to the time evolution of the meteorological parameters presented above, in particular the radar reflectivity, we separate the AR event into 4 distinct precipitation stages: pre-frontal Stage I before 03:30 UTC (purple bar), first frontal Stage II between 03:30 and 07:00 UTC (blue bar), a second frontal Stage III between 07:00 and 14:30 UTC (red bar), dominated by stratiform precipitation processes, and a post-frontal Stage IV after 14:30 UTC (yellow bar) that is dominated by convective precipitation. The four stages are indicated with corresponding colour bars at the top and bottom of Fig. 3.

The drop size distribution followed a similar evolution as the precipitation rate (Fig. 3c). At the beginning of the event, raindrop number concentration maxima were small, with the drop size maximum near 0.4 mm (Fig. 4a, Stage I). The drop size spectra started to show a more pronounced peak from 01:30 UTC, as well as an increase of raindrop number concentrations (Fig. 4a, Stage II). On some occasions during Stage II, a bi-modal distribution in drop sizes was observed. Drop size spectra had pronounced maxima at the smallest drop size categories between 09:00 and 11:00 UTC, and became broader between 13:00 to 14:30 UTC (Fig. 4a, Stage III). A small number of large raindrops (>1 mm) had appeared during Stage II and III. The large raindrops had disappeared after entering Stage IV, except for some intense precipitation periods between 18:30 and 20:20 UTC, around 21:30 UTC, and around 22:40 UTC. A particular feature for Stage IV is that the amount of large raindrops

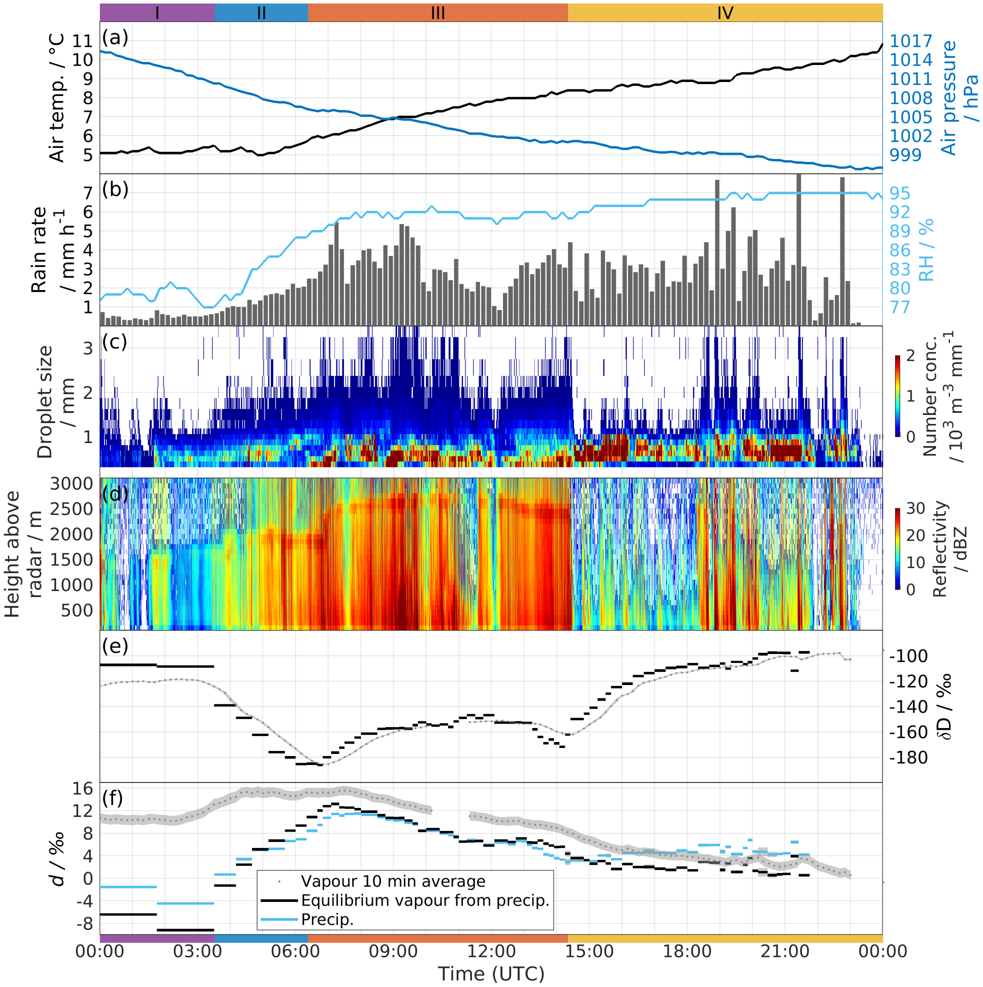

Figure 3. Time series of observations at ∼45 m a.s.l. in Bergen between 00 UTC 07 December and 00 UTC 08 December 2016. **(a)** Local temperature (black line) and air pressure (blue line) from the automatic weather station (AWS-2700). **(b)** 10 min averaged rain rate from the Total Precipitation Sensor (grey shading) and relative humidity from AWS-2700 (blue line). **(c)** Droplet number concentrations from the Parsivel^2. **(d)** Reflectivity from the Micro Rain Radar. **(e)** δD of the 10 min averaged vapour (grey dots) and δD of the equilibrium vapour from precipitation (black segments). The uncertainties are 0.60 ‰ and 0.11 ‰ for δD of vapour and of the equilibrium vapour from precipitation, respectively. **(f)** Same as in **(e)** but for *d*-excess, including *d*-excess of precipitation (blue segments). The uncertainty is 0.83 ‰ for *d*-excess of vapour, and 0.20 ‰ for *d*-excess of the equilibrium vapour from precipitation and precipitation. Precipitation periods I–IV are indicated with color bars at top and bottom of the figure.

(0.5–1.0 mm) increase substantially at the expense of raindrops with <0.5 mm diameter (Fig. 4a, Stage IV). This feature is likely to be associated with the shift from stratiform to convective precipitation.

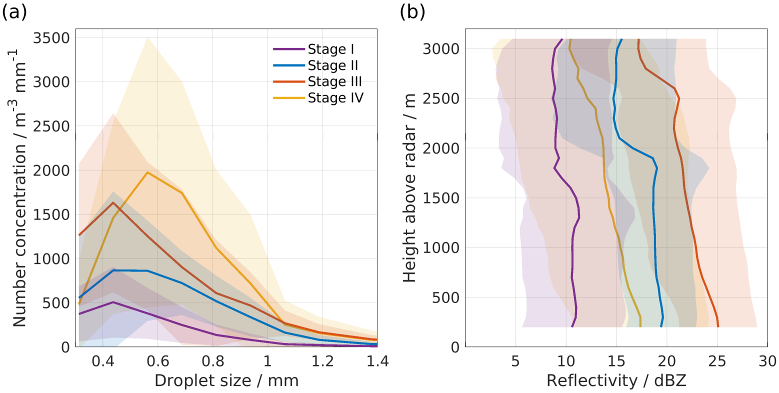

Figure 4. Averaged **(a)** number concentration of rain droplet per droplet size, and **(b)** reflectivity profile from the Micro Rain Radar at each precipitation stage during the AR precipitation event on 07 December 2016. The shading indicates one standard deviation. The lowermost layer of the reflectivity profiles has been removed due to ground clutter.

The vertical pointing MRR2 reveals hydrometeor profiles and melting layer height during the event (Fig. 3d). Before 03:30 UTC, precipitation was weak and did not continuously reach the surface, indicating the presence of evaporation of falling hydrometeors, or below-cloud evaporation. The overall reflectively is low at this stage (Fig. 4b, Stage I). As precipitation gradually intensified after 03:30 UTC, a melting layer started to appear, as well as ice-phase hydrometeors aloft, in particular after 05:00 UTC. The melting height increased from 1600 to about 1900 m between 03:30 and 04:30 UTC and stayed there until 07:00 UTC. The melting layer height then increased substantially to 2500 m at 07:00 UTC, thereafter varying between 2500 and 2700 m until 14:30 UTC, with two precipitation gaps at 11:00 and 12:00 UTC. The increase of the melting height between Stage II and III is also clearly reflected on the averaged MRR2 profiles (Fig. 4b, Stage II and III). At 07:00 UTC, the second warm front arrives over the measurement location, in close agreement with surface frontal charts and regional weather prediction model forecasts (Fig. 2). Notably, the transition to the second warm front is almost undetectable in surface temperature, precipitation and relative humidity. It is also worth to note that during the periods of most intense precipitation (i.e. between 06:30 and 11:20 UTC, and between 13:30 and 14:30 UTC), an increase in reflectivity below 500–1000 m indicates droplet growth in the lowest 1500 m above ground (Fig. 4b, Stage III), underlining the importance of water vapour in lower atmospheric layers for the surface precipitation. Almost instantly after 14:30 UTC and until the end of the event, precipitation becomes more intermittent, and no more melting layer was detected (Fig. 4b, Stage IV). This swift change reflected the shift from a more stratiform phase, dominated by warm frontal airmasses, to a dominantly convective phase of the precipitation event as the upper-level cold front arrives (Fig. 2c, e). We speculate that the melting layer vanishes either because the convection was

https://doi.org/10.5194/wcd-2020-58
Preprint. Discussion started: 9 December 2020

too shallow to reach above the 0 °C isothermal line, or because the precipitation was too intermittent to expose a clear melting layer.

4 Observed stable isotope signature in vapour and precipitation

The measured isotope composition in the surface vapour and precipitation samples is now compared in relation to the four precipitation stages identified above. For the surface vapour, the 10 min averaged $\delta \mathrm{D}_\mathrm{v}$ initially showed a relatively stable value of -120 ‰ at Stage I (dotted line, Fig. 3e). Then $\delta \mathrm{D}_\mathrm{v}$ gradually decreased at the start of Stage II (03:30 UTC), until reaching a minimum of -185 ‰ at the end of this stage (07:00 UTC). At Stage III, corresponding to the arrival of the second, merged warm front, the value gradually returns to a less depleted level of -160 ‰ at 09:00 UTC and then varies between -160 and -145 ‰ until 13:30 UTC. As the upper-level cold front arrives, the precipitation regime is about to change from stratiform to a more convective regime, at which the $\delta \mathrm{D}_\mathrm{v}$ first drops to a secondary minimum of -172 ‰, before during Stage IV (after 14:30 UTC) increasing again first rapidly, then more slowly to -110 ‰ around 18:00 UTC and finally -100 ‰ after 21:00 UTC (the least depleted values of the event). The resulting stretched-out "W" shape of the water vapour isotopes resembles earlier observations made in precipitation samples (Muller et al., 2015). The amplitude of 72 ‰ is substantial but smaller than for example observed in rainfall by C08. The relative evolution of $\delta^{18}\mathrm{O}_\mathrm{v}$ closely follows that of $\delta \mathrm{D}_\mathrm{v}$ (not shown).

The equilibrium vapour from precipitation $\delta \mathrm{D}_\mathrm{p,eq}$ approximately follow the pattern of surface vapour (Fig. 3e, black segments). There surface vapour isotope signal appears to lag the isotope signal in precipitation by about 30 min. Comparison of specific humidity from the isotope spectrometer with specific humidity calculated from the AWS shows no apparent time lag or offset at 1-min measuring frequency, indicating that atmospheric effects cause this time lag. Overall, the $\delta \mathrm{D}_\mathrm{p,eq}$ is more variable than the $\delta \mathrm{D}_\mathrm{v}$ time series. At Stage I, the isotope signal in $\delta \mathrm{D}_\mathrm{p,eq}$ is substantially less depleted than $\delta \mathrm{D}_\mathrm{v}$. This reverses at the beginning Stage II (after 03:30 UTC), and during the transition to Stage III, $\delta \mathrm{D}_\mathrm{p,eq}$ reaches a minimum, before it again is less depleted than $\delta \mathrm{D}_\mathrm{v}$ until about 08:30 UTC. Thereafter, differences between $\delta \mathrm{D}_\mathrm{v}$ and $\delta \mathrm{D}_\mathrm{p,eq}$ are small. An exception is the last hour of Stage III from 13:30 to 14:30 UTC, where $\delta \mathrm{D}_\mathrm{p,eq}$ is highly variable, and more depleted than $\delta \mathrm{D}_\mathrm{v}$. Right at the beginning of Stage IV, the $\delta \mathrm{D}_\mathrm{p,eq}$ is again more enriched than $\delta \mathrm{D}_\mathrm{v}$, before approaching equilibrium after about 18:00 UTC. The time offset, and the relative enrichment and depletion characteristics of vapour and precipitation are further examined in Sect. 5.

We now investigate the time evolution of the secondary isotope parameter *d*-excess in vapour and precipitation. After a value of 11 ‰ during Stage I, the surface vapour *d*-excess (d_v) increases to 14 ‰ at Stage II, and stays around that level until the beginning of Stage III at 08:00 UTC, one hour after the second warm front arrives (Fig. 3f, dotted line). Then the d_v gradually decreases throughout the rest of the event, with a more rapid decrease from about 10 ‰ as the upper-level cold front arrives at 14:30 UTC, to d_v varying around 4 ‰ between 18:00 and 21:30 UTC and eventually reaching 0 ‰ at 23:00 UTC.

The *d*-excess of the equilibrium vapour from precipitation $d_\mathrm{p,eq}$ shows a remarkable difference to d_v at the beginning of the event (Fig. 3f, Stage I and II, black line segments). Here, $d_\mathrm{p,eq}$ are substantially lower than the d_v, with the lowest values even being negative (-7 and -9 ‰) during Stage I. This results in a large difference between d_v and $d_\mathrm{p,eq}$ of 18 and 20 ‰, respectively. During Stage II, $d_{\text{p,eq}}$ gradually approaches d_{v}, remaining about 2–4 ‰ lower than d_{v}. Similar to d_{v}, $d_{\text{p,eq}}$ then shows a continuous decrease between 07:00 UTC and 16:30 UTC, then stabilising (with some variability) around 2 ‰. The original d-excess of precipitation, d_p (Fig. 3f, blue line segments), should theoretically be equal to $d_{\text{p,eq}}$. Small discrepancies at Stage I, Stage IV, and the two depletion minima, may at least partly arise from the definition of the d-excess (Dütsch et al., 2017).

As is evident from the results presented above, the precipitation and vapour isotope measurements, especially when combining δD and d-excess parameters, clearly provide signals that are not apparent in standard meteorological observations (such as air temperature and precipitation rate). Following our hypothesis that the isotope signature at each stage reflects the impact of several atmospheric processes, including moisture origin, processes during advection and mixing, condensation processes in clouds, as well as below cloud interaction, we now attempt to disentangle the individual contributions from these processes on the observed isotope signature at the surface during the AR event.

5 Impacts on the stable water isotope signature

The precipitation isotope signal during a weather event results from a convolution of different processes. We now proceed backwards from the last process, the below-cloud interaction, to weather system and transport influences, to the moisture source signal, to investigate how different processes contribute throughout the event.

5.1 Contribution from below-cloud interaction processes

Below-cloud interaction processes consist of the continuous exchange of falling precipitation below cloud base with the surrounding vapour in the atmospheric column. In near-saturated conditions, liquid precipitation will exchange with surrounding vapour in a near-equilibrium process. In undersaturated conditions, the vapour exchange will lead to a net mass loss of the droplets. Resulting from the same underlying process, both exchanges are strongly influenced by drop size, whereby smaller droplets being affected more strongly (Graf, 2017).

We investigate the change in isotope composition due to below cloud processes using the $\Delta\delta\Delta d$-diagram (Graf et al., 2019). The $\Delta\delta\Delta d$-diagram uses the differences between equilibrium vapour from precipitation and ambient vapour in terms of both δD and d-excess ($\Delta\delta$ and Δd, Sect. 2.3) as its axes (Fig. 5). The diagram is divided by the zero reference lines into four quadrants. The closer data points are located near the origin, the closer the equilibrium between the vapour and liquid precipitation. Data points located in the lower right quadrant have positive $\Delta\delta$ and negative Δd values, reflecting the impact of strong evaporation below cloud base. Conversely, data points in the lower-left quadrant have undergone moderate below-cloud evaporation and equilibration. Negative $\Delta\delta$ values indicate that below-cloud evaporation has been incomplete, and does not yet entirely overprint the more depleted isotope signal in the liquid precipitation at cloud base.

The temporal evolution of the precipitation samples during the AR event proceeds from the lower right quadrant, with the first to samples from Stage I displaying the strongest influence of below-cloud evaporation (Fig. 5a, letter A). Samples from Stage II are in the bottom left quadrant, first reflecting moderate below-cloud evaporation and some equilibration (letter B).

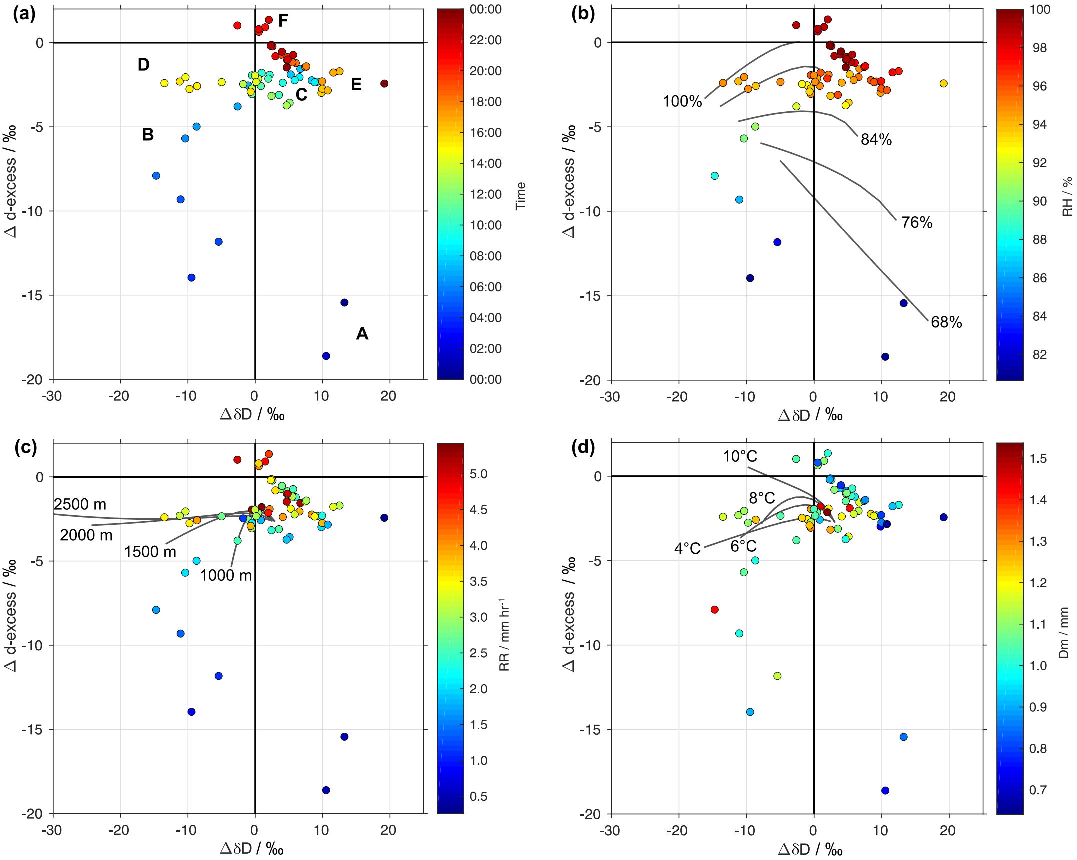

Figure 5. $\Delta\delta\Delta d$-diagram for precipitation samples collected during the AR event on 07 December 2016. Samples coloured according to **(a)** sampling start time (UTC), **(b)** relative humidity at the surface (RH$_s$, %), **(c)** precipitation rate (RR, $\mathrm{mm\,h^{-1}}$), and **(d)** droplet mean diameter (D_m, mm). Letters in panel (a) mark time periods (see text for details). Grey lines in panels (b–d) show sensitivity experiments with the idealized below-cloud interaction model of Graf et al. (2019) regarding the parameters surface air temperature (T_a), cloud base height (z_c), and relative humidity at the surface (RH$_s$) with regard to a reference simulation where $T_a = 5$ °C, $z_c = 1500\,\mathrm{m}$, and RH$_s = 90\,\%$ (see text for details).

Towards Stage III (08:30 UTC), samples are close to equilibrium with surface vapour, with slightly negative Δd values (0 to -4 ‰) and a relatively large spread of both positive and negative $\Delta\delta$D values (12 to -12 ‰, letter C). An interesting phenomenon then occurs at the transition to Stage IV, when first a stronger cloud influence is apparent, with data points near -10 ‰ for $\Delta\delta$ (Fig. 5a, letter D), before directly jumping to $+10$ ‰ after 15:00 UTC (Fig. 5a, letter E). For the remainder of Stage IV, data points then progressively move closer to equilibrium conditions, corresponding to the origin of the coordinate axes (letter F). Note that the samples from different stages are well separated in the diagram, indicating different dominating processes at each stage.

A key factor of influence for the below-cloud evaporation is RH below cloud base. When coloured by RH from the AWS, it is evident that the samples most affected by below-cloud evaporation coincide with below 90 % RH at the surface (Fig. 5b). At 90–95 % RH, the precipitation samples remain at non-equilibrium and reach the origin only for above 95 % RH. A sensitivity study with idealized simulations using BCIM (below-cloud interaction model, Graf et al., 2019) provides the coordinate system of drop-size dependent effects of RH on raindrops falling from 1500 m to the surface with initial conditions approximately resembling the situation during Stage I and II (see details in Appendix B). Albeit offset by about 10–15 % from observed RH, the sensitivity study shows a clear tendency towards lower Δd with lower below-cloud RH.

While RH is a key driver of below-cloud interaction, several other factors are also important, for example, precipitation rate. The two samples with the lowest rain rates of about 0.5 $\mathrm{mm\,h^{-1}}$ (during Stage I) are located in the lower right quadrant of the $\Delta\delta\Delta d$-diagram (Fig. 5c). Several subsequent samples with slightly higher rain rate ($\sim$ 0.9–2.2 $\mathrm{mm\,h^{-1}}$) are located in the left quadrant, ranging from about -15 to -6 ‰ in Δd. As the rain rate of the sample further increases and the ambient air nearly saturates, the effect from below cloud evaporation weakens. Samples with relatively heavy rain rates (mostly between 3 and 5 $\mathrm{mm\,h^{-1}}$) are found during the rest period of the event; they are located close to the zero Δd line, indicating weak influences from below cloud interactions. A sensitivity analysis of the formation height parameter in the BCIM model shows weak sensitivity, that aligns horizontally along the $\Delta\delta$ axis with increasing height. Interestingly, this agrees with data points at the transition to Stage III when the melting layer was among the highest (Fig. 3d).

The small precipitation rates are also a consequence of the below-cloud evaporation in an undersaturated environment. This below-cloud evaporation also leads to a reduced size of precipitation droplets, characterised by the droplet mean diameter. In the $\Delta\delta\Delta d$-diagram, the samples with the lowest rain rates also have a small droplet mean diameter of below 0.9 mm (Fig. 5d). There are further samples with mean diameters below 1 mm during Stage IV of the precipitation event. At these times, rather than being due to evaporation effects, the small drop sizes and the near-saturation conditions indicate that droplet growth may be taking place actively. An analysis of the sensitivity to the temperature profile with the BCIM shows a sloping of the sensitivity from a horizontal to a diagonal orientation with warmer temperatures. This is in qualitative agreement with the observations during the event with surface warming continuing from Stage III through Stage IV.

In summary, we observe strong below cloud interaction at the beginning of the rainfall event. The period (Stage I and II) is characterised with the least saturated ambient air, the lowest rain rate, the smallest droplet size, and the lowest melting layer height. All these features except the melting layer height favour the occurrence of the below-cloud interaction. Transition phases between stages increase the disequilibrium between surface vapour and precipitation, with the precipitation signal leading the

https://doi.org/10.5194/wcd-2020-58
Preprint. Discussion started: 9 December 2020

vapour in characteristic ways (Fig. 5a, letters A–F). The non-equilibrium fractionation during the evaporation causes the rain droplets to be more enriched in heavy isotopes (i.e., higher δ^{18}O and δD values). At the same time, more HDO is transferred to the vapour phase, yielding to a low or even negative d-excess in the remaining rain droplet. These isotopic signatures match the precipitation samples taken during this period (Fig. 3e, f; Fig. 5). The variation during Stage III and IV, however, shows that these two stages are less affected by below-cloud interactions, and more related to a change in parameters related to the weather system, such as formation height and the temperature profiles. We, therefore, focus now on the potential contribution of weather-system related changes to the isotope composition of surface vapour and precipitation during the AR event.

5.2 Weather-system contribution

Now, we use the 4 stages, defined based on the surface meteorological observations (Fig. 3) to investigate the relationship between the observed isotope signatures and weather-system characteristics. The precipitation event was dominated by two warm fronts, passing over Bergen in close sequence (Sect. 3). The fronts are apparent as marked gradients in air temperature at 850 hPa around 06 UTC (Fig. 2c).

A more continuous display of the frontal passage is provided by a time-height cross-section of equivalent potential temperature (θ_e), cloud water, and precipitation, using hourly ERA5 reanalysis data (Fig. 6). The cross-section depicts a constantly increasing temperature on the surface (below 850 hPa), consistent with the surface meteorological observations (shading), as well as a descending cloud base (black dotted line). A relatively deep layer of cold air near the surface present at the beginning of Stage I is replaced by warmer and more humid air. The cloud base is initially near 850 hPa, as seen by the gradient in cloud water, just below the melting layer, which is at about 830 hPa at this time (purple solid line). Towards Stage II, there is an increasing contribution of ice-phase processes to the surface precipitation, with cloud ice of above $0.15\,\mathrm{g\,kg^{-1}}$ near 450 hPa (white dotted lines). Snowfall rates increase from 0.1 to above $0.4\,\mathrm{mm\,h^{-1}}$ above the melting layer (white solid line), indicating riming of the ice particles between 600–750 hPa as an important contribution to the precipitation. The adequacy of this overall sequence is supported by the MRR2 radar observations (Fig. 3d) but indicates a delay of about 2–3 h in the ERA5 dataset.

The surface vapour and precipitation isotope composition during Stage I and II are initially dominated by below-cloud interaction. Both surface vapour and equilibrium vapour from precipitation exhibited relatively enriched δD (Fig. 3e), although probably for different reasons. The low depletion of -120 ‰ in δD for the surface vapour is probably related to the pre-frontal boundary-layer airmass that originated from local evaporation, and had not undergone rain-out processes (e.g. a short distance moisture source). As identified in Sect. 5.1, the observed enrichment in the precipitation is probably the result of below-cloud evaporation, as reflected in the observed negative d-excess of -6 to -9 ‰ in the precipitation samples. With the precipitation signal leading the vapour isotope composition, the weather-system signal progressively becomes more dominant throughout Stage II, levelling at -180 ‰ between 05:00 and 06:00 UTC. We consider this the actual δD isotope signature of the first frontal airmass.

From Stage I to Stage II, the d-excess of surface vapour increased from 12 to 15 ‰. We consider two possible influencing factors for this increase. First, the increase could reflect the gradual shift from the pre-frontal to the newly arriving warm-frontal airmass. However, there was a large distance between the d-excess of equilibrium vapour from precipitation and that of

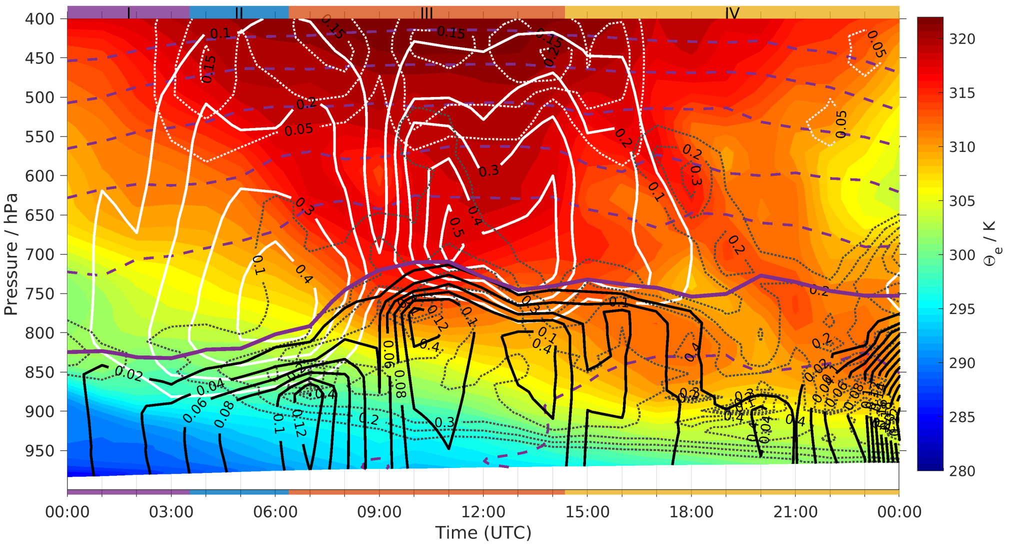

Figure 6. Hourly equivalent potential temperature from ERA5 reanalysis for the observation site at Bergen between 00 UTC 07 December and 00 UTC 08 December 2016. Solid white line indicates specific snow water content and dotted white line specific cloud ice water content. Solid black line indicates specific rain water content and dotted black line specific cloud liquid water content. The unit of all contours for different water species is $\mathrm{g\,kg^{-1}}$. Thick purple line indicates the 0 °C isothermal line and dashed purple lines indicate isothermal lines deviating from 0 °C isothermal line with 5 °C intervals. Colour bars at top and bottom indicate precipitation periods I–IV.

surface vapour (up to ∼12 ‰). This indicates the influence of the below-cloud exchange. At the end of Stage II, the evolution of *d*-excess of equilibrium vapour from precipitation and *d*-excess of surface vapour converge, indicating a balance between column vapour and precipitation. Following this interpretation, we consider the ∼14 ‰ as the most likely value for *d*-excess signal of the first warm front.

The transition to Stage III with the second warm front is indicated by a substantial jump in melting layer height around 07–08 UTC to 700 hPa (Fig. 6, purple line), and a gap in snowfall and intensified precipitation around 09 UTC. At this time, the cloud becomes markedly deeper, and regions of cloud liquid and cloud ice overlap at 550 hPa. Precipitation shows a maximum above 800 hPa, and decreases below. This rain evaporation may be overestimated by the reanalysis since the precipitation radar instead shows an increase in reflectivity in the lowest 1000 m above the surface (Fig. 3d).

The isotopic signal of this second warm front is less depleted, and produces a transition to about −160 ‰ for δD, led by the precipitation (Fig. 3e). In addition to being warmer, cloud processes extend over a deeper section of the lower and middle troposphere during the second front. The enriching trend probably corresponds to a gradual lowering of the effective

https://doi.org/10.5194/wcd-2020-58
Preprint. Discussion started: 9 December 2020

condensation level. The lowering here appears connected to the lower of cloud base height, allowing an increased contribution to falling raindrops that gain mass from, for example, the collision with droplets formed at low levels. Indeed, we observe a noticeable increase of radar reflectivity at the surface level below 1 km during Stage III (Fig. 3d and 4b). The contribution of low-level vapour to surface precipitation is also consistent with the arguments by Yoshimura et al. (2010) based on a regional model study of an AR event that the precipitation isotope signal can be influenced by a deep section of the atmosphere.

The plateau in δD reached after about 09:00 UTC indicates that this likely is the actual isotopic signal of the second warm front. While both warmer temperatures and more contribution from lower atmospheric layers are consistent with the lower depletion, it is also possible that a different transport process has contributed to the different isotope signal of this airmass (see next section). The d-excess of both surface vapour and equilibrium vapour from precipitation during Stage III gradually decreased from 15 to 9 ‰ for the vapour, and from 13 to 6 ‰ for precipitation. A plateau reached in the precipitation d-excess after 11:00 UTC indicates that the steady state in below cloud exchange has been reached thus the signal of the airmass is likely apparent at the surface level at this time.

In the ERA5 reanalysis, the middle and lower troposphere starts to become more unstable after 14:00 UTC, as indicated by θ_e changing from about 320 K to about 305 K towards the end of the day. Noting the shift by 3 h in relation to observations, the transition to Stage IV is marked by the disappearance of ice-phase precipitation, with a tongue of cloud water reaching above 600 hPa, and cold air overrunning the warm front at about 720 hPa at 18:00 UTC (Fig. 2b). The such created instability may explain the very intense precipitation lasting for a 1-h period at the end of Stage III, associated with strong deviations in the $\Delta\delta\Delta d$-diagram. The local δD minimum of -175 ‰ at the transition of Stage III to Stage IV would then represent a higher-elevation cloud signal, reflecting the isotopic gradients in the column.

The stable stratification weakens further during the remainder of Stage IV, leading to a change from stratiform to convective precipitation. Precipitation formation shifts to the lower troposphere, mostly below the melting layer height, consistent with MRR2 measurements (Fig. 3d). The apparent lack of a melting layer implies condensation temperatures above 0 °C. The δD of both surface vapour and equilibrium vapour from precipitation gradually becomes less depleted, reaching -110 ‰ around 18:00 UTC and finally -100 ‰ after 21:00 UTC, even less depleted comparing with the values during Stage I (Fig. 3e). The increased δD values reflected the shift to precipitation formation dominated by low-level water vapour. The d-excess plateaus at about 4 ‰ after about 16:00 UTC, with the equilibrium vapour trending towards 0 ‰ towards the end of the event. With the cloud water isolines nearing the surface, and near-saturated conditions in observations, the isotope signal essentially reflects conditions within a condensing airmass.

To understand the isotope signals of surface precipitation with a rain out perspective, we modelled the observed δD of surface precipitation at different stages using the Rayleigh fractionation model of Jouzel and Merlivat (1984). The model assumes that ice crystals are formed below 0 °C under the condition of supersaturation over ice, thus including a kinetic effect during vapour-ice phase transition. Supersaturation is represented with a linear formula $S_i = 1 - 0.004T$ (T in °C) after Risi et al. (2010). The initial conditions are taken from global average conditions according to Craig and Gordon (1965) as $T_0 = 20$ °C, $\mathrm{RH}_0 = 0.75$, $\delta^{18}\mathrm{O}_0 = -13$ ‰, $\delta\mathrm{D}_0 = -94$ ‰. Precipitation is then produced by atmospheric vapour condensation under (pseudo)-adiabatic

https://doi.org/10.5194/wcd-2020-58
Preprint. Discussion started: 9 December 2020

conditions during airmass ascent. The condensation temperature of the precipitation is obtained when the modelled δD became equivalent to the observed δD in surface precipitation. The model results are shown in Table 1.

Table 1. The observed precipitation rate (RR) and isotope compositions (δD, d-excess), and the corresponding model estimate of condensation temperature (T_c), condensation height (Z_c), and d-excess (d_c) of the surface precipitation during the AR precipitation event on 07 Dec 2016 in Bergen. The model estimates are calculated using the observed δD values of the surface precipitation, according to a Rayleigh fractionation model of Jouzel and Merlivat (1984). Supersaturation over ice S_i is assumed to occur during ice formation and is represented with a linear formula $S_i = 1 - 0.004T$ (T in °C) after Risi et al. (2010). Input conditions have thereby been taken from global average conditions according to Craig and Gordon (1965) as $T_0 = 20$ °C, RH$_0 = 0.75$, δ^{18}O$_0 = -13$ ‰, δD$_0 = -94$ ‰.

	From (UTC)	To (UTC)	RR (mm)	δD (‰)	d (‰)	T_c (°C)	Z_c (m)	d_c (‰)
Stage I	00:00	03:30	1.8	−14.9	−3.2	14.1	1280	11.7
Stage II	03:30	06:00	3.4	−76.0	4.4	0.9	3900	9.9
1st minimum	06:00	06:50	2.0	−101.2	8.2	−4.1	4790	1.6
Stage III	08:30	13:15	13.8	−68.3	8.3	2.4	3600	10.1
2nd minimum	13:35	14:15	2.4	−85.7	3.8	−2.3	4480	0.2
Stage IV	17:00	21:45	17.0	−16.7	5.0	13.6	1380	11.7
Entire event	00:00	21:45	55.3	−51.9	6.2	5.8	2970	10.7

The modelled condensation temperature of Stage I reaches above 14 °C, substantially higher than the actual surface temperature (∼5 °C). With a condensation temperature well below ∼5 °C, the δD of formed precipitation is expected to be quite depleted. The modelled d-excess from the Rayleigh model is 11.7 ‰, in large contrast to the observed −3.2 ‰. The observed enriched δD and negative d-excess indicates that the cloud signal of precipitation has been substantially modified by below cloud evaporation. At Stage II, the modelled condensation temperature dropped to 0.9 °C, which is in better agreement with the concurrent temperature profile (Fig. 6). The reduced difference between modelled and observed d-excess supports a lower influence from below cloud evaporation. However, cloud tops in ERA5 reach temperatures below −25 °C, which is not reflected in the Rayleigh model. In Stage III, the modelled condensation temperature increases to 2.4 °C, corresponding to the more enriched δD in precipitation. The modelled d-excess of 10.1 ‰ agrees well with the observed value of 8.3 ‰. Expecting very limited below cloud evaporation during Stage III, the overall good agreement between model and observation may indicate that the moisture origin for the water vapour at this stage is to a good extent represented by the model initial conditions (i.e. an ocean surface vapour mass with $T_0 = 20$ °C, RH$_0 = 0.75$, δ^{18}O$_0 = -13$ ‰, and δD$_0 = -94$ ‰). Still, the relatively warm condensation temperature compared to the depth of the stratiform cloud underlines that lower atmospheric layers contribute substantially to the rainfall total. At Stage IV, the modelled condensation temperature is again far too warm, with 13.6 °C. The overestimation probably reflects that more local evaporation conditions should be used in this case. The modelled condensation temperatures for the two most depleted δD periods are −4.1 and −2.3 °C respectively. The low d-excess from the model may be associated with the high sensitivity of d-excess on the representation of supersaturation conditions during ice formation in cloud (Jouzel and Merlivat, 1984) and should be considered with caution. Also in these two most depleted situations, the condensation temperature from the Rayleigh model is more consistent with a mass-weighted average of condensation, rather than cloud-top temperatures.

It is also worth to note that the precipitation amount collected during Stage I and II only contributes about 9.4 % of the total precipitation amount collected during the entire event. Hence the effect of below cloud evaporation will unlikely be detected in a precipitation sample that is collected on an event basis, or daily and longer time scales.

Based on the isotope signals of the different airmasses during Stage II to IV, we now explore to what extent these reflect the moisture source and transport conditions.

5.3 Relation of moisture sources to meteorological evolution

We now consider the synoptic development over the three days proceeding the precipitation event, with a focus on how moisture sources and moisture transport to Bergen are connected to the weather system configuration.

On 4 December 2016, two low-pressure systems are located south of Greenland and in the North Atlantic. Strong moisture transport takes place at the southern flank in the warm sector region, displayed as IVT above 800 $\mathrm{kg\,(ms)^{-1}}$ (Fig. 7a). This region is connected to widespread cloudiness at the northern edge of an airmass with high humidity (Fig. 7b, green shading). Bergen (red cross) is under the influence of a weak pressure gradient, with an onshore flow from NE, and lower humidity. Moisture uptakes contributing to precipitation in Bergen during the AR event are identified for the respective time periods. The most substantial moisture uptake (thick blue contours) contributing to the precipitation on 07 Dec 2016 coincides with the boundary between the dry and cold air to the north (Fig. 7b, red and blue shades), and the moist airmass to the south (green shades) over the central and western North Atlantic. At this boundary, extensive cloud formation occurs, ranging from deep clouds (white) to low-level stratus clouds (light green).

On 5 December, the two low pressure systems have merged, with a core low below 975 hPa near Iceland (Fig. 7c,d). IVT and cloudiness in the frontal band have intensified. South of Norway and central Europe, high pressure is starting to form, with a 1030 hPa core pressure. The moisture uptake has moved further north and overlaps now with the IVT maximum. This warm frontal band coincides with the two warm fronts passing southern Norway during the event (Fig. 2a).

On 6 December at 12 UTC high wispy cirrus clouds mark the surface warm front over Bergen (Fig. 7f). The cyclone had entirely separated from its frontal bands and started to fill in. High pressure over Europe increased to 1040 hPa, with the pressure gradient further accelerating the onshore flow, supporting an intense meridional IVT of above 800 $\mathrm{kg\,(ms)^{-1}}$, which just straddled over Scotland. Moisture sources advanced substantially further to the northeast, with the IVT maximum and now concentrated south of the British Isles.

On 7 December, a small, secondary cyclone dominated the moisture flux in the north, while the southern part of the IVT structure remained supported by yet another low-pressure system downstream (Fig. 7g). Moisture uptakes are identified over the North Sea near Scotland, contributing to precipitation in Bergen later that day (blue contours). The area over Scotland corresponded to relatively cold air with broken clouds intruding at the rear side, over the UK, belonging to the cold frontal air during Stage IV (Fig. 7h).

https://doi.org/10.5194/wcd-2020-58
Preprint. Discussion started: 9 December 2020

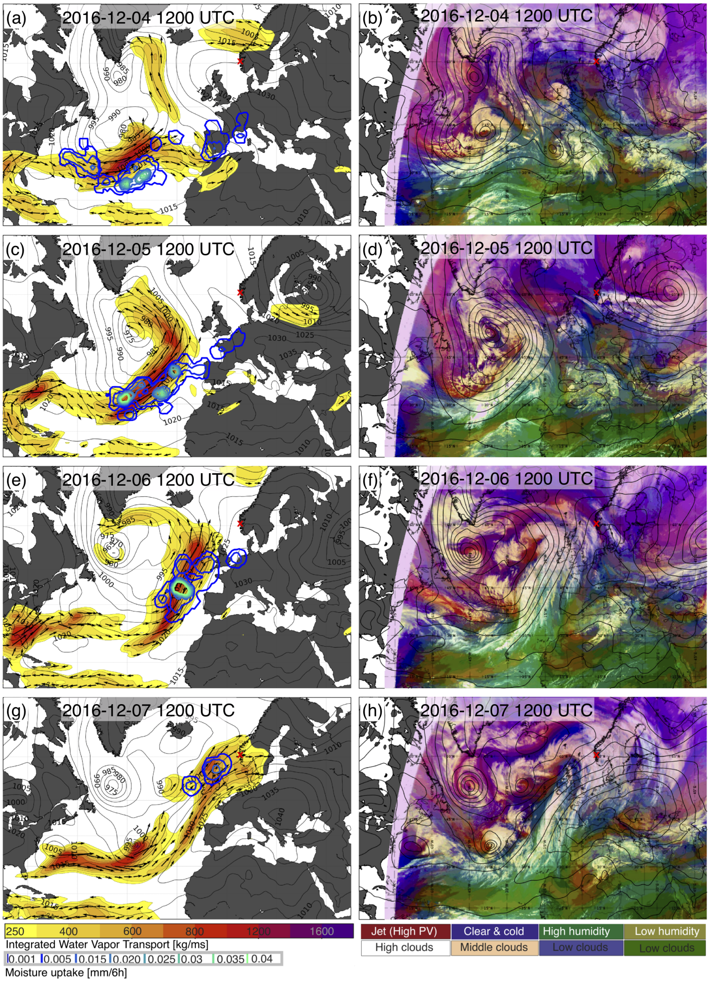

Figure 7. Synoptic situation at 12 UTC on the day of the precipitation event, 7th of December 2016 **(g,h)**, and three days prior **(a-f)**. Mean sea level pressure every 50 hPa in black contours. Left column: Integrated water vapour Transport (IVT, $\mathrm{kg\,(ms)^{-1}}$) >250 $\mathrm{kg\,(ms)^{-1}}$, filled contours), with the previously concurrent moisture uptake ($\mathrm{mm\,(6\,h)^{-1}}$, blue-green contours) that precipitated between 00 UTC on 7th December and 8th of December in the target area. Right column: Satellite Meteosat Second Generation (MSG) Airmass RGB (source http://eumetrain.org/). Colorbar adapted from airmass RGB interpretation EUMETSAT (Zavodsky et al., 2013). Red cross indicates the measurement site at Bergen.

In summary, moisture transport and moisture uptakes were clearly connected to the frontal structures during the AR event. The most substantial moisture uptake was occurring in the vicinity of the IVT maximum, embedded in the fused warm frontal bands. As the time window to the precipitation event shortened, the moisture uptake moved substantially further northward over the North Sea. This change in moisture source distance corresponds at least qualitatively to progressively less depleted isotopic signature during the event. We now investigate more quantitatively how different the evaporation conditions at the moisture sources were for Stages II, III and IV.

5.3.1 Moisture source contribution

The evaporation conditions at the moisture sources identified above determine the vapour isotope composition before the start of the condensation processes. Here we investigate if the stepwise decrease in precipitation d-excess observed during Stage II and Stage III can be related to changes in moisture source conditions. Moisture source conditions are quantified here in terms of moisture source distance, surface temperature, relative humidity with respect to sea surface temperature (Fig. 8a-c).

The large majority of moisture uptakes took place within a distance of 8000 km (Fig. 8a). The histogram for the main precipitation event at 12 UTC on 07 Dec 2016 is shown in grey shading, while the preceding time steps are shown in bold, and the later ones with dashed lines. During the sequence of the event, moisture sources shifted from local sources (less than 1000 km distance during 00 UTC on 07 Dec 2016) to the most distant at 12 UTC, and finally again to closer locations (3000–4000 km distance), with a combination of local and remote sources at 00 UTC on 08 Dec 2016. An analysis of the corresponding moisture lifetime (not shown) provides the shortest lifetimes during the main precipitation phase at 12 UTC, with a median of about 3 days. This timing corresponding to uptake locations from 04 to 07 Dec 2016, shown in Fig. 7. In earlier and later stages, lifetime distributions also peak at less than 5 days, while including more notable contributions with more than 5 days since evaporation.

Along with the shift in the moisture source location, evaporation conditions also changed. The most frequent temperature at the moisture sources was about 23 °C throughout the event, yet including a range of colder temperature conditions (Fig. 8b). Colder temperatures contributed in particular during the beginning of the event, when the average moisture source temperature was 17.6 °C at 00 UTC on 07 Dec 2016 (green line), and moisture sources were more local. Overall, the range of moisture source temperature variations was relatively limited throughout the event (within 2 °C).

The relative humidity with respect to the SST (RH_{SST}) is a key factor in kinetic fractionation during evaporation (Craig and Gordon, 1965). Throughout the event, mean RH_{SST} is around 65–70 % (Fig. 8c). The peak at near 100 % is an artefact of the contribution from land regions where RH_{SST} is not defined. The maximum RH_{SST} shifts during the event, from above 60 % before the most intense precipitation period to 55 % at 12 UTC on 07 Dec 2016. It appears that the most intense precipitation stage was thus also associated with the most intense evaporation due to the strongest humidity gradient over the North Atlantic moisture sources.

For comparison with the stable isotope measurements, we predict the d-excess at the moisture source from the empirical relation between RH_{SST} and d-excess by Pfahl and Sodemann (2014) (Fig. 8d). The highest d-excess from the moisture sources is predicted during the peak of the precipitation event, with a maximum at 16 ‰ (grey shading). As for RH_{SST}, land

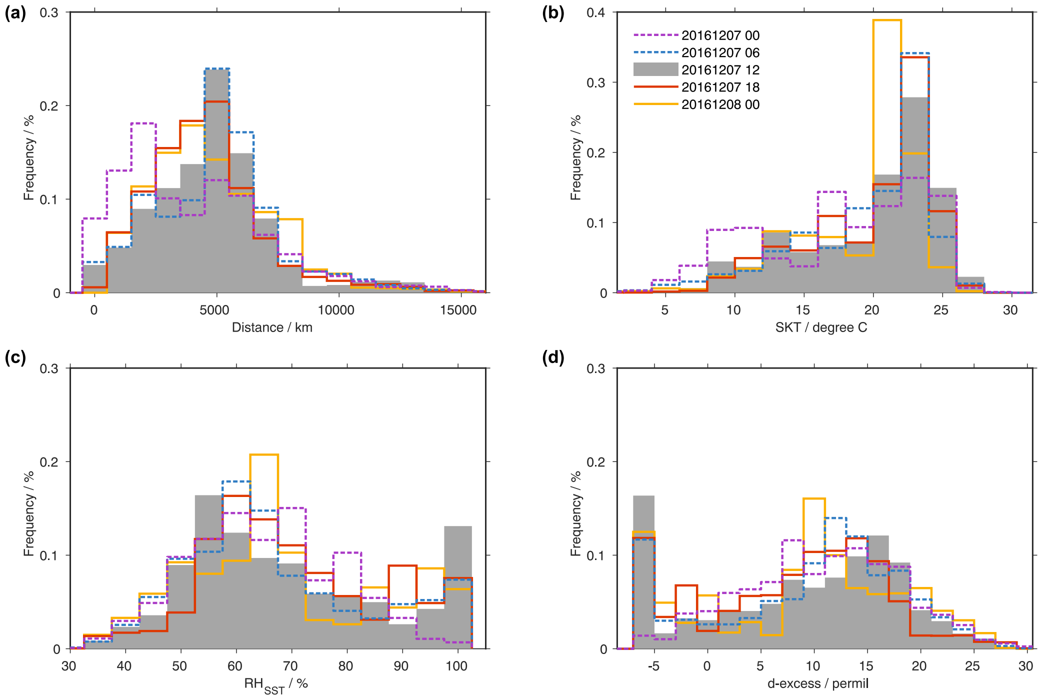

Figure 8. Histograms of moisture source conditions identified with the Lagrangian moisture source diagnostics from 20-day backward trajectories during the AR precipitation event in southwestern Norway. **(a)** Moisture source distance (km), **(b)** moisture source temperature (°C), **(c)** moisture source relative humidity with respect to sea surface temperature (RH$_{SST}$), and **(d)** d-excess estimated from the empirical relation of (Pfahl and Sodemann, 2014). Grey filled bars show the most intense period of the event (Phase III, 07 Dec 2016 at 12 UTC), solid lines the 12 h before (Stage I and II), and dotted lines the 12 h after the central period (Stage IV). Histograms represent the normalized contributions of each moisture source location to the precipitation at the arrival region on a respective date.

sources produce an artefact for d-excess below -5 ‰. Both before and after the main precipitation period, the maximum in the d-excess distribution is shifted to lower values. This sequence from low to high to low d-excess throughout the event is qualitatively consistent with the observed d-excess signal. The initial low and even negative d-excess in precipitation during Stage I is thus likely a combination of the moisture source conditions, amplified by below-cloud evaporation. The source d-excess is more sensitive to RH_{SST} than to SST (Merlivat and Jouzel, 1979; Aemisegger et al., 2014). Considering additionally that the source temperatures only change slightly during the event, the humidity gradient above the moisture sources appears as the dominant driver of the d-excess changes observed here.

Considering a longer time period around the case investigated here, the Lagrangian diagnostic indicates a rather constant d-excess value during the whole precipitation event (Fig. C1d). The observed d-excess variation is not captured by the Lagrangian diagnostic. The detailed inspection of Fig. 8 indicates the lack of variability is likely due to averaging the complex histograms to one value at the arrival location. The key characteristic of the histogram distribution is the maximum probability, but skewed and bimodal distributions make it difficult to provide more robust statistic measures. To represent the full variability of the moisture source conditions, detailed inspection of the moisture source properties throughout the event is therefore needed.

6 Discussion

We now return to the initially mentioned dispute in the literature regarding the interpretation of the precipitation isotope signal from an AR case making landfall at the coast of California. From sampling precipitation at a 30 min time interval during the AR event, C08 found a remarkable variation in δD of 60 ‰, progressing from less depleted to depleted and back. Both the shape and amplitude of the stable isotope variation were similar to the case studied here. C08 based the interpretation of the variability primarily on changes in cloud height, i.e. the temperature of condensation (Scholl et al., 2007). Using a Rayleigh distillation model, C08 proposed that the initial phase precipitation would originate from low clouds with an average condensation temperature ($\mathrm{T_c}$) of 10.0 °C, followed by deeper clouds with an average $\mathrm{T_c}$ of -4.2 °C, and again shallow clouds with $\mathrm{T_c}$ of 9.7 °C.

Y10 then simulated the same AR event with a regional isotope-enabled model, leading them to propose a fundamentally different explanation for the isotope variation in surface precipitation observed by C08. According to that interpretation, the initial drop from less depleted to depleted precipitation would be caused by below-cloud evaporation. Furthermore, Y10 found from their simulation that up to one-third of the condensate would be contributed from the lower troposphere (below 800 hPa), with an increasing tendency throughout the event. Notably, the contribution from the cloud top would decrease during the most depleted phase of the event. Despite uncertainties in some model parameters and parameterisations, Y10 concluded from their analysis that cloud microphysics, below-cloud exchange and advection all play a role for the observed isotope variation during different phases of the event.

Expanding the dataset to 43 events sampled with a network of automatic rain samplers across northern California, Coplen et al. (2015) (henceforth C15) confirmed the pronounced isotope variation during events as seen in the case discussed in C08.

https://doi.org/10.5194/wcd-2020-58
Preprint. Discussion started: 9 December 2020

C15 argue that if the below-cloud kinetic exchange were to explain the initial enrichment in C08 as proposed by Y10, kinetic effects due to evaporation should have led to characteristic deviations from the GMWL.

The above controversy revolves around two questions: (i) What is the contribution from below-cloud interaction, and in particular evaporation, to the precipitation isotope signal? (ii) Are Rayleigh-type models adequate to explain the surface precipitation signal during AR cases? Based on our highly detailed analysis of an AR event, with high-resolution precipitation sampling and simultaneous water vapour measurements, we are in a situation to contribute constructively to both aspects of this scientific controversy.

6.1 Contribution from below-cloud interaction to the isotope composition in surface precipitation

Y10 proposed that below-cloud processes can explain the isotopic enrichment in precipitation observed at the beginning of the C08 event, rather than cloud height. The joint observation of both surface vapour and precipitation in this study shows a characteristic time lag of the vapour over the precipitation signal. One plausible explanation for this time lag is that diffusional interaction takes place between precipitation and the surrounding vapour over extended time periods. Even though the total column mass of precipitation in a column is typically only about 1/10th of the IWV, precipitation persisting over longer periods will imprint on ambient vapour isotope composition, and vice versa. As more precipitation falls, the below-cloud air gradually saturates, reduce the vertical isotope gradient, and eventually reach isotopic equilibrium with the precipitation. At that point, the time lag between precipitation and vapour isotopes would vanish. Here, we find this time lag to be on the order of 30 min.

As long as the surface air is unsaturated, net mass transfer is directed away from raindrops, thus below-cloud evaporation reduces drop sizes and rainfall amounts, causing characteristic deviations in the $\Delta\delta\Delta$D framework that reflect kinetic fractionation effects. The rainfall contributed during Stage I in this study was however too small to markedly influence the isotope composition of the rainfall total (Table 1). Concerning the scientific controversy introduced above, we note that below-cloud processes can influence precipitation and surface vapour, but that the signal can be too small to detect if samples are too long, or due to sampling and analytical uncertainty. It is therefore not possible to confirm that the initial enrichment in C08 dataset was actually due to below-cloud evaporation, in particular without additional vapour measurements. Other factors, such as advection effects or progressive vapour/precipitation exchange could also have contributed to the initial enrichment.

6.2 Adequacy of the Rayleigh model to explain the isotope composition in surface precipitation

The majority of the precipitation in ARs is arriving with the strong onshore flow of the warm sector, led by the warm front and dominated by long-range transport. Large-scale ascent, enforced by orographic lifting and condensation heating during landfall leads to condensation and predominantly stratiform cloud formation. The warm conveyor belt (WCB) model is often used to describe the strongest precipitation-generating airflow in the warm sector of cyclones (Madonna, 2013). According to a common classification criterion, airmasses in the WCB airstream rise 300 hPa or more in 48 h, corresponding to vertical ascent on the order of several $\mathrm{cm\,s^{-1}}$. Precipitation from cold-sector airmasses, in contrast, has a more convective nature, characterized by an isolated ascent in updrafts, and dominated by vertical motions on the order of up to several $\mathrm{m\,s^{-1}}$.

https://doi.org/10.5194/wcd-2020-58
Preprint. Discussion started: 9 December 2020

From the Rayleigh model simulation presented in Sect.5.2, we find that the condensation temperature of the surface precipitation is most consistent with the temperature profiles in the reanalysis data (Fig. 6, purple contours) when interpreted as a representation of the vapour-mass-weighted average in the column rather than the cloud base or cloud top temperatures. MRR2 reflectivity profiles for the four precipitation stages considered here confirm that lower levels contribute substantially to the surface precipitation.

Variants of the Rayleigh distillation model are often used to represent the isotope fractionation during condensation processes (e.g. Jouzel and Merlivat, 1984). In nature, however, precipitation will enter from above into subsequent air parcels from below. This process, as well as the isotopic exchange of the falling precipitation with air parcel vapour (in case of liquid phase), is not part of Rayleigh distillation model. Indeed, the Rayleigh model may thus only be adequate to simulate the vapour composition in a rising air parcel, and the precipitation falling directly from it, which can be adequate for some convective-type precipitation processes. In the case of the more slowly ascending warm-sector airmasses, however, where clouds contribute to condensation at a range of atmospheric layers, a single air parcel appears insufficient to capture the actual precipitation process. Conceptually, it could be possible to consider instead an entire stack of Rayleigh-model air parcels as a better representation of stratiform cloud processes. Each air parcel in the column is at or near saturation, contains cloud droplets, and will receive input of hydrometeors from above. Each air parcel will thus contribute to the precipitation by condensation or deposition, riming, scavenging, and partially equilibrate with the water vapour on passing through. The vertical connection of an entire stack of Rayleigh-type parcels creates a more efficient, coupled fractionation process than an isolated Rayleigh-type parcel as in the convective case. Given such a vertically coupled perspective, a single cloud top or condensation temperature from one Rayleigh process appears too limited to capture the influences on the fractionation process in the entire cloud. This is underlined by the fact that the Rayleigh model used in C08 only needed temperatures down to -4.2 °C to explain the observed precipitation isotopes, which could not be reconciled by the range of temperatures throughout the entire column found by Y10. A similar observation was made here with the Rayleigh model of Jouzel and Merlivat (1984).

As the precipitating warm-frontal airmass is advected horizontally with the AR, it will produce a coherent isotopic signal at the surface, as noted by the displacement times in C15. C15 also noted that there is no immediate relation between the isotopic depletion and either the total amount or the intensity of precipitation during landfall. Both of these findings are consistent with the interpretation that the isotope composition of the stratiform cloud can obtain a coherent, depleted isotope signature from a sustained lifting process. The isotopic signal of stratiform cloud then reflects a time-integrated condensation history of the airmasses, whereas surface precipitation is a combination of the airmass signature, the surface vapour, and the below-cloud interaction processes.

We conclude from this discussion that since the isotopic precipitation signal is intimately coupled to the cloud microphysics and dynamics, the Rayleigh perspective can be adequate to represent the isotope composition near cloud top and in some convective situations. However, for surface precipitation, and precipitation from deep stratiform clouds in frontal systems, such as ARs, the Rayleigh model reaches conceptual limitations. Despite their own uncertainties, it, therefore, appears necessary to invoke more complex numerical tools in the interpretation, such as isotope-enabled numerical weather prediction models, or Rayleigh-type models adapted to stratiform clouds.

https://doi.org/10.5194/wcd-2020-58
Preprint. Discussion started: 9 December 2020

7 Conclusions and further remarks

We have presented a high-resolution stable isotope signature of a land-falling atmospheric river event in southwestern Norway during winter 2016. Figure 9 provides a conceptual summary of the sequence of events, by providing a spatial depiction of the airmasses arriving at Bergen. In surface precipitation, we observe δD that develops in a stretched "W" shape (between -180 and -100 ‰ for equilibrium vapour of precipitation), and d-excess that increases from -9 to 13 ‰, followed by a gradual decrease to 0 ‰. In surface vapour, δD exhibits the same "W" shape, following closely to the precipitation isotope variation, with a lag of about 30 min. The d-excess in vapour differs in the beginning markedly from precipitation signal, increasing from 10 to 16 ‰. As relative humidity below cloud base increases, the vapour d-excess follows the same trend as that of precipitation, reaching 0 ‰ at the end of the event.

Combining isotope and meteorological observations, we have identified four different precipitation stages during the event. At each stage, weather-system processes imprint on the isotope variations (Fig 9). Specifically, at the beginning of the event (Stage I), below-cloud evaporation is substantial, contributing to the low and even negative d-excess and relatively enriched δD in surface precipitation. At Stage II, the gradual weakening of below-cloud evaporation as ambient air becomes more saturated, and the involvement of hydrometeors from above the melting layer results in a gradual drop of δD and an increase in d-excess. At Stage III, deep clouds allow hydrometeors formed at high levels to gain moisture from low levels, leading to intermediately depleted values in δD. Stage IV is characterised by numerous convective showers that are formed at relatively low elevation, leading to the most enriched δD values during the event. The gradual drop of the d-excess in both surface precipitation and vapour during Stage III and IV can at least partly be explained by a change in moisture source conditions.

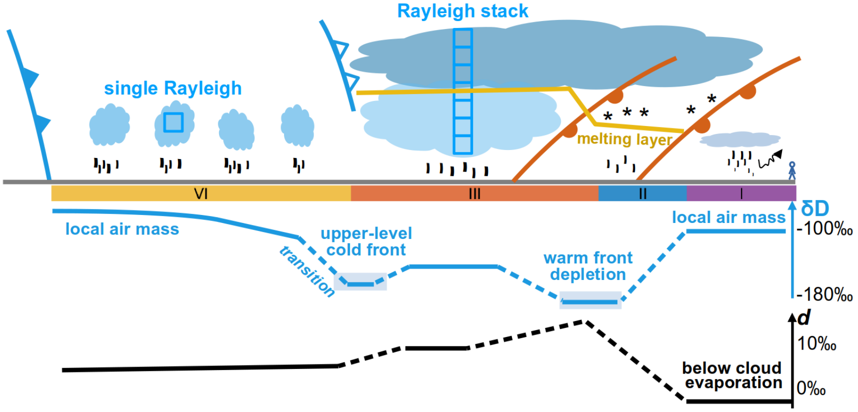

Figure 9. Weather diagram for the precipitation event at Bergen on 07 December 2016. δD and d-excess lines represent the evolution of isotope composition of surface vapour or equilibrium vapour from surface precipitation. Precipitation periods (I, II, III and IV) are indicated with color bars at the bottom. isotope Note that the timeline is from right to left.

https://doi.org/10.5194/wcd-2020-58
Preprint. Discussion started: 9 December 2020

Regarding the controversial discussion of the isotopic signal during previous AR events in the literature (C08, Y10, C15), we emphasize from our results that the isotopic precipitation signal is intimately coupled to the cloud microphysics and dynamics. Idealized Rayleigh models may be adequate to represent the isotope composition of water vapour near cloud top during convective precipitation events. However, additional factors and more complex models should be considered to interpret the isotopic signal in surface precipitation, in particular for deep, stratiform clouds. A stack of Rayleigh models could be a more adequate conceptual view for these cloud types (Fig 9).

Our case study provides a unique isotope dataset of an AR event in southwestern Norway. More cases should be performed in the future to test the more general validity of the results obtained in this case study. However, from one case already it is apparent that the isotopic information from combined (paired) water vapour and precipitation isotope sampling can be highly valuable for future data-model comparison studies with isotope-enabled weather prediction models.

Data availability. Datasets are available in the supplement.

Appendix A: Comparison of precipitation rate measurement

The precipitation rate at the sampling site (45 m a.s.l.) is measured by two instruments, i.e. Total Precipitation Sensor (TPS-3100) and Parsivel^2 distrometer. Fig. A1 shows a comparison of hourly precipitation rate during the precipitation period between the measurements of these two instruments and that of the rain gauge measurement from the closest meteorological station (70 m away, 12 m a.s.l.). The comparison shows that the TPS-3100 measures a slightly higher precipitation rate while the Parsivel^2 recorded a substantially lower precipitation rate, particularly in the situation of heavy precipitation. Since the TPS-3100 measurements agree well with the rain gauge measurements, we choose to use the precipitation rate from TPS-3100 for the analysis in this study. We did not choose to calibrate the TPS-3100 measurements against the rain gauge measurements because the small discrepancy can be due to the different locations and elevations of the two instruments.

Appendix B: Sensitivity studies with the Below-Cloud Interaction Model (BCIM)

Idealized simulations with the BCIM model help to reveal the sensitivity to factors influencing the below cloud processes. The background profiles of the BCIM model were here obtained from the moist adiabatic ascent of an air parcel that is lifted from the surface with initial values of $T_0 = 5$ °C and $RH_0 = 90$ %. The background isotope profiles are obtained correspondingly from Rayleigh fractionation with a surface composition of $\delta D = -160$ ‰ and *d*-excess $= 10$ ‰. A formation height of 1500 m was used in this reference simulation. Other simulations are obtained in the same way with an adiabatic ascent of an air parcel, while modifying one of the initial values as detailed below:

- The sensitivity to RH was evaluated by modifying the surface RH in steps of 2 % between 64 and 100 % while keeping all other parameters unchanged.

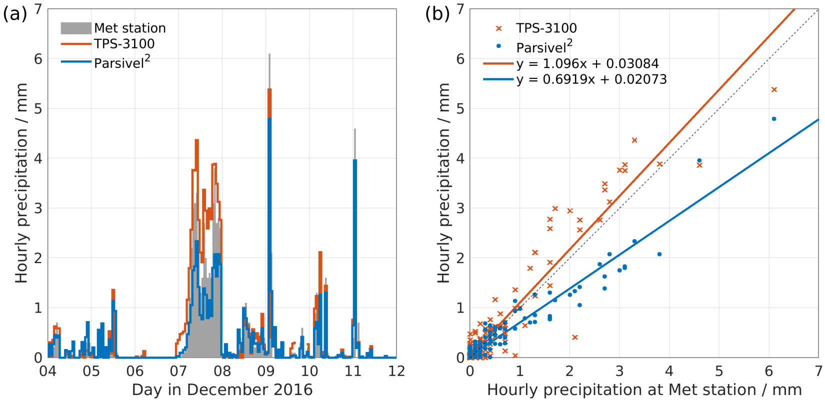

Figure A1. (a) Hourly precipitation rate during 04-11 December 2016 measured by rain gauge at WMO station (shading), TPS-3100 (red) and Parsivel^2 (blue). **(b)** Scatter plots and corresponding fits for the measurements of TPS-3100 (red) and of Parsivel^2 (blue) against those from rain gauge at WMO station.

- The sensitivity to formation height was evaluated by modifying the formation height in steps of 250 from 500 m to 3000 m while keeping all other parameters unchanged.
- The sensitivity to the temperature profile was evaluated by modifying the surface temperature in steps of 1 $^\circ\mathrm{C}$ while keeping all other parameters unchanged.

While BCIM provides helpful insights, its limitation should be noted. The model only considers a single falling hydrometeor and assumes that the background isotope profile of the atmosphere is not affected by evaporating hydrometeor or other processes during the simulation. However, in our AR case presented here, it can be clearly seen that the precipitation has a profound influence on the isotopic evolution of surface vapour.

The BCIM is available from the website https://git.app.uib.no/Harald.Sodemann/bcim (see Graf et al. (2019) for more details).

Appendix C: Long term observations and Lagrangian diagnostics

To examine our AR precipitation event in the context of the longer-term weather evolution, we present here selected observations at the sampling site as well as the Lagrangian moisture source diagnostics for the Bergen region between 04 and 11 December 2016 (Fig. C1).

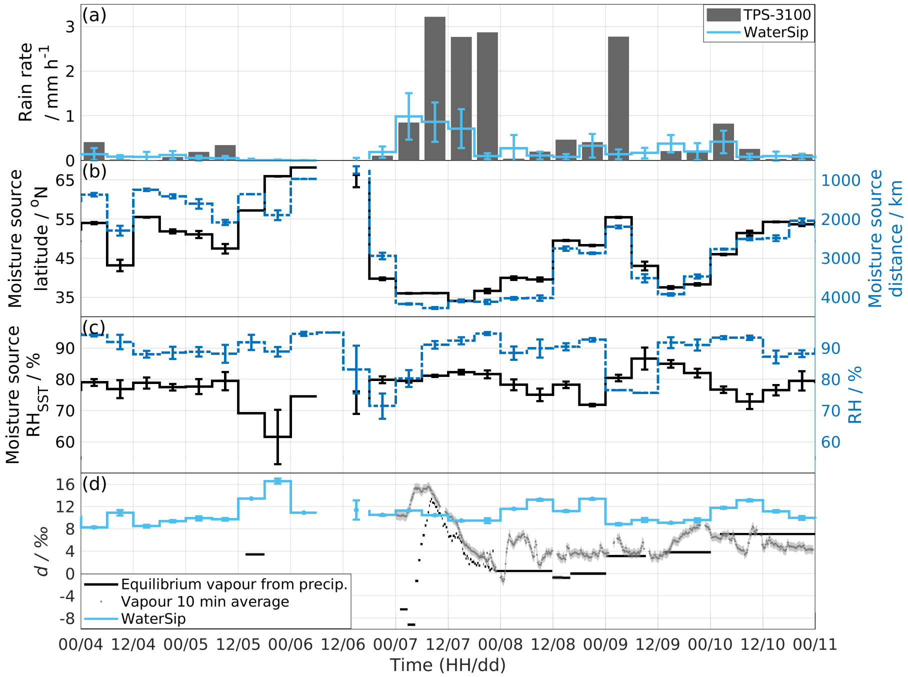

Figure C1. Seven days time series of observations at sampling site and Lagrangian diagnostic (WaterSip) output for the Bergen region between 00 UTC 04 December and 00 UTC 11 December 2016. **(a)** 6 hourly averaged rain rate observed from Total Precipitation Sensor (blue line) and estimated rain rate from WaterSip (grey shading). **(b)** Moisture source latitude (solid black line) and source distance (dashed blue line) estimated by WaterSip. **(c)** Moisture source RH$_{SST}$ (solid black line) estimated by WaterSip and 6 hourly averaged RH at sampling site (dashed blue line). **(d)** d-excess of the 10 min averaged vapour (grey dots), of the equilibrium vapour from precipitation (black segments) at 45 m above ground, and WaterSip estimate (light blue). The width of the black segment indicates the period over which the precipitation sample was collected. The uncertainties are 0.83 ‰ and 0.20 ‰ for d-excess of vapour and of the equilibrium vapour from precipitation, respectively. The error bars in **(a-d)** indicate one standard deviation. The missing data of the WaterSip on 12 UTC 6 December is due to bad data quality. The observation of d-excess is only available from 07 December.

A dry period of one and a half day precedes the AR precipitation event. Following the AR precipitation, discontinuous, moderate precipitation occurs (Fig. C1a). The comparison of the precipitation time series shows a qualitative agreement, but with substantially lower precipitation intensities estimated by the Lagrangian diagnostic. The discrepancy in the precipitation intensity likely arises from the neglect of microphysical processes in the trajectory-based diagnostic, and from the limitation of comparing a regional estimate with a single-point ground observation. The Lagrangian moisture source diagnostic shows that the dominating moisture source for the dry period pre the AR precipitation came from the north of Bergen (N of 65 °N; Fig. C1b, black solid line). During the AR precipitation, the moisture source shifted markedly to the south, reaching 35 °N. After the AR event, the moisture source gradually shifts back to the north, reaching 55 °N on 9 December, followed by another south-to-north variation. Closely following the source latitude, the moisture source distance reveals the airmass evolution from a local airmass pre AR event, to a substantial remote airmass during the AR event, and a moderate-distance airmass after the AR event (Fig. C1b, blue dashed line). The estimated RH$_{SST}$ at moisture source indicates relatively intense evaporation condition at the moisture source before the AR event (RH$_{SST}$ reaching 62 $\%$), more moderate evaporation condition during the AR event (RH$_{SST} \approx 80$ $\%$), and varying evaporation conditions afterwards (RH$_{SST}$ varying between 72 and 85 $\%$; Fig. C1c, black solid line). The local RH at the sampling site stays high (above 90 $\%$) during the entire period, except at the beginning of the AR event and between UTC 00 and 12 on 9th December (Fig. C1c, blue dashed line).

Finally, we examine the d-excess of near-surface vapour, of equilibrium vapour from precipitation, and the d-excess estimation based on Lagrangian diagnostics (Fig. C1d). The d-excess of surface vapour exhibits a peak (above 8 ‰, with a maximum of about 16 ‰) during the first half-day of the AR event. Thereafter, the d-excess of surface vapour remains at low levels mostly between 0 and 8 ‰. The low d-excess can be due to the calm evaporation conditions at the moisture source or a contribution from land regions. The d-excess of equilibrium vapour from precipitation follows the overall variation of d-excess of surface vapour. The lower d-excess values for the quasi-daily precipitation samples collected after the AR precipitation event can be due to below cloud evaporation, and cloud microphysical processes.

Author contributions. YW and HS designed the study jointly. Observation and data analysis was led by YW with contributions from AJ and HS. All authors contributed to the writing of the paper.

Competing interests. The authors declare that no competing interests are present in this study.

Acknowledgements. We thank Ole Edvard Grov for managing and providing the data from Automatic Weather Station (AWS-2700) and Norwegian Met office for high-resolution precipitation data at the Bergen-Florida station. This research has been supported by the Research Council of Norway SNOWPACE (grant no. 262710) and FARLAB (grant no. 245907).

References

Aemisegger, F.: On the link between the North Atlantic storm track and precipitation deuterium excess in Reykjavik, Atmospheric Science Letters, 19, e865, 2018.

Aemisegger, F. and Papritz, L.: A climatology of strong large-scale ocean evaporation events. Part I: Identification, global distribution, and associated climate conditions, Journal of Climate, 31, 7287–7312, https://doi.org/10.1175/JCLI-D-17-0591.1, 2018.

Aemisegger, F. and Sjolte, J.: A climatology of strong large-scale ocean evaporation events. Part II: Relevance for the deuterium excess signature of the evaporation flux, Journal of Climate, 31, 7313–7336, 2018.

Aemisegger, F., Pfahl, S., Sodemann, H., Lehner, I., Seneviratne, S., and Wernli, H.: Deuterium excess as a proxy for continental moisture recycling and plant transpiration, Atmospheric Chemistry And Physics, 14, 4029–4054, 2014.

Aemisegger, F., Spiegel, J., Pfahl, S., Sodemann, H., Eugster, W., and Wernli, H.: Isotope meteorology of cold front passages: A case study combining observations and modeling, Geophysical Research Letters, 42, 5652–5660, 2015.

Azad, R. and Sorteberg, A.: Extreme daily precipitation in coastal western Norway and the link to atmospheric rivers, Journal of Geophysical Research: Atmospheres, 122, 2080–2095, https://doi.org/10.1002/2016JD025615, 2017.

Barras, V. and Simmonds, I.: Observation and modeling of stable water isotopes as diagnostics of rainfall dynamics over southeastern Australia, Journal of Geophysical Research: Atmospheres, 114, 2009.

Battan, L. J.: Radar observation of the atmosphere, Quarterly Journal of the Royal Meteorological Society, 99, 793–793, https://doi.org/10.1002/qj.49709942229, 1973.

Bengtsson, L., Andrae, U., Aspelien, T., Batrak, Y., Calvo, J., de Rooy, W., Gleeson, E., Hansen-Sass, B., Homleid, M., Hortal, M., et al.: The HARMONIE–AROME model configuration in the ALADIN–HIRLAM NWP system, Monthly Weather Review, 145, 1919–1935, https://doi.org/10.1175/MWR-D-16-0417.1, 2017.

Bony, S., Risi, C., and Vimeux, F.: Influence of convective processes on the isotopic composition (δ^{18}O and δD) of precipitation and water vapor in the tropics: 1. Radiative-convective equilibrium and Tropical Ocean–Global Atmosphere–Coupled Ocean-Atmosphere Response Experiment (TOGA-COARE) simulations, Journal of Geophysical Research: Atmospheres, 113, https://doi.org/10.1029/2008JD009942, 2008.

Coplen, T. B., Neiman, P. J., White, A. B., Landwehr, J. M., Ralph, F. M., and Dettinger, M. D.: Extreme changes in stable hydrogen isotopes and precipitation characteristics in a landfalling Pacific storm, Geophysical Research Letters, 35, https://doi.org/10.1029/2008GL035481, 2008.

Coplen, T. B., Neiman, P. J., White, A. B., and Ralph, F. M.: Categorisation of northern California rainfall for periods with and without a radar brightband using stable isotopes and a novel automated precipitation collector, Tellus B: Chemical and Physical Meteorology, 67, 28 574, https://doi.org/10.3402/tellusb.v67.28574, 2015.

Craig, H. and Gordon, L. I.: Deuterium and oxygen 18 variations in the ocean and the marine atmosphere., in: Stable Isotopes in Oceanographic Studies and Paleotemperatures, edited by Tongiorgi, E., pp. 9–130, Laboratorio di Geologia Nucleare, Pisa, Italy, 1965.

Dansgaard, W.: The abundance of O^{18} in atmospheric water and water vapour, Tellus, 5, 461–469, 1953.

Dansgaard, W.: Stable isotopes in precipitation, Tellus, 16, 436–468, 1964.

Dütsch, M., Pfahl, S., and Sodemann, H.: The impact of nonequilibrium and equilibrium fractionation on two different deuterium excess definitions, Journal of Geophysical Research: Atmospheres, 122, 12,732–12,746, https://doi.org/10.1002/2017JD027085, 2017.

Ehhalt, D., Knott, K., Nagel, J., and Vogel, J.: Deuterium and oxygen 18 in rain water, Journal of Geophysical Research, 68, 3775–3780, 1963.

Gat, J. R.: Oxygen and hydrogen isotopes in the hydrologic cycle, Annual Review of Earth and Planetary Sciences, 24, 225–262, 1996.

Graf, P.: The effect of below-cloud processes on short-term variations of stable water isotopes in surface precipitation, Ph.d. thesis, https://doi.org/10.3929/ethz-b-000266387, 2017.

Graf, P., Wernli, H., Pfahl, S., and Sodemann, H.: A new interpretative framework for below-cloud effects on stable water isotopes in vapour and rain, Atmospheric Chemistry and Physics, 19, 747–765, 2019.

Guan, H., Zhang, X., Skrzypek, G., Sun, Z., and Xu, X.: Deuterium excess variations of rainfall events in a coastal area of South Australia and its relationship with synoptic weather systems and atmospheric moisture sources, Journal of Geophysical Research: Atmospheres, 118, 1123–1138, 2013.

Hersbach, H., Bell, B., Berrisford, P., Hirahara, S., Horányi, A., Muñoz-Sabater, J., Nicolas, J., Peubey, C., Radu, R., Schepers, D., Simmons, A., Soci, C., Abdalla, S., Abellan, X., Balsamo, G., Bechtold, P., Biavati, G., Bidlot, J., Bonavita, M., De Chiara, G., Dahlgren, P., Dee, D., Diamantakis, M., Dragani, R., Flemming, J., Forbes, R., Fuentes, M., Geer, A., Haimberger, L., Healy, S., Hogan, R. J., Hólm, E., Janisková, M., Keeley, S., Laloyaux, P., Lopez, P., Lupu, C., Radnoti, G., de Rosnay, P., Rozum, I., Vamborg, F., Villaume, S., and Thépaut, J.-N.: The ERA5 global reanalysis, Quarterly Journal of the Royal Meteorological Society, 146, 1999–2049, https://doi.org/10.1002/qj.3803, 2020.

IAEA: Reference Sheet for VSMOW2 and SLAP2 international measurement standards, 2009.

Jouzel, J. and Merlivat, L.: Deuterium and oxygen 18 in precipitation: Modeling of the isotopic effects during snow formation, Journal of Geophysical Research-Atmospheres, 89, 11 749 – 11 759, 1984.

Läderach, A. and Sodemann, H.: A revised picture of the atmospheric moisture residence time, Geophysical Research Letters, 43, 924–933, 2016.

Lavers, D. A., Pappenberger, F., and Zsoter, E.: Extending medium-range predictability of extreme hydrological events in Europe, Nature communications, 5, 5382, 2014.

Lavers, D. A., Waliser, D. E., Ralph, F. M., and Dettinger, M. D.: Predictability of horizontal water vapor transport relative to precipitation: Enhancing situational awareness for forecasting western U.S. extreme precipitation and flooding, Geophysical Research Letters, 43, 2275–2282, https://doi.org/10.1002/2016GL067765, 2016.

Liotta, M., Favara, R., and Valenza, M.: Isotopic composition of the precipitations in the central Mediterranean: Origin marks and orographic precipitation effects, Journal of Geophysical Research: Atmospheres, 111, 2006.

Madonna, E.: Warm conveyor belts. Climatology and forecast performance, Ph.D. thesis, ETH Zurich, Zürich, https://doi.org/10.3929/ethz-a-009976676, 2013.

Majoube, M.: Fractionnement en oxygéne 18 et en deutérium entre l'eau et sa vapeur, J. Chem. Phys., 10, 1423–1436, 1971.

Merlivat, L. and Jouzel, J.: Global climatic interpretation of the deuterium-oxygen 18 relationship for precipitation, Journal of Geophysical Research, 84(C8), 5029–5033, 1979.

METEK Meteorologische Messtechnik GmbH: MRR-2 Micro Rain Radar user manual, 2012.

Miyake, Y., Matsubaya, O., and Nishihara, C.: An isotopic study on meteoric precipitation, Papers in Meteorology and Geophysics, 19, 243–266, 1968.

Mook, W. G. and De Vries, J.: Introduction: Theory, methods, review, Environmental isotopes in the hydrological cycle: Principles and applications, International Hydrological Programme (IHP-V), Technical Documents in Hydrology (IAEA/UNESCO), 1, 1–164, 2001.

Muller, C. L., Baker, A., Fairchild, I. J., Kidd, C., and Boomer, I.: Intra-event trends in stable isotopes: Exploring midlatitude precipitation using a vertically pointing Micro Rain Radar, Journal of Hydrometeorology, 16, 194–213, https://doi.org/10.1175/JHM-D-14-0038.1, 2015.

Munksgaard, N. C., Wurster, C. M., Bass, A., and Bird, M. I.: Extreme short-term stable isotope variability revealed by continuous rainwater analysis, Hydrological Processes, 26, 3630–3634, https://doi.org/10.1002/hyp.9505, 2012.

Nayak, M. A., Villarini, G., and Lavers, D. A.: On the skill of numerical weather prediction models to forecast atmospheric rivers over the central United States, Geophysical Research Letters, 41, 4354–4362, https://doi.org/10.1002/2014GL060299, 2014.

OTT Hydromet GmbH: Operating instructions: Present weather sensor OTT Parsivel^2, 2015.

Papritz, L. and Sodemann, H.: Characterizing the local and intense water cycle during a cold air outbreak in the Nordic Seas, Monthly Weather Review, 146, 3567–3588, 2018.

Papritz, L. and Spengler, T.: A Lagrangian climatology of wintertime cold air outbreaks in the Irminger and Nordic Seas and their role in shaping air–sea heat fluxes, Journal of Climate, 30, 2717–2737, https://doi.org/10.1175/JCLI-D-16-0605.1, 2017.

Pfahl, S. and Sodemann, H.: What controls deuterium excess in global precipitation?, Climate of the Past, 10, 771–781, 2014.

Pfahl, S., Wernli, H., and Yoshimura, K.: The isotopic composition of precipitation from a winter storm–a case study with the limited-area model COSMOiso, Atmos. Chem. Phys, 12, 1629–1648, 2012.

Ralph, F. M., Neiman, P. J., and Wick, G. A.: Satellite and CALJET aircraft observations of atmospheric rivers over the eastern North Pacific Ocean during the winter of 1997/98, Monthly Weather Review, 132, 1721–1745, 2004.

Raupach, T. H. and Berne, A.: Correction of raindrop size distributions measured by Parsivel disdrometers, using a two-dimensional video disdrometer as a reference, Atmospheric Measurement Techniques, 8, 343–365, https://doi.org/10.5194/amt-8-343-2015, 2015.

Risi, C., Bony, S., Vimeux, F., and Jouzel, J.: Water-stable isotopes in the LMDZ4 general circulation model: Model evaluation for present-day and past climates and applications to climatic interpretations of tropical isotopic records, Journal of Geophysical Research: Atmospheres, 115, https://doi.org/10.1029/2009JD013255, 2010.

Scholl, M. A., Giambelluca, T. W., Gingerich, S. B., Nullet, M. A., and Loope, L. L.: Cloud water in windward and leeward mountain forests: The stable isotope signature of orographic cloud water, Water Resources Research, 43, https://doi.org/https://doi.org/10.1029/2007WR006011, 2007.

Sodemann, H.: Beyond Turnover Time: Constraining the Lifetime Distribution of Water Vapor from Simple and Complex Approaches, Journal of the Atmospheric Sciences, 77, 413–433, https://doi.org/10.1175/JAS-D-18-0336.1, 2020.

Sodemann, H. and Stohl, A.: Moisture origin and meridional transport in atmospheric rivers and their association with multiple cyclones, Monthly Weather Review, 141, 2850–2868, 2013.

Sodemann, H., Schwierz, C., and Wernli, H.: Interannual variability of Greenland winter precipitation sources: Lagrangian moisture diagnostic and North Atlantic Oscillation influence, Journal of Geophysical Research: Atmospheres (1984–2012), 113, 2008.

Stohl, A., Forster, C., Frank, A., Seibert, P., and Wotawa, G.: Technical note: The Lagrangian particle dispersion model FLEXPART version 6.2, Atmospheric Chemistry and Physics, 5, 2461–2474, https://doi.org/10.5194/acp-5-2461-2005, 2005.

Stohl, A., Forster, C., and Sodemann, H.: Remote sources of water vapor forming precipitation on the Norwegian west coast at 60^{o}N–a tale of hurricanes and an atmospheric river, Journal of Geophysical Research: Atmospheres (1984–2012), 113, 2008.

Thurnherr, I., Kozachek, A., Graf, P., Weng, Y., Bolshiyanov, D., Landwehr, S., Pfahl, S., Schmale, J., Sodemann, H., Steen-Larsen, H. C., Toffoli, A., Wernli, H., and Aemisegger, F.: Meridional and vertical variations of the water vapour isotopic composition in the marine boundary layer over the Atlantic and Southern Ocean, Atmospheric Chemistry And Physics, 20, 5811–5835, https://doi.org/10.5194/acp-20-5811-2020, 2020.

Uemura, R., Matsui, Y., Yoshimura, K., Motoyama, H., and Yoshida, N.: Evidence of deuterium excess in water vapor as an indicator of ocean surface conditions, Journal of Geophysical Research: Atmospheres, 113, 2008.

Wang, S., Zhang, M., Che, Y., Zhu, X., and Liu, X.: Influence of below-cloud evaporation on deuterium excess in precipitation of arid central Asia and its meteorological controls, Journal of Hydrometeorology, 17, 1973–1984, 2016.

Weng, Y., Touzeau, A., and Sodemann, H.: Correcting the impact of the isotope composition on the mixing ratio dependency of water vapour isotope measurements with cavity ring-down spectrometers, Atmospheric Measurement Techniques, 13, 3167–3190, https://doi.org/10.5194/amt-13-3167-2020, 2020.

Wernli, H. and Schwierz, C.: Surface cyclones in the ERA-40 dataset (1958–2001). Part I: Novel identification method and global climatology, Journal of the atmospheric sciences, 63, 2486–2507, 2006.

White, A. B., Gottas, D. J., Strem, E. T., Ralph, F. M., and Neiman, P. J.: An automated brightband height detection algorithm for use with Doppler radar spectral moments, Journal of Atmospheric and Oceanic Technology, 19, 687–697, 2002.

White, A. B., Neiman, P. J., Ralph, F. M., Kingsmill, D. E., and Persson, P. O. G.: Coastal orographic rainfall processes observed by radar during the California Land-Falling Jets Experiment, Journal of Hydrometeorology, 4, 264–282, 2003.

Winschall, A., Sodemann, H., Pfahl, S., and Wernli, H.: How important is intensified evaporation for Mediterranean precipitation extremes?, Journal of Geophysical Research: Atmospheres, 119, 5240–5256, https://doi.org/https://doi.org/10.1002/2013JD021175, 2014.

Yankee Environmental Systems, Inc.: TPS-3100 Total Precipitation Sensor installation and user guide (version 2.0), 2011.

Yoshimura, K., Kanamitsu, M., and Dettinger, M.: Regional downscaling for stable water isotopes: A case study of an atmospheric river event, Journal of Geophysical Research: Atmospheres, 115, 2010.

Yoshimura, K., Miyoshi, T., and Kanamitsu, M.: Observation system simulation experiments using water vapor isotope information, Journal of Geophysical Research: Atmospheres, 119, 7842–7862, 2014.

Zavodsky, B. T., Molthan, A. L., and Folmer, M. J.: Multispectral imagery for detecting stratospheric air intrusions associated with mid-Latitude cyclones, Journal of Operational Meteorology, 1, https://doi.org/10.15191/nwajom.2013.0107, 2013.

Zhu, Y. and Newell, R. E.: A proposed algorithm for moisture fluxes from atmospheric rivers, Monthly weather review, 126, 725–735, 1998.

Appendix A

^{17}O-excess

Analogous to *d*-excess, ^{17}O-excess is defined as the surplus of ^{17}O caused by non-equilibrium processes, i.e. the diffusive transport of water vapour in air (*Barkan and Luz*, 2007):

$$^{17}\text{O-excess} = ln(\delta^{17}\text{O}+1) - 0.528 ln(\delta^{18}\text{O}+1). \tag{A.1}$$

For a triple isotope system, the isotope ratios, ^{17}R and ^{18}R, in a fractionation process are related by a power law (*Barkan and Luz*, 2007; *Craig*, 1957b; *Mook and De Vries*, 2001):

$$\frac{^{17}\text{R}_A}{^{17}\text{R}_B} = \left(\frac{^{18}\text{R}_A}{^{18}\text{R}_B}\right)^{\theta} \quad \text{or} \quad \theta = \frac{ln^{17}\alpha}{ln^{18}\alpha}, \tag{A.2}$$

where the subscripts A and B can refer to two samples or one sample and one standard. To obtain a linear relation, ^{17}O-excess is therefore expressed in a logarithmic notation.

Based on the observations of a large set of globally distributed samples, the exponent θ is found to be about 0.528. This value is first established by *Meijer and Li* (1998) and later confirmed by *Barkan and Luz* (2007) and *Landais et al.* (2008). Based on all these data, the Global Meteoric Water Line (GMWL) for oxygen isotopes is defined as (*Barkan and Luz*, 2007):

$$ln(\delta^{17}\text{O}+1) = 0.528 ln(\delta^{18}\text{O}+1) + 0.000033. \tag{A.3}$$

Barkan and Luz (2005, 2007) have experimentally determined θ values for the case of vapour-liquid equilibrium ($\theta_{eq} = 0.529$) and the case triggered by diffusive transport of water vapour in air (i.e. kinetic fractionation; $\theta_{diff} = 0.518$). These values can be used to explain the two origins of the ^{17}O-excess. (1) During the evaporation process over the ocean, relatively stronger kinetic fractionation leads to an increase of ^{17}O-excess in the water vapour. The extent of this increase is anti-correlated with the relative humidity at the moisture origin. (2) During the process of condensation (an equilibrium process), precipitation is formed with higher ^{17}O-excess than its source vapour since $\theta_{eq} = 0.529$ is greater than 0.528.

Within experimental precision, the equilibrium fractionation factor for ^{17}O is found to be independent of temperature (*Barkan and Luz*, 2005). Thus the effect of sea surface temperature is negligible in the case of ^{17}O-excess. In other words, while the dominating factor to interpret the traditional *d*-excess is debated between the relative humidity and the sea surface temperature, ^{17}O-excess is thought to be a direct proxy for the humidity conditions of the moisture origin irrespective of time scale.

Since ^{17}O comprises only 0.037 ‰ of all naturally occurring oxygen isotopes, the ^{17}O-excess values are very small numbers in the order of 10~40 ppm. It was due to this high demand in precision that the measurement of ^{17}O has not been feasible until recently (*Luz and Barkan*, 2010, and references therein). Despite its potential of adding new information, the study of triple oxygen isotopes in natural waters is still in its initial stage.

Appendix B

Isotope modelling

There have been efforts in modelling the isotope fractionation during phase changes (i.e. evaporation and condensation under different circumstances) in the hydrological cycle. In this appendix, I provide an overview of the isotope modelling by reviewing classical studies.

B.1 Phase change and Rayleigh distillation model

A *Rayleigh distillation model* describes the evolution of a multiple-phase system in which molecules in one phase are continuously moved to the other phase through fractional distillation. Despite its simplicity, it is a powerful framework to describe the isotopic enrichment or depletion as material moves between reservoirs in an equilibrium process.

The Rayleigh equation is normally applied to an open system from which the formed material is immediately removed. In this sense, the evaporation of the natural water bodies, and the formation of falling precipitation can be approximately considered as open systems. However, the Rayleigh equation can also be applied to other systems. One such system is a closed system (or two-phase equilibrium model; *Gat*, 1996), where the material removed from one reservoir accumulates in a second reservoir in such a manner that isotopic equilibrium is maintained between the two reservoirs. An example would be the condensation of vapour to rain droplets in a cloud (with no precipitation falling).

B.1.1 Mathematical derivation

The isotopic enrichment or depletion by the Rayleigh process for both open and closed systems can be mathematically established using different approaches (Fig. B.1). In the following, the terms with primed symbols refer to the parameters or variables for the rare isotopologues ($H_2^{18}O$ or $HD^{16}O$; the same notation applies throughout this appendix).

(a) There are normally two mathematical approaches to demonstrate the Rayleigh process in an open system. In the first approach (Fig. B.1a), we investigate the change of isotope ratio per unit of the amount change:

$$\frac{dR}{dN} = \frac{d(\frac{N'}{N})}{dN} = \frac{1}{dN}(\frac{1}{N}dN' - \frac{N'}{N^2}dN) = \frac{1}{N}(\frac{dN'}{dN} - \frac{N'}{N}) = \frac{1}{N}(\alpha R - R). \tag{B.1}$$

Thus we obtain a relationship between R and N as:

$$\frac{dR}{R} = (\alpha - 1)\frac{dN}{N}, \tag{B.2}$$

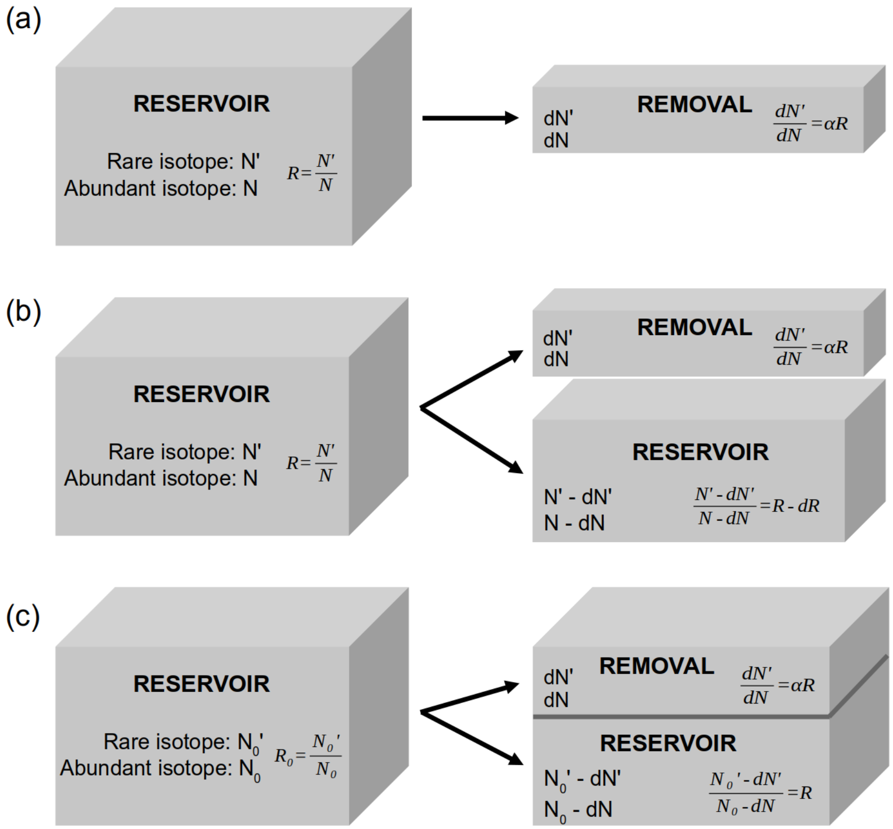

Figure B.1: Schematic presentation of the mathematical approaches of the Rayleigh model in open system ***(a, b)*** *and closed system* ***(c)****. Adapted from Gat et al. (2001).*
(a) *From a reservoir containing N abundant isotopologues (e.g.* $H_2^{16}O$*) and* N' *rare isotopologues (e.g.* $H_2^{18}O$ *or* $HD^{16}O$*) small amounts of both species, dN and dN′ respectively, are being removed under equilibrium fractionation conditions:* $dN'/dN = \alpha R$*.*
(b) *The changing isotope composition of the reservoir is calculated from a mass balance consideration for the rare isotopologues:* $RN = (R-dR)(N-dN)+\alpha R dN$*.*
(c) *In closed system, the changing isotope composition of the reservoir can be calculated from a mass balance consideration for the rare isotopologues:* $R_0N_0 = R(N_0-dN)+\alpha R dN$*, with the remaining fraction* $f = \frac{N_0-dN}{N_0}$*.*

whose integral form after applying the boundary condition of $R = R_0$ at $N = N_0$ is:

$$R = R_0\left(\frac{N}{N_0}\right)^{\alpha-1} = R_0 f^{\alpha-1}, \tag{B.3}$$

where $f = \frac{N+N'}{N_0+N_0'} \approx \frac{N}{N_0}$ is the fraction of the remaining material. Eq. (B.3) is simply the Rayleigh distillation equation. If written in δ notation ($\delta = \frac{R}{R_{\mathrm{ref}}} - 1$), Eq. (B.2) and (B.3) become:

$$\frac{d\delta}{1+\delta} = (\alpha-1)\frac{dN}{N}, \tag{B.4}$$

$$\delta = (1+\delta_0)f^{\alpha-1} - 1. \tag{B.5}$$

Eq. (B.4) can be also written in logarithmic form as: $ln(\frac{1+\delta}{1+\delta_0}) = (\alpha-1)lnf$, which gives $\delta - \delta_0 = \varepsilon lnf$, where ε ($\varepsilon = \alpha - 1$) is used to represent the enrichment ($\varepsilon > 0$) or the depletion ($\varepsilon < 0$) of the rare isotopes during the Rayleigh process.

(b) The second approach considers the mass balance of rare isotopologues (Fig. B.1b), which gives:

$$RN = (R-dR)(N-dN) + \alpha RdN. \tag{B.6}$$

Neglecting the products of differentials (i.e. $dRdN$), we obtain the same equation as Eq. (B.2).

(c) In a closed system, the isotope ratio of the remaining material can be written as:

$$R = \frac{N_0' - dN'}{N_0 - dN} = \frac{R_0 - \frac{dN'}{N_0}}{1-\frac{dN}{N_0}} = \frac{R_0 - \frac{dN'}{dN}\frac{dN}{N_0}}{f} = \frac{R_0 - \alpha R(1-f)}{f}, \tag{B.7}$$

$$\Leftrightarrow \quad R = \frac{R_0}{f + \alpha(1-f)}, \tag{B.8}$$

or in δ notation,

$$\delta = \frac{\delta_0 - (\alpha-1)(1-f)}{f+\alpha(1-f)}, \tag{B.9}$$

where $f = \frac{N_0 - dN}{N_0} = 1 - \frac{dN}{N_0}$ is the fraction of the remaining material. Following the same approach as in **(b)**, Eq. (B.8) can also be derived from a mass balance consideration in a straightforward manner:

$$R(N_0 - dN) + \alpha RdN = N_0R_0, \tag{B.10}$$

$$\Leftrightarrow \quad Rf + \alpha R(1-f) = R_0. \tag{B.11}$$

In above I have derived the isotope ratio of the reservoir. It is also relevant to calculate the isotope ratio of the total removed material. In the case of a closed system, the total removed material is always in equilibrium with that of the remaining reservoir at the time. In the case of an open system, the total removed material is gradually accumulated by the infinitesimal increments dN. This is not a simple additive procedure, since the isotope ratio of the reservoir changes during the process and thus also that of the increments dN.

For an open system, the average isotope ratio of the formed material at a certain time, R_Σ, can be derived using the mass conservation of rare isotopes between the reservoir and the formed removal. One approach is to directly integrate the rare isotope of the formed increments

dN of all the infinitesimal steps (*Mook and De Vries*, 2001) as:

$$R_\Sigma(N_0 - N) = \int_N^{N_0} \alpha R dN = \alpha \int_N^{N_0} R_0 f^{\alpha-1} dN = \frac{\alpha R_0}{N_0^{\alpha-1}} \int_N^{N_0} N^{\alpha-1} dN = \frac{R_0(N_0^\alpha - N^\alpha)}{N_0^{\alpha-1}}, \tag{B.12}$$

$$\Rightarrow \quad R_\Sigma = \frac{R_0\left(1 - \left(\frac{N}{N_0}\right)^\alpha\right)}{1 - \frac{N}{N_0}} = \frac{R_0(1 - f^\alpha)}{1 - f}. \tag{B.13}$$

The other approach simply considers only the stationary state at the time. By taking advantage of the fraction of the remaining and the formed materials, one can have:

$$R_r N_0 f + R_\Sigma N_0 (1 - f) = R_0 N_0, \tag{B.14}$$

$$\Rightarrow \quad R_\Sigma = \frac{R_0 - f R_r}{1 - f}, \tag{B.15}$$

where R_r is the isotope ratio of the remaining material in the system.

If the temperature is such that the condensation involves both liquid and solid phases, R_Σ is calculated by two stages, considering the different fractionation factor formulas of the two phase changes. Here, we take the second approach as an example. The first stage is the stage of only liquid formation. Following Eq. (B.15), the total liquid removal at the end of this stage is calculated as $R_{\Sigma l} = (R_0 - f R_{v0})/(1 - f)$, where R_{v0} is the isotope ratio of the remaining vapour at the end of the liquid phase stage. The second stage is the stage of only solid formation. At this stage, we consider a separate Rayleigh process with initial condition of $R = R_{v0}$ at $f_i = 1$, where f_i is the fraction of remaining vapour with respect to solid formation. Thus the isotope ratio of the total solid removal is calculated by:

$$R_{vi} f_i + R_{\Sigma i}(1 - f_i) = R_{v0}, \tag{B.16}$$

where R_{vi} is the isotope ratio of the remaining vapour in the second-stage Rayleigh process. Finally, we obtain the isotope ratio of the total removed material through:

$$R_\Sigma(1 - f f_i) = R_{\Sigma l}(1 - f) + R_{\Sigma i} f (1 - f_i). \tag{B.17}$$

The Rayleigh equation was originally derived for the situation where the removed material is in instantaneous isotopic equilibrium with the material in the reservoir. Similar equations can also be derived for cases that include kinetic or diffusive processes. In these cases, appropriate fractionation factors need to be introduced instead of the equilibrium fractionation factors. In the following, an overview is provided for the Rayleigh model including kinetic effects in supersaturated or undersaturated conditions.

B.1.2 Rayleigh model including kinetic effect

This section presents an overview of the Rayleigh model including the kinetic effect (RMK) that was introduced in *Jouzel and Merlivat* (1984). In short, the RMK model replaces the equilibrium fractionation factor with respect to the solid phase (α_{sv}) in Rayleigh model with a new fractionation factor that combines equilibrium and kinetic effects ($\alpha_{sv}\alpha_k$). In this context, the section mainly reviews the derivation of α_k following the work of *Jouzel and Merlivat* (1984). Also, a RMK model for the evaporation of an isolated water body in an undersaturated environment is presented.

It is noteworthy that two assumptions have been applied here by default. (1) The first assumption underlies in the Rayleigh distillation model for an open system, where all the formed material is assumed to be immediately removed from the system. In practical, for a precipitating cloud, a very small proportion (most likely < 20 % or much lower; *Ciais and Jouzel*, 1994) of the condensed phase (water droplets and/or ice crystals) would remain in the cloud instead of immediately forming precipitation. Fortunately, the amount of remnant in the cloud is shown to only play a minor role in predicting the isotopic evolution of the precipitation (*Ciais and Jouzel*, 1994). On the other hand, this may explain the overall good performances of the simple Rayleigh-type models. (2) The second assumption is that the transport of water molecules is considered purely diffusive for all the cases discussed here. Given that the condensation/evaporation flux is proportional to D^n (D is water molecular diffusivity and $n \in [0,1]$ a tunable exponent indicating the ratio of diffusive over turbulent transport of water molecules), $n = 1$ is applied here (see also Sect. B.2).

Vapour deposition on a cold plane surface

To verify the existence of a kinetic effect during vapour depostion, *Jouzel and Merlivat* (1984) conducted a laboratory experiment where the environmental water vapour ($T = 20$ °C) condensates on a cold plane surface ($T = -20$ °C). Assuming that the condensation process takes place in a pure molecular regime (no turbulent resistance), the fluxes to the plane surface for the abundant and the rare water isotopologues are:

$$F \propto D(e_v - e_i), \tag{B.18}$$

$$F' \propto D'(e'_v - e'_i), \tag{B.19}$$

where D is the molecular diffusivity in air ($D_{\mathrm{H_2^{18}O}}/D_{\mathrm{H_2^{16}O}} = 0.9723 \pm 0.0007$, $D_{\mathrm{HD^{16}O}}/D_{\mathrm{H_2^{16}O}} = 0.9755 \pm 0.0009$; *Merlivat and Jouzel*, 1979), e_v the partial pressure, and e_i the saturation vapour pressure over ice. The terms with primed symbols correspond to the parameters or variables for the rare isotopologues. The partial and saturation vapour pressure between the abundant and rare isotopologues are related to the isotope ratios as:

$$R_v = \frac{e'_v}{e_v}, \tag{B.20}$$

$$R_a = \frac{R_s}{\alpha_{sv}} = \frac{e'_i}{e_i}, \tag{B.21}$$

where R_v, R_a, and R_s are the isotope ratio of the remaining vapour, of the saturated vapour above ice surface, and of the formed ice, respectively; α_{sv} ($\alpha_{sv} > 1$) is the equilibrium fractionation factor.

Because of the low diffusivities of water molecules in ice, it is considered that there is no homogenization of the isotopes in ice. Thus the isotope ratio of the formed ice is directly related to the ratio of the fluxes F and F' through:

$$R_s = \frac{F'}{F} = \frac{D'(e_v R_v - e_i R_s/\alpha_{sv})}{D(e_v - e_i)}. \tag{B.22}$$

This gives:

$$R_s = \alpha_k \alpha_{sv} R_v, \tag{B.23}$$

$$i.e. \quad 1+\delta_s = \alpha_k \alpha_{sv}(1+\delta_v), \tag{B.24}$$

where

$$\alpha_k = \frac{S_i}{\alpha_{sv}\frac{D}{D'}(S_i-1)+1}, \quad \text{with} \quad S_i = \frac{e_v}{e_i}. \tag{B.25}$$

The term α_k is the kinetic fractionation factor that accounts for the kinetic effect during the form of ice. S_i is the saturation ratio with respect to ice at the ice temperature. Since α_{sv}, $\frac{D}{D'}$, and S_i are all greater than the unity, α_k is lower than the unity.

The laboratory experiment from *Jouzel and Merlivat* (1984) shows that, comparing with the source vapour, the formed ice has a lower δ^{18}O value (-15.9 ‰ for vapour and -21.4 ‰ for ice) and a much higher *d*-excess (13 ‰ for vapour and 88 ‰ for ice). The corresponding S_i based on Eq. (B.24) and (B.25) is found to be approximately 2 (though this value was not assessed for the conducted experiment in *Jouzel and Merlivat*, 1984). The experiment well verified the existence of a kinetic effect during vapour deposition.

Vapour deposition in a cloud

In a cloud, the growth of ice crystals by vapour deposition is governed by a general equation (*Pruppacher and Klett*, 1980; *Rogers and Yau*, 1996):

$$\frac{dm}{dt} = 4\pi CDf(e_v - e_i), \tag{B.26}$$

$$\frac{dm'}{dt} = 4\pi CD'f'(e'_v - e'_i), \tag{B.27}$$

where $\frac{dm}{dt}$ is the change of mass per unit of time, C the crystal capacitance depending only on the the crystal geometry, and f an experimentally determined ventilation coefficient that takes into account the effect of ventilation (when the crystal has grown to a size at which it has an appreciable fall velocity).

Analogous to Eq. (B.22), the isotope ratio of the formed ice is directly related to the ratio of the mass changes through:

$$R_s = \frac{\frac{dm'}{dt}}{\frac{dm}{dt}} = \frac{D'f'(e_v R_v - e_i R_s/\alpha_{sv})}{Df(e_v - e_i)}. \tag{B.28}$$

And the kinetic fractionation factor in this case becomes:

$$\alpha_k = \frac{S_i}{\alpha_{sv}\frac{Df}{D'f'}(S_i-1)+1}, \tag{B.29}$$

where the $\frac{f}{f'}$ ratio is very near to 1 and can be neglected as a reasonable first approach.

From thermodynamical considerations (*Pruppacher and Klett*, 1980), S_i can be related to S, the saturation ratio with respect to ice at air temperature (note that the ice temperature is raised above that of the ambient temperature because of the latent heat released from deposition), through a coefficient A (which is depending on the air temperature and pressure):

$$A = \frac{e_v - e_a}{e_v - e_i} = \frac{1-\frac{1}{S}}{1-\frac{1}{S_i}}, \tag{B.30}$$

where e_a is saturation vapour pressure over ice at air temperature.

Since at the same temperature the saturation vapour pressure over water is greater than over ice, in a mixed cloud, the ice crystal would be formed under supersaturated conditions and it would grow at the expense of liquid water droplets (known as *Bergeron-Findeisen effect*). In a mixed cloud, the saturation over liquid water gives the maximum saturation ratio, and it corresponds to increasing values of S_i from 1 (at 0 °C) to 1.61 (at −50 °C).

Evaporation of an isolated water body

In above I have reviewed the kinetic effect that occurs under supersaturated conditions during ice formation. The kinetic effect also occurs during evaporation when the environment is undersaturated. The classical Rayleigh evaporation model usually considers a saturation case where only equilibrium fractionation occurs. Here, we consider an undersaturation case where both equilibrium and kinetic fractionation are taken into account.

We consider an isolated water body of confined volume (such as water in a beaker) that is evaporating in a stable environment with a constant temperature (e.g. 20 °C) and a constant relative humidity, h (e.g. 75 %). Following the same reasoning as that followed for the vapour deposition on a cold plane surface, we have the evaporating fluxes from the water surface entering the ambient air as:

$$E \propto D(e_l - e_v), \tag{B.31}$$

$$E' \propto D'(e'_l - e'_v), \tag{B.32}$$

where e_l is the saturation vapour pressure over liquid water. The relationship between the saturation vapour pressure and the isotope ratio of the liquid is written as:

$$R_a = \frac{R_l}{\alpha_{lv}} = \frac{e'_l}{e_l}, \tag{B.33}$$

where R_l is the isotope ratio of the remaining liquid, and α_{lv} ($\alpha_{lv} > 1$) is the equilibrium fractionation factor.

Using the same approach as in Eq. (B.22), we obtain the δ_v value of the formed vapour as:

$$1 + \delta_v = \frac{1}{\alpha_k \alpha_{lv}}(1 + \delta_l), \tag{B.34}$$

where

$$\alpha_k = \frac{D}{D'}(1 - h) + h, \quad \text{with} \quad h = \frac{e_v}{e_l}. \tag{B.35}$$

α_k is greater than the unity since $\frac{D}{D'}$ is greater than the unity and h is lower than the unity.

B.2 Evaporation in a fixed atmosphere and Craig–Gordon model

The classical Rayleigh model has described the evaporation process in an ideal situation where no interaction is considered between the evaporating water and the ambient atmosphere. Such situations can occur in laboratories. One example is the evaporation in a completely dry atmosphere (e.g. in carrier gases such as dry air, nitrogen or helium). In nature, however, evaporation normally occurs in an ambient atmosphere of certain humidity and isotope composition;

the influence of the ambient atmosphere on the evaporating process must be considered. *Craig et al.* (1963) observed through their experiments that an isolated body of water in contact with an ambient atmosphere comes to an isotopic stationary state long before the total mass of liquid has evaporated away. This observation can not be explained by the classical Rayleigh model, where no steady-state is expected and the evaporating water would continue to enrich in heavy isotopes and reach rather extreme values (as shown for the open system in Fig. 2.2a). *Craig et al.* (1963) hence concluded that the exchange with ambient atmospheric water vapour plays an important role in limiting the enrichment of heavy isotopes in the evaporating water.

In addition, in their experiment with a dry atmosphere (using dry nitrogen as the carrier gas), *Craig et al.* (1963) found that the observed fractionation factors differ from the equilibrium fractionation factors used in the classical Rayleigh model. They observed a δD–δ^{18}O slope of about 5.5, instead of 7.7 as expected from the equilibrium fractionation. Similar slopes (mostly between 4 and 6) were also observed in the other evaporation experiments in an open air (*Craig et al.*, 1963) and the evaporation of natural water bodies (*Craig*, 1957a, 1961). All these pieces of evidence suggested the existence of a kinetic effect during the removal of vapour in undersaturated conditions.

With the above-mentioned isotope effects, namely the exchange with the ambient atmospheric water vapour and the kinetic effect, *Craig and Gordon* (1965) suggested a laminar layer model (hereafter the *C–G model*) as a frame to quantitatively describe the isotope fractionation during evaporation in an atmosphere of fixed humidity and isotope composition (also called "free atmosphere").

B.2.1 For an isolated water body

We first discuss a simple case of an isolated water body evaporating into a "free atmosphere". As is schematically shown in Fig. B.2, the C–G model considers three discrete layers:

(1) a liquid-vapour interface where the air is saturated (i.e. $h_V = h_S = 1$ and equilibrium fractionation exists (i.e. $R_V = \alpha^* R_S$, here α^* is the equilibrium fractionation factor; and $R_S = R_L$ at the isotopic steady state);

(2) a laminar layer where molecular diffusion dominates; and

(3) a turbulent section where turbulent or eddy diffusion dominates, assuming no isotopic fractionation.

Above the turbulent section is the "free atmosphere" where the humidity and the isotope composition are constant and unaffected by the evaporation process.

The C–G model follows a vertical flux of isotopic water molecules through the discrete liquid and atmospheric layers into the fixed "free atmosphere". The flux through each layer is modelled approximately linearly proportional to the concentration difference between the adjacent layers and inversely proportional to the transport resistance (analogous to *Ohm's law*). The overall flux between the water surface and the bottom of the "free atmosphere" can be described as:

$$E = \frac{h_V - h}{\rho} = \frac{1-h}{\rho}, \quad \text{with} \quad \rho = \rho_M + \rho_T, \tag{B.36}$$

$$E' = \frac{h_V R_V - h R_A}{\rho'} = \frac{\alpha^* R_L - h R_A}{\rho'}, \quad \text{with} \quad \rho' = \rho'_M + \rho'_T, \tag{B.37}$$

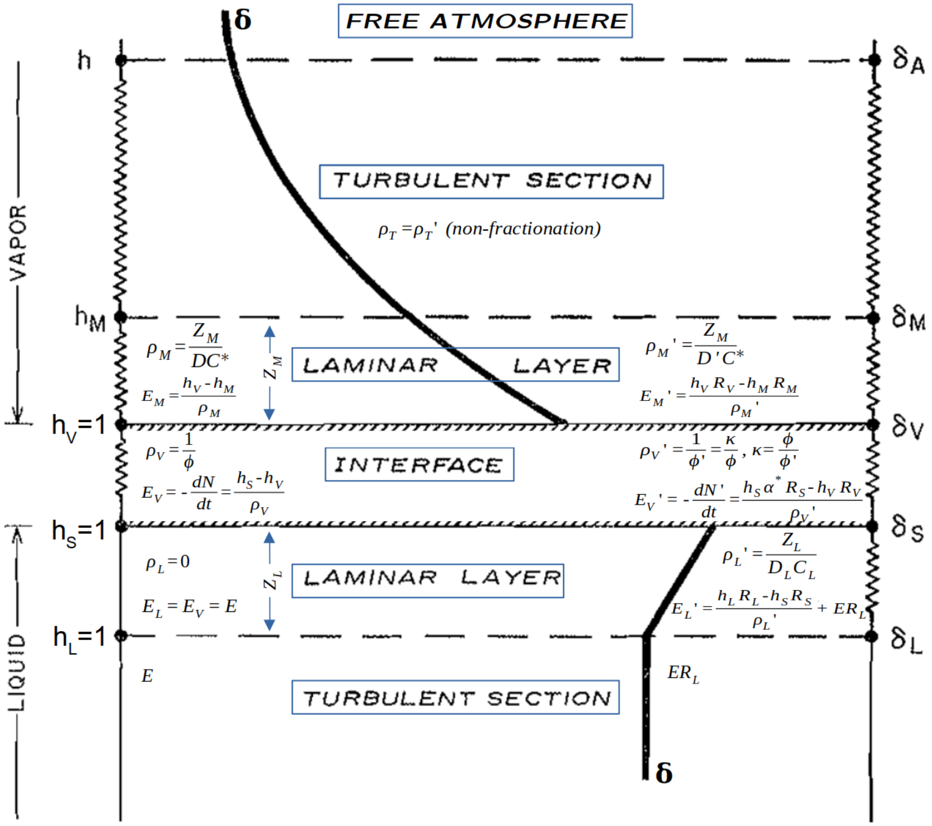

Figure B.2: Schematic presentation of the Craig-Gordon evaporation model for an isolated water body. Adapted from Craig and Gordon (1965).

where h is the relative humidity normalised to the specific humidity of the saturated air at the liquid-vapour interface, and ρ the total transport resistance. It is assumed here $\delta_S = \delta_L$.

The isotope ratio of the evaporation flux can be written as:

$$R_E = \frac{E'}{E} = \frac{\alpha^* R_L - hR_A}{(1-h)\frac{\rho'}{\rho}}. \tag{B.38}$$

Converting to the δ notation, the above equation becomes:

$$\delta_E = \frac{\alpha^* \delta_L - h\delta_A - \varepsilon^* - \Delta\varepsilon}{(1-h) + \Delta\varepsilon}, \tag{B.39}$$

with

$$\varepsilon^* = 1 - \alpha^*, \tag{B.40}$$

$$\Delta\varepsilon = E(\rho' - \rho) = (1-h)(\frac{\rho'}{\rho} - 1), \tag{B.41}$$

where ε^* is the isotopic enrichment due to equilibrium fractionation, $\Delta\varepsilon$ the isotopic enrichment due to kinetic fractionation.[1] It is sometimes convenient to define a total effective enrichment as:

$$\varepsilon = \varepsilon^* + \Delta\varepsilon. \tag{B.42}$$

Note that the absolute numbers (e.g. $h = 0.75$, $\Delta\varepsilon = 0.005$) should be used in the calculation using Eq. (B.39).

The C–G evaporation model for an isolated water body can also be written in the form of Rayleigh model as Eq. (B.3), following the two mathematical approaches for an open system in Sect. B.1.1. In this case the instantaneous fractionation factor will be:

$$\alpha = \frac{R_E}{R_L} = \frac{\alpha^* - h\frac{R_A}{R_L}}{(1-h)\frac{\rho'}{\rho}} = \frac{\alpha^* - h\frac{1+\delta_A}{1+\delta_L}}{(1-h)+\Delta\varepsilon}. \tag{B.43}$$

It can be seen that the instantaneous fractionation factor changes as δ_L evolves during the evaporation process. When the fractionation factor becomes unity, the evaporating water reaches isotopic steady state, i.e. $\delta_E = \delta_L$ thus $\frac{dR}{dN} = 0$ (see Eq. B.2 or B.4). This gives the steady-state isotope composition of an isolated water body as:

$$\delta_E^s = \delta_L^s = \frac{h\delta_A + \varepsilon}{h - \varepsilon} \approx \delta_A + \frac{\varepsilon}{h}. \tag{B.44}$$

In the steady state, E' and E are the same in all horizontal sections, and the isotopic composition of the vapour (δ_z) at any height (z) is fixed by the value of h at the same height (h_z). Thus from (B.44), we have:

$$\delta_z \approx \delta_L^s - \frac{\varepsilon_z}{h_z}. \tag{B.45}$$

Since $\Delta\varepsilon = E(\rho' - \rho)$ (Eq. B.41), ε will be a function of z until reaching a height above which the transport resistances are the same (i.e. $\rho' - \rho = constant$). This height is likely reached just above the laminar atmospheric layer, assuming the turbulent resistances to be the same (Fig. B.2). It is worth to note that, once it is determined at which height $\Delta\varepsilon$ becomes constant, then any values of δ_z and h_z measured at any level above this height can be used in Eq. (B.44) to calculate the values of $\Delta\varepsilon$ or δ_E^s, without having to measure δ_A and h of the "free atmosphere". This is of practical importance for in-situ sampling over the oceans.

The kinetic fractionation effect

From its introduction, a major issue in the C–G model has been how to determine accurately the kinetic, diffusion-controlled isotope effect (the fractionation enrichment, $\Delta\varepsilon$, defined by Eq. B.41) associated with the transport resistance of water molecules under various conditions. Recalling the assumption that no fractionation occurs in the turbulent section (i.e. $\rho_T = \rho_T'$), the term containing transport resistance in Eq. (B.41) can be written as:

$$\frac{\rho' - \rho}{\rho} = \frac{(\rho_M' - \rho_M) + (\rho_T' - \rho_T)}{\rho} = \frac{\rho_M' - \rho_M}{\rho} = \frac{\rho_M}{\rho}\left(\frac{\rho_M'}{\rho_M} - 1\right). \tag{B.46}$$

The transport resistance in the laminar layer, ρ_M, is largely proportional to D^{-n}, where D is the water molecular diffusivity in the air. Thus we can express $\Delta\varepsilon$ as:

$$\Delta\varepsilon = (1-h)\frac{\rho_M}{\rho}\left(\frac{\rho_M'}{\rho_M} - 1\right) = (1-h)\theta\left(\left(\frac{D}{D'}\right)^n - 1\right) \approx (1-h)\theta n\left(\frac{D}{D'} - 1\right), \tag{B.47}$$

---

[1] The epsilon terms are here defined such that they are always positive. Note the sign difference between these epsilon terms and the epsilon terms defined in Sect. 2.2.1 and B.1.1.

where,

$$\theta = \frac{\rho_M}{\rho} = \frac{1-h_M}{1-h}. \tag{B.48}$$

The weighting term θ is usually close to unity, i.e. molecular diffusion usually constitutes a main part of the transport resistance. However, for water bodies whose strong evaporation fluxes perturb the ambient moisture significantly, θ has been shown to have a lower value (*Gat*, 1996). For example, θ has a value of 0.88 in the North American Great Lakes (*Gat et al.*, 1994) and a value of close to 0.5 in the eastern Mediterranean Sea (*Gat et al.*, 1996).

The ratio of the water molecular diffusivities in the air has been experimentally determined by *Merlivat* (1978) to be $D_{HD^{16}O}/D_{H_2^{16}O} = 0.9755 \pm 0.0009$ and $D_{H_2^{18}O}/D_{H_2^{16}O} = 0.9723 \pm 0.0007$. Note that these values differ from the estimated values by *Craig and Gordon* (1965) based on the kinetic theory of gases.[2] *Craig and Gordon* (1965) found that their calculated diffusivities cannot explain the observed deuterium fractionation; in order to explain their observations, they had to assume a difference between the condensation coefficients of $H_2^{18}O$ and $HD^{16}O$. However, the experiments from *Merlivat* (1978) indicated that the condensation coefficients are identical for the isotopic molecules. It turns out that when following the values determined by *Merlivat* (1978), which show a larger deuterium isotope effect than given by the kinetic theory of gases, the C–G model comes to agree with the observations (*Gat*, 2008). It appears that the relative mass difference between the isotopologues alone cannot account for the observed diffusivities; a possible reason is that the displacement of the centre of gravity (*Merlivat*, 1978) and/or some hydrogen bonding in the gas phase (*Gat*, 2008) play a role here.[3]

The tunable exponent n varies from 0 to 1, and controls the ratio of diffusive transport over turbulent transport of water molecules (*Pfahl and Wernli*, 2009). For example, when $n = 0$, the tranport is solely turbulent, thus kinetic fractionation does not exist; when $n = 1$, the transport is purely diffusive.[4] For an open water body under natural conditions, $n = 0.5$

---

[2] The molecular diffusion coefficient can be expressed within the framework of the simple kinetic theory of gases as $D = \overline{v}\overline{\lambda}/3$, where $\overline{v}$ and $\overline{\lambda}$ are the mean velocity and mean free-path of the gas molecules, respectively (*Horita et al.*, 2008). Also according to the kinetic theory of gases, all molecules in a gas (mixture) have equal temperature and thus equal kinetic energy $\frac{1}{2}M\overline{v}^2$, where M is the molecular mass. This results in the proportionality between the average molecular velocity and $M^{-1/2}$ (Graham's law). In the case of diffusion involving the movement of two gases, i.e. the diffusion of one gas within the other medium gas, M needs to be replaced by the reduced mass $\mu = \frac{M_1 M_2}{M_1+M_2}$. In the end, the ratio of water molecular diffusivities in the air can be calculated according to (*Chapman*, 1970):

$$\frac{D}{D'} = \left(\frac{\Gamma' + \Gamma_a}{\Gamma + \Gamma_a}\right)^2 \left(\frac{M'(M+M_a)}{M(M'+M_a)}\right)^{\frac{1}{2}},$$

where M, M', and M_a are the molecular mass of $H_2^{16}O$, of $H_2^{18}O$ (or $HD^{16}O$), and of air, respectively; Γ, Γ', and Γ_a are the collision diameter of $H_2^{16}O$, of $H_2^{18}O$ (or $HD^{16}O$), and of air, respectively. Assuming $\Gamma = \Gamma'$, *Craig and Gordon* (1965) obtained: $D_{HD^{16}O}/D_{H_2^{16}O} = 0.9836$ and $D_{H_2^{18}O}/D_{H_2^{16}O} = 0.9687$.

[3] An alternative explanation is proposed by *Cappa et al.* (2003). Instead of considering the difference of collision diameters between the isotopic water molecules as suggested by *Merlivat* (1978), *Cappa et al.* (2003) argued that the mismatch between the measurement from *Merlivat* (1978) and the prediction from the kinetic theory of gases results from neglecting the surface cooling during the evaporation. For example, they showed that a surface cooling of 4.1 ℃ explains the measurements in *Merlivat* (1978) without invoking different collision diameters. Such surface cooling of several degrees has been observed under laboratory conditions (e.g. *Fang and Ward*, 1999; *Ward and Stanga*, 2001). In the ocean, however, cooling usually is not that large owing to more dynamic conditions; values of up to 0.6 ℃ have been observed (*Wick et al.*, 1996). Based on their measurements, *Cappa et al.* (2003) suggested to use the diffusivities predicted by the kinetic theory of gases.

[4] In this sense, n is closely associated to θ. When $n \to 0$, $\theta \to 0$; and when $n \to 1$, $\theta \to 1$.

seems appropriate (*Gat*, 1996). In the case of evaporation of water through a stagnant air layer, such as from the soils (*Barnes and Allison*, 1988) or leaves (*Allison et al.*, 1985), $n \approx 1$ fits the data well. In the case of evaporation of a falling raindrop, $n = 0.58$ is found to be appropriate (*Stewart*, 1975).

B.2.2 For a water body in an open system

The natural water bodies are normally not isolated. We now consider an evaporating water body in an open system, using the same C–G model as shown in Fig. B.2 but adding a liquid input, I, into the water body. We only discuss the case where the mass steady state, $E = I$, has been attained. In this case, the transient isotopic equation is:

$$N_L \frac{\delta_L}{dt} = I\delta_I - E\delta_E = E(\delta_I - \delta_E), \tag{B.49}$$

where N_L is the mass of water, and δ_E is given by Eq. (B.39). The isotopic steady state simply requires $\delta_E^s = \delta_I$. This gives the isotope composition of the evaporating liquid (considering $\alpha^* \approx 1$ and $\Delta\varepsilon \ll 1-h$) as:

$$\delta_L^s = \frac{1}{\alpha^*}((1-h+\Delta\varepsilon)\delta_I + h\delta_A + \varepsilon) \approx (1-h)\delta_I + h\delta_A + \varepsilon. \tag{B.50}$$

It can be shown that the open system model conforming to Eq. (B.50) explains the δD–δ^{18}O slope ranging from 4 to 6 (i.e. the "evaporation line") observed for the evaporating water bodies in nature. In a catchment area, precipitation is the source of liquid input, thus one can assume the atmospheric vapour is in isotopic equilibrium with the liquid input of the area. Then we have:

$$R_A = \alpha^* R_I, \tag{B.51}$$

$$i.e. \quad \delta_A = \alpha^* \delta_I - \varepsilon^*. \tag{B.52}$$

Inserting the above equation into Eq. (B.50), we have approximately:

$$\delta_L^s - \delta_I \approx (1-h)\varepsilon^* + \Delta\varepsilon. \tag{B.53}$$

The δD–δ^{18}O slope is simply the ratio of Eq. (B.53) for HD^{16}O and H$_2^{18}$O. *Craig and Gordon* (1965) has taken $\varepsilon^* = 69$ and 9 ‰ (at 25 °C), and $\Delta\varepsilon = 19$ and 5 ‰ (mean values of the experiments by *Craig et al.*, 1963), for HD^{16}O and H$_2^{18}$O respectively. The calculated δD–δ^{18}O slope varies from 6.3 to 3.8 over the humidity range from 0 to 100 %. At humidities of 75 and 50 %, the slopes are 5.0 and 5.6 respectively, corresponding to the observed values of most of the highly evaporated natural water bodies.

B.2.3 For the ocean-atmosphere system

The ocean-atmosphere system in nature is analogous to the open system with the input liquid being the precipitation. However, when it comes to considering the ocean, there is no independent "free atmosphere"; the atmospheric properties are adjusted to a self-determined, more-or-less steady state fixed by the cyclical return of precipitation and by the mixing in the atmosphere.

The isotopic steady state over the ocean

A simple case can be considering a marine region with a rather uniform descending air (e.g. downward branch of the Hadley cell) that has an isotope composition of δ_A and humidity of h. Within the region, the horizontal gradients are negligible. In this case, this general descent of drier air is treated as the equivalent of a "free atmosphere". The formulation of the steady-state isotope composition of the evaporating liquid is same as Eq. (B.50), with $\delta_I = \delta_P$.

The single-stage precipitation model

We continue to assume a homogeneous vapour over the ocean. However, we now assume that the upward flux of moisture in the precipitation sites is very large compared to the mean precipitation rate, i.e. only a small part of the moisture carried up is precipitated, and the rest is cycled by mixing (about 1/3 precipitated and 2/3 cycled as indicated in Fig. B.3). In such a case of single-stage precipitation, the isotope composition of the precipitation is supposed to be in equilibrium with that of the atmospheric vapour, i.e. $R_A = \alpha^* R_P$, which in δ notion can be written as:

$$\delta_A = \alpha_P^* \delta_P - \varepsilon_P^*. \tag{B.54}$$

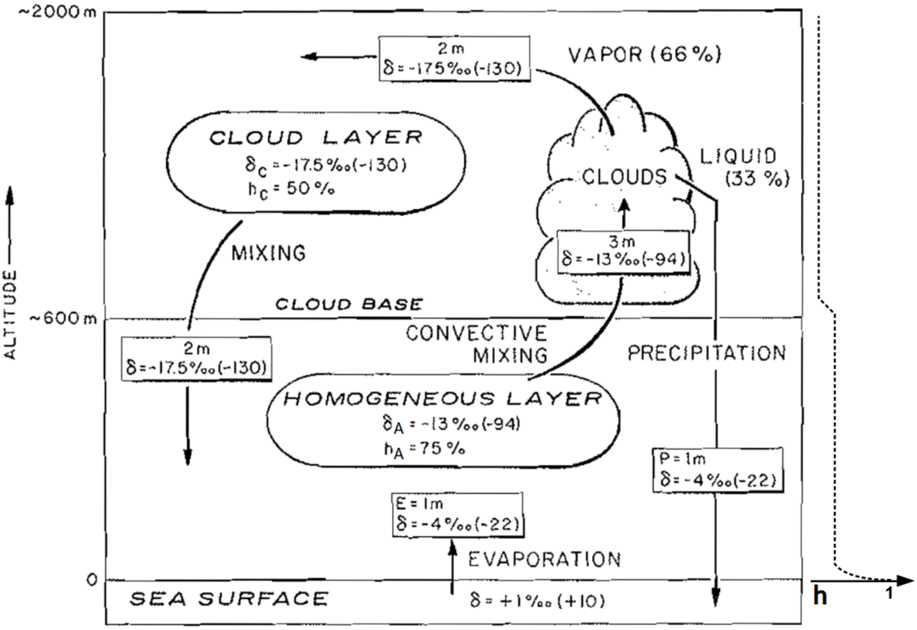

Figure B.3: Schematic presentation of the ocean-atmosphere isotope model by Craig and Gordon (1965). The model consists of two well-mixed layers (a lower "homogeneous layer" and above a "cloud layer") of essentially uniform but different moisture content. The water transport is indicated with arrows and the amount shown in units of metre/year of liquid water. The relative humidity is normalised to sea surface temperature. The isotope compositions are given in δ values: first $\delta^{18}O$ and in parenthesis δD. The d-excess value is 10 ‰ for all components except the sea surface water (2 ‰). The model follows three assumptions: (1) mass balance within the closed system (e.g. $E = P$, $\delta_A = \frac{1}{3}\delta_E + \frac{2}{3}\delta_C$); (2) steady-state correlation between isotope composition and relative humidity given as: $h_A(\delta_P - \delta_A) = h_C(\delta_P - \delta_C)$; (3) isotopic equilibrium between precipitation and homogeneous water vapour, i.e. $(\delta_E =)\delta_P = \delta_A/\alpha$. Figure adapted from Craig and Gordon (1965).

We can now characterise the steady-state relationships of all components of interest, namely δ_L^s, δ_P $(= \delta_E^s)$, δ_A, and δ_A^* the equilibrium vapour of surface water (i.e. $\delta_A^* = \alpha^* \delta_P - \varepsilon^*$), in the δD–δ^{18}O diagram. These relationships can all be obtained from Eq. (B.39) or (B.50) after applying the above precipitation restriction (i.e. Eq. B.54) and the steady state requirement $\delta_E^s = \delta_P$. The resulting relationships are:

$$\delta_L^s - \delta_P \approx (1-h)\varepsilon^* + \Delta\varepsilon, \tag{B.55}$$

$$\delta_A^* - \delta_A \approx (1-h)\varepsilon_P^* + \Delta\varepsilon, \tag{B.56}$$

$$\delta_L^s - \delta_A^* \approx \varepsilon^*, \tag{B.57}$$

$$\delta_P - \delta_A \approx \varepsilon_P^*, \tag{B.58}$$

$$\delta_L^s - \delta_A \approx (2-h)\varepsilon^* + \Delta\varepsilon, \tag{B.59}$$

$$\delta_P - \delta_A^* \approx h\varepsilon^* - \Delta\varepsilon. \tag{B.60}$$

The δD–δ^{18}O slopes are again simply the ratios of the left hand sides of the above equations for HD^{16}O and H$_2^{18}$O. The δD–δ^{18}O slope of $\delta_L^s - \delta_P$ is unsurprisingly the same as in the case of the evaporation of a water body in an open system (Eq. B.53); this slope is about 5.5. The slopes of $\delta_L^s - \delta_A^*$ and $\delta_P - \delta_A$ are fixed by the ratio of ε^* only, and will be about 8.0, the slope of the global meteoric water line (GMWL). The slope of $\delta_E^s - \delta_A^*$ (identical to $\delta_P - \delta_A^*$) indicates that, under normal situations, the evaporating vapour will be more enriched in heavy isotopes than the equilibrium vapour. These relationships between the different components are sketched in Fig. B.4.

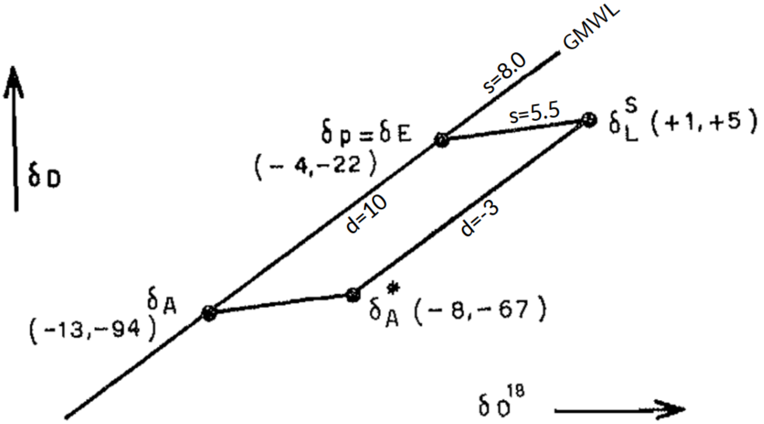

Figure B.4: Schematic presentation of the isotopic relationships between the different components in the ocean-atmosphere isotope model by Craig and Gordon (1965). The approximate isotope compositions are shown in parenthesis (in ‰): first δ^{18}O and then δD. Adapted from Craig and Gordon (1965).

The C–G model has several limitations. It does not account for the possible contribution from the evaporation of droplets and sea spray. It has also neglected the potential concentration gradient at the water surface. Finally, the restriction on the precipitation process may be oversimplified. Despite these limitations and its great simplicity, the C–G model successfully explains the observed evaporation in nature. It is often used to provide a knowledge of the isotope compositions of the (oceanic) evaporation flux, which are the initial conditions for the subsequent distillation calculations (e.g. *Ciais and Jouzel*, 1994). Since its introduction in 1965, the C–G model has been recognised as a cornerstone of the isotopic studies of the hydrological cycle.

B.2.4 Adaptations of the C–G model

The closure assumption

In the C–G model, the determination of the isotope composition of the evaporating flux, δ_E (Eq. B.39), requires a knowledge of the isotope composition of the water body (δ_L, the isotope composition of the ocean surface water is quite fixed (close to 0) and is assumed to be not affected by the evaporation due to its very large volume), the isotope composition and relativity of the "free atmosphere" (δ_A and h, can be measured at an elevation of about $10 \sim 20$ m in the marine region), the equilibrium fractionation effect (α^* or ε^*, a temperature-dependant variable that can be experimentally determined), and the kinetic fractionation effect ($\Delta\varepsilon$, can be observed or experimentally determined).

Since, as mentioned previously, there is no fixed and independent "free atmosphere" in the ocean-atmosphere system, the information of δ_A must be treated in detail for the region of interest. This approach is generally impractical considering the paucity of adequate observations on the ocean surface and the conceptual difficulty of separating the advective contribution from the evaporative contribution to δ_A (*Jouzel and Koster*, 1996). However, we can consider a simple case where a mass balance is assumed within a steady-state global-scale hydrological cycle. In this case, the evaporation is balanced with precipitation, and all the water in the atmosphere is in the end precipitated, therefore $\delta_E = \delta_A = \delta_P$ (*Merlivat and Jouzel*, 1979). Applying this *closure assumption* to Eq. (B.38) and (B.39), we have:

$$R_E^c = R_A^c = \frac{\alpha^* R_L}{h + (1-h)\frac{\rho'}{\rho}}, \tag{B.61}$$

$$i.e. \quad \delta_E^c = \delta_A^c = \frac{\alpha^* \delta_L - \varepsilon}{1 + \Delta\varepsilon}. \tag{B.62}$$

In this simplified way, δ_E can be calculated from h, SST, and the molecular diffusivities of water in air, without including the feedback from δ_A.

Although the closure assumption is initially formulated for the closed global-scale cycle, *Aemisegger and Sjolte* (2018) suggest that it can also be justified on a regional scale where the evaporation flux contributes substantially to the local humidity. Otherwise, despite its usefulness, the closure assumption is shown to be generally invalid on the local scale, leading to a systematic bias in the modelled isotope compositions (*Jouzel and Koster*, 1996). To overcome this bias, *Jouzel and Koster* (1996) recommend, instead of assuming $\delta_A = \delta_E$, taking δ_A from the general circulation model (GCM) estimates in grid boxes overlying ocean squares, as the GCM calculations are not limited by the closure assumption.

The importance of boundary layer mixing

The closure assumption proposed by *Merlivat and Jouzel* (1979) can be extended to include a vertical mixing from isotopically depleted air in the lower troposphere, as originally suggested in the C–G ocean-atmosphere model (Fig. B.3). In this way, the isotope ratio of near surface vapour (R_A) is simply a result of a two end-member mixing of the evaporation flux (R_E) and the lower tropospheric air (R_C; equivalent to the "free atmosphere" in C–G model). As proposed by *Benetti et al.* (2015), the isotope ratio of the near surface vapour can be calculated as:

$$R_A = (1-r)R_E + rR_C, \tag{B.63}$$

with $r = q_C/q_A$, the ratio of lower troposphere to near surface specific humidity, representing the contribution from lower tropospheric air. An estimate of q_C and R_C can be obtained from

GCMs. R_E is given by C–G model with Eq. (B.38). Thus we have:

$$R_A = \frac{(1-r)\alpha^* R_L + r(1-h)\frac{\rho'}{\rho}R_C}{(1-r)h + (1-h)\frac{\rho'}{\rho}}. \tag{B.64}$$

The case when $r = 0$ simply corresponds to the closure assumption by *Merlivat and Jouzel* (1979); the isotope ratio R_A in this case is already given in above by Eq. (B.61).

Substituting Eq. (B.61) to Eq. (B.64) and reorganizing, we can obtain:

$$R_A = (1-b)R_E^c + bR_C, \tag{B.65}$$

$$i.e. \quad \delta_A = (1-b)\delta_E^c + b\delta_C, \tag{B.66}$$

with $b = \frac{r(1-h)\frac{\rho'}{\rho}}{(1-r)h+(1-h)\frac{\rho'}{\rho}}$.

Using this mixing-approach, *Benetti et al.* (2015) have simulated the isotope composition of near-surface vapour over the subtropical North Atlantic Ocean. Comparing to their measurements, they have concluded that the inclusion of boundary mixing is critical for correctly reproducing the isotope compositions (especially for δD) of near-surface vapour.

B.3 Below-cloud evaporation and equilibration

A raindrop falling below the cloud base undergoes evaporation (when the ambient air is undersaturated) and equilibration (with ambient vapour when the ambient air is near to saturation) processes. That is to say, although the precipitation is formed by condensation processes within the cloud, the isotope composition of the sampled precipitation on the ground can be strongly modified by the post condensation processes.

B.3.1 Below-cloud evaporation

The evaporation process of a single raindrop can be essentially described by the C–G model for an isolated water body (see Sect. B.2). After all, a raindrop is simply an isolated water body that has a spherical shape and moves in a fixed atmosphere. Again, equilibrium fractionation is assumed at the liquid-atmosphere interface, and no isotope gradient exits within the liquid (despite the high evaporation rates of the drops). For a falling raindrop, the evaporation flux is proportional to the change of mass, which can be calculated as (*Stewart*, 1975):

$$\frac{dm}{dt} = 4\pi akD^n(\rho_\infty - \rho_a), \tag{B.67}$$

$$\frac{dm'}{dt} = 4\pi ak(D')^n(\rho'_\infty - \rho'_a), \tag{B.68}$$

where a is the raindrop radius; $k = F\left(\frac{aV}{2\pi}\right)^{\frac{1}{2}}$ is an empirical coefficient depending on the ventilation factor (F), the raindrop radius (a), and the fall velocity of the raindrop (V); ρ_∞ and ρ_a are the water vapour density of the ambient air and of the thin layer of saturation air at the raindrop surface, respectively. The quantities associated with isotopic water molecules are denoted with a prime symbol.

Analogous to Eq. (B.38), the isotope composition of the evaporation flux for a falling raindrop will be:

$$R_E = \frac{\frac{dm'}{dt}}{\frac{dm}{dt}} = \frac{(D')^n(\rho'_\infty - \rho'_a)}{D^n(\rho_\infty - \rho_a)} = \frac{hR_\infty - R_a}{\left(\frac{D}{D'}\right)^n (h-1)} = \frac{\alpha^* R_L - hR_\infty}{(1-h)\left(\frac{D}{D'}\right)^n}, \tag{B.69}$$

where

$$R_\infty = \frac{\rho'_\infty}{\rho_\infty}, \quad \alpha^* R_L = R_a = \frac{\rho'_a}{\rho_a}, \quad h = \frac{\rho_\infty}{\rho_a}, \tag{B.70}$$

with R_∞, R_a, and R_L being the isotope ratio of the ambient air, of the thin layer of saturation air at the raindrop surface, and of the raindrop itself, respectively.

With $\frac{dR_L}{dm} = \frac{d\left(\frac{m'}{m}\right)}{dm} = \frac{1}{m}\left(\frac{dm'}{dm} - \frac{m'}{m}\right) = \frac{1}{m}(R_E - R_L) = \frac{R_L}{m}(\alpha - 1)$, we can show again that the isotopic evolution of the raindrop can be essentially described by $R_L = R_0 f^{\alpha-1}$ (Eq. B.3), i.e. a Rayleigh-type distillation process. The only difference emerges in the fractionation factor, which is analogous to the case for an isolated water body (Sect. B.2.1), continuously evolving and is given as:

$$\alpha = \frac{R_E}{R_L} = \frac{\alpha^* - h\frac{R_\infty}{R_L}}{(1-h)\left(\frac{D}{D'}\right)^n}. \tag{B.71}$$

When the raindrop evaporates in a completely dry air, i.e. $h = 0$, the evaporation process is identical to the classical Rayleigh distillation with a constant fractionation factor $\alpha = \alpha^* \left(\frac{D'}{D}\right)^n$.

When the evaporating raindrop reaches isotopic steady state, i.e. $\frac{dR_L}{dm} = 0$, the fractionation factor becomes unity (see Eq. B.2). This gives the steady-state isotope composition of the raindrop as:

$$R_L^s = \frac{hR_\infty}{\alpha^* - (1-h)\left(\frac{D}{D'}^n\right)}, \tag{B.72}$$

$$i.e. \quad 1 + \delta_L^s = \frac{h(1+\delta_\infty)}{\alpha^* - (1-h)\left(\frac{D}{D'}^n\right)}. \tag{B.73}$$

B.3.2 Isotopic equilibration or exchange

A raindrop falling in a (near-)saturated atmosphere ($h = 100$ %, $\rho_a = \rho_\infty$) gradually attains isotopic equilibrium with the atmospheric vapour, i.e. $R_L \to R_L^s = \frac{R_\infty}{\alpha^*}$. It is apparent that, in a saturated atmosphere, the mass of the abundant water molecules would not change with time, i.e. $\frac{dm}{dt} = 0$ (Eq. B.67). In other words, the isotopic evolution of the raindrop is determined by the change of mass of the rare water molecules which is described by Eq. (B.68). Remembering $R_L = \frac{m'}{m}$, $R_\infty = \frac{\rho'_\infty}{\rho_\infty}$, $R_a = \frac{\rho'_a}{\rho_a}$, and applying the above conditions (i.e. $\rho_a = \rho_\infty$, $R_L^s = \frac{R_\infty}{\alpha^*}$), Eq. (B.68) can be written as:

$$\frac{dR_L}{dt} = \frac{1}{\tau}(R_L^s - R_L), \tag{B.74}$$

where

$$\tau = \frac{m}{4\pi ak(D')^n \rho_\infty \alpha^*} = \frac{mR_wT}{4\pi ak(D')^n P\alpha^*} \tag{B.75}$$

is the relaxation time. Integration of the above equation gives:

$$R_L = R_L^s + (R_0 - R_L^s)e^{-\frac{t}{\tau}}, \tag{B.76}$$

$$i.e. \quad \delta_L = \delta_L^s + (\delta_0 - \delta_L^s)e^{-\frac{t}{\tau}}. \tag{B.77}$$

Stewart (1975) obtained from their experiment that the relaxation time for a water drop in a vertical stream of near-saturated ($RH = 99.5$ %) N_2 is about 148 s. In comparison, the falling time of a raindrop (supposing the raindrop falling from 2 km above ground) can range from $\sim$ 230 (raindrop diameter of 4 mm) to $\sim$ 1200 s (raindrop diameter of 0.4 mm; *Rogers and Yau*, 1996). *Jouzel* (1986) also noted that the time taken for the falling water drops to equilibrate with the environment is usually comparable, and often shorter than, the time required to fall. This could explain why the isotope compositions of liquid precipitation are often at equilibrium with those of near-surface vapour.

Setting water drops to suspend in vertical streams of N_2, Ar, or He gas with relative humidities of around 0, 50, and 100 %, *Stewart* (1975) performed experiments to determine the effects of evaporation and isotopic exchange of the drops. They found that the observed isotopic enrichments of the water drops in a dry or unsaturated atmosphere or their equilibration in a saturated atmosphere are in agreement with the above model predictions, using equilibrium fractionation factor from *Majoube* (1971a), water molecular diffusivities from *Merlivat* (1970), and $n = 0.58$ from *Kinzer and Gunn* (1951).

B.4 Isotope-enabled general circulation models

In above, I have reviewed the classical Rayleigh distillation model, the C–G evaporation model, and the model describing below-cloud evaporation and equilibration. Essentially, the C–G evaporation model and the below-cloud evaporation model are also Rayleigh-type distillation models. All these models are often referred to as *simple isotope models*, and they model the isotope fractionation at each phase change within an isolated air mass or a simple box-budget system. As shown above, these simple models are extremely valuable for accounting for the underlying mechanisms, hence providing first-order descriptions of water isotope distributions. However, they are limited since (1) they often require appropriate initial conditions to be provided; (2) they require gross simplifications (e.g. cloud and other exchange processes); and most importantly, (3) they cannot account for dynamical transport and mixing of air masses in any detail (*Noone and Sturm*, 2010).

Overcoming these limitations requires more comprehensive and dynamical models. A natural approach is to incorporate the isotopic cycle into an atmospheric general circulation model (GCM) or a regional meteorological model. Since a water cycle already exists in these models, the incorporation of stable water isotopes is simply to introduce a parallel water cycle which does not affect other model components and is used as a purely diagnostic tool. In other words, all prognostic moisture fields, which are simulated by the model in terms of specific humidities, are duplicated twice, representing the specific humidities of $H_2^{18}O$ and $HD^{16}O$, respectively (*Pfahl et al.*, 2012). These additional moisture fields are affected by the same physical processes as the original humidity (e.g. they are transported by large scale winds and are involved in the formation of clouds and precipitation); they only behave differently during phase changes owing to isotopic fractionation.

The atmospheric water cycle in an isotope-enabled dynamical model can be described by the evaluation of the following tendency equations (*Noone and Sturm*, 2010):

$$\frac{\partial q}{\partial t} = -\mathbf{V}\cdot\nabla q + D\nabla_h^2 q + \frac{\partial}{\partial P}\left(\overline{\omega' q'}\right) + E - C + S, \tag{B.78}$$

$$\frac{\partial q_i}{\partial t} = -\mathbf{V}\cdot\nabla q_i + D\nabla_h^2 q_i + \frac{\partial}{\partial P}\left(\overline{\omega' q_i'}\right) + R_E E - R_C C + R_S S. \tag{B.79}$$

The first three terms on the right side represent large-scale advection ($-\mathbf{V}\cdot\nabla q$) which is resolved by the model, horizontal diffusion ($D\nabla_h^2 q$), and vertical transport due to small scale processes ($\frac{\partial}{\partial P}\left(\overline{\omega' q'}\right)$) which are not resolved but parametrised in models. The sum of these three terms captures the total transport and mixing of air masses; and it is the explicit evaluation of them which is a unique element of dynamical models. Beyond transport, the tendency depends on the sources (E; evaporation and evapo-transpiration at the surface and evaporation of falling hydrometeors) and sinks (C; loss of water via condensation). The additional term, S, accounts for other minor sources or sinks (*Noone and Sturm*, 2010). Note that the isotopic quantities are here denoted with subscript i. R_E, R_C, and R_S are the isotope ratios determined by the fractionation processes. It is apparent that the isotopic water content is conserved during transport and is only exposed to changes through the source terms where phase changes are involved. The isotopic fractionation during phase changes is implemented on the basis of simple isotope models. Commonly-used approaches among many isotope-enabled GCMs are summarised in Table B.1.

Table B.1: Summary of the commonly-used isotopic parametrisations in isotope-enabled GCMs.

	Source/Description
Equilibrium fractionation	*Majoube* (1971a,b)
Molecular diffusivity	*Merlivat* (1978), *Cappa et al.* (2003)
Open water evaporation	*Craig and Gordon* (1965), *Merlivat and Jouzel* (1979)
Raindrop evaporation	*Stewart* (1975)
Ice formation in mixed cloud	*Jouzel and Merlivat* (1984), *Ciais and Jouzel* (1994)
Sea water	constant (δ^{18}O = δD = 0)

An isotope-enabled GCM can be run "freely" or "nudged" to meteorological fields from reanalyses. For a free-running simulation, the model needs basically three pieces of information as a boundary condition: (1) the solar insolation at the top of the atmosphere, (2) the concentration of greenhouse gases, and (3) the sea surface temperatures over the ocean. Rather than allowing the atmosphere to run "freely", GCMs can also be "nudged" toward large-scale meteorological fields from reanalyses (e.g. *Risi et al.*, 2012a; *Yoshimura et al.*, 2008). Consequently, since the nudged simulations are equipped with much-accurate meteorological variables, the robustness of simulated isotopic variability on both daily and longer time scales also increases. The nudged simulations are useful when trying to reproduce observed inter-annual variability or a particular meteorological event (e.g. *Aemisegger et al.*, 2015; *Pfahl et al.*, 2012; *Yoshimura et al.*, 2010).

All isotope-enabled GCMs can be used to either reproduce some set of data or to test the importance of some specific physics or processes being modelled. The global scale isotope-enabled GCMs are especially useful in providing a climatological understanding of isotope distributions. Hypothesis testing via sensitivity tests using isotope-enabled GCMs can inform which types of mechanisms influence a given set of measurements (e.g. *Risi et al.*, 2012b; *Yoshimura et al.*, 2010).

While the advantages of comprehensive models are substantial, they are subject to a different set of limitations experienced by simpler models. (1) Being based on some underlying dynamical model, any biases in simulated meteorological variables (temperature, precipitation, boundary layer dynamics, etc.) are reflected in the simulated isotopic distribution. (2) Numerical inaccuracies in transport processes introduce artificial fractionation. As noted by *Noone and Sturm* (2010), water vapour abundance changes by at least four orders of magnitude in nature, plus three more orders of magnitude for deviations (i.e. δ values in ‰); an appropriate numerical scheme must be able to resolve this range. (3) The model resolution is limited in part because of computational demand. Because of the relatively coarse resolution, the isotope-enabled GCMs are often not able to match observed isotope distributions. This is of particular concern when the isotope composition depends on geographic structures (e.g. topography, vegetation classification, coastlines), which are not well captured by low-resolution global models. (4) Simulating isotopes within GCMs is a task limited by appropriate datasets for validation and testing. While evaporation from the oceans is one of the most important processes in the hydrological cycle, observations are sparse over the oceans. Besides, compared to the long-term and world-wide observations of precipitation isotopes, most of the observations of the vapour isotopes (particularly in the field) have expanded in scope only over the last decade or so (*Galewsky et al.*, 2016).

Some of the model limitations are already being addressed to some extent. For example, to counteract the computational burden of increasing spatial resolution, one possible option is to use regional circulation models (RCMs) for high-resolution isotope studies (e.g. *Aemisegger et al.*, 2015; *Pfahl et al.*, 2012; *Yoshimura et al.*, 2010). The advances in measurement techniques are continuously expanding the observational datasets, including in situ vapour measurement using low-cost commercial laser spectrometers (e.g. *Benetti et al.*, 2017; *Steen-Larsen et al.*, 2015, 2014a), nearly global satellite measurements of water vapour isotope composition (e.g. *Frankenberg et al.*, 2009; *Worden et al.*, 2006), and ground-based remote sensing data (e.g. *Rokotyan et al.*, 2014; *Schneider et al.*, 2012). The expanding set of observations allow more detailed testing of specific isotope physics within comprehensive models, and will likely facilitate model improvements.

Numerous isotope-enabled GCMs have been developed worldwide since the pioneering work by *Joussaume et al.* (1984). A brief overview of selected models is presented in Table B.2. More comprehensive reviews on isotope-enabled GCMs can be found in *Hoffmann et al.* (2000) (focusing on present-day climate and model developments from 1960s to 1990s), *Sturm and Knohl* (2010) (focusing on paleoclimate studies), *Noone and Sturm* (2010) (including mathematical treatments in the models), *Xi* (2014) (focusing on the key advances in model development and validation from 2000 to 2014), and *Galewsky et al.* (2016) (focusing on atmospheric water vapour). Efforts have also been made in comparing isotope-enabled GCM results across modelling groups, such as Stable Water Isotope Intercomparison Group, Phase 2 (SWING2, `http://www.giss.nasa.gov/projects/swing2`).

Table B.2: Selected isotope-enabled GCMs and their characteristics.

Model	Reference	Resolution[a]	Some key features
LMD	*Joussaume et al.* (1984)	$7.5^\circ \times 11.25^\circ$ (24×32), L11	Grid point; first isotope-enabled GCM
	Joussaume and Jouzel (1993)	$50^b \times 64$, L11	First forward modelling under paleoclimate conditions (LGM)
LMDZ4	*Risi et al.* (2010)	$2.5^\circ \times 3.75^\circ$, L19	Grid point; free-running or nudged to ECMWF
GISS II	*Jouzel et al.* (1987, 1991)	$8^\circ \times 10^\circ$, L9	Grid point
GISS ModelE	*Schmidt et al.* (2005)	$4^\circ \times 5^\circ$, L20/L23	Grid point
GISS ModelE-R	*Schmidt et al.* (2007)	$4^\circ \times 5^\circ$, L20	Spectral; free-running or nudged to NCEP; first coupled atmosphere-ocean model with water isotopes
ECHAM3	*Hoffmann et al.* (1998)	$2.8^\circ \times 2.8^\circ$ (T42) $5.6^\circ \times 5.6^\circ$ (T21)	Spectral; separate equilibration for convective and stratiform clouds; first model estimates of temporal temperature and amount effects
ECHAM4	*Werner et al.* (2001)	$3.75^\circ \times 3.75^\circ$ (T30), L19	Spectral
ECHAM5	*Werner et al.* (2011)	3.8°-$0.75^\circ \times 3.8^\circ$-$0.75^\circ$ (T31-T159), L19/L31	Spectral; high resolution
MUGCM	*Noone and Simmonds* (2002)	$3.25^\circ \times 5.625^\circ$ (54×64 or R21), L9	Spectral
GENESIS	*Mathieu et al.* (2002)	$\sim 3.75^\circ \times 3.75^\circ$ (T31), L18	Spectral
CLIMBER-2	*Roche et al.* (2004)	$10^\circ \times \sim 51^\circ$	First isotope-enabled intermediate-complexity climate model
REMO	*Sturm et al.* (2005)	$0.5^\circ \times 0.5^\circ$ ($\sim$ 55 km), L19	First isotope-enabled high-resolution regional model
CAM2	*Lee et al.* (2007)	$2.8^\circ \times 2.8^\circ$ (T42), L26	Spectral
GSM	*Yoshimura et al.* (2008)	T62, L28	Spectral
RSM	*Yoshimura et al.* (2010)	10 km, L28	Spectral; nudged to NCEP/DOE reanalysis 2
HadCM3	*Tindall et al.* (2009)	$2.5^\circ \times 3.75^\circ$, L19	Grid point
MIROC3.2	*Kurita et al.* (2011)	$1.1^\circ \times 1.1^\circ$ (T106), L40	Spectral; nudged to JCDAS
COSMO	*Pfahl et al.* (2012)	T159, L60	First implementation in non-hydrostatic forecasting model; regional
SPEEDY-IER	*Dee et al.* (2015)	T30	Fast physics GCM

[a] Horizontal resolution given as degrees, and/or number of grid points, in latitude × longitude; and/or given as spectral resolution denoted by triangular truncation of the harmonic series wave number. Vertical resolution given as the number of vertical levels.

[b] Regularly spaced in sine of latitude.

Appendix C

Isotope signatures of selected weather events

This appendix presents stable isotope signatures of selected weather systems that influence our study region (Fig. C.1), and meteorological and isotopic observations of several selected weather events observed at Bergen (Fig. C.2-C.12).

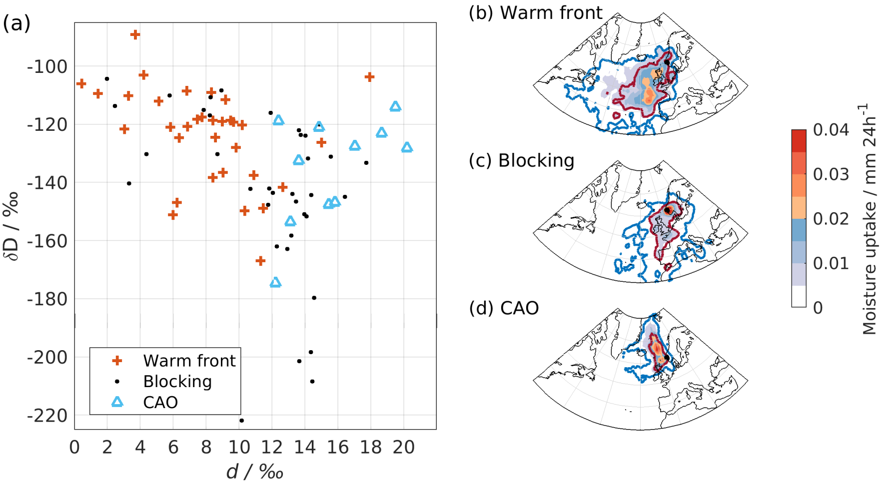

*Figure C.1: **(a)** Daily-average isotope signatures (δD vs d-excess) of surface vapour and **(b-d)** corresponding moisture origins for selected weather systems passing Bergen (black rectangle;* $59.9-60.9$ *°N,* $4.3-6.3$ *°E, including both land and ocean). Moisture uptake is diagnosed using WaterSip. The 50th and 80th percentiles of the mass contribution are shown in red and blue contours, respectively. Weather systems are selected based on the following criterion. Warm frontal system: humidity increase > 1.5 g kg^{-1} between 2 consecutive days and rain rate of the day > 0.3 mm h^{-1}. Cold air outbreak (CAO): humidity decrease > 1.5 g kg^{-1}, average wind direction of the day > 260 °, and average air temperature of the day < 10 °C. Blocking: average air pressure of the day > 1020 hPa, average rain rate of the day $<= 0.5$ mm h^{-1}, and the conditions lasting at least 5 days.*

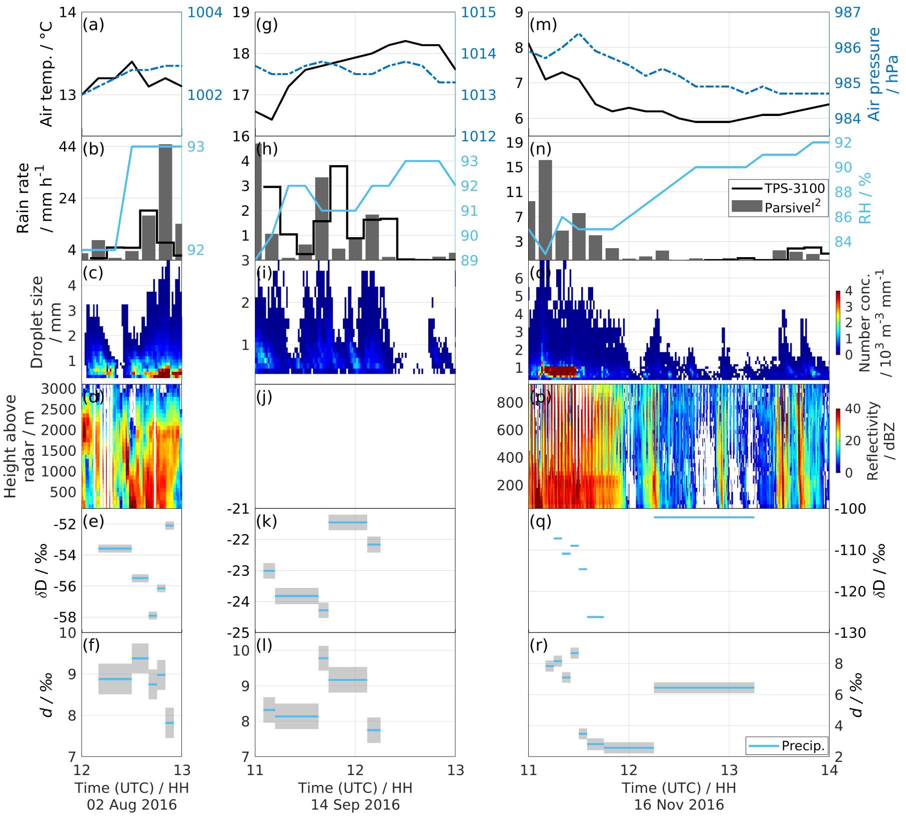

Figure C.2: Time series of observations on the rooftop (∼45 m a.s.l) during ***three shower events in Bergen between 02 August and 16 November 2016****.* ***(a, g, m)*** *Temperature (solid black line) and air pressure (broken blue line) from Automatic Weather Station (AWS 2700).* ***(b, h, n)*** *10 min averaged rain rate from Total Precipitation Sensor (black line) and Parsivel^2 (grey bar), and relative humidity from AWS (light blue line).* ***(c, i, o)*** *Number concentrations of droplet per droplet size from Parsivel^2.* ***(d, j, p)*** *Reflectivity from Micro Rain Radar (MRR-2). The data for* ***(j)*** *is missing.* ***(e, k, q)*** *δD of precipitation. The length of the bar indicates the period over which the precipitation samples were collected, and the width of grey shading indicates the measurement uncertainty (standard deviation). The averaged uncertainty is 0.26 ‰.* ***(f, l, r)*** *Same as in* ***(e, k, q)*** *but for d-excess. The averaged uncertainty is 0.36 ‰. Note the scale is different for each event.*

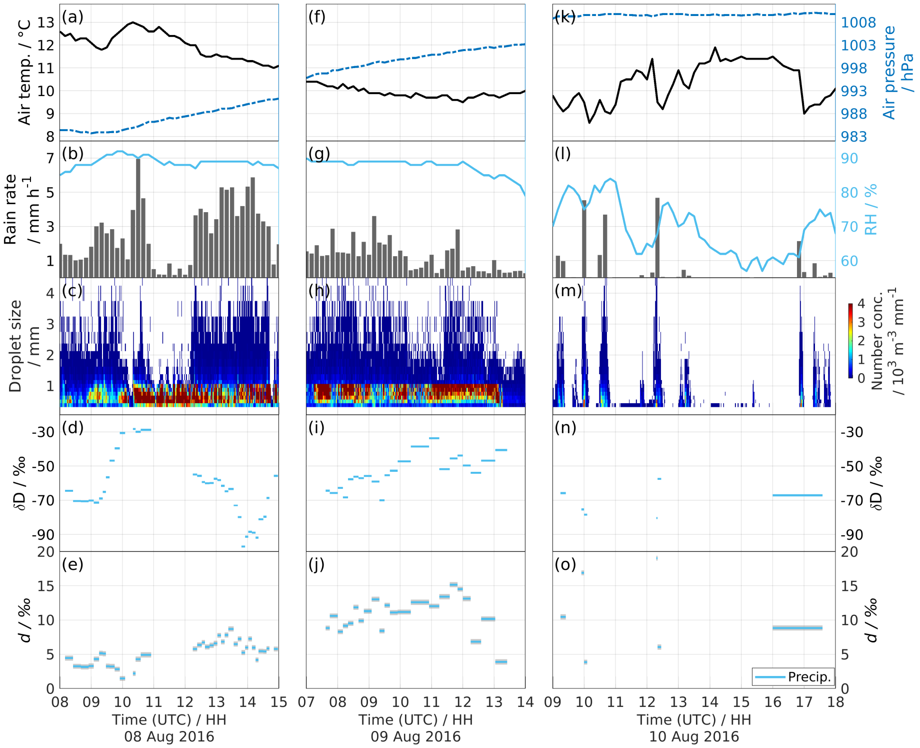

Figure C.3: Time series of observations on the rooftop (∼45 m a.s.l) during ***an occluded frontal system passing Bergen between 08 August and 09 August 2016****.* ***(a, f, k)*** *Temperature (solid black line) and air pressure (broken blue line) from Automatic Weather Station (AWS 2700).* ***(b, g, l)*** *10 min averaged rain rate from Parsivel^2 (grey bar), and relative humidity from AWS (light blue line).* ***(c, h, m)*** *Number concentrations of droplet per droplet size from Parsivel^2.* ***(d, i, n)*** *δD of precipitation. The length of the bar indicates the period over which the precipitation samples were collected, and the width of grey shading indicates the measurement uncertainty (standard deviation). The averaged uncertainty is 0.26 ‰ (invisible in this case).* ***(e, j, o)*** *Same as in* ***(d, i, n)*** *but for d-excess. The averaged uncertainty is 0.37 ‰.*

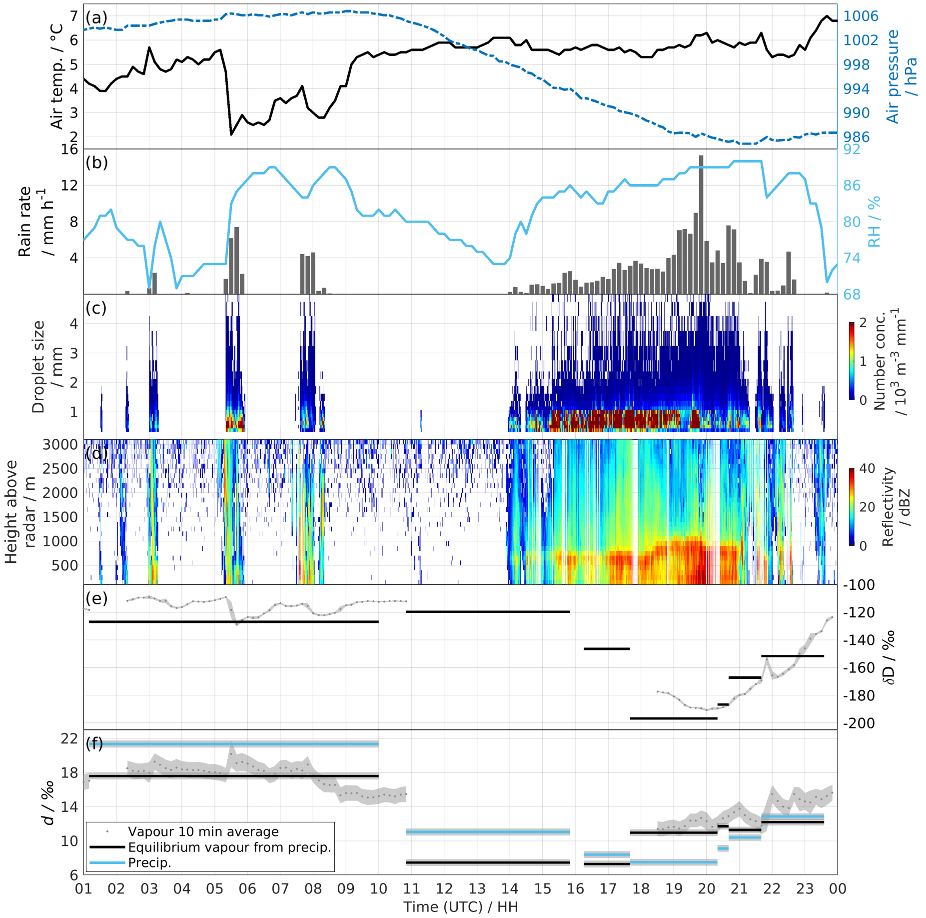

Figure C.4: Time series of observations on the rooftop (~45 m a.s.l) during ***a warm frontal system passing Bergen between 14 and 21 UTC 23 December 2016****.* ***(a)*** *Temperature (solid black line) and air pressure (broken blue line) from Automatic Weather Station (AWS 2700).* ***(b)*** *10 min averaged rain rate from Total Precipitation Sensor (grey bar), and relative humidity from AWS (light blue line).* ***(c)*** *Number concentrations of droplet per droplet size from Parsivel^2.* ***(d)*** *Reflectivity from Micro Rain Radar (MRR-2).* ***(e)*** *δD of 10 min averaged near-surface vapour (black dotted line) and of the equilibrium vapour from precipitation (black bars). The length of the bar indicates the period over which the precipitation samples were collected, and the width of grey shading indicates the measurement uncertainty (standard deviation). The averaged uncertainty is 1.06 and 0.24 ‰ (invisible in this case) for the vapour and the equilibrium vapour from precipitation, respectively.* ***(f)*** *Same as in* ***(e)*** *but for d-excess, including d-excess of the precipitation (light blue bars). The averaged uncertainty is 0.95, 0.40, and 0.40 ‰ for the vapour, the equilibrium vapour from precipitation, and the precipitation, respectively.*

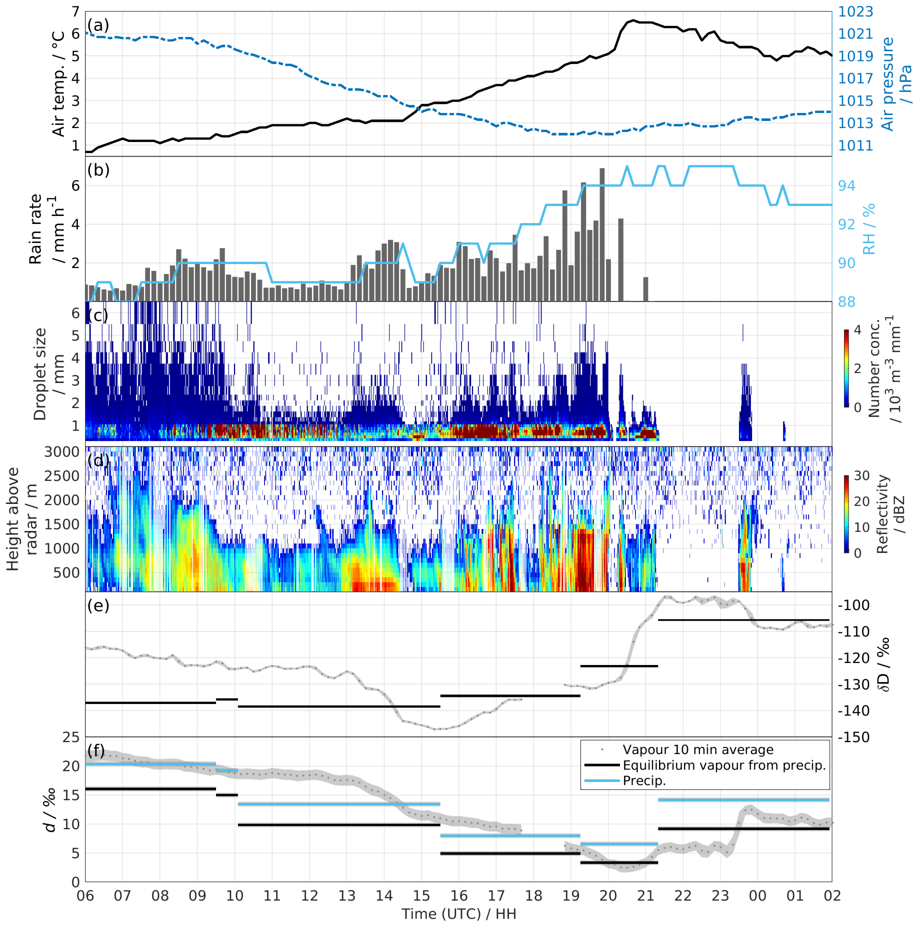

*Figure C.5: Time series of observations on the rooftop (∼45 m a.s.l) during **a warm frontal system passing Bergen on 06 January 2017**. **(a)** Temperature (solid black line) and air pressure (broken blue line) from Automatic Weather Station (AWS 2700). **(b)** 10 min averaged rain rate from Total Precipitation Sensor (grey bar), and relative humidity from AWS (light blue line). **(c)** Number concentrations of droplet per droplet size from Parsivel^2 (data partly missing). **(d)** Reflectivity from Micro Rain Radar (MRR-2). **(e)** δD of 10 min averaged near-surface vapour (black dotted line) and of the equilibrium vapour from precipitation (black bars). The length of the bar indicates the period over which the precipitation samples were collected, and the width of grey shading indicates the measurement uncertainty (standard deviation). The averaged uncertainty is 0.64 and 0.24 ‰ (invisible in this case) for the vapour and the equilibrium vapour from precipitation, respectively. **(f)** Same as in **(e)** but for d-excess, including d-excess of the precipitation (light blue bars). The averaged uncertainty is 0.95, 0.40, and 0.40 ‰ for the vapour, the equilibrium vapour from precipitation, and the precipitation, respectively.*

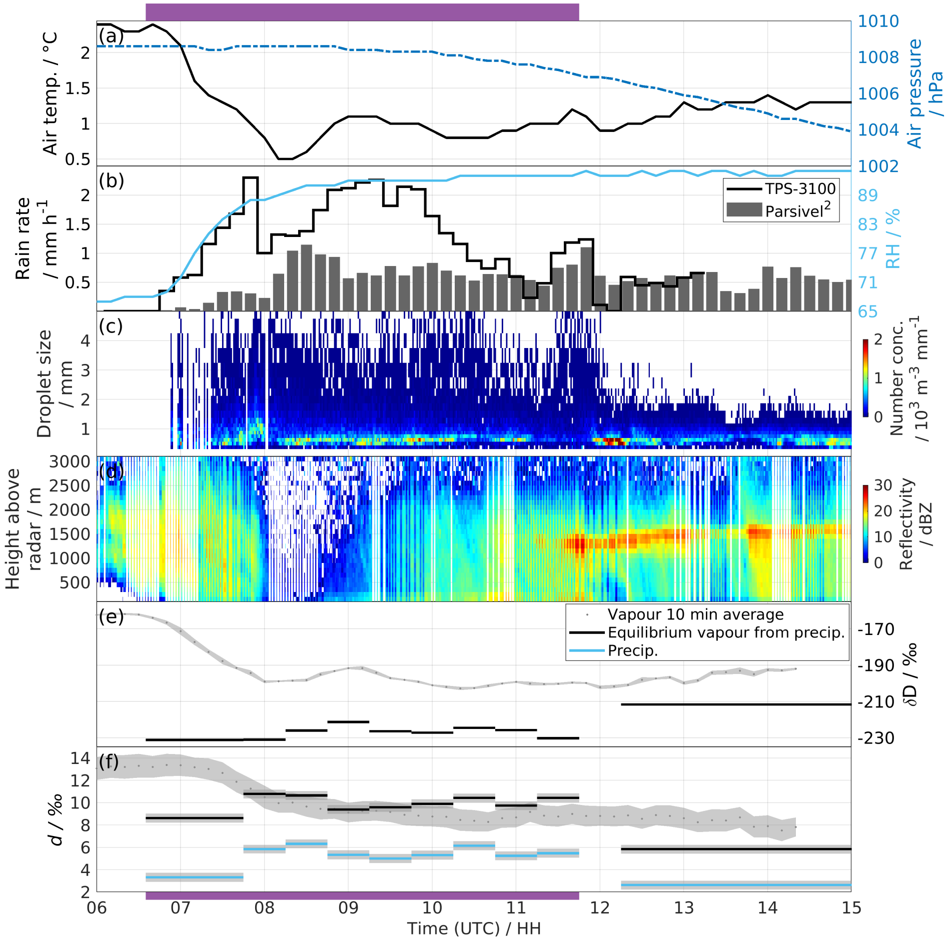

*Figure C.6: Time series of observations on the rooftop (∼45 m a.s.l) during **a snowfall-to-rainfall event in Bergen between 06 and 15 UTC 01 February 2017**. **(a)** Temperature (solid black line) and air pressure (broken blue line) from Automatic Weather Station (AWS 2700). **(b)** 10 min averaged rain rate from Total Precipitation Sensor (black line) and Parsivel^2 (grey bar), and relative humidity from AWS (light blue line). **(c)** Number concentrations of droplet per droplet size from Parsivel^2 (data partly missing). **(d)** Reflectivity from Micro Rain Radar (MRR-2). **(e)** δD of 10 min averaged near-surface vapour (black dotted line) and of the equilibrium vapour from precipitation (black bars). The length of the bar indicates the period over which the precipitation samples were collected, and the width of grey shading indicates the measurement uncertainty (standard deviation). The averaged uncertainty is 0.73 and 0.24 ‰ (invisible in this case) for the vapour and the equilibrium vapour from precipitation, respectively. **(f)** Same as in **(e)** but for d-excess, including d-excess of the precipitation (light blue bars). The averaged uncertainty is 0.96, 0.40, and 0.40 ‰ for the vapour, the equilibrium vapour from precipitation, and the precipitation, respectively. The color bar (purple) at the top and bottom of the figure indicates the snow period.*

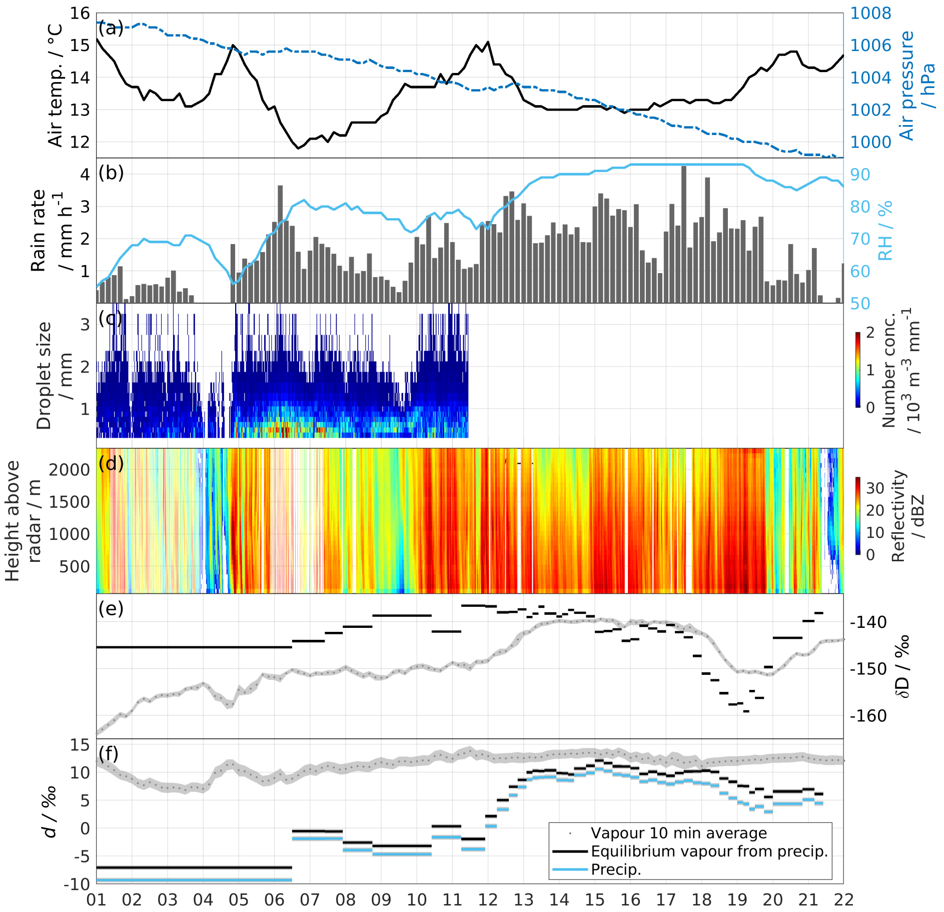

Figure C.7: Time series of observations on the rooftop (∼45 m a.s.l) during ***an occluded frontal system passing Bergen between 01 and 22 UTC 05 September 2017****.* ***(a)*** *Temperature (solid black line) and air pressure (broken blue line) from Automatic Weather Station (AWS 2700).* ***(b)*** *10 min averaged rain rate from Total Precipitation Sensor (grey bar), and relative humidity from AWS (light blue line).* ***(c)*** *Number concentrations of droplet per droplet size from Parsivel^2 (data partly missing).* ***(d)*** *Reflectivity from Micro Rain Radar (MRR-2).* ***(e)*** *δD of 10 min averaged near-surface vapour (black dotted line) and of the equilibrium vapour from precipitation (black bars). The length of the bar indicates the period over which the precipitation samples were collected, and the width of grey shading indicates the measurement uncertainty (standard deviation). The averaged uncertainty is 0.56 and 0.26 ‰ (invisible in this case) for the vapour and the equilibrium vapour from precipitation, respectively.* ***(f)*** *Same as in* ***(e)*** *but for d-excess, including d-excess of the precipitation (light blue bars). The averaged uncertainty is 0.90, 0.41, and 0.43 ‰ for the vapour, the equilibrium vapour from precipitation, and the precipitation, respectively.*

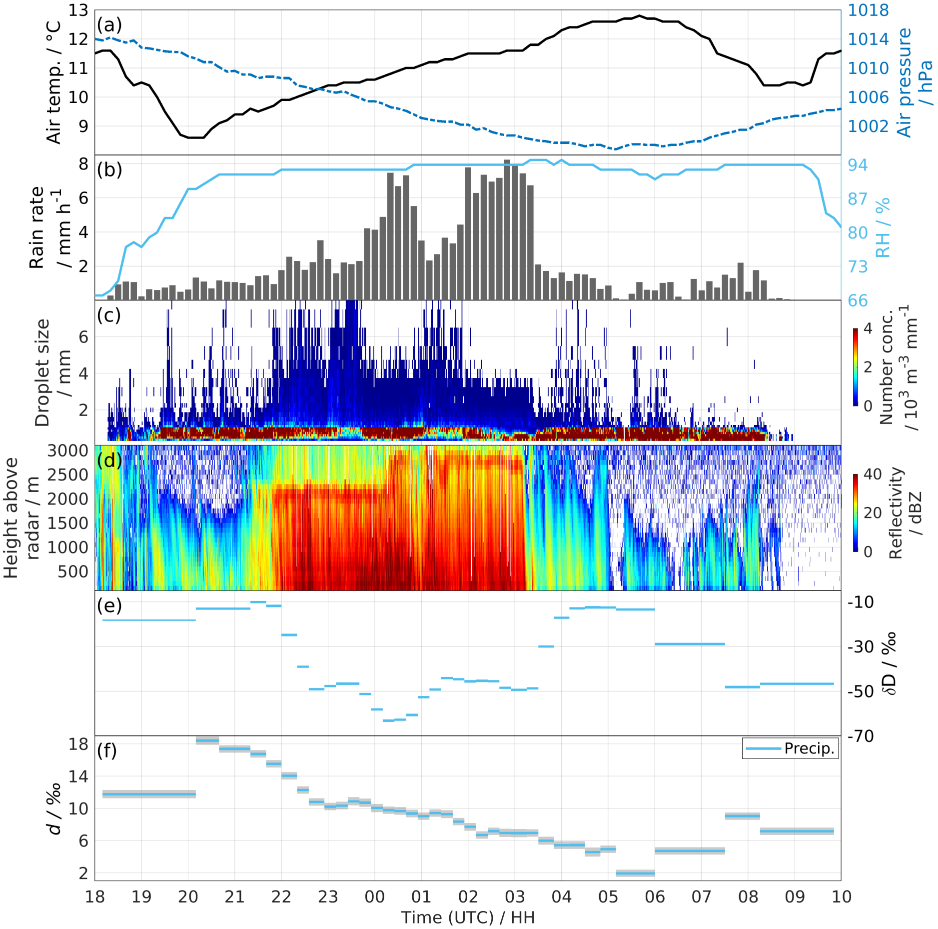

Figure C.8: Time series of observations on the rooftop (~45 m a.s.l) during ***a warm frontal system passing Bergen between 20 UTC 25 September and 06 UTC 26 September 2018****.* ***(a)*** *Temperature (solid black line) and air pressure (broken blue line) from Automatic Weather Station (AWS 2700).* ***(b)*** *10 min averaged rain rate from distrometer Parsivel^2 (grey bar), and relative humidity from AWS (light blue line).* ***(c)*** *Number concentrations of droplet per droplet size from Parsivel^2.* ***(d)*** *Reflectivity from Micro Rain Radar (MRR-2).* ***(e)*** *δD of precipitation. The length of the bar indicates the period over which the precipitation samples were collected, and the width of grey shading indicates the measurement uncertainty (standard deviation). The averaged uncertainty is 0.22 ‰ (invisible in this case).* ***(f)*** *Same as in* ***(e)*** *but for d-excess. The averaged uncertainty is 0.48 ‰.*

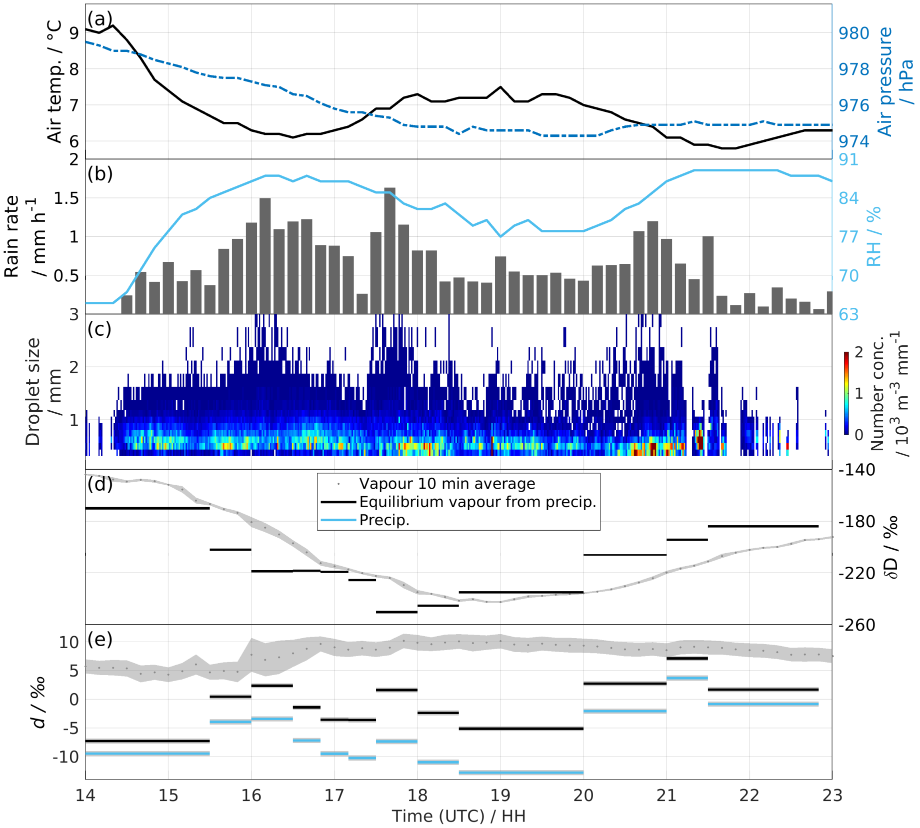

Figure C.9: Time series of observations on the rooftop (∼45 m a.s.l) during ***an occluded frontal system passing Bergen between 14 and 23 UTC 07 December 2018****.* ***(a)*** *Temperature (solid black line) and air pressure (broken blue line) from Automatic Weather Station (AWS 2700).* ***(b)*** *10 min averaged rain rate from Total Precipitation Sensor (grey bar), and relative humidity from AWS (light blue line).* ***(c)*** *Number concentrations of droplet per droplet size from Parsivel^2.* ***(d)*** *δD of 10 min averaged near-surface vapour (black dotted line) and of the equilibrium vapour from precipitation (black bars). The length of the bar indicates the period over which the precipitation samples were collected, and the width of grey shading indicates the measurement uncertainty (standard deviation). The averaged uncertainty is 0.94 and 0.19 ‰ (invisible in this case) for the vapour and the equilibrium vapour from precipitation, respectively.* ***(e)*** *Same as in* ***(d)*** *but for d-excess, including d-excess of the precipitation (light blue bars). The averaged uncertainty is 1.29, 0.44, and 0.45 ‰ for the vapour, the equilibrium vapour from precipitation, and the precipitation, respectively.*

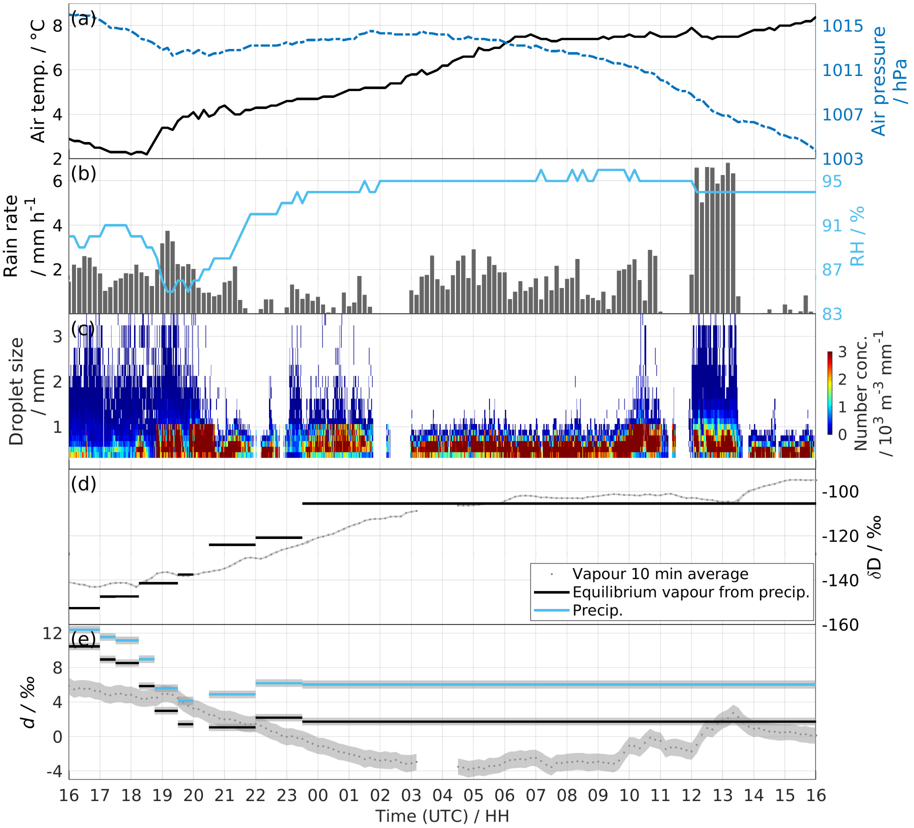

Figure C.10: Time series of observations on the rooftop (∼45 m a.s.l) during ***a warm frontal system passing Bergen between 16 UTC 30 December and 16 UTC 31 December 2018****.* ***(a)*** *Temperature (solid black line) and air pressure (broken blue line) from Automatic Weather Station (AWS 2700).* ***(b)*** *10 min averaged rain rate from Total Precipitation Sensor (grey bar), and relative humidity from AWS (light blue line).* ***(c)*** *Number concentrations of droplet per droplet size from Parsivel^2.* ***(d)*** *δD of 10 min averaged near-surface vapour (black dotted line) and of the equilibrium vapour from precipitation (black bars). The length of the bar indicates the period over which the precipitation samples were collected, and the width of grey shading indicates the measurement uncertainty (standard deviation). The averaged uncertainty is 0.53 and 0.19 ‰ (invisible in this case) for the vapour and the equilibrium vapour from precipitation, respectively.* ***(e)*** *Same as in* ***(d)*** *but for d-excess, including d-excess of the precipitation (light blue bars). The averaged uncertainty is 1.00, 0.44, and 0.46 ‰ for the vapour, the equilibrium vapour from precipitation, and the precipitation, respectively.*

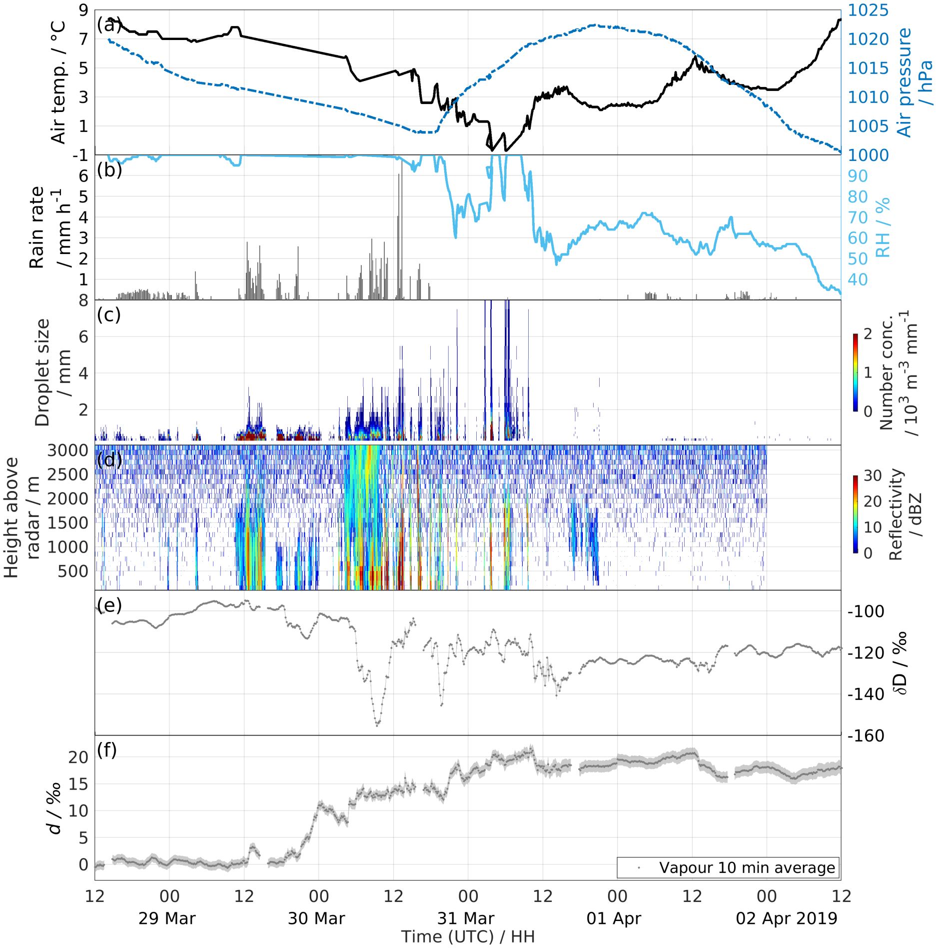

Figure C.11: Time series of observations on the rooftop (∼45 m a.s.l) during ***a cold air outbreak (CAO) passing Bergen between 12 UTC 28 Mar and 12 UTC 02 Apr 2019****.* ***(a)*** *Temperature (solid black line) and air pressure (broken blue line) from Automatic Weather Station (AWS 2700).* ***(b)*** *10 min averaged rain rate from Total Precipitation Sensor (grey bar), and relative humidity from AWS (light blue line).* ***(c)*** *Number concentrations of droplet per droplet size from Parsivel^2.* ***(d)*** *Reflectivity from Micro Rain Radar (MRR-2).* ***(e)*** *δD of 10 min averaged near-surface vapour (black dotted line). The width of grey shading indicates the measurement uncertainty (standard deviation). The averaged uncertainty is 0.65 ‰ (invisible in this case).* ***(f)*** *Same as in* ***(e)*** *but for d-excess. The averaged uncertainty is 0.87 ‰.*

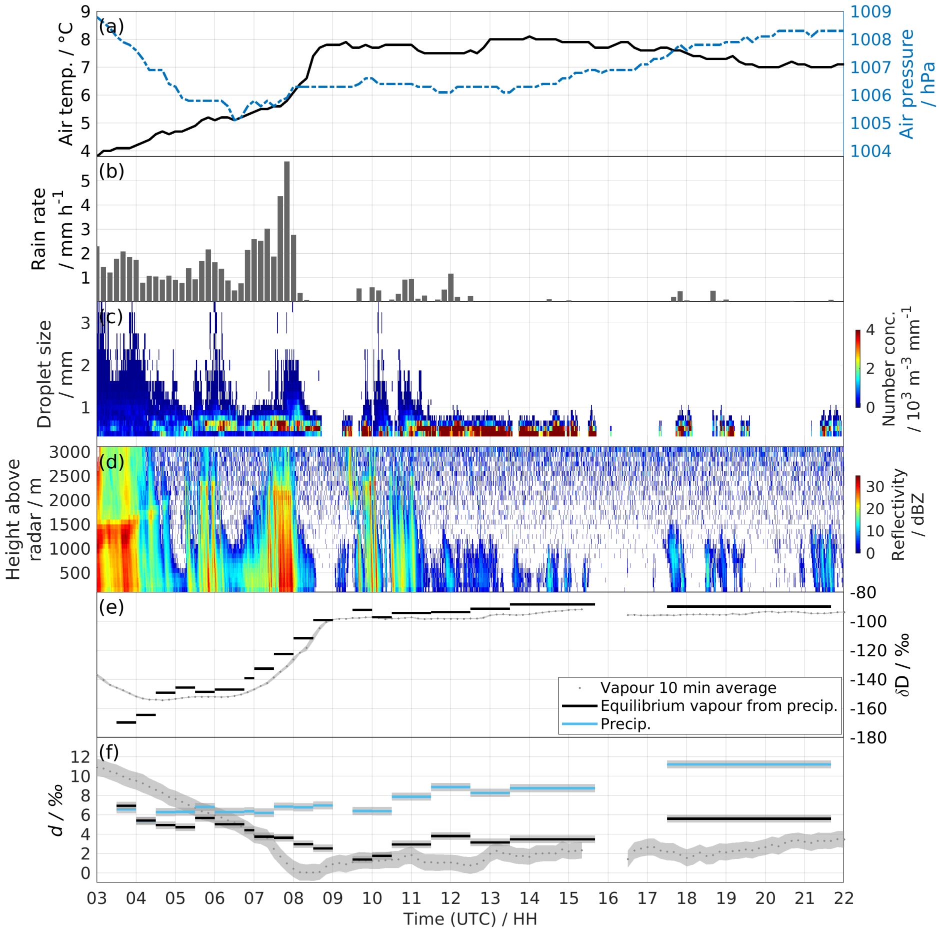

Figure C.12: Time series of observations on the rooftop (∼45 m a.s.l) during ***a warm frontal system passing Bergen between 03 and 09 UTC 03 December 2019****.* ***(a)*** *Temperature (solid black line) and air pressure (broken blue line) from Automatic Weather Station (AWS 2700).* ***(b)*** *10 min averaged rain rate from Total Precipitation Sensor (grey bar).* ***(c)*** *Number concentrations of droplet per droplet size from Parsivel^2.* ***(d)*** *Reflectivity from Micro Rain Radar (MRR-2).* ***(e)*** *δD of 10 min averaged near-surface vapour (black dotted line) and of the equilibrium vapour from precipitation (black bars). The length of the bar indicates the period over which the precipitation samples were collected, and the width of grey shading indicates the measurement uncertainty (standard deviation). The averaged uncertainty is 0.53 and 0.24 ‰ (invisible in this case) for the vapour and the equilibrium vapour from precipitation, respectively.* ***(f)*** *Same as in* ***(e)*** *but for d-excess, including d-excess of the precipitation (light blue bars). The averaged uncertainty is 0.87, 0.39, and 0.42 ‰ for the vapour, the equilibrium vapour from precipitation, and the precipitation, respectively.*

Bibliography

Aemisegger, F. (2018), On the link between the North Atlantic storm track and precipitation deuterium excess in Reykjavik, *Atmospheric Science Letters*, *19*(12), e865. 10

Aemisegger, F., and J. Sjolte (2018), A climatology of strong large-scale ocean evaporation events. Part II: Relevance for the deuterium excess signature of the evaporation flux, *Journal of Climate*, *31*(18), 7313–7336. 10, 12, 163

Aemisegger, F., P. Sturm, P. Graf, H. Sodemann, S. Pfahl, A. Knohl, and H. Wernli (2012), Measuring variations of δ^{18}O and δ^{2}H in atmospheric water vapour using two commercial laser-based spectrometers: an instrument characterisation study, *Atmospheric Measurement Techniques*, *5*(7), 1491–1511, doi:10.5194/amt-5-1491-2012. 27, 28

Aemisegger, F., S. Pfahl, H. Sodemann, I. Lehner, S. Seneviratne, and H. Wernli (2014), Deuterium excess as a proxy for continental moisture recycling and plant transpiration, *Atmospheric Chemistry And Physics*, *14*, 4029–4054. 40, 42

Aemisegger, F., J. Spiegel, S. Pfahl, H. Sodemann, W. Eugster, and H. Wernli (2015), Isotope meteorology of cold front passages: A case study combining observations and modeling, *Geophysical Research Letters*, *42*(13), 5652–5660. 13, 167, 168

Alfnes, E., and E. J. Førland (2006), Trends in extreme precipitation and return values in Norway 1900–2004, *Norwegian Meteorological Institute Report*, *2*, 2006. 1

Allison, G., J. Gat, and F. Leaney (1985), The relationship between deuterium and oxygen-18 delta values in leaf water, *Chemical Geology: Isotope Geoscience section*, *58*(1), 145 – 156, doi:10.1016/0168-9622(85)90035-1. 160

Angert, A., J.-E. Lee, and D. Yakir (2008), Seasonal variations in the isotopic composition of near-surface water vapour in the eastern Mediterranean, *Tellus B: Chemical and Physical Meteorology*, *60*(4), 674–684. 9

Araguás-Araguás, L., K. Froehlich, and K. Rozanski (2000), Deuterium and oxygen-18 isotope composition of precipitation and atmospheric moisture, *Hydrological Processes*, *14*(8), 1341–1355, doi:10.1002/1099-1085(20000615)14:8<1341::AID-HYP983>3.0.CO;2-Z. 2

Azad, R., and A. Sorteberg (2017), Extreme daily precipitation in coastal western Norway and the link to atmospheric rivers, *Journal of Geophysical Research: Atmospheres*, *122*(4), 2080–2095, doi:10.1002/2016JD025615. 17

Bao, J.-W., S. A. Michelson, P. J. Neiman, F. M. Ralph, and J. M. Wilczak (2006), Interpretation of enhanced integrated water vapor bands associated with extratropical cyclones: Their formation and connection to tropical moisture, *Monthly Weather Review*, *134*(4), 1063–1080, doi:10.1175/MWR3123.1. 17

Barkan, E., and B. Luz (2005), High precision measurements of $^{17}O/^{16}O$ and $^{18}O/^{16}O$ ratios in H_2O, *Rapid Communications in Mass Spectrometry*, *19*(24), 3737–3742, doi:10.1002/rcm.2250. 147

Barkan, E., and B. Luz (2007), Diffusivity fractionations of $H_2^{16}O/H_2^{17}O$ and $H_2^{16}O/H_2^{18}O$ in air and their implications for isotope hydrology, *Rapid Communications in Mass Spectrometry*, *21*(18), 2999–3005, doi:10.1002/rcm.3180. 147

Barnes, C., and G. Allison (1988), Tracing of water movement in the unsaturated zone using stable isotopes of hydrogen and oxygen, *Journal of Hydrology*, *100*(1), 143 – 176, doi:10.1016/0022-1694(88)90184-9. 160

Barras, V., and I. Simmonds (2009), Observation and modeling of stable water isotopes as diagnostics of rainfall dynamics over southeastern Australia, *Journal of Geophysical Research: Atmospheres*, *114*(D23). 11

Battan, L. J. (1973), Radar observation of the atmosphere, *Quarterly Journal of the Royal Meteorological Society*, *99*(422), 793–793, doi:10.1002/qj.49709942229. 23

Begley, I. S., and C. M. Scrimgeour (1997), High-precision δ^2H and δ^{18}O measurement for water and volatile organic compounds by continuous-flow pyrolysis isotope ratio mass spectrometry, *Analytical Chemistry*, *69*(8), 1530–1535. 23

Benetti, M., G. Aloisi, G. Reverdin, C. Risi, and G. Sèze (2015), Importance of boundary layer mixing for the isotopic composition of surface vapor over the subtropical North Atlantic Ocean, *Journal of Geophysical Research: Atmospheres*, *120*(6), 2190–2209. 163, 164

Benetti, M., H. C. Steen-Larsen, G. Reverdin, Á. E. Sveinbjörnsdóttir, G. Aloisi, M. B. Berkelhammer, B. Bourlès, D. Bourras, G. De Coetlogon, A. Cosgrove, et al. (2017), Stable isotopes in the atmospheric marine boundary layer water vapour over the Atlantic Ocean, 2012–2015, *Scientific data*, *4*(1), 1–17, doi:10.1038/sdata.2016.128. 3, 168

Bigeleisen, J., M. L. Perlman, and H. C. Prosser (1952), Conversion of hydrogenic materials to hydrogen for isotopic analysis, *Analytical Chemistry*, *24*(8), 1356–1357. 23

Bonne, J.-L., V. Masson-Delmotte, O. Cattani, M. Delmotte, C. Risi, H. Sodemann, and H. Steen-Larsen (2014), The isotopic composition of water vapour and precipitation in Ivittuut, southern Greenland, *Atmospheric Chemistry and Physics*, *14*(9), 4419–4439. 28, 42

Bonne, J.-L., H. C. Steen-Larsen, C. Risi, M. Werner, H. Sodemann, J.-L. Lacour, X. Fettweis, G. Cesana, M. Delmotte, O. Cattani, et al. (2015), The summer 2012 Greenland heat wave: In situ and remote sensing observations of water vapor isotopic composition during an atmospheric river event, *Journal of Geophysical Research: Atmospheres*, *120*(7), 2970–2989. 42

Bonne, J.-L., M. Behrens, H. Meyer, S. Kipfstuhl, B. Rabe, L. Schönicke, H. C. Steen-Larsen, and M. Werner (2019), Resolving the controls of water vapour isotopes in the Atlantic sector, *Nature communications*, *10*(1), 1–10. 3, 9

Bonne, J.-L., H. Meyer, M. Behrens, J. Boike, S. Kipfstuhl, B. Rabe, T. Schmidt, L. Schönicke, H. C. Steen-Larsen, and M. Werner (2020), Moisture origin as a driver of temporal variabilities of the water vapour isotopic composition in the Lena River Delta, Siberia, *Atmospheric Chemistry and Physics*, *20*(17), 10,493–10,511, doi:10.5194/acp-20-10493-2020. 39

Bony, S., C. Risi, and F. Vimeux (2008), Influence of convective processes on the isotopic composition (δ^{18}O and δD) of precipitation and water vapor in the tropics: 1. Radiative-convective equilibrium and Tropical Ocean–Global Atmosphere–Coupled Ocean-Atmosphere Response Experiment (TOGA-COARE) simulations, *Journal of Geophysical Research: Atmospheres*, *113*(D19), doi:10.1029/2008JD009942. 2, 11

Brand, W. A., H. Geilmann, E. R. Crosson, and C. W. Rella (2009), Cavity ring-down spectroscopy versus high-temperature conversion isotope ratio mass spectrometry: a case study on δ^{2}H and δ^{18}O of pure water samples and alcohol/water mixtures, *Rapid Communications in Mass Spectrometry*, *23*(12), 1879–1884. 23

Cappa, C. D., M. B. Hendricks, D. J. DePaolo, and R. C. Cohen (2003), Isotopic fractionation of water during evaporation, *Journal Of Geophysical Research-Atmospheres*, *108*(D16), 4525. 159, 167

Cassou, C. (2008), Intraseasonal interaction between the Madden–Julian oscillation and the North Atlantic Oscillation, *Nature*, *455*(7212), 523–527, doi:10.1038/nature07286. 19

Chapman, S. (1970), The mathematical theory of non-uniform gases : an account of the kinetic theory of viscosity, thermal conduction and diffusion in gases. 159

Ciais, P., and J. Jouzel (1994), Deuterium and oxygen 18 in precipitation: Isotopic model, including mixed cloud processes, *Journal of Geophysical Research: Atmospheres*, *99*(D8), 16,793–16,803, doi:10.1029/94JD00412. 41, 153, 162, 167

Coplen, T. B., P. J. Neiman, A. B. White, J. M. Landwehr, F. M. Ralph, and M. D. Dettinger (2008), Extreme changes in stable hydrogen isotopes and precipitation characteristics in a landfalling Pacific storm, *Geophysical Research Letters*, *35*(21), doi:10.1029/2008GL035481. 2, 3, 23

Coplen, T. B., P. J. Neiman, A. B. White, and F. M. Ralph (2015), Categorisation of northern California rainfall for periods with and without a radar brightband using stable isotopes and a novel automated precipitation collector, *Tellus B: Chemical and Physical Meteorology*, *67*(1), 28,574, doi:10.3402/tellusb.v67.28574. 2, 23

Craig, H. (1957a), Deuterium–oxygen 18–tritium relationships in natural waters, in *Proceedings of the 1957 Conference on New Research Methods in Hydrology, Comm. on Research in Water Resources*, p. 15, California University, Scripps Institute of Oceanography La Jolla. 156

Craig, H. (1961), Isotopic variations in meteoric waters, *Science*, *133*(3465), 1702–1703. 2, 8, 25, 156

Craig, H., and L. I. Gordon (1965), Deuterium and oxygen 18 variations in the ocean and the marine atmosphere., in *Stable Isotopes in Oceanographic Studies and Paleotemperatures*, edited by E. Tongiorgi, pp. 9–130, Laboratorio di Geologia Nucleare, Pisa, Italy. 9, 12, 13, 156, 157, 159, 160, 161, 162, 167

Craig, H., L. I. Gordon, and Y. Horibe (1963), Isotopic exchange effects in the evaporation of water: 1. Low-temperature experimental results, *Journal of Geophysical Research (1896-1977)*, *68*(17), 5079–5087, doi:10.1029/JZ068i017p05079. 12, 156, 160

Craig, H., H. (1957b), Isotopic standards for carbon and oxygen and correction factors for mass-spectrometric analysis of carbon dioxide, *Geochimica Et Cosmochimica Acta*, *12*(1-2), 133–149, doi:10.1016/0016-7037(57)90024-8. 147

Crawford, J., C. E. Hughes, and S. D. Parkes (2013), Is the isotopic composition of event based precipitation driven by moisture source or synoptic scale weather in the Sydney Basin, Australia?, *Journal of Hydrology*, *507*, 213–226. 2

Criss, R. E. (1999), *Principles of stable isotope distribution*, New York: Oxford University Press. 7

Crosson, E. R. (2008), A cavity ring-down analyzer for measuring atmospheric levels of methane, carbon dioxide, and water vapor, *Applied Physics B: Lasers and Optics*, *92*(3), 403–408. 2, 24, 40

Dansgaard, W. (1953), The abundance of O^{18} in atmospheric water and water vapour, *Tellus*, *5*(4), 461–469. 1

Dansgaard, W. (1954), The O^{18}-abundance in fresh water, *Geochimica et Cosmochimica Acta*, *6*(5-6), 241–260. 1

Dansgaard, W. (1964), Stable isotopes in precipitation, *Tellus*, *16*(4), 436–468. 1, 2, 8, 9, 10, 11, 25, 40

De Groot, P. A. (2004), *Handbook of stable isotope analytical techniques*, vol. 1, Elsevier. 23

Dee, D. P., S. M. Uppala, A. Simmons, P. Berrisford, P. Poli, S. Kobayashi, U. Andrae, M. Balmaseda, G. Balsamo, d. P. Bauer, et al. (2011), The ERA-Interim reanalysis: Configuration and performance of the data assimilation system, *Quarterly Journal of the royal meteorological society*, *137*(656), 553–597. 19, 34

Dee, S., D. Noone, N. Buenning, J. Emile-Geay, and Y. Zhou (2015), SPEEDY-IER: A fast atmospheric GCM with water isotope physics, *Journal of Geophysical Research: Atmospheres*, *120*(1), 73–91, doi:10.1002/2014JD022194. 169

Dütsch, M., S. Pfahl, and H. Wernli (2016), Drivers of δ^2H variations in an idealized extratropical cyclone, *Geophysical Research Letters*, *43*(10), 5401–5408, doi:10.1002/2016GL068600. 42

Eckhardt, S., A. Stohl, H. Wernli, P. James, C. Forster, and N. Spichtinger (2004), A 15-year climatology of warm conveyor belts, *Journal of Climate*, *17*(1), 218–237, doi:10.1175/1520-0442(2004)017<0218:AYCOWC>2.0.CO;2. 17

Epstein, S. (1956), Variations in the 18O/16O ratios of freshwater and ice, *Natnl. Acad. Sc. Nucl. Science Series Report*, *19*, 20–28. 1

Epstein, T., S. Mayeda (1953), Variations of ^{18}O content of waters from natural sources., *Geochimica Cosmochimica Acta*, *4*, 213–224. 2, 23

Fang, G., and C. A. Ward (1999), Temperature measured close to the interface of an evaporating liquid, *Phys. Rev. E*, *59*, 417–428, doi:10.1103/PhysRevE.59.417. 159

Ferranti, L., S. Corti, and M. Janousek (2015), Flow-dependent verification of the ECMWF ensemble over the Euro-Atlantic sector, *Quarterly Journal of the Royal Meteorological Society*, *141*(688), 916–924. 19

Field, R. D., D. Kim, A. N. LeGrande, J. Worden, M. Kelley, and G. A. Schmidt (2014), Evaluating climate model performance in the tropics with retrievals of water isotopic composition from Aura TES, *Geophysical Research Letters*, *41*(16), 6030–6036. 2

Frankenberg, C., K. Yoshimura, T. Warneke, I. Aben, A. Butz, N. Deutscher, D. Griffith, F. Hase, J. Notholt, M. Schneider, H. Schrijver, and T. Röckmann (2009), Dynamic processes governing lower-tropospheric HDO/H_2O ratios as observed from space and ground, *Science*, *325*(5946), 1374–1377, doi:10.1126/science.1173791. 168

Fremme, A., and H. Sodemann (2019), The role of land and ocean evaporation on the variability of precipitation in the Yangtze River valley, *Hydrology and Earth System Sciences*, *23*(6), 2525–2540. 34

Galewsky, J., H. C. Steen-Larsen, R. D. Field, J. Worden, C. Risi, and M. Schneider (2016), Stable isotopes in atmospheric water vapor and applications to the hydrologic cycle, *Reviews of Geophysics*, *54*(4), 809–865, doi:10.1002/2015RG000512. 2, 40, 41, 168

Gat, J. R. (1996), Oxygen and hydrogen isotopes in the hydrologic cycle, *Annual Review of Earth and Planetary Sciences*, *24*(1), 225–262. 1, 149, 159, 160

Gat, J. R. (2008), The isotopic composition of evaporating waters – review of the historical evolution leading up to the Craig–Gordon model, *Isotopes in Environmental and Health Studies*, *44*(1), 5–9, doi:10.1080/10256010801887067. 159

Gat, J. R., C. J. Bowser, and C. Kendall (1994), The contribution of evaporation from the Great Lakes to the continental atmosphere: estimate based on stable isotope data, *Geophysical Research Letters*, *21*(7), 557–560, doi:10.1029/94GL00069. 159

Gat, J. R., A. Shemesh, E. Tziperman, A. Hecht, D. Georgopoulos, and O. Basturk (1996), The stable isotope composition of waters of the eastern Mediterranean Sea, *Journal of Geophysical Research: Oceans*, *101*(C3), 6441–6451, doi:10.1029/95JC02829. 159

Gat, J. R., W. G. Mook, and H. A. Meijer (2001), Atmospheric water, *Environmental isotopes in the hydrological cycle: Principles and applications, International Hydrological Programme (IHP-V), Technical Documents in Hydrology (IAEA/UNESCO)*, *2*, 1–175. 5, 6, 150

Gat, J. R., B. Klein, Y. Kushnir, W. Roether, H. Wernli, R. Yam, and A. Shemesh (2003), Isotope composition of air moisture over the Mediterranean Sea: an index of the air-sea interaction pattern, *Tellus B: Chemical and Physical Meteorology*, *55*(5), 953–965, doi:10.3402/tellusb.v55i5.16395. 9

Gehre, M., H. Geilmann, J. Richter, R. Werner, and W. Brand (2004), Continuous flow $^2H/^1H$ and $^{18}O/^{16}O$ analysis of water samples with dual inlet precision, *Rapid Communications in Mass Spectrometry*, *18*(22), 2650–2660. 23

Gonfiantini, R. (1978), Standards for stable isotope measurements in natural compounds, *Nature*, *271*(5645), 534–536, doi:10.1038/271534a0. 24

Gonfiantini, R., and E. Picciotto (1959), Oxygen isotope variations in Antarctic snow samples, *Nature*, *184*(4698), 1557–1558, doi:10.1038/1841557a0. 2

Graf, P., H. Wernli, S. Pfahl, and H. Sodemann (2019), A new interpretative framework for below-cloud effects on stable water isotopes in vapour and rain, *Atmospheric Chemistry and Physics*, *19*(2), 747–765. 13, 22, 39

Grams, C. M., R. Beerli, S. Pfenninger, I. Staffell, and H. Wernli (2017), Balancing Europe's wind-power output through spatial deployment informed by weather regimes, *Nature climate change*, *7*(8), 557–562. 15, 19, 20

Groisman, P. Y., T. R. Karl, D. R. Easterling, R. W. Knight, P. F. Jamason, K. J. Hennessy, R. Suppiah, C. M. Page, J. Wibig, K. Fortuniak, V. N. Razuvaev, A. Douglas, E. Førland, and P.-M. Zhai (1999), *Changes in the probability of heavy precipitation: Important indicators of climatic change*, pp. 243–283, Springer Netherlands, Dordrecht, doi:10.1007/978-94-015-9265-9_15. 1

Gröning, M. (2011), Improved water δ^2H and δ^{18}O calibration and calculation of measurement uncertainty using a simple software tool, *Rapid Communications in Mass Spectrometry*, *25*(19), 2711–2720. 29

Guan, H., X. Zhang, G. Skrzypek, Z. Sun, and X. Xu (2013), Deuterium excess variations of rainfall events in a coastal area of South Australia and its relationship with synoptic weather systems and atmospheric moisture sources, *Journal of Geophysical Research: Atmospheres*, *118*(2), 1123–1138. 2

Hanssen-Bauer, I. (2005), Regional temperature and precipitation series for Norway: Analyses of time-series updated to 2004, *Met. no report*, *15*(2005), 1–34. 1

Hoefs, J. (2004), *Stable Isotope Geochemistry*, Springer Science & Business Media. 7

Hoffmann, G., M. Werner, and M. Heimann (1998), Water isotope module of the ECHAM atmospheric general circulation model: A study on timescales from days to several years, *Journal of Geophysical Research: Atmospheres*, *103*(D14), 16,871–16,896. 169

Hoffmann, G., J. Jouzel, and V. Masson (2000), Stable water isotopes in atmospheric general circulation models, *Hydrological Processes*, *14*(8), 1385–1406, doi:10.1002/1099-1085(20000615)14:8<1385::AID-HYP989>3.0.CO;2-1. 168

Horita, J., K. Rozanski, and S. Cohen (2008), Isotope effects in the evaporation of water: a status report of the Craig–Gordon model, *Isotopes In Environmental and Health Studies*, *44*(1), 23–49, doi:10.1080/10256010801887174. 159

Hut, G. (1987), Consultants' group meeting on stable isotope reference samples for geochemical and hydrological investigations. 24

IAEA (2009), Reference sheet for VSMOW2 and SLAP2 international measurement standards. 1, 6, 24, 25

IPCC (2014), *Climate Change 2013: The physical science basis: Working group I contribution to the fifth assessment report of the Intergovernmental Panel on Climate Change*, Cambridge University Press. 1

Johnsen, S. J., W. Dansgaard, and J. W. C. White (1989), The origin of Arctic precipitation under present and glacial conditions, *Tellus*, *41B*, 452–468. 2, 9, 40

Joussaume, S., and J. Jouzel (1993), Paleoclimatic tracers: An investigation using an atmospheric general circulation model under ice age conditions: 2. Water isotopes, *Journal of Geophysical Research: Atmospheres*, *98*(D2), 2807–2830, doi:10.1029/92JD01920. 169

Joussaume, S., R. Sadourny, and J. Jouzel (1984), A general circulation model of water isotope cycles in the atmosphere, *Nature*, *311*(5981), 24–29. 168, 169

Jouzel, J. (1986), Isotopes in cloud physics: Multiphase and multistage condensation processes, *Handbook of environmental isotope geochemistry*, *2*, 61–112. 39, 166

Jouzel, J., and R. D. Koster (1996), A reconsideration of the initial conditions used for stable water isotope models, *Journal of Geophysical Research: Atmospheres (1984–2012)*, *101*(D17), 22,933–22,938. 12, 163

Jouzel, J., and L. Merlivat (1984), Deuterium and oxygen 18 in precipitation: Modeling of the isotopic effects during snow formation, *Journal of Geophysical Research-Atmospheres*, *89*(D7), 11,749 – 11,759. 10, 11, 14, 41, 42, 152, 153, 154, 167

Jouzel, J., L. Merlivat, and C. Lorius (1982), Deuterium excess in an East Antarctic ice core suggests higher relative humidity at the oceanic surface during the last glacial maximum, *Nature*, *299*(5885), 688–691, doi:10.1038/299688a0. 9, 40

Jouzel, J., G. L. Russell, R. J. Suozzo, R. D. Koster, J. W. C. White, and W. S. Broecker (1987), Simulations of the HDO and $H_2^{18}O$ atmospheric cycles using the NASA GISS general circulation model: The seasonal cycle for present-day conditions, *Journal of Geophysical Research: Atmospheres*, *92*(D12), 14,739–14,760, doi:10.1029/JD092iD12p14739. 169

Jouzel, J., R. D. Koster, R. J. Suozzo, G. L. Russell, J. W. C. White, and W. S. Broecker (1991), Simulations of the HDO and $H_2^{18}O$ atmospheric cycles using the NASA GISS general circulation model: Sensitivity experiments for present-day conditions, *Journal of Geophysical Research: Atmospheres*, *96*(D4), 7495–7507, doi:10.1029/90JD02663. 169

Kerstel, E. (2004), Chapter 34 - Isotope Ratio Infrared Spectrometry, in *Handbook of Stable Isotope Analytical Techniques*, edited by P. A. [de Groot], pp. 759 – 787, Elsevier, Amsterdam, doi:10.1016/B978-044451114-0/50036-3. 2, 6, 40

Kerstel, E., and L. Gianfrani (2008), Advances in laser-based isotope ratio measurements: selected applications, *Applied Physics B-Lasers And Optics*, *92*(3), 439–449. 2, 23, 40

Kerstel, E. R. T., R. van Trigt, N. Dam, J. Reuss, and H. A. J. Meijer (1999), Simultaneous determination of the $^2H/^1H$, $^{17}O/^{16}O$ and $^{18}O/^{16}O$ isotope abundance ratios in water by means of laser spectrometry, *Analytical Chemistry*, *71*(23), 5297–5303. 23

Kinzer, G. D., and R. Gunn (1951), The evaporation, temperature and thermal relaxation-time of freely falling waterdrops, *Journal of Atmospheric Sciences*, *8*(2), 71 – 83, doi:10.1175/1520-0469(1951)008<0071:TETATR>2.0.CO;2. 166

Kurita, N., D. Noone, C. Risi, G. A. Schmidt, H. Yamada, and K. Yoneyama (2011), Intraseasonal isotopic variation associated with the Madden-Julian Oscillation, *Journal of Geophysical Research: Atmospheres*, *116*(D24), doi:10.1029/2010JD015209. 169

Läderach, A., and H. Sodemann (2016), A revised picture of the atmospheric moisture residence time, *Geophysical Research Letters*, *43*(2), 924–933. 34

Landais, A., E. Barkan, and B. Luz (2008), Record of δ^{18}O and ^{17}O-excess in ice from Vostok Antarctica during the last 150,000 years, *Geophysical Research Letters*, *35*(2), doi:10.1029/2007GL032096. 147

Lavers, D. A., F. Pappenberger, and E. Zsoter (2014), Extending medium-range predictability of extreme hydrological events in Europe, *Nature communications*, *5*, 5382. 16

Lavers, D. A., D. E. Waliser, F. M. Ralph, and M. D. Dettinger (2016), Predictability of horizontal water vapor transport relative to precipitation: Enhancing situational awareness for forecasting western U.S. extreme precipitation and flooding, *Geophysical Research Letters*, *43*(5), 2275–2282, doi:10.1002/2016GL067765. 16

Lawrence, R. J., and D. S. Gedzelman (1996), Low stable isotope ratios of tropical cyclone rains, *Geophysical Research Letters*, *23*(5), 527–530. 11

Lee, J.-E., and I. Fung (2008), “Amount effect” of water isotopes and quantitative analysis of post-condensation processes, *Hydrological Processes: An International Journal*, *22*(1), 1–8. 2

Lee, J.-E., I. Fung, D. J. DePaolo, and C. C. Henning (2007), Analysis of the global distribution of water isotopes using the NCAR atmospheric general circulation model, *Journal of Geophysical Research: Atmospheres*, *112*(D16), doi:10.1029/2006JD007657. 169

Leroy-Dos Santos, C., V. Masson-Delmotte, M. Casado, E. Fourré, H. C. Steen-Larsen, M. Maturilli, A. Orsi, A. Berchet, O. Cattani, B. Minster, J. Gherardi, and A. Landais (2020), A 4.5 year-long record of Svalbard water vapor isotopic composition documents winter air mass origin, *Journal of Geophysical Research: Atmospheres*, *125*(n/a), e2020JD032,681, doi:10.1029/2020JD032681, Accepted Author Manuscript. 39, 42

Lin, Y., R. N. Clayton, and M. Groning (2010), Calibration of δ^{17}O and δ^{18}O of international measurement standards - VSMOW, VSMOW2, SLAP, and SLAP2, *Rapid Communications In Mass Spectrometry*, *24*(6), 773–776, doi:10.1002/rcm.4449. 24, 25

Luz, B., and E. Barkan (2010), Variations of ^{17}O/^{16}O and ^{18}O/^{16}O in meteoric waters, *Geochimica et Cosmochimica Acta*, *74*(22), 6276 – 6286, doi:10.1016/j.gca.2010.08.016. 148

Majoube, M. (1971a), Fractionnement en oxygéne 18 et en deutérium entre l’eau et sa vapeur, *J. Chem. Phys.*, *10*, 1423–1436. 8, 9, 13, 166, 167

Majoube, M. (1971b), Fractionnement en oxygéne 18 entre la glace et la vapeur d’eau, *J. Chim. Phys.*, *68*, 625–636, doi:10.1051/jcp/1971680625. 167

Mathieu, R., D. Pollard, J. E. Cole, J. W. C. White, R. S. Webb, and S. L. Thompson (2002), Simulation of stable water isotope variations by the GENESIS GCM for modern conditions, *Journal of Geophysical Research: Atmospheres*, *107*(D4), ACL 2-1–ACL 2-18, doi:10.1029/2001JD900255. 169

Mauritsen, T., B. Stevens, E. Roeckner, T. Crueger, M. Esch, M. Giorgetta, H. Haak, J. Jungclaus, D. Klocke, D. Matei, et al. (2012), Tuning the climate of a global model, *Journal of advances in modeling Earth systems*, *4*(3). 41

Meijer, H. A. J., and W. J. Li (1998), The use of electrolysis for accurate δ^{17}O and δ^{18}O isotope measurements in water, *Isotopes in Environmental and Health Studies*, *34*(4), 349–369, doi:10.1080/10256019808234072. 147

Merlivat, L. (1970), L'étude quantitative de bilans de lacs à l'aide des concentrations en deuterium et oxygène-18 dans l'eau, in *Isotope hydrology*, pp. 89–107, IAEA Vienna. 166

Merlivat, L. (1978), Molecular diffusivities of $H_2^{16}O$, $HD^{16}O$, and $H_2^{18}O$ in gases, *Journal of Chemical Physics*, *69*(6), 2864–2871, doi:10.1063/1.436884. 12, 159, 167

Merlivat, L., and J. Jouzel (1979), Global climatic interpretation of the deuterium-oxygen 18 relationship for precipitation, *Journal of Geophysical Research*, *84(C8)*, 5029–5033. 8, 9, 12, 41, 153, 163, 164, 167

Merlivat, L., and G. Nief (1963), Fractionnement isotopique lors des changements d'états solide-vapeur et liquide-vapeur de l'eau à des tempbratures infbrieures à 0°C, *Tellus*. 8

METEK Meteorologische Messtechnik GmbH (2012), *MRR-2 Micro Rain Radar user manual*. 22

Michel, C., and G. Rivière (2011), The link between Rossby wave breakings and weather regime transitions, *Journal of the atmospheric sciences*, *68*(8), 1730–1748. 19

Michelangeli, P.-A., R. Vautard, and B. Legras (1995), Weather regimes: Recurrence and quasi stationarity, *Journal of the atmospheric sciences*, *52*(8), 1237–1256. 19

Miyake, Y., O. Matsubaya, and C. Nishihara (1968), An isotopic study on meteoric precipitation, *Papers in Meteorology and Geophysics*, *19*, 243–266. 2, 11

Mook, W. G., and J. De Vries (2001), Introduction: Theory, methods, review, *Environmental isotopes in the hydrological cycle: Principles and applications, International Hydrological Programme (IHP-V), Technical Documents in Hydrology (IAEA/UNESCO)*, *1*, 1–164. 6, 7, 147, 152

Muller, C. L., A. Baker, I. J. Fairchild, C. Kidd, and I. Boomer (2015), Intra-event trends in stable isotopes: Exploring midlatitude precipitation using a vertically pointing Micro Rain Radar, *Journal of Hydrometeorology*, *16*, 194–213, doi:10.1175/JHM-D-14-0038.1. 2, 11, 23

Munksgaard, N. C., C. M. Wurster, A. Bass, and M. I. Bird (2012), Extreme short-term stable isotope variability revealed by continuous rainwater analysis, *Hydrological Processes*, *26*(23), 3630–3634, doi:10.1002/hyp.9505. 2

Newell, R. E., N. E. Newell, Y. Zhu, and C. Scott (1992), Tropospheric rivers? – A pilot study, *Geophysical Research Letters*, *19*(24), 2401–2404, doi:10.1029/92GL02916. 16

Noone, D., and I. Simmonds (2002), Associations between δ^{18}O of water and climate parameters in a simulation of atmospheric circulation for 1979–95, *Journal of Climate*, *15*(22), 3150–3169, doi:10.1175/1520-0442(2002)015<3150:ABOOWA>2.0.CO;2. 169

Noone, D., and C. Sturm (2010), *Comprehensive dynamical models of global and regional water isotope distributions*, pp. 195–219, Springer Netherlands, Dordrecht, doi:10.1007/978-90-481-3354-3_10. 166, 167, 168

O'Keefe, A., and D. A. Deacon (1988), Cavity ring-down optical spectrometer for absorption measurements using pulsed laser sources, *Review of scientific instruments*, *59*(12), 2544–2551. 24

OTT Hydromet GmbH (2015), *Operating instructions: Present weather sensor OTT Parsivel^2*. 21

Papritz, L., and C. M. Grams (2018), Linking low-frequency large-scale circulation patterns to cold air outbreak formation in the northeastern North Atlantic, *Geophysical Research Letters*, *45*(5), 2542–2553. 17, 19

Papritz, L., and H. Sodemann (2018), Characterizing the local and intense water cycle during a cold air outbreak in the Nordic Seas, *Monthly Weather Review*, *146*(11), 3567–3588. 17

Papritz, L., and T. Spengler (2017), A Lagrangian climatology of wintertime cold air outbreaks in the Irminger and Nordic Seas and their role in shaping air–sea heat fluxes, *Journal of Climate*, *30*(8), 2717–2737, doi:10.1175/JCLI-D-16-0605.1. 17

Pasquier, J., S. Pfahl, and C. M. Grams (2019), Modulation of atmospheric river occurrence and associated precipitation extremes in the North Atlantic region by European weather regimes, *Geophysical Research Letters*, *46*(2), 1014–1023. 15, 19

Pellaud, C. (2018), Vertical stable isotope gradients in Bergen valley, Master's thesis, University of Bergen. 4

Penna, D., B. Stenni, M. Šanda, S. Wrede, T. Bogaard, A. Gobbi, M. Borga, M. Bonazza, and Z. Chárová (2010), On the reproducibility and repeatability of laser absorption spectroscopy measurements for δ^2H and δ^{18}O isotopic analysis, *Hydrology and Earth System Sciences*, *14*(8), 1551–1566. 29

Penna, D., B. Stenni, M. Šanda, S. Wrede, T. Bogaard, M. Michelini, A. Gobbi, N. Mantese, G. Zuecco, M. Borga, et al. (2012), Technical Note: Evaluation of between-sample memory effects in the analysis of δ^2H and δ^{18}O of water samples measured by laser spectroscopes, *Hydrology and Earth System Sciences*, *16*(10), 3925–3933. 29

Pfahl, S., and H. Sodemann (2014), What controls deuterium excess in global precipitation?, *Climate of the Past*, *10*(2), 771–781. 8, 9, 41

Pfahl, S., and H. Wernli (2008), Air parcel trajectory analysis of stable isotopes in water vapor in the eastern Mediterranean, *Journal of Geophysical Research: Atmospheres*, *113*(D20). 9

Pfahl, S., and H. Wernli (2009), Lagrangian simulations of stable isotopes in water vapor: An evaluation of nonequilibrium fractionation in the Craig-Gordon model, *Journal of Geophysical Research: Atmospheres (1984–2012)*, *114*(D20). 159

Pfahl, S., H. Wernli, and K. Yoshimura (2012), The isotopic composition of precipitation from a winter storm–a case study with the limited-area model COSMOiso, *Atmos. Chem. Phys*, *12*(3), 1629–1648. 3, 41, 42, 166, 167, 168, 169

Pruppacher, H. R., and J. D. Klett (1980), Microphysics of clouds and precipitation, *Nature*, *284*(5751), 88–88. 154

Ralph, F. M., P. J. Neiman, and G. A. Wick (2004), Satellite and CALJET aircraft observations of atmospheric rivers over the eastern North Pacific Ocean during the winter of 1997/98, *Monthly Weather Review*, *132*(7), 1721–1745. 15, 17

Ralph, F. M., P. J. Neiman, G. A. Wick, S. I. Gutman, M. D. Dettinger, D. R. Cayan, and A. B. White (2006), Flooding on California's Russian River: Role of atmospheric rivers, *Geophysical Research Letters*, *33*(13), doi:10.1029/2006GL026689. 17

Raupach, T. H., and A. Berne (2015), Correction of raindrop size distributions measured by Parsivel disdrometers, using a two-dimensional video disdrometer as a reference, *Atmospheric Measurement Techniques*, *8*(1), 343–365, doi:10.5194/amt-8-343-2015. 22

Richet, P., Y. Bottinga, and M. Javoy (1977), A review of hydrogen, carbon, nitrogen, oxygen, sulphur, and chlorine stable isotope fractionation among gaseous molecules, *Annual Review of Earth and Planetary Sciences*, *5*(1), 65–110. 8

Risi, C., S. Bony, and F. Vimeux (2008), Influence of convective processes on the isotopic composition (δ^{18}O and δD) of precipitation and water vapor in the tropics: 2. Physical interpretation of the amount effect, *Journal of Geophysical Research: Atmospheres*, *113*(D19). 2

Risi, C., S. Bony, F. Vimeux, and J. Jouzel (2010), Water-stable isotopes in the LMDZ4 general circulation model: Model evaluation for present-day and past climates and applications to climatic interpretations of tropical isotopic records, *Journal of Geophysical Research: Atmospheres*, *115*(D12), doi:10.1029/2009JD013255. 14, 41, 169

Risi, C., D. Noone, J. Worden, C. Frankenberg, G. Stiller, M. Kiefer, B. Funke, K. Walker, P. Bernath, M. Schneider, D. Wunch, V. Sherlock, N. Deutscher, D. Griffith, P. O. Wennberg, K. Strong, D. Smale, E. Mahieu, S. Barthlott, F. Hase, O. García, J. Notholt, T. Warneke, G. Toon, D. Sayres, S. Bony, J. Lee, D. Brown, R. Uemura, and C. Sturm (2012a), Process-evaluation of tropospheric humidity simulated by general circulation models using water vapor isotopologues: 1. Comparison between models and observations, *Journal of Geophysical Research: Atmospheres*, *117*(D5), doi:10.1029/2011JD016621. 167

Risi, C., D. Noone, J. Worden, C. Frankenberg, G. Stiller, M. Kiefer, B. Funke, K. Walker, P. Bernath, M. Schneider, S. Bony, J. Lee, D. Brown, and C. Sturm (2012b), Process-evaluation of tropospheric humidity simulated by general circulation models using water vapor isotopic observations: 2. Using isotopic diagnostics to understand the mid and upper tropospheric moist bias in the tropics and subtropics, *Journal of Geophysical Research: Atmospheres*, *117*(D5), doi:10.1029/2011JD016623. 168

Roche, D., D. Paillard, and E. Cortijo (2004), Constraints on the duration and freshwater release of Heinrich event 4 through isotope modelling, *Nature*, *432*(7015), 379–382. 169

Rogers, R. R., and M. K. Yau (1996), *A short course in cloud physics*, Elsevier. 39, 154, 166

Rokotyan, N. V., V. I. Zakharov, K. G. Gribanov, M. Schneider, F.-M. Bréon, J. Jouzel, R. Imasu, M. Werner, M. Butzin, C. Petri, T. Warneke, and J. Notholt (2014), A posteriori calculation of δ^{18}O and δD in atmospheric water vapour from ground-based near-infrared

FTIR retrievals of $H_2{}^{16}O$, $H_2{}^{18}O$, and $HD^{16}O$, *Atmospheric Measurement Techniques*, *7*(8), 2567–2580, doi:10.5194/amt-7-2567-2014. 168

Rozanski, K., L. Araguás-Araguás, and R. Gonfiantini (1993), Isotopic patterns in modern global precipitation, *Climate change in continental isotopic records*, *78*, 1–36. 2

Schmidt, G. A., G. Hoffmann, D. T. Shindell, and Y. Hu (2005), Modeling atmospheric stable water isotopes and the potential for constraining cloud processes and stratosphere-troposphere water exchange, *Journal of Geophysical Research: Atmospheres*, *110*(D21). 169

Schmidt, G. A., A. N. LeGrande, and G. Hoffmann (2007), Water isotope expressions of intrinsic and forced variability in a coupled ocean-atmosphere model, *Journal of Geophysical Research: Atmospheres*, *112*(D10), doi:10.1029/2006JD007781. 169

Schneider, M., S. Barthlott, F. Hase, Y. González, K. Yoshimura, O. E. García, E. Sepúlveda, A. Gomez-Pelaez, M. Gisi, R. Kohlhepp, S. Dohe, T. Blumenstock, A. Wiegele, E. Christner, K. Strong, D. Weaver, M. Palm, N. M. Deutscher, T. Warneke, J. Notholt, B. Lejeune, P. Demoulin, N. Jones, D. W. T. Griffith, D. Smale, and J. Robinson (2012), Ground-based remote sensing of tropospheric water vapour isotopologues within the project MUSICA, *Atmospheric Measurement Techniques*, *5*(12), 3007–3027, doi:10.5194/amt-5-3007-2012. 168

Seager, R. (2006), The Source of Europe's Mild Climate: The notion that the Gulf Stream is responsible for keeping Europe anomalously warm turns out to be a myth, *American Scientist*, *94*(4), 334–341. 15

Seager, R., D. S. Battisti, J. Yin, N. Gordon, N. Naik, A. C. Clement, and M. A. Cane (2002), Is the Gulf Stream responsible for Europe's mild winters?, *Quarterly Journal of the Royal Meteorological Society*, *128*(586), 2563–2586, doi:10.1256/qj.01.128. 15

Sodemann, H. (2006), Tropospheric transport of water vapour: Lagrangian and Eulerian perspectives, Ph.D. thesis, ETH Zurich, doi:10.3929/ethz-a-005215132. 10

Sodemann, H., and A. Stohl (2013), Moisture origin and meridional transport in atmospheric rivers and their association with multiple cyclones, *Monthly Weather Review*, *141*(8), 2850–2868. 17

Sodemann, H., C. Schwierz, and H. Wernli (2008a), Interannual variability of Greenland winter precipitation sources: Lagrangian moisture diagnostic and North Atlantic Oscillation influence, *Journal of Geophysical Research: Atmospheres (1984–2012)*, *113*(D3). 34

Sodemann, H., V. Masson-Delmotte, C. Schwierz, B. M. Vinther, and H. Wernli (2008b), Interannual variability of Greenland winter precipitation sources: 2. Effects of North Atlantic Oscillation variability on stable isotopes in precipitation, *Journal of Geophysical Research: Atmospheres (1984–2012)*, *113*(D12). 34

Sodemann, H., F. Aemisegger, S. Pfahl, M. Bitter, U. Corsmeier, T. Feuerle, P. Graf, R. Hankers, G. Hsiao, H. Schulz, A. Wieser, and H. Wernli (2017), The stable isotopic composition of water vapour above Corsica during the HyMeX SOP1 campaign: insight into vertical mixing processes from lower-tropospheric survey flights, *Atmospheric Chemistry and Physics*, *17*(9), 6125–6151, doi:10.5194/acp-17-6125-2017. 3

Steen-Larsen, H., A. Sveinbjörnsdottir, T. Jonsson, F. Ritter, J.-L. Bonne, V. Masson-Delmotte, H. Sodemann, T. Blunier, D. Dahl-Jensen, and B. Vinther (2015), Moisture sources and synoptic to seasonal variability of North Atlantic water vapor isotopic composition, *Journal of Geophysical Research: Atmospheres*, *120*(12), 5757–5774. 2, 9, 42, 168

Steen-Larsen, H. C., A. E. Sveinbjörnsdottir, A. J. Peters, V. Masson-Delmotte, M. P. Guishard, G. Hsiao, J. Jouzel, D. Noone, J. K. Warren, and J. W. C. White (2014a), Climatic controls on water vapor deuterium excess in the marine boundary layer of the North Atlantic based on 500 days of in situ, continuous measurements, *Atmospheric Chemistry and Physics*, *14*(15), 7741–7756, doi:10.5194/acp-14-7741-2014. 2, 9, 42, 168

Steen-Larsen, H. C., V. Masson-Delmotte, M. Hirabayashi, R. Winkler, K. Satow, F. Prié, N. Bayou, E. Brun, K. M. Cuffey, D. Dahl-Jensen, M. Dumont, M. Guillevic, S. Kipfstuhl, A. Landais, T. Popp, C. Risi, K. Steffen, B. Stenni, and A. E. Sveinbjörnsdottír (2014b), What controls the isotopic composition of Greenland surface snow?, *Climate of the Past*, *10*(1), 377–392, doi:10.5194/cp-10-377-2014. 40, 42

Steensen, B. M., H. Olafsson, and M. O. Jonassen (2011), An extreme precipitation event in Central Norway, *Tellus A: Dynamic Meteorology and Oceanography*, *63*(4), 675–686, doi:10.1111/j.1600-0870.2011.00522.x. 1

Stewart, M. K. (1975), Stable isotope fractionation due to evaporation and isotopic exchange of falling waterdrops: Applications to atmospheric processes and evaporation of lakes, *Journal of Geophysical Research*, *80*(9), 1133–1146. 12, 13, 39, 160, 164, 166, 167

Stohl, A., C. Forster, A. Frank, P. Seibert, and G. Wotawa (2005), Technical note: The Lagrangian particle dispersion model FLEXPART version 6.2, *Atmospheric Chemistry and Physics*, *5*(9), 2461–2474, doi:10.5194/acp-5-2461-2005. 34

Stohl, A., C. Forster, and H. Sodemann (2008), Remote sources of water vapor forming precipitation on the Norwegian west coast at 60°N–a tale of hurricanes and an atmospheric river, *Journal of Geophysical Research: Atmospheres (1984–2012)*, *113*(D5). 1, 17

Sturm, K., G. Hoffmann, B. Langmann, and W. Stichler (2005), Simulation of δ^{18}O in precipitation by the regional circulation model REMOiso, *Hydrological Processes*, *19*(17), 3425–3444, doi:10.1002/hyp.5979. 169

Sturm, P., and A. Knohl (2010), Water vapor δ^2H and δ^{18}O measurements using off-axis integrated cavity output spectroscopy, *Atmospheric Measurement Techniques*, *3*(1), 67–77. 168

Svensson, A., K. K. Andersen, M. Bigler, H. B. Clausen, D. Dahl-Jensen, S. M. Davies, S. J. Johnsen, R. Muscheler, F. Parrenin, S. O. Rasmussen, R. Roethlisberger, I. Seierstad, J. P. Steffensen, and B. M. Vinther (2008), A 60 000 year Greenland stratigraphic ice core chronology RID A-2643-2010 RID B-5560-2008, *Climate of the Past*, *4*(1), 47–57. 41

Tindall, J. C., P. J. Valdes, and L. C. Sime (2009), Stable water isotopes in HadCM3: Isotopic signature of El Niño–Southern Oscillation and the tropical amount effect, *Journal of Geophysical Research: Atmospheres*, *114*(D4), doi:10.1029/2008JD010825. 169

Uemura, R., Y. Matsui, K. Yoshimura, H. Motoyama, and N. Yoshida (2008), Evidence of deuterium excess in water vapor as an indicator of ocean surface conditions, *Journal of Geophysical Research: Atmospheres*, *113*(D19). 9

Uemura, R., V. Masson-Delmotte, J. Jouzel, A. Landais, H. Motoyama, and B. Stenni (2012), Ranges of moisture-source temperature estimated from Antarctic ice cores stable isotope records over glacial–interglacial cycles, *Climate of the Past*, *8*(3), 1109–1125, doi:10.5194/cp-8-1109-2012. 9, 40

van Geldern, R., and J. A. C. Barth (2012), Optimization of instrument setup and post-run corrections for oxygen and hydrogen stable isotope measurements of water by isotope ratio infrared spectroscopy (IRIS), *Limnology and Oceanography-methods*, *10*, 1024–1036, doi:10.4319/lom.2012.10.1024. 29

Vautard, R. (1990), Multiple weather regimes over the North Atlantic: Analysis of precursors and successors, *Monthly Weather Review*, *118*(10), 2056 – 2081, doi:10.1175/1520-0493(1990)118<2056:MWROTN>2.0.CO;2. 19

Wang, Y. J., H. Cheng, R. L. Edwards, Z. S. An, J. Y. Wu, C. C. Shen, and J. A. Dorale (2001), A high-resolution absolute-dated Late Pleistocene monsoon record from Hulu Cave, China, *Science*, *294*(5550), 2345–2348, doi:10.1126/science.1064618. 41

Ward, C. A., and D. Stanga (2001), Interfacial conditions during evaporation or condensation of water, *Phys. Rev. E*, *64*, 051,509, doi:10.1103/PhysRevE.64.051509. 159

Werner, M., M. Heimann, and G. Hoffmann (2001), Isotopic composition and origin of polar precipitation in present and glacial climate simulations, *Tellus B: Chemical and Physical Meteorology*, *53*(1), 53–71, doi:10.3402/tellusb.v53i1.16539. 169

Werner, M., P. M. Langebroek, T. Carlsen, M. Herold, and G. Lohmann (2011), Stable water isotopes in the ECHAM5 general circulation model: Toward high-resolution isotope modeling on a global scale, *Journal of Geophysical Research: Atmospheres*, *116*(D15), doi:10.1029/2011JD015681. 169

Wernli, H., and C. Schwierz (2006), Surface cyclones in the ERA-40 dataset (1958–2001). Part I: Novel identification method and global climatology, *Journal of the atmospheric sciences*, *63*(10), 2486–2507. 15

White, A. B., D. J. Gottas, E. T. Strem, F. M. Ralph, and P. J. Neiman (2002), An automated brightband height detection algorithm for use with Doppler radar spectral moments, *Journal of Atmospheric and Oceanic Technology*, *19*(5), 687–697. 23

White, A. B., P. J. Neiman, F. M. Ralph, D. E. Kingsmill, and P. O. G. Persson (2003), Coastal orographic rainfall processes observed by radar during the California Land-Falling Jets Experiment, *Journal of Hydrometeorology*, *4*(2), 264–282. 23

White, W. M. (2015), *Stable isotope geochemistry*, pp. 361–420, John Wiley & Sons. 6, 8

Wick, G. A., W. J. Emery, L. H. Kantha, and P. Schlüssel (1996), The behavior of the bulk – skin sea surface temperature difference under varying wind speed and heat flux, *Journal of Physical Oceanography*, *26*(10), 1969–1988, doi:10.1175/1520-0485(1996)026<1969:TBOTBS>2.0.CO;2. 159

Woollings, T., D. Barriopedro, J. Methven, S.-W. Son, O. Martius, B. Harvey, J. Sillmann, A. R. Lupo, and S. Seneviratne (2018), Blocking and its response to climate change, *Current climate change reports*, *4*(3), 287–300, doi:10.1007/s40641-018-0108-z. 18

Worden, J., K. Bowman, D. Noone, R. Beer, S. Clough, A. Eldering, B. Fisher, A. Goldman, M. Gunson, R. Herman, S. S. Kulawik, M. Lampel, M. Luo, G. Osterman, C. Rinsland, C. Rodgers, S. Sander, M. Shephard, and H. Worden (2006), Tropospheric Emission Spectrometer observations of the tropospheric HDO/H_2O ratio: Estimation approach and characterization, *Journal of Geophysical Research: Atmospheres*, *111*(D16), doi: 10.1029/2005JD006606. 168

Xi, X. (2014), A review of water isotopes in atmospheric general circulation models: Recent advances and future prospects, *International Journal of Atmospheric Sciences*, *2014*, Art–No, doi:10.1155/2014/250920. 168

Yankee Environmental Systems, Inc. (2011), *TPS-3100 Total Precipitation Sensor installation and user guide (version 2.0)*. 21

Yoshimura, K., M. Kanamitsu, D. Noone, and T. Oki (2008), Historical isotope simulation using reanalysis atmospheric data, *Journal of Geophysical Research: Atmospheres (1984–2012)*, *113*(D19). 41, 42, 167, 169

Yoshimura, K., M. Kanamitsu, and M. Dettinger (2010), Regional downscaling for stable water isotopes: A case study of an atmospheric river event, *Journal of Geophysical Research: Atmospheres*, *115*(D18). 3, 167, 168, 169

Yoshimura, K., T. Miyoshi, and M. Kanamitsu (2014), Observation system simulation experiments using water vapor isotope information, *Journal of Geophysical Research: Atmospheres*, *119*(13), 7842–7862. 2

Zhu, Y., and R. E. Newell (1998), A proposed algorithm for moisture fluxes from atmospheric rivers, *Monthly Weather Review*, *126*(3), 725–735, doi:10.1175/1520-0493(1998) 126<0725:APAFMF>2.0.CO;2. 15, 16, 17

Graphic design: Communication Division, UiB / Print: Skipnes Kommunikasjon AS

UNIVERSITAS BERGENSIS

uib.no

ISBN: 9788230849460 (print)
9788230842010 (PDF)